



UNIVERSITAT<sub>DE</sub>  
BARCELONA

## Memory-induced complex contagion in spreading phenomena on networks

Xavier Roderic Hoffmann



Aquesta tesi doctoral està subjecta a la llicència **Reconeixement- Compartlqual 4.0. Espanya de Creative Commons.**

Esta tesis doctoral está sujeta a la licencia **Reconocimiento - Compartirlqual 4.0. España de Creative Commons.**

This doctoral thesis is licensed under the **Creative Commons Attribution-ShareAlike 4.0. Spain License.**

PhD thesis

**Memory-induced complex contagion  
in spreading phenomena on networks**

Xavier Roderic Hoffmann



UNIVERSITAT DE  
BARCELONA



*Memory-induced complex contagion  
in spreading phenomena on networks*

Memòria presentada per optar al grau de doctor  
per la Universitat de Barcelona



Programa de doctorat: Física

Línia de recerca: Física de la Matèria Condensada

Autor: Xavier Roderic Hoffmann

Director: Dr. Marián Boguñá Espinal

Tutor: Dr. Giancarlo Franzese

Barcelona, juny 2021

A handwritten signature in black ink, consisting of a large, stylized 'X' followed by a horizontal line and a vertical line, with some additional scribbles.

Xavier Roderic Hoffmann



*a l'Anton i en Pep, i totes les meves professores*



Nunca nada será como antes, como siempre fue.

*José Enrique Ruiz-Domènec*

There's 360 degrees. Why stick to 1?

*Zaha Hadid*

Volen que faci el que els mola però jo no passo per el aro.

*Lildami*



# Acknowledgments

To Marián,  
for his valuable counsel and continued guidance,

to my fellow *lileros*, *becadis*, *zuleros*, *clabbers*, and *dribios*,  
for their emotional support,

to my parents,  
for their financial support,

to the gobeernment and the conwinement,  
for their timely encouragement and inspiration,

to my family, friends, and colleagues:

thank you, gràcies, dankuwel, gracias, Danke.



# Abstract

Epidemic modeling has proven to be an essential framework for the study of contagion phenomena in biological, social, and technical systems. Albeit epidemic models have evolved into powerful predictive tools, most assume memoryless agents and independent transmission channels. Nevertheless, many real-life examples are manifestly time-sensitive and show strong correlations. Moreover, recent trends in agent-based modeling support a generalized shift from edge-based descriptions toward node-centric approaches.

Here I develop an infection mechanism that is endowed with memory of past exposures and simultaneously incorporates the joint effect of multiple infectious sources. A notion of social reinforcement/inhibition arises organically, without being incorporated explicitly into the model. As a result, the concepts of non-Markovian dynamics and complex contagion become intrinsically coupled. I derive mean-field approximations for random degree-regular networks and perform extensive stochastic simulations for nonhomogeneous networks.

The analysis of the SIS model reveals a sophisticated interplay between two memory modes, displayed by a collective memory loss and the dislocation of the critical point into two phase transitions. An intermediate region emerges where the system is either excitable or bistable, exhibiting fundamentally distinct behaviors compared to the customary healthy and endemic phases. Additionally, the transition to the endemic phase becomes hybrid, showing both continuous and discontinuous properties.

These results provide renewed insights on the interaction between microscopic mechanisms and topological aspects of the underlying contact networks, and their joint effect on the properties of spreading processes. In particular, this type of modeling approach that combines memory effects and complex contagion could be suitable to describe ecological interactions between biological and social pathogens.



# Resum

El modelatge epidèmic ha demostrat ser un marc essencial per a l'estudi dels fenòmens de contagi en sistemes biològics, socials i tècnics. Tot i que els models epidèmics han evolucionat cap a potents eines de predicció, la majoria assumeixen agents sense memòria i canals de transmissió independents. No obstant això, molts exemples de la vida real mostren fortes correlacions temporals i estructurals. A més, les tendències recents en la modelització basada en agents donen suport a un canvi generalitzat de les descripcions basades en els enllaços cap a enfocaments on els nodes són centrals.

Aquí desenvolupo un mecanisme d'infecció dotat de memòria a exposicions passades i que simultàniament incorpora l'efecte conjunt de múltiples fonts infeccioses. Una noció de reforç/inhibició social sorgeix de manera orgànica, sense incorporar-se explícitament al model. Com a resultat, els conceptes de dinàmica no markoviana i contagi complex s'acoblen intrínsecament. Derivo aproximacions de camp mitjà per a xarxes aleatòries de grau fix i realitzo extenses simulacions estocàstiques per a xarxes no homogènies.

L'anàlisi del model SIS revela una interacció sofisticada entre dos modes de memòria, que es manifesta mitjançant una pèrdua de memòria col·lectiva i la dislocació del punt crític en dues transicions de fase. Apareix una regió intermitja on el sistema és excitable o bistable, amb comportaments fonamentalment diferents en comparació amb les fases sanes i endèmiques habituals. A més, la transició a la fase endèmica esdevé híbrida, mostrant propietats contínues i també discontinües.

Aquests resultats proporcionen una visió renovada sobre la interacció entre mecanismes microscòpics i aspectes topològics de les xarxes de contacte subjacents, i el seu efecte conjunt sobre les propietats dels processos de propagació. En particular, aquest tipus de modelització que combina efectes de memòria i contagi complex podria ser adequat per descriure interaccions ecològiques entre patògens biològics i socials.



# Contents

<b>Acknowledgments</b>	<b>ix</b>
<b>Abstract</b>	<b>xi</b>
<b>Resum</b>	<b>xiii</b>
<b>1 Introduction</b>	<b>1</b>
1.1 The history of epidemiology . . . . .	1
1.2 Mathematical modeling of infectious diseases . . . . .	2
1.3 Network epidemiology . . . . .	5
1.4 Spreading beyond infectious diseases . . . . .	7
1.5 The assumption of Markovianity . . . . .	10
1.6 Thesis outline . . . . .	11
<b>2 The SI model</b>	<b>13</b>
2.1 Standard SI model . . . . .	13
2.1.1 Analytic approximation . . . . .	14
2.1.2 Random degree-regular networks . . . . .	15
2.1.3 Gillespie algorithm . . . . .	16
2.2 Memory-induced complex contagion SI model . . . . .	18
2.2.1 Infection probabilities and interevent times . . . . .	19
2.2.2 Weibull distribution . . . . .	21
2.2.3 Simple and complex contagion . . . . .	22
2.2.4 Analytic approximation . . . . .	25
2.2.5 Non-Markovian Gillespie algorithm . . . . .	27
2.2.6 Discussion . . . . .	28
<b>3 The SIR model</b>	<b>31</b>
3.1 Standard SIR model . . . . .	31
3.1.1 Transient and late-time behavior . . . . .	32
3.1.2 Simulation results . . . . .	33
3.2 Memory-induced complex contagion SIR model . . . . .	33
3.2.1 Dormant nodes . . . . .	34
3.2.2 Parameter selection . . . . .	35

3.2.3	Late-time and transient behavior . . . . .	37
3.2.4	Discussion . . . . .	39
<b>4</b>	<b>The SIS model</b>	<b>43</b>
4.1	Standard SIS model . . . . .	43
4.1.1	Analytic approximation . . . . .	44
4.1.2	Late-time limit and mean-field approximation . . . . .	45
4.1.3	Simulation results . . . . .	46
4.2	Memory-induced complex contagion SIS model . . . . .	49
4.2.1	Short-term memory . . . . .	51
4.2.2	Long-term memory . . . . .	59
4.2.3	Medium-term memory . . . . .	67
4.2.4	Discussion . . . . .	78
<b>5</b>	<b>Nonhomogeneous networks</b>	<b>81</b>
5.1	Network topology . . . . .	81
5.2	Clustering . . . . .	83
5.3	Node heterogeneity . . . . .	86
5.4	Discussion . . . . .	87
<b>6</b>	<b>The voter model</b>	<b>91</b>
6.1	Standard voter model . . . . .	91
6.1.1	Continuous-time opinion transmissions . . . . .	92
6.1.2	Simulation results . . . . .	94
6.2	Memory-induced complex contagion voter model . . . . .	94
6.2.1	Simulation results . . . . .	96
6.2.2	Discussion . . . . .	99
<b>7</b>	<b>Airport delays</b>	<b>101</b>
7.1	Dataset description and exploratory analysis . . . . .	101
7.2	Delays, infective periods, and infectors . . . . .	104
<b>8</b>	<b>Conclusions</b>	<b>111</b>
8.1	Background . . . . .	111
8.2	Results . . . . .	113
8.3	Outlook . . . . .	116
<b>A</b>	<b>Mathematical derivations</b>	<b>119</b>

<b>Contents</b>	<b>xvii</b>
<hr/>	
<b>B Synthetic networks</b>	<b>139</b>
<b>C Computational implementations</b>	<b>141</b>
<b>D Supplementary figures</b>	<b>157</b>
<b>References</b>	<b>163</b>



# Introduction

---

## 1.1 The history of epidemiology

Since its dawning, humankind has endured the burden of disease. The earliest evidence of smallpox, for example, traces back to 3rd century BCE Egyptian mummies [28]; however, it is believed to have appeared in the first agricultural settlements around 6000 BCE [86]. Despite major improvements in public health management, humanity of the 21st is far from overcoming the hurdle of infectious diseases. Global warming has driven the spread of malaria, dengue, and yellow fever into new regions [175, 137]. Misuse and overuse of antibiotics has accelerated the appearance of drug-resistant strains of tuberculosis, pneumonia, and ghonorrea [178]. And the ongoing AIDS and COVID-19 pandemics leave no doubt about the latent threat of novel infections [62, 49].

For centuries, shamans, menders, doctors, and scientists have attempted to fathom the outbreak and spread of these illnesses. Besides curing the sick, they devised and evaluated strategies such as inoculation and isolation plans in order to reduce mortality rates. Over the years, epidemiology became a cornerstone of public health and preventive medicine. Nowadays, epidemic modeling is one of the principal tools to study the spreading mechanisms of pathogens, predict the evolution of an outbreak, and assess containment protocols.

The first systematic epidemiological study appeared in 1662, when John Graunt published his analysis of births, deaths, and causes of death in London [146, 50]. A pioneer in demography and descriptive analytics, he presented one of the first life-tables and reported time-trends for many diseases.<sup>1</sup> Almost a century later, Europe was immersed in a devastating smallpox epidemic. Motivated by the controversy surrounding mass inoculation in France, Daniel Bernoulli developed a revolutionary analytical approach to quantify the benefits of eradicating the disease [58, 13]. His 1766 paper concluded that, in

---

<sup>1</sup>He also refuted the idea that plague outbreaks coincide with the reign of a new monarch.

absence of smallpox, the life expectancy at birth in Breslau would increase by around 3 years, and that the median age of the population would jump from about 11.5 to 25.5 years.

This brief review of early advances ends with John Snow, often credited as the founder of modern epidemiology. His investigations during the 1854 London cholera outbreak identified a well in Soho as the source of one of the infection hotspots [154, 71]. Although he lacked conclusive biological evidence about the harm posed by the water, the cluster of affected households around the water pump persuaded the local authorities to disable it (see Fig. 1.1). His work also refuted the then-prevailing miasma theory [105], which blamed high infection rates in impoverished areas on bad air quality instead of addressing the underlying issues of poor nutrition and sanitation.

## 1.2 Mathematical modeling of infectious diseases

The previous examples—as well as many other efforts—preceded the development of modern germ theory during the late 19th century [21]. A major breakthrough came with the ability to differentiate infectious diseases, which can be passed between individuals (for instance, influenza), from noninfectious diseases, which develop over an individual’s lifespan (think about arthritis, for example). In addition, advances in microbiology allowed to classify pathogens as either micro- or macroparasitic. The former are small (usually single-cell) organisms such as viruses, bacteria, protoza, or prions. The latter are any larger form of pathogens, including helminths, flukes, and other parasitic worms. Macroparasites exhibit a complex life-cycle within the host, which must be modeled explicitly. In contrast, microparasitic infections develop rapidly, so the internal dynamics of the pathogen within the host can often be safely ignored [98].

The comprehensive understanding of the biology behind the spread of infections allowed for evermore sophisticated models, which lead to the establishment of epidemiology as a core pillar of preventive medicine. Over time, the increasing demand in statistical rigor attracted a variety of scientists and prompted the foundation of a new interdisciplinary subfield, nowadays identified as mathematical epidemiology. For instance, in their attempt to describe the recurrence of measles outbreaks, Pyotr Dimitrievich En’ko (in 1899) and William Hamer (in 1906) independently introduced the hypothesis of homo-

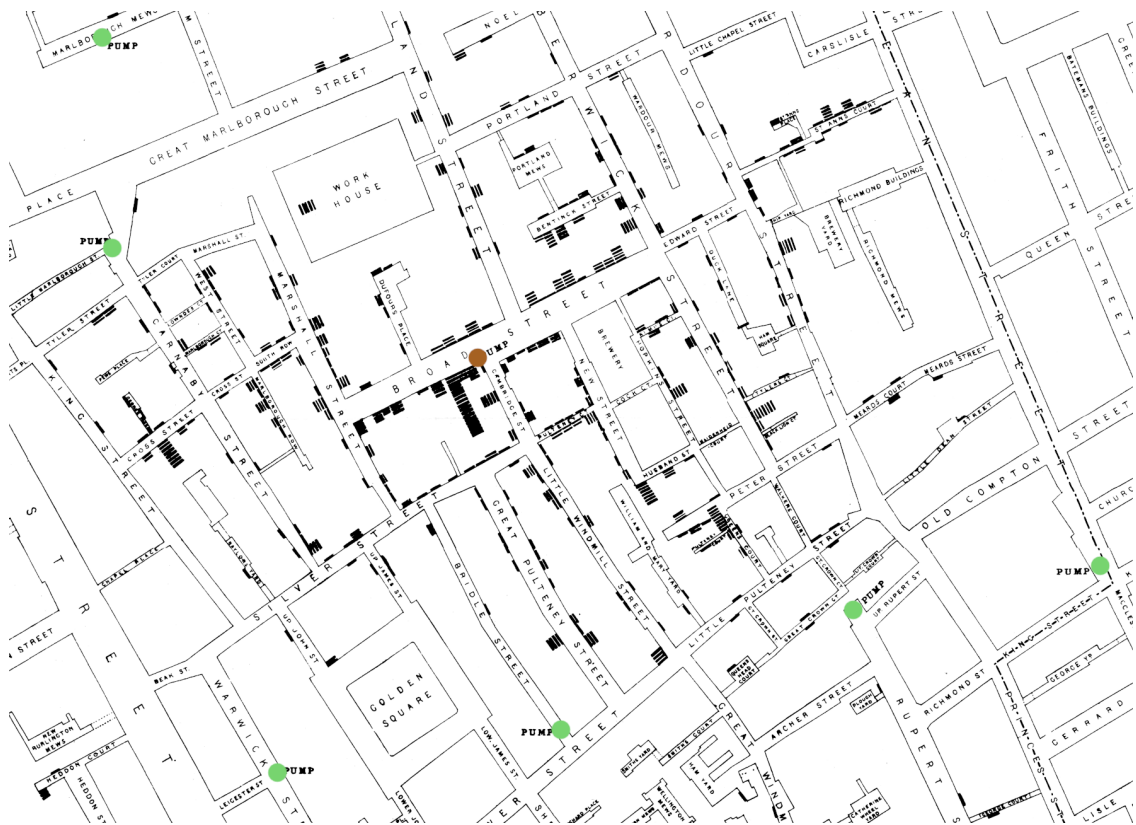


Figure 1.1: **1854 Broad Street cholera outbreak.** Aided by Reverend Henry Widehead, John Snow tracked down the homes of the deceased (black stacks) and identified a pump on Broad Street as the source of the Soho outbreak (brown dot, other nearby pumps in green). It was later discovered that the public well had been dug less than a meter from an old cesspit that had begun to leak fecal bacteria. Map originally published in [154], adapted from [153].

geneous mixing [63, 50, 86, 152]. Inspired by the law of mass action, they assumed individuals interact uniformly with all others. Nobel Prize winner Ronald Ross used a similar approach in 1911, when he developed a host-vector model for the transmission of malaria between mosquitos and humans [86, 21].

The establishment of epidemic modeling is usually attributed to Kermack and McKendrick, who published a series of seminal papers between 1927 and 1933 [99, 100, 101]. In short, their modeling scheme consists in i) dividing the population into a discrete number of categories (i.e., homogeneous compartments), ii) translating all biological properties of the disease into mathematical parameters, and iii) specifying the rules that govern the transitions between compartments (see Fig. 1.2). The success of their approach lies in the balance

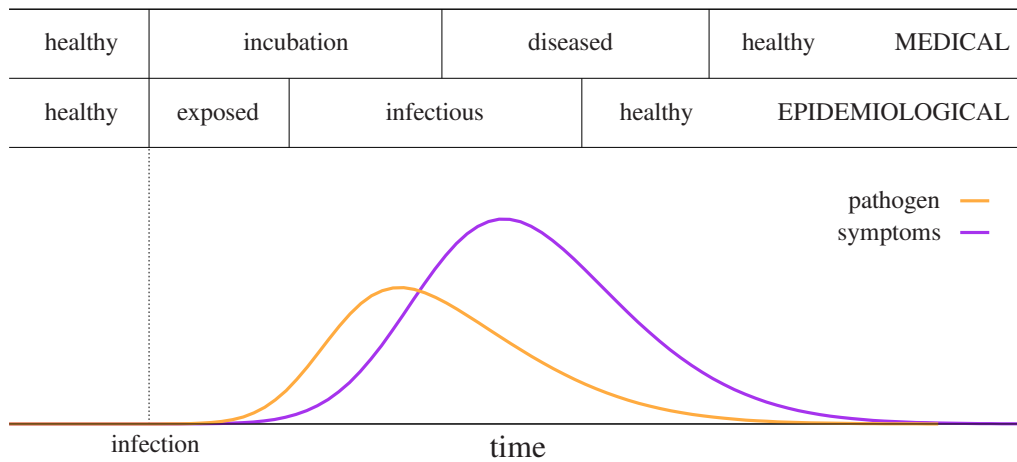


Figure 1.2: **Timeline and stages of an infection.** Schematic evolution of the pathogen dynamics (orange) and host immune response (purple). Medically, the host becomes diseased after a period of incubation. From an epidemiological point of view, the host first undergoes an exposed period, during which it is not yet infectious. Note that medical and epidemiological compartments are not necessarily correlated.

between generality and simplicity; this versatility allows to study a large variety of pathologies and gauge the effect of different preventive interventions. Nevertheless, the use of differential equations implicitly assumes continuous variables, which presents a major drawback when (some of) the population groups are small. For these cases, the model developed by Reed and Frost is more suitable [74, 72]. First mentioned in a Cutter lecture at Harvard in 1928, it was not deemed worthy of publishing by the authors.<sup>2</sup> Their microscopic, probabilistic approach provided an easy mapping between stochastic and deterministic formalisms, a feature that proved fundamental for later developments.

Mathematical epidemiology experienced a surge in the mid-to-late 20th century [6, 4]. The possibility of including a wide array of factors, such as age, birth, death, migration, or immunity, allowed for evermore sophisticated and accurate models [98]. A noteworthy development was the ability to thoroughly evaluate inoculation strategies, which could aid in achieving herd immunity. These theoretical advances led to the design of aggressive, global vaccina-

<sup>2</sup>In fact, it did not appear in print until 1976.

tion programs. Success—and worldwide joy—arrived on May 8, 1980, when the 33rd World Health Assembly officially declared the eradication of smallpox [28]. Nowadays, compartmental-like models remain the starting point of the majority of research efforts.

## 1.3 Network epidemiology

The birth of network science in the late 90s revolutionized many fields, including epidemiology. Old-fashioned homogeneous mixing was gradually replaced by the idea that individuals interact with a limited number of peers. This is nicely represented through a network: a collection of nodes that are connected by a set of links [1, 123]. As it turns out, the structural properties of the underlying contact network play an essential role when it comes to disease propagation.

One of the first important findings was that many real-life networks are small-world [173]. This means that i) my contacts usually also interact between them,<sup>3</sup> and ii) I can reach any other individual with the help of only a small number of intermediary contacts.<sup>4,5</sup> In terms of spreading, the small-world effect significantly increases the propagation speed; consequently, weaker pathogens are able to evolve into endemic outbreaks. Another pioneering result was the discovery of fat-tailed distributions in real-life networks. While the large majority of individuals have very little contacts, only a handful are connected to many others. This scale-free property was found in a wide variety of social [142, 108], biological [114, 92], and technical systems [67, 2, 89]. A new, suitably modified theoretical framework showed that the epidemic threshold vanishes in scale-free networks, implying that even the weakest infection could cause a persistent outbreak [134].<sup>6</sup>

Faced with the threat of super-weak—but-mega-destructive pathogens, one could be tempted to give up on transmission-reducing interventions. Taking a look at the implications for vaccinations, however, reveals a much brighter picture. If we select individuals randomly, we would have to immunize 95% of

---

<sup>3</sup>In technical words, the networks have high clustering.

<sup>4</sup>In technical words, the networks have a small diameter.

<sup>5</sup>In the field of sociology, this feature was discovered in 1967 by Milgram in his famous “six degrees of separation” experiment [116, 160].

<sup>6</sup>This striking result sparked a heated debate between theorists and experimentalists alike [61, 16, 95, 149].

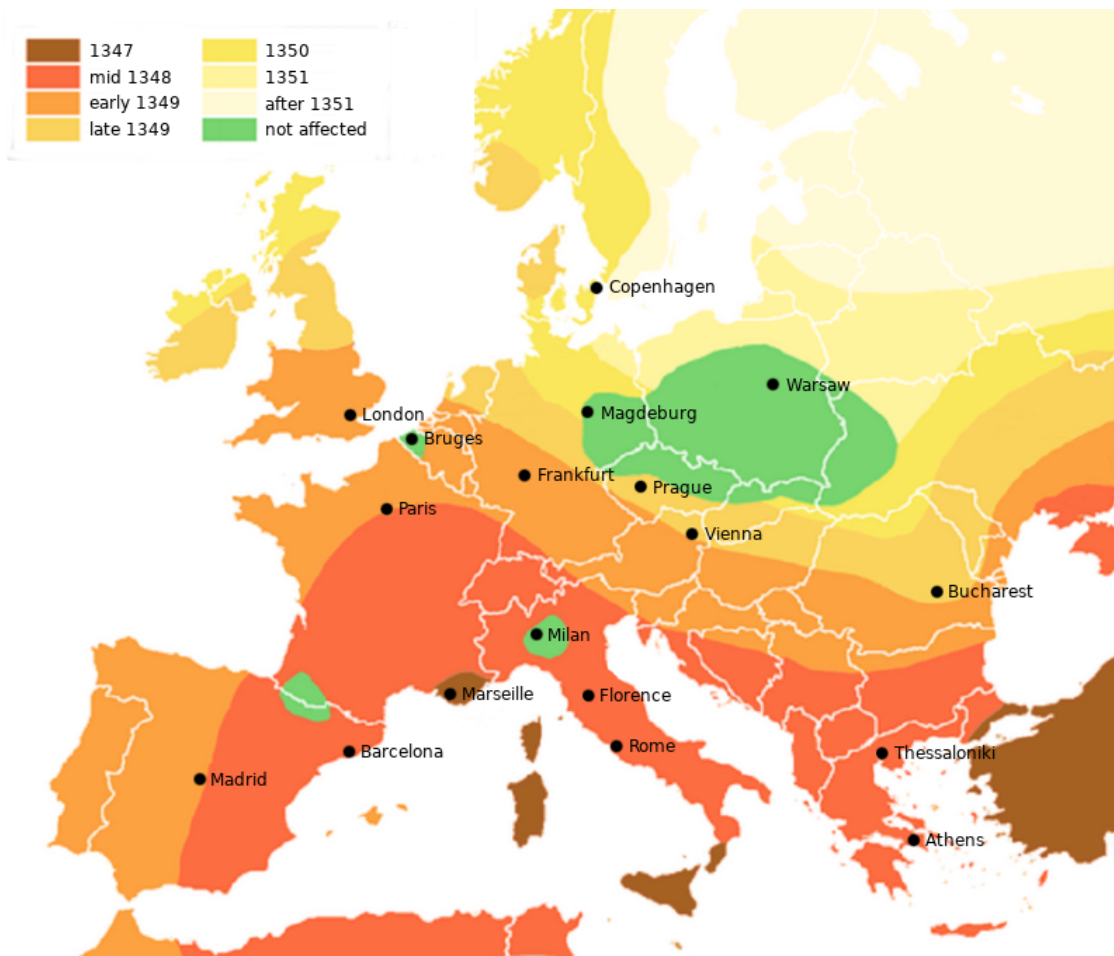


Figure 1.3: **Spread of the bubonic plague in Europe.** Merchant ships fleeing the Crimean port city of Kaffa transported the disease to Constantinople, Venice, Messina, Genoa, and Marseille. From there it slowly spread over land at an almost constant pace (see dates in legend). Green indicates areas with little or no incidence; white lines correspond to contemporary borders. Cities are included for reference. Image derived from [181].

the population in order to eradicate measles [4]. Similarly, random immunization strategies for computer viruses would require to install the appropriate antivirus software on more than 99% of devices [136]. On the other hand, only a small number of nodes would need to be inoculated if we choose those with the highest number of connections [135, 57]. Unfortunately, this targeted strategy requires a detailed map of the interactions, which we often lack. An alternative is acquaintance immunization, where we start at a random node and proceed iteratively by randomly selecting one of their neighbors [42]; given

the topological properties of the contact network we only need a few steps to reach a highly connected individual. By replicating this procedure in multiple parts of the network, eradication can be achieved with an immunization rate as low as 30%.

Killing an estimated 200 million people world-wide, the Black Death is the deadliest pandemic recorded in human history [54]. People in the 14th century traveled by land and water, causing a slow, wave-like propagation of the bubonic plague (see Fig. 1.3). In our day and age, airplanes take us to the other side of the Earth in no time, and diseases fly with us [44, 43]. The potential dangers derived from an evermore globalized world materialized during the 2003 SARS epidemic. Being the first outbreak to be monitored live by the scientific community, thorough analysis of the disease dynamics and spreading patterns has demonstrated the crucial role played by human mobility (see Fig. 1.4). For example, 144 of Singapore's 206 cases (roughly 70%) were traced back to the wanderings of only four superspreaders [112, 125].

Luckily, the widespread use of digital technologies has enabled the acquisition of detailed, multi-scale mobility data. Combined with the theoretical advances of network epidemiology, this has led to the development of powerful predictive tools such as the global epidemic and mobility (GLEAM) project [8, 9]. This team of scientists was successful in forecasting the peak of the 2009 swine flu pandemic—two months in advance [10, 159]. Additionally, these comprehensive models allow to accurately gauge and quantify preventive interventions such as travel bans. For example, the 40% drop in air traffic to and from Mexico delayed the global spread of the swine flu by only 2 days. Moreover, if restrictions had reached 90% the outbreak would have simply been shifted by 2 weeks [7]. Although still in its infancy, predictive epidemic modeling has consistently proven its potential<sup>7</sup> and is gradually becoming an indispensable tool to inform and shape public health policies.

## 1.4 Spreading beyond infectious diseases

As I mentioned in passing in the previous section, epidemic modeling can be straightforwardly applied to the propagation of digital viruses in computers and mobile devices [170, 180]. Nonetheless, the framework can be adapted

---

<sup>7</sup>Some examples are the 2012–2014 MERS [141] and 2015–2016 Zika [182] outbreaks, or the on-going COVID-19 pandemic [33].

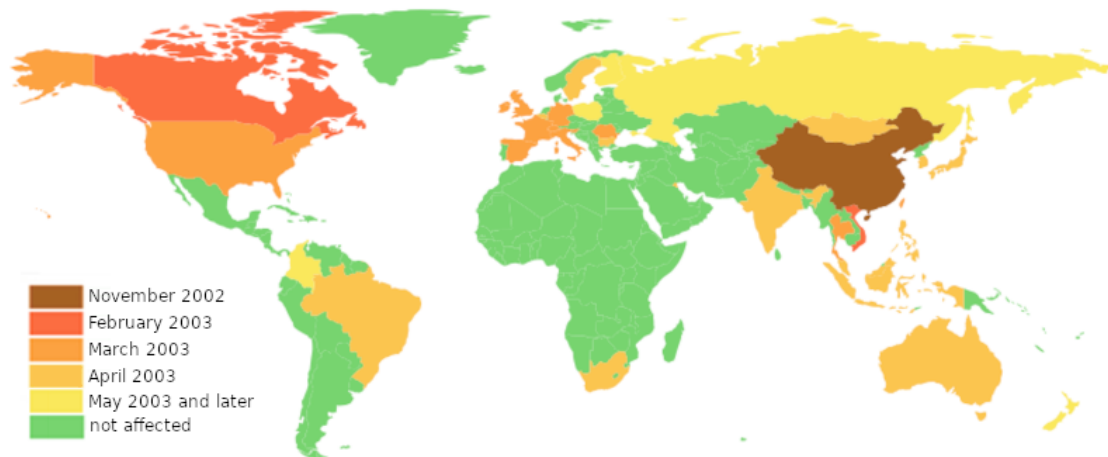


Figure 1.4: **Worldwide spread of the 2003 SARS epidemic.** The outbreak was first identified in mid November 2002 in Foshan, China; the disease had been exported to Vietnam and Canada by the end of February 2003. A few months later, cases had been confirmed in Brazil, Colombia, South Africa, United States, and various countries in Asia, Europe, and Oceania (see dates in legend). Green indicates countries that were not affected. Based on data from [56].

to a variety of “pathogens”. Already in the 1960s various studies explored the mapping from diseases to information and rumors [79, 50]. In recent years, this approach has been redirected toward the spread of true and fake news [94, 167] and the circulation of memes and viral content on social media [5, 174]. Another relevant topic is the diffusion of social, cultural, and technological innovations. Examples include the uptake of menstrual cups [130], the adoption of VoIP services [96], and the dissemination of scientific advances [12, 55]. Last but not least, spreading phenomena also occur in sociotechnical systems. Typical cases are routing and congestion in communication networks [126], and the spread of cascading failures in power networks [145].

Albeit their similarities, biological and social contagions are fundamentally distinct [30, 29]. While repeated contact with an infected individual can increase the likelihood of catching the disease, this is not the case when we think about the adoption of a novel technology. For instance, I would never buy a fax machine if only one of my friends owned one—even if they insisted on repeated occasions. However, if my whole group of friends switched to faxing I would need to buy one in order to stay in touch. Therefore we distin-

guish simple contagion, for which a single contact may suffice, from complex contagion, which requires reinforcement from distinct contacts.<sup>8</sup>

These two contagion mechanisms interact very differently with the meso-scale structure of the underlying network. Real networks are organized in communities; roughly speaking, nodes are more densely linked within their community than outside of it [73]. On one hand, links between communities (weak ties) allow simple contagions to permeate the network more rapidly [82, 127]. On the other, the existence of links within a community (strong ties) facilitates social reinforcement, as required by complex contagion [30, 20, 174]. Combining spreading mechanisms with network topologies offers a virtually endless array of possibilities, as reflected by the vast amount of modeling schemes that have appeared in the last decade (see [26, 84] for examples).

Earlier I described the diffusion of news, information, and ideas, but I purposely omitted the topic of opinion formation. For example, imagine that you and I have opposing opinions about a particular issue. Through dialog and discussion, each of us can cause the other to switch their opinion; i.e., both you and I can transmit our opinion. However, this is not the case for infections. While an infected individual is capable of transmitting the pathogen to its contacts, a healthy individual is unable to spread antibodies that can heal the ill. From a modeling point of view, opinions are symmetric and contagious diseases are not. This fundamental difference warranted the development of a parallel field of spreading phenomena, generically identified as opinion dynamics [26]. One of the most noteworthy contributions is the voter model, which describes the formation of opinions by random imitation [40, 88]. Recently, this simple mechanism was used to explain the statistical fluctuations observed in 1980–2012 U.S. presidential elections [70].

Unfortunately, the simplicity of mathematical models is often overthrown by the complexities of human behavior. In 2016, 74% of world-wide deaths were due to noncommunicable diseases (NCDs); i.e., pathologies that are not transmitted through an infectious agent [177]. That same year, the lead cause of death was cardiovascular disease, accounting for a staggering 27% of global deaths. This and other NCDs are associated to unhealthy practices such as smoking, excessive alcohol consumption, or lack of exercise. These risk factors possess a high social component: people smoke and drink more abundantly at social gatherings, and physical activity is often performed in

---

<sup>8</sup>Interestingly, some memes spread as simple pathogens while others are governed by the rules of complex contagion [174].

groups. Research has shown that bad health attitudes such as obesity [37], smoking [38], and substance abuse [39] are transmitted as a complex contagion and facilitate contracting NCDs. Additionally, the coupling between opinion dynamics and disease propagation is very relevant in the context of social awareness. For instance, the dissemination of prophylactic measures for preventing HIV [41], initiatives to quit smoking [122], or mass vaccination campaigns [81] are heavily reliant on their acceptance by the general public; resistance by rebel factions (e.g., anti-vaccination movements) can cause tremendous harm in terms of public health [148, 25]. Finally, studies have shown competitive dynamics between positive (jogging) and negative (smoking) health practices [104]. Altogether, these advances pave the way toward a framework of ecological interactions among lifestyle choices, health attitudes, and biological pathogens.

## 1.5 The assumption of Markovianity

The evolution of epidemic outbreaks is highly nondeterministic; therefore, their randomness can be adequately modeled via stochastic processes. The Markov property requires that the conditional probability of future states, conditioned on both past and present states, depends only on the present state; the sequence of preceding events is irrelevant. Stochastic processes that satisfy the Markov property are called Markovian or, in less technical jargon, memoryless; mathematically, they are characterized by exponential interevent time distributions [48, 83].

A widespread approach when modeling spreading phenomena is to assume Markovian dynamics; nevertheless, empirical observations contrast starkly with this assumption. The clearest evidence is found for infectious periods, i.e., the lag between infection and recovery: instead of being exponentially distributed, recovery times typically follow a bell curve and have a well-defined average and bounded spread<sup>9</sup> [123]. Additionally, nonexponential incubation periods<sup>10</sup> have been measured for HIV [14], Ebola [36], and foot-and-mouth disease and smallpox [157]. On the other hand, social contagion is strongly influenced by the fact that human activity patterns are predominantly bursty, showing stretches of high activity separated by long periods of inactivity [168,

---

<sup>9</sup>For example, 2–7 days in the case of dengue fever [176].

<sup>10</sup>The lag between being exposed and being infectious.

169]. Mathematically, this translates into heavy-tailed interevent time distributions,<sup>11</sup> which have been found in email responses, online gaming sessions, and financial transactions [97].

Although acknowledging the blatant discordance between model and data, most research efforts continue to apply the Markovian assumption. The reason for this apparent contradiction is simple: non-Markovian dynamics are much harder to tackle; their analytic tractability is low, and their computational complexity is high. Recent advances in terms of processing capacity have encouraged some researchers to surmount this hindrance. These early explorations have yielded promising results and lead the way toward a scarcely explored but potentially transformative area of epidemic modeling.

## 1.6 Thesis outline

Roughly speaking, the forefront of research in epidemic spreading can be divided in three areas. In terms of modeling transmission mechanisms, the current focus is on cooperation and competition between pathogens [31, 140, 90]. These ecological interactions are also of prominent interest in social contagion [121, 93] and coupled opinion-disease dynamics [75, 161]. Regarding the topological properties of the underlying contact structures, attention is distributed among embeddings and metric spaces [22, 129, 76], multilayer [53, 51, 138] and temporal networks [158, 162, 163, 140, 179], and descriptions that go beyond pairwise interactions [91, 11]. Finally, concerning the technical details of the temporal dynamics, many efforts are directed toward overcoming the assumption of Markovianity. This can be achieved by introducing nonexponential recoveries [103, 52, 109] or infections [165, 155, 110, 164], or both [102, 151, 68]. Alternatively, memory effects can be included indirectly. For instance, through two-step infection processes [35, 34], time-varying transmission probabilities [59, 113, 171, 183], or non-Markovian activation times in temporal networks [158, 179].

This thesis contributes to the examination of memory effects in spreading phenomena. However, the premise is to deviate from the typical framework of edge-based transmissions and recast the infection process as a node-centric mechanism. In short, the memory-induced complex contagion model describes individuals that aggregate past exposures to multiple infectious sources.

---

<sup>11</sup>By definition, heavy-tailed distributions are not well described by an exponential.

A notion of social reinforcement/inhibition arises organically, and the concepts of non-Markovian dynamics and complex contagion become intrinsically coupled. This combined approach could be particularly suitable to describe ecological interactions between biological and social pathogens. Notwithstanding, the motivation behind this research is of a more theoretic nature. Besides exploring potentially novel phenomenology, this work also challenges and validates the robustness of established modeling assumptions.

The focus of the thesis is the systematic analysis of the memory-induced complex contagion infection mechanism and its interaction with other components and properties of various spreading phenomena. I begin in Chapter 2 with the SI model, the simplest description of epidemic spreading, where the only possible transition is from healthy to infected. Afterward, in Chapter 3 agents are allowed to recover (SIR model), and I include reinfections (SIS model) in Chapter 4. Throughout the thesis, I combine analytic approximations with extensive simulations. Chapter 5 is dedicated to studying the interplay with nonhomogeneous network topologies, and in Chapter 6 I explore the effects of the memory-induced complex contagion mechanism in the voter model, a paradigmatic description of opinion dynamics. Chapter 7 investigates the merits and shortcomings of epidemic modeling by analyzing an empirical dataset of airport delays. Finally, Chapter 8 summarizes the results and comments on potential ways forward. Regarding additional material, mathematical derivations are detailed in Appendix A, and Appendix B provides notes on the generation of synthetic networks. Furthermore, Appendix C outlines various computational implementations, and supplementary figures are included in Appendix D.

As I mentioned earlier, epidemic-like models are employed for a variety of dynamics, such as opinion formation, rumor spreading, and innovation adoption. Although I use the original disease-specific terminology throughout this work, the scope and applicability of the analysis extends to all these fields.

# The SI model

---

## 2.1 Standard SI model

The susceptible-infected (SI) model describes a population of individuals that can be either susceptible (healthy) or infected (infectious). Infected agents transmit the pathogen to their susceptible nearest-neighbors, which forever remain in the infected state (they cannot recover). The population is embedded on a contact network, encoded by the adjacency matrix  $\mathbf{a}$ . In this work we limit our analysis to undirected and unweighted networks, hence  $a_{ij} = a_{ji} = 1$  if nodes  $i$  and  $j$  are connected and  $a_{ij} = 0$  otherwise. Moreover, the network is nonspatial (it carries no information about the agents' physical position) and static (it remains fixed over time). A typical application of the SI model is innovation diffusion, where individuals that have adopted a new technology are modeled as infected, and susceptible agents refer to individuals that have not yet adopted the innovation.

Consider  $i$  and  $j$ , a pair of healthy neighbors. At time  $t = 0$ , node  $i$  becomes infected and the transmission from  $i$  to  $j$  is activated. Inevitably, at some time  $t > 0$  node  $j$  will also become infected (because nothing else can happen). The standard SI model assumes memoryless dynamics. With continuous time, this implies that the instantaneous transmission probability does not vary over time, i.e., the transmission rate,  $\beta_{i \rightarrow j}$ , is constant. Now imagine susceptible node  $j$  with two infected neighbors,  $i_1$  and  $i_2$ . The standard SI model additionally assumes simple contagion. This means that the transmission from  $i_1$  to  $j$  is completely unaffected by the fact that the transmission from  $i_2$  is also active (and vice versa). So we can write the total instantaneous probability that node  $j$  becomes infected as  $\omega_j = \beta_{i_1 \rightarrow j} + \beta_{i_2 \rightarrow j}$ . In this work we limit our analysis to homogeneous transmission rates (the same for all pairs), thus  $\omega_j = \beta z_j$ , with  $z_j$  the number of  $j$ 's neighbors that are infected.

### 2.1.1 Analytic approximation

Globally, the system has an unstable absorbing state where all agents are healthy (no one can start an outbreak) and a stable attractor where all agents are infected; note that this attractor is also absorbing (no healthy targets remain). Thus any small perturbation to the healthy state will evolve toward a fully infected state. The interesting analysis is to characterize the transient from the former to the latter.

At time  $t$ , node  $i$  is described by its state  $n_i(t)$ , a discrete variable that takes two values,  $n_i = 0$  if it is susceptible or  $n_i = 1$  if it is infected. The state of node  $i$  only changes when it transitions from healthy to infected. A relevant nonindependent variable is the number of  $i$ 's neighbors that are infected at time  $t$ ,  $z_i(t) = \sum_j a_{ij}n_j(t)$ , with  $a_{ij}$  the elements of the adjacency matrix. The evolution of these variables is governed by a microscopic, dichotomous, stochastic process  $\pi$ . Susceptible node  $i$  becomes infected ( $\pi_i = 1$ ) or remains susceptible ( $\pi_i = 0$ ) given by the hazard rate  $\omega_i(t) = \beta z_i(t)$ . In short,  $\omega_i(t)dt$  measures the probability that the infection of node  $i$  takes place between  $t$  and  $t + dt$ , conditioned on not having occurred before time  $t$  [48]. At  $O(dt)$ , the corresponding probabilities are

$$\pi_i = \begin{cases} 1 & \omega_i(t)dt \\ 0 & 1 - \omega_i(t)dt \end{cases} . \quad (2.1)$$

The state of node  $i$  at time  $t + dt$  is

$$n_i(t + dt) = n_i(t) + (1 - n_i(t))\pi_i , \quad (2.2)$$

where the first term corresponds to node  $i$  being infected (and remaining so) and the second term corresponds to node  $i$  being susceptible ( $1 - n_i(t)$ ) and becoming infected ( $\pi_i$ ). In order to obtain the dynamic equation, we first compute the expectation value conditioned on time  $t$ , which only affects the stochastic variable

$$\mathbb{E}[n_i(t + dt) | t] = n_i(t) + (1 - n_i(t)) \mathbb{E}[\pi_i | t] \quad (2.3)$$

$$= n_i(t) + (1 - n_i(t))\omega_i(t)dt \quad (2.4)$$

$$= n_i(t) + (1 - n_i(t))\beta z_i(t)dt . \quad (2.5)$$

Taking the ensemble average yields

$$\langle n_i(t + dt) \rangle = \langle \mathbb{E}[n_i(t + dt) | t] \rangle = \langle n_i(t) \rangle + \beta \langle (1 - n_i(t))z_i(t) \rangle dt , \quad (2.6)$$

from where we find

$$\frac{d\langle n_i(t) \rangle}{dt} = \frac{\langle n_i(t + dt) \rangle - \langle n_i(t) \rangle}{dt} = \beta \langle (1 - n_i(t)) z_i(t) \rangle. \quad (2.7)$$

Finding a closed-form solution for this equation ranges from achievable to impossible, depending on the topology of the contact network.

### 2.1.2 Random degree-regular networks

For now we consider random degree-regular networks, where all nodes have the same degree  $k$  and edges are placed completely at random. This choice eliminates any interference from the network topology and allows us to concentrate solely on the infection mechanism. Applying a mean-field approximation for uncorrelated networks, the topology term in the RHS of Eq. (2.7) can be written as [133]

$$\langle (1 - n_i(t)) z_i(t) \rangle = \langle (1 - n_i(t)) \sum_j a_{ij} n_j(t) \rangle \quad (2.8)$$

$$= \sum_j a_{ij} (\langle n_j(t) \rangle - \langle n_i(t) n_j(t) \rangle) \quad (2.9)$$

$$\approx \sum_j \frac{k_i k_j}{N \langle k \rangle} (\langle n_j(t) \rangle - \langle n_i(t) \rangle \langle n_j(t) \rangle), \quad (2.10)$$

with  $k_i$  and  $k_j$  the degrees of nodes  $i$  and  $j$ , respectively, and  $\langle k \rangle$  the average degree. Particularly, in random degree-regular networks we have  $k_i = k_j = \langle k \rangle = k$ , and due to homogeneity,  $\langle n_i(t) \rangle = \langle n_j(t) \rangle = \rho(t)$ . Then we find an equation for the prevalence,  $\rho(t)$ , which measures the fraction of infected individuals at time  $t$

$$\frac{d\rho(t)}{dt} = \beta k \rho(t) (1 - \rho(t)). \quad (2.11)$$

The solution is a sigmoid-like curve<sup>1</sup>

$$\rho(t) = \frac{\rho_0 e^{\beta k t}}{1 - \rho_0 + \rho_0 e^{\beta k t}}, \quad (2.12)$$

---

<sup>1</sup>See Appendix A.1 for a detailed derivation.

with  $\rho_0$  the fraction of infected individuals at  $t = 0$ . As expected, the prevalence increases monotonically; after an initial exponential growth it gradually saturates at  $\rho = 1$  (all agents infected). Note that we can rescale time as  $t' = \beta kt$  without changing the functional form of the solution (see Fig. 2.1).

### 2.1.3 Gillespie algorithm

We perform simulations in order to verify the mean-field approximation and to gauge any finite-size effects. The state of our system changes whenever a susceptible agent becomes infected, yielding a sequence of events that constitute a mixture of temporal point processes. Since we assume memoryless processes, the global dynamics can be simulated using Markovian stochastic algorithms capable of generating statistically exact realizations, such as the seminal method developed by Gillespie [77, 78].

Consider at time  $t_0$  a set of  $M$  statistically independent, discrete, stochastic, memoryless processes. The interevent time distribution for process  $j$  is  $\psi_j(\tau) = \theta_j e^{-\theta_j \tau}$ , with  $\theta_j$  its constant hazard rate. This means that, with probability  $\psi_j(\tau) d\tau$ , the interval between process  $j$ 's activation and occurrence is of length  $\tau$ . Globally, the next-occurring event will take place in the interval  $t \in (t_0, t_0 + \tau]$  with probability  $\Xi(\tau) = 1 - e^{-\tau \Theta}$  and will correspond to process  $i$  with probability  $\Pi_i = \theta_i \Theta^{-1}$ , where  $\Theta = \sum_j \theta_j$ . Algorithm-wise, two uniform random numbers are needed,  $u_1, u_2 \in U(0, 1)$ .  $u_1$  samples the interval,  $\tau = -\log(u_1) \Omega^{-1}$ , and  $u_2$  the next-occurring process from the discrete distribution  $\Pi$ . If the system is in an absorbing state ( $M = 0$ ) the algorithm diverges ( $\Omega^{-1} \rightarrow \infty$ ) and the simulation must be halted.

In the standard SI model, each link that connects an infected node with a susceptible one represents a possible transmission event. Since all of these infectious links are equivalent (they have the same transmission rate  $\beta$ ), the most efficient option is to keep a list of the  $N_T$  active links. Then the total hazard rate is  $\Omega = \beta N_T$  and the probability that the next event corresponds to active link  $i$  is simply  $\Pi_i = 1/N_T$ . Before moving to the next iteration, time is increased ( $t \leftarrow t + \tau$ ) and the system's state is updated (a node switches state and the corresponding links become infectious or deactivated).

Our simulations start with a single randomly chosen infected node in a fully healthy system and terminate when all nodes are infected.<sup>2</sup> We use a ran-

---

<sup>2</sup>See Appendix C.1.1 for an outline of the core algorithm.

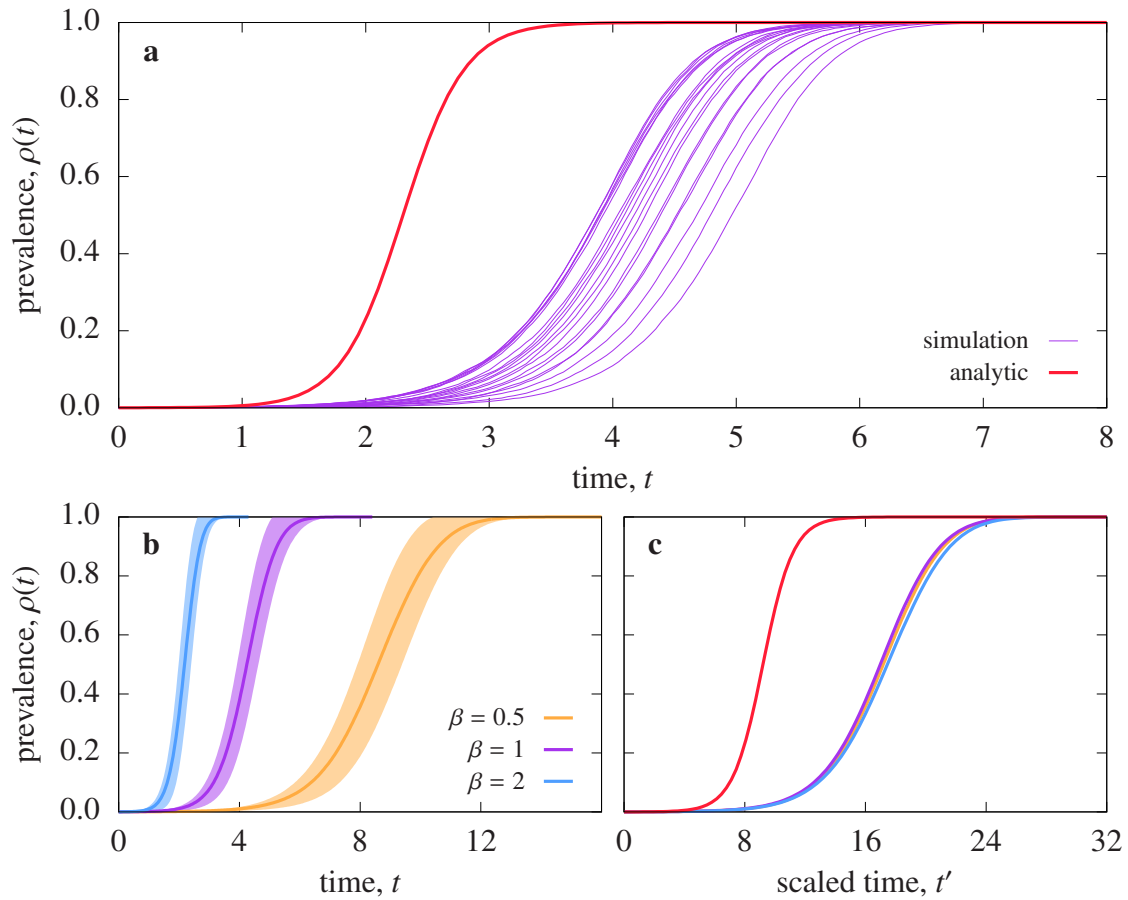


Figure 2.1: **Temporal evolution of the prevalence in the standard SI model.** Results for a random degree-regular network with  $k = 4$  and  $N = 10^4$ . **(a)** Analytic approximation (red) and 20 independent simulations (purple) of single-seed outbreaks with transmission rate  $\beta = 1$ . **(b)** Average (solid curve) and standard deviation (shaded area) of 100 independent simulations (transmission rate in legend). **(c)** Averaged curves (colors as in **b**) and analytic approximation (red) with scaled time  $t' = \beta kt$ .

dom degree-regular network with degree  $k = 4$  and  $N = 10^4$  nodes<sup>3</sup> and compute the prevalence as  $\rho(t) = N_I(t)/N$ , with  $N_I(t)$  the number of infected nodes at time  $t$ .<sup>4</sup> As we can see in Fig. 2.1(a), each of the 20 realizations is slightly different but all present the same qualitative behavior. The analytic curve (Eq. (2.12) with  $\rho_0 = 1/N = 10^{-4}$ ) reproduces the functional form but underestimates the characteristic outbreak time and duration.<sup>5</sup> Figure 2.1(b) shows the average trajectory of 100 independent simulations for different transmission rates.<sup>6</sup> As expected, a more virulent outbreak (higher transmission rate  $\beta$ ) requires a shorter time to invade the population. Finally, in Fig. 2.1(c) we verify that time can be rescaled as  $t' = \beta kt$ .

In conclusion, the mean-field approximation derived in Section 2.1.2 correctly captures the qualitative behavior of the system's evolution but fails to produce a satisfactory quantitative estimation. Furthermore, finite-size effects are adequately described by the average and spread of independent realizations.

## 2.2 Memory-induced complex contagion SI model

A reasonable alternative to the standard model is to assume that nodes become infected by the joint effect of multiple infectors. We develop a model that moves away from the customary edge-based description and, instead, includes a node-centric infection mechanism. The memory-induced complex contagion (micc) model describes infected nodes as infectious sources that spread doses of pathogen to their neighbors. Susceptible nodes, on the other hand, gather the toxins from all their neighbors and become infected given the total viral load they have amassed. Hence the infection process is mediated by the viral load, a sort of “messenger variable” that aggregates all the infectious sources and blurs the causality chain from infector to infectee.

This conceptual framework requires to mathematically characterize the ac-

<sup>3</sup>See Appendix B.1 for details on how to generate these synthetic networks.

<sup>4</sup>See Appendix C.1.3 for simulation details.

<sup>5</sup>It is known that pairwise approximations are more suitable for random degree-regular networks, but the math is considerably more involved [102, 106].

<sup>6</sup>Note that there is no need to average over network realizations since random degree-regular networks are self-averaging.

cumulation of viral load and the infection probability, which can be more or less sophisticated. For instance, we could use nonlinear growth to describe beyond pairwise interactions or model interacting pathogens through a common viral load but distinct infection probabilities. Nevertheless, for starters we keep things simple: we consider that infected nodes have a constant infectivity rate,  $\nu$ , and continuously spread doses of contagion toward their entire neighborhood. They target all of their first neighbors equally, transmitting pathogen along each edge at constant rate  $\nu$ . Susceptible nodes collect these toxins from all their neighbors, amassing a total viral load  $\kappa$ , and transition to the infected state with probability  $\psi_{\text{inf}}^*(\kappa)d\kappa$ , where  $\psi_{\text{inf}}^*(\kappa)$  is the infection probability density. Infected nodes are unaffected by the toxins they receive (their viral load does not change).

In 1983, Sellke introduced a construction in terms of exposition times akin to ours, but only as a byway for some mathematical proofs [150]. More recently, Dodds and Watts applied the idea to a generalized model of contagion [59, 60], and Wang et al. proposed a general social contagion model with reinforcement derived from nonredundant information memory [171, 183]. However, both these models present two major differences with respect to our contribution. First, we use continuous time instead of discrete temporal steps,<sup>7</sup> and second, infection threshold are stochastic and annealed rather than deterministic and quenched.<sup>8</sup> Hypothetically, quenched thresholds would interfere with the model's intrinsic properties,<sup>9</sup> an effect we wish to minimize.

### 2.2.1 Infection probabilities and interevent times

Consider susceptible agent  $j$ , characterized by its infection probability density,  $\psi_j^*(\kappa)$ , and corresponding “survival” probability,

$$\Psi_j^*(\kappa) = \int_{\kappa}^{\infty} \psi_j^*(\kappa') d\kappa' . \quad (2.13)$$

---

<sup>7</sup>Discretizing time leads to restrictions on the parameter values that can be accurately studied, can affect the value of the epidemic threshold, and produces biased results when using synchronous-type updating schemes for numerical simulations [69].

<sup>8</sup>With deterministic thresholds, a susceptible node becomes infected inevitably if its viral load surpasses a fixed value, whereas any amount of viral load can cause the infection if thresholds are stochastic.

<sup>9</sup>As observed, for example, with degree distributions [133].

$\psi_j^*(\kappa)d\kappa$  measures the probability that node  $j$  becomes infected when it has accumulated viral load in the interval  $(\kappa, \kappa + d\kappa]$ . Additionally,  $\Psi_j^*(\kappa)$  measures the probability that node  $j$  becomes infected when it has amassed a viral load of  $\kappa$  or more. Conversely,  $\psi_j(t)dt$  measures the probability that node  $j$ 's infection occurs between  $t$  and  $t + dt$ , with  $\psi_j(t)$  the corresponding interevent time distribution. The infection probability density and the interevent time distribution are related through the normalization condition

$$\psi_j(t)dt = \psi_j^*(\kappa)d\kappa . \quad (2.14)$$

Since the activity in  $j$ 's neighborhood varies over time (more and more neighbors become infected over time), the rate at which it accumulates viral load is generally nonconstant. Imagine that at time  $t$  it has amassed  $\kappa_j(t)$  units of viral load and has  $z_j(t)$  infected neighbors. If the system remains unaltered in an interval  $dt$ , node  $j$  will accumulate an additional  $d\kappa = \tilde{v}_j(t)dt$ , with  $\tilde{v}_j(t) = \sum_{i=1}^{z_j(t)} \nu_i$  its instantaneous amassment rate and  $\nu_i$  the infectivity rate of infected neighbor  $i$ . Substituting in Eq. (2.14) we find

$$\psi_j(t) = \tilde{v}_j(t)\psi_j^*(\kappa_j(t)) , \quad (2.15)$$

and for the survival probability we have

$$\Psi_j(t) = \int_t^\infty \psi_j(t')dt' = \int_{\kappa_j(t)}^\infty \psi_j^*(\kappa')d\kappa' = \Psi_j^*(\kappa_j(t)) , \quad (2.16)$$

which yields the instantaneous hazard rate

$$\omega_j(t) = \frac{\psi_j(t)}{\Psi_j(t)} = \tilde{v}_j(t) \frac{\psi_j^*(\kappa_j(t))}{\Psi_j^*(\kappa_j(t))} . \quad (2.17)$$

For a Poisson point process, the interevent times are distributed exponentially and the hazard rate is therefore constant. In general, interevent time distributions that decay slower (respectively, faster) than exponential lead to asymptotically decreasing (increasing) hazard rates [83].

Note that we can always write  $t = t_0 + \tau$ , with  $t_0$  the time at which the system last changed and  $\tau \geq 0$ . Then the instantaneous amassment rate remains constant in the interval  $(t_0, t]$ , so  $\tilde{v}_j(t) = \tilde{v}_j(t_0)$  and  $\kappa_j(t) = \kappa_j(t_0) + \tau\tilde{v}_j(t_0)$ .

### 2.2.2 Weibull distribution

In general, the infectivity rate,  $\nu_i$ , and the infection probability density,  $\psi_i^*(\kappa)$ , may vary from node to node. For example, one could model distinct age groups by segregating the population and assigning different values of the parameters to each subpopulation. Notwithstanding, in order to eliminate the effects of node heterogeneities, in the present work we use the same  $\nu$  and  $\psi_{\text{inf}}^*(\kappa)$  for all nodes. Since all infectors have the same infectivity rate, the instantaneous amassment rate of susceptible node  $j$  becomes  $\tilde{\nu}_j(t) = \nu z_j(t)$ , with  $z_j(t)$  the number of its neighbors that are infected at time  $t$ .

Infections are governed by the versatile Weibull distribution, with shape parameter  $\alpha$  and scale parameter  $\mu$

$$\psi_{\text{inf}}^*(\kappa) = \alpha \mu^\alpha \kappa^{\alpha-1} e^{-(\mu\kappa)^\alpha} \quad (2.18)$$

$$\Psi_{\text{inf}}^*(\kappa) = e^{-(\mu\kappa)^\alpha} . \quad (2.19)$$

For  $\alpha > 1$  it presents a peak, resembling a bell curve,  $\alpha = 1$  corresponds to an exponential distribution, and for  $\alpha < 1$  it has power law–like fat tails (see Fig. 2.2(a)). These characteristics are reflected in the coefficient of variation

$$\text{CV}(\alpha) = \sqrt{\frac{\langle \kappa^2 \rangle}{\langle \kappa \rangle^2} - 1} = \sqrt{\frac{2\alpha\Gamma(2\alpha^{-1})}{[\Gamma(\alpha^{-1})]^2} - 1} , \quad (2.20)$$

with  $\Gamma(x)$  the gamma function. This coefficient is independent of the scale parameter, satisfies  $\text{CV}(1) = 1$ , and decreases monotonically [143]. Then for  $\alpha < 1$  there is no characteristic scale, while for  $\alpha > 1$  nodes must accumulate a well-defined amount of viral load in order to become infected. Finally, the instantaneous hazard rate is

$$\omega_{\text{inf}}(t) = \nu \alpha \mu^\alpha z(t) [\kappa(t)]^{\alpha-1} , \quad (2.21)$$

with  $z(t)$  the number of infected neighbors at time  $t$ . When  $\alpha > 1$  (respectively,  $\alpha < 1$ ),  $\omega_{\text{inf}}(t)$  increases (decreases) monotonically with  $\kappa(t)$  (see Fig. 2.2(b)).

Notice that with  $\alpha = 1$  we recover the customary expression of the standard model,  $\omega_{\text{inf}} \propto z(t)$ . For  $\alpha \neq 1$ , however, Eq. (2.21) cannot be written as a linear superposition of independent transmission channels. Hence the agent's memory induces a complex contagion scheme, even though the model does not explicitly incorporate any social reinforcement/inhibition mechanisms.

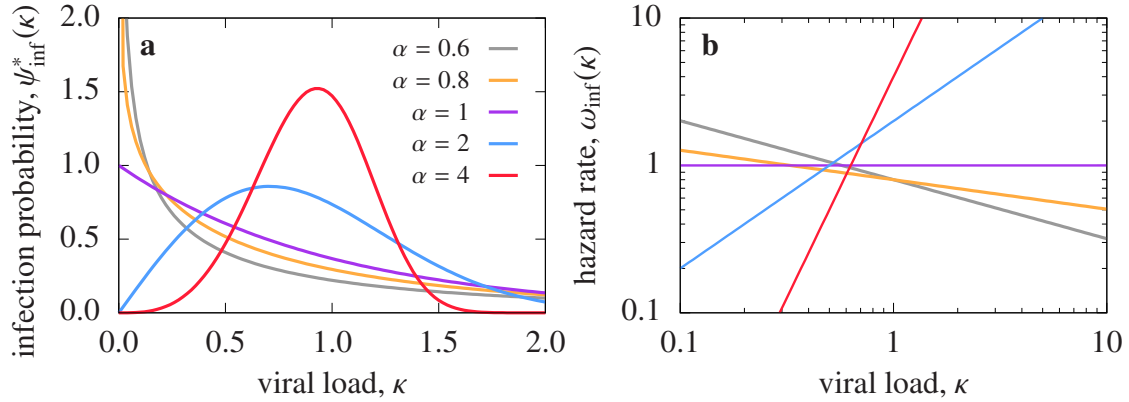


Figure 2.2: **Weibull distribution.** (a) Infection probability density and (b) hazard rate for  $\mu = 1$  (shape parameter in legend). Note the double log-scale in the right panel.

### 2.2.3 Simple and complex contagion

Simple contagion describes purely dyadic interactions, thus we can identify each edge that connects a healthy node with an infected one as an isolated transmission channel. Consider at time  $t$  a susceptible node  $j$  and its infected neighbor  $i$ , which became infected at  $t_i < t$ . The probability that node  $i$  infects node  $j$  within the interval  $(t, t + dt]$  is  $\omega_{i \rightarrow j}(t | t_i)dt$ , regardless of the rest of the system. If node  $j$  has  $z_j(t)$  infectors at time  $t$ , the previous statement holds for each of them.

The total probability that node  $j$  becomes infected at time  $t$  depends on all of its incoming transmission channels. Since these are statistically independent, we can write

$$\omega_j(t) = \sum_{i=1}^{z_j(t)} \omega_{i \rightarrow j}(t | t_i), \quad (2.22)$$

where  $\omega_j(t)$  is the instantaneous hazard rate of node  $j$ 's infection process (i.e., the probability per unit of time that node  $j$  becomes infected at time  $t$ ). Using

$$\Omega_j(t) = \frac{1}{z_j(t)} \sum_{i=1}^{z_j(t)} \omega_{i \rightarrow j}(t | t_i) \quad (2.23)$$

we can write Eq. (2.22) as

$$\omega_j(t) = \Omega_j(t)z_j(t), \quad (2.24)$$

thus the total hazard rate is proportional to the number of current infectors. When  $\omega_{i \rightarrow j}(t | t_i) = \beta$  are constants (and homogenous for all pairs of nodes), we recover the standard SI model with the familiar expression  $\omega_j(t) = \beta z_j(t)$ . If the transmission rates  $\omega_{i \rightarrow j}$  are time-dependent, the dynamics has memory effects; thus simple contagion can be non-Markovian (as in [165, 155], for example).

When the dynamics are described by interactions that are not strictly dyadic, the contagion becomes complex. These processes usually incorporate an explicit social reinforcement or inhibition mechanism. Although the classification of complex contagion processes is yet to be formalized, they can be broadly categorized into two groups:

- Edge-centric approaches still consider the transmission channel from infected node  $i$  to susceptible node  $j$ . Now, however, the transmission rate  $\omega_{i \rightarrow j}$  is affected by the neighborhoods of  $i$  and/or  $j$ . Considering only nearest-neighbors, the transmission rate from node  $i$  to node  $j$  at time  $t$ ,  $\omega_{i \rightarrow j}(t | z_i(t), z_j(t))$ , is a function of their current infected neighbors,  $z_i(t)$  and  $z_j(t)$ . Although we can still write the total hazard rate  $\omega_j(t)$  as in Eq. (2.22), the instantaneous average defined in Eq. (2.23) has an explicit dependence on  $z_i(t)$  and  $z_j(t)$ . Consequently,  $\omega_j(t)$  can be superlinear (reinforcement) or sublinear (inhibition) with the number of current infectors,  $z_j(t)$  (for specific examples see [139, 80, 111]).
- On the other hand, node-centric approaches forgo the notion of transmission channels and directly prescribe the instantaneous hazard rate  $\omega_j(t)$ . These usually incorporate thresholds, such as  $\omega_j(t) = \delta(T_j - z_j(t))$  [172] or  $\omega_j(t) = z_j(t)\Theta(T_j - z_j(t)) + \beta\Theta(z_j(t) - T_j)$  [131], which explicitly evidence the nonlinearity of  $\omega_j(t)$  with  $z_j(t)$ .

### 2.2.3.1 Memory-induced complex contagion

Consider an isolated pair of nodes  $i$  and  $j$  in the miccSI model; both are healthy when node  $i$  becomes infected at time  $t_i$ . The total amount of viral load that  $j$  has amassed at time  $t > t_i$  is  $\kappa_j(t) = \nu\Delta t_i$ , with  $\Delta t_i = t - t_i$ . The instantaneous hazard rate of node  $j$ 's infection is

$$\omega_j(t) = \nu\alpha\mu^\alpha z_j(t)[\kappa_j(t)]^{\alpha-1}, \quad (2.25)$$

but, since  $j$  has only one infected neighbor, it is given solely by the exposure to node  $i$ :  $\omega_j(t) = \omega_{i \rightarrow j}(t | t_i)$ , with

$$\omega_{i \rightarrow j}(t | t_i) = \nu \alpha \mu^\alpha [\nu \Delta t_i]^{\alpha-1} . \quad (2.26)$$

Imagine at time  $t_0$  a group of healthy nodes, formed by susceptible node  $j$  and its first-neighbors. After a while, at time  $t$  node  $j$  has a set of  $\{i\}$  infected neighbors that became infected at times  $\{t_i\}$ , with  $t_0 < t_i < t$ ,  $\forall i = 1, 2, \dots, z_j(t)$ . The total amount of viral load that  $j$  has amassed at time  $t$  is

$$\kappa_j(t) = \sum_{i=1}^{z_j(t)} \nu \Delta t_i . \quad (2.27)$$

By substituting Eq. (2.27) in Eq. (2.25) we find

$$\omega_j(t) = \nu \alpha \mu^\alpha z_j(t) \left[ \sum_{i=1}^{z_j(t)} \nu \Delta t_i \right]^{\alpha-1} , \quad (2.28)$$

which, using Eq. (2.26), can be written for  $\alpha \neq 1$  as

$$\omega_j(t) = z_j(t) \left[ \sum_{i=1}^{z_j(t)} \left[ \omega_{i \rightarrow j}(t | t_i) \right]^{\frac{1}{\alpha-1}} \right]^{\alpha-1} . \quad (2.29)$$

Notice that the second term cannot be written as Eq. (2.23), a linear superposition of transmission channels. Therefore, while the exposures to infectious sources are initially described as isolated events, the agents' memory causes them to become entangled.

With  $\alpha = 2$ , for instance, Eq. (2.29) can be written as

$$\omega_j(t) = \Omega(t) [z_j(t)]^2 , \quad (2.30)$$

which has an explicit quadratic dependence on  $z_j(t)$ . The simple contagion of the standard SI model can be recovered only with  $\alpha = 1$ , for which Eq (2.25) equates with Eq (2.24). In conclusion, the non-Markovianity of the miccSI model induces an effective social reinforcement/inhibition even though it was not incorporated in the initial description of the model.

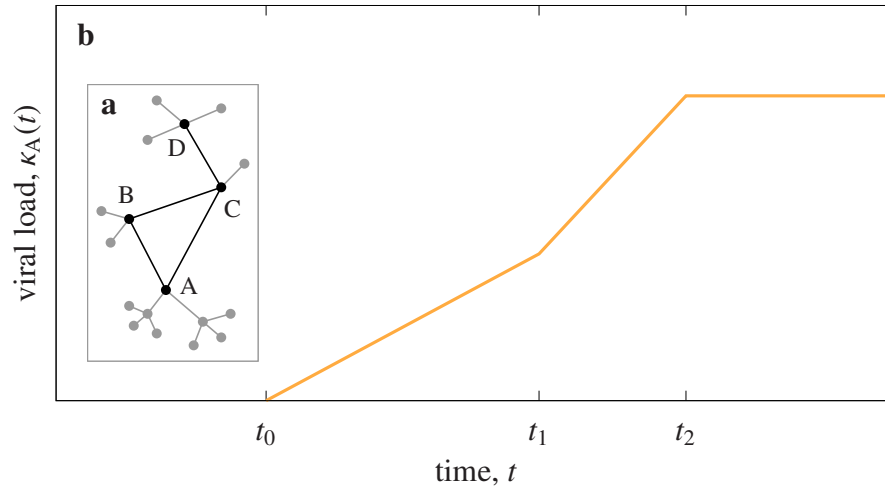


Figure 2.3: **Viral load accumulation in the miccSI model.** (a) Small system considered in example. (b) Evolution of A's viral load. Before  $t_0$ , node A's neighborhood is completely healthy and it cannot become infected ( $\omega_A = 0$ ).  $\kappa_A$  grows at rate  $\nu$  between  $t_0$  and  $t_1$  and at rate  $2\nu$  in the interval  $t \in [t_1, t_2]$ . After node A's infection at time  $t_2$  its viral load remains unaltered.

## 2.2.4 Analytic approximation

For illustrative purposes, consider the small system depicted in Fig. 2.3(a), where all nodes are initially healthy except for D. Node C becomes infected at time  $t_0$  and subsequently infects B at  $t_1$ . During the interval  $t \in [t_0, t_1]$ , node A's viral load,  $\kappa_A$ , grows with rate  $\nu$ , but from  $t_1$  onward it will increase with rate  $2\nu$ . Finally, node A becomes infected at  $t_2$  and  $\kappa_A$  stops growing. Figure 2.3(b) shows the evolution of  $\kappa_A$ .

We need two variables to describe node  $i$  at time  $t$  in the miccSI model: its state  $n_i(t)$  and its viral load  $\kappa_i(t)$ . As before, the former is a discrete variable that can take two values:  $n_i(t) = 0$  if it is susceptible or  $n_i(t) = 1$  if it is infected. The viral load, on the other hand, is a continuous variable with  $\kappa_i(t) \geq 0$ . Recall that the number of infected neighbors is  $z_i(t) = \sum_j a_{ij}n_j(t)$ , with  $a_{ij}$  the elements of the adjacency matrix.

The state of node  $i$  only changes when it transitions from healthy to infected; on the other hand, the viral load only increases while node  $i$  is susceptible (proportionally to the number of infected neighbors). The evolution of

these variables is again governed by the infection process

$$\pi_i = \begin{cases} 1 & \omega_i(t)dt \\ 0 & 1 - \omega_i(t)dt \end{cases}, \quad (2.31)$$

where the instantaneous hazard rate of node  $i$  is  $\omega_i(t) = \nu\alpha\mu^\alpha z_i(t) [\kappa_i(t)]^{\alpha-1}$ .

The equation for the state of node  $i$  at time  $t + dt$  reads

$$n_i(t + dt) = n_i(t) + (1 - n_i(t))\pi_i, \quad (2.32)$$

where the first term corresponds to node  $i$  being infected (and remaining so) and the second term corresponds to node  $i$  being susceptible ( $1 - n_i(t)$ ) and becoming infected ( $\pi_i$ ). Additionally, the equation for the viral load of node  $i$  at time  $t + dt$  is

$$\kappa_i(t + dt) = \kappa_i(t) + (1 - n_i(t))(1 - \pi_i)\nu z_i(t)dt, \quad (2.33)$$

where the first term indicates the accumulated viral load until time  $t$  ( $\kappa_i(t)$ , which never disappears) and the second term corresponds to node  $i$  being susceptible ( $1 - n_i(t)$ ) and amassing additional viral load ( $\nu z_i(t)dt$ ), but not becoming infected ( $1 - \pi_i$ ).

Applying the same procedure as in Section 2.1.1 (expectation value conditioned on time  $t$  followed by ensemble average), we find the dynamic equations<sup>10</sup>

$$\frac{d\langle n_i(t) \rangle}{dt} = \nu\alpha\mu^\alpha \langle (1 - n_i(t))z_i(t) [\kappa_i(t)]^{\alpha-1} \rangle \quad (2.34)$$

$$\frac{d\langle \kappa_i(t) \rangle}{dt} = \nu \langle (1 - n_i(t))z_i(t) \rangle. \quad (2.35)$$

These equations are coupled through the nonlinear term  $[\kappa_i(t)]^{\alpha-1}$  and also with the equations of other nodes (through the variable  $z_i(t)$ ). Adding the explicit temporal dependency and the nontrivial contact topology, the search for an analytic solution presents itself as a quixotic endeavor. We rather resort directly to simulations.

<sup>10</sup>See Appendix A.2 for a detailed derivation.

### 2.2.5 Non-Markovian Gillespie algorithm

Overall, the system's evolution is determined by the set of infection processes (one for each node). Here we describe the generalized non-Markovian Gillespie algorithm, capable of simulating memoryfull dynamics in continuous time [17]. Consider a set of  $M$  statistically independent, discrete, stochastic processes, each with an interevent time distribution  $\psi_j(\tau)$  and corresponding survival probability  $\Psi_j(\tau) = \int_{\tau}^{\infty} \psi_j(\tau') d\tau'$ . If process  $j$  was activated at time  $t = 0$ , its next event will occur at time  $t \in (\tau, \tau + d\tau]$  with probability  $\psi_j(\tau)d\tau$ . Moreover, the next event of process  $j$  will occur at time  $t \geq \tau$  with probability  $\Psi_j(\tau)$ .

At a certain moment in time  $t_0$ , process  $j$  has been active for  $t_j$  units of time (i.e., it was activated at time  $t = t_0 - t_j$ ). Let  $\phi(\tau, i | \{t_k\})d\tau$  denote the joint probability that the next-occurring event takes place in the interval  $t \in (t_0 + \tau, t_0 + \tau + d\tau]$  and corresponds to process  $i$ , conditioned by the set of elapsed times  $\{t_k\}$ . This probability density can be expressed as

$$\phi(\tau, i | \{t_k\}) = \frac{\psi_i(t_i + \tau)}{\Psi_i(t_i + \tau)} \Phi(\tau | \{t_k\}), \quad (2.36)$$

where

$$\Phi(\tau | \{t_k\}) = \prod_{j=1}^M \frac{\Psi_j(t_j + \tau)}{\Psi_j(t_j)} \quad (2.37)$$

is the survival probability of  $\tau$ , i.e., the conditional probability that no event takes place before  $t_0 + \tau$ . Then the probability that the next event takes place in the interval  $t \in (t_0, t_0 + \tau]$  is

$$\Xi(\tau | \{t_k\}) = 1 - \Phi(\tau | \{t_k\}). \quad (2.38)$$

Once the interval  $\tau$  is known, the probability that the next-occurring event corresponds to process  $i$  is given by

$$\Pi(i | \tau, \{t_k\}) = \frac{\omega_i(t_i + \tau)}{\sum_{j=1}^M \omega_j(t_j + \tau)}, \quad (2.39)$$

with  $\omega_j(t) = \psi_j(t)/\Psi_j(t)$  the instantaneous hazard rate of process  $j$ . Recall that  $\omega_j(t)$  measures the probability per unit of time that process  $j$  takes place between  $t$  and  $t + dt$ , conditioned on not having occurred before time  $t$  [48].<sup>11</sup>

<sup>11</sup>Note the difference with  $\psi_j(t)$ , which measures the corresponding unconditional probability per unit of time.

Eqs. (2.38) and (2.39) provide an algorithm that generates statistically correct sequences of events:

- i) draw the interval by solving  $\Xi(\tau | \{t_k\}) = u$ , with  $u \in U(0, 1)$ ,
- ii) increase the system time as  $t \leftarrow t + \tau$ ,
- iii) draw the process from the discrete distribution  $\Pi(i | \tau, \{t_k\})$ ,
- iv) revise the list of active processes, and
- v) update the set of elapsed times as  $t_j \leftarrow t_j + \tau$  (setting  $t_j = 0$  for newly activated processes).

Once again, we start our simulations with a single randomly chosen infected node in a fully healthy system and stop when all nodes are infected.<sup>12</sup> Recall that we use a random degree-regular network with degree  $k = 4$  and  $N = 10^4$  nodes and compute the prevalence as  $\rho(t) = N_I(t)/N$ , with  $N_I(t)$  the number of infected nodes at time  $t$ . Without loss of generality, hereon forward we use units of the viral load  $\kappa$  such that  $v = 1$ .<sup>13</sup> In Fig. 2.4(a) we verify that the miccSI model with  $\alpha = 1$  and  $\mu = 1$  is equivalent to the standard SI model with  $\beta = 1$ .<sup>14</sup> Figure 2.4(b) shows the results for shape parameter  $\alpha = 2$ . As we can see, a larger value of the scale parameter  $\mu$  causes more virulent outbreaks; nonetheless, time can be adequately rescaled as  $t' = \mu t$ . Finally, Fig. 2.4(c) shows outbreaks for various values of the shape parameter, all with  $\mu = 1$ . We observe that the outbreak time increases with  $\alpha$  (outbreaks take longer to take-off), but the final stage of invasion become shorter (outbreaks saturate earlier); additionally, the spread decreases with  $\alpha$ .

## 2.2.6 Discussion

Summarizing, the miccSI model allows to model a variety of scenarios. On the one hand,  $\alpha < 1$  yields outbreaks that evolve rapidly during their initial phase but saturate very slowly; moreover, the wide spread indicates a large variability between different outbreaks. Recall that the hazard rate decreases

<sup>12</sup>See Appendix C.1.2 for an outline of the core algorithm.

<sup>13</sup>See Appendix C.1.3 for simulation details.

<sup>14</sup>In general, to recover the standard SI model with  $\alpha = 1$  we must simply substitute  $\beta$  for  $\mu$ .

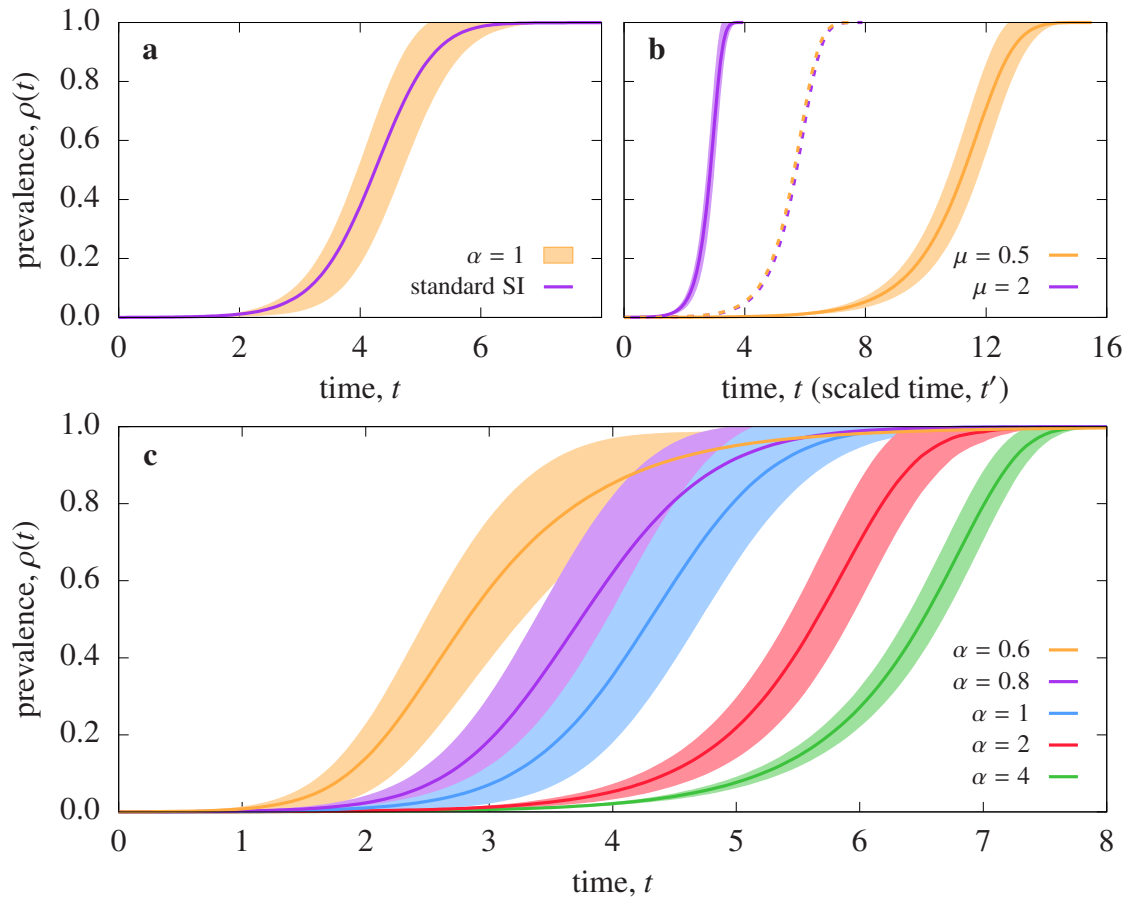


Figure 2.4: **Temporal evolution of the prevalence in the miccSI model.** Results for 100 independent simulations of single-seed outbreaks in a random degree-regular network with  $k = 4$  and  $N = 10^4$ . **(a)** Standard deviation for the miccSI model (orange shaded area) with shape parameter  $\alpha = 1$  and scale parameter  $\mu = 1$ ; average for the standard SI model (purple curve) with transmission rate  $\beta = 1$ . **(b)** Average (solid) and standard deviation (shaded) for  $\alpha = 2$  (scale parameter in legend); averaged curves with scaled time  $t' = \mu t$  (dashed). **(c)** Average (solid) and standard deviation (shaded) for  $\mu = 1$  (shape parameter in legend).

monotonically with the amount of accumulated viral load. Hence nodes are very likely to become infected with small values, causing a chain reaction of rapid infections. However, the nodes that are not infected shortly after their first exposure develop a sort of resistance to the pathogen, which intensifies as time goes by. Although eventually they do become infected, the full infection of the system is greatly delayed by their opposition. This scenario could be used, for instance, to describe early adopters, who are eager to embrace innovative technologies and do not wish to miss out on them [144].

With  $\alpha > 1$ , on the other hand, outbreaks show a very gradual initial growth, followed by a quick complete invasion. Different outbreaks are also more regular in terms of temporal patterns, as indicated by the small spread. In these cases the infection probability has a bell curve-like shape. Thus nodes are required to amass a more or less bounded amount of viral load in order to become infected. Consequently, healthy agents are likely to become infected at more or less the same time, causing a very rapid system-wide expansion of the pathogen. In terms of technology adoption, this scenario could describe the so-called late majority, who are more conservative and typically skeptical toward innovation [144].

All in all, the memory-induced complex contagion infection mechanism commences to (timidly) exhibit its singular features. The true nature of this novel infection mechanism is revealed in Chapter 3, where nodes are allowed to recover, and specially in Chapter 4, when we include reinfections.

# The SIR model

---

## 3.1 Standard SIR model

As I discussed in the previous chapter, the SI model is suitable to describe phenomena such as innovation adoption, where the transition from “healthy” to “infected” is irreversible. For instance, after swapping out your old flip-phone for a modern smartphone, you are unlikely to go back to using decades-old technology. When we look at diseases, however, the picture is very different.<sup>1</sup> An infected individual usually recovers from their illness after a certain amount of time, ceases to be infectious, and becomes immune.

The susceptible-infected-recovered (SIR) model extends the SI model by including a third state, commonly referred to as recovered.<sup>2</sup> Agents transition spontaneously from infected to recovered, without the need of any external mechanism. Recovered agents acquire immunity from the disease, thus re-infections are not allowed. As before, infected agents transmit the pathogen to their susceptible nearest-neighbors, and the population is embedded on a contact network.

In the standard SIR model, the recovery of infected node  $j$  is described by a memoryless process, characterized by a constant recovery rate  $\eta_j$ . The corresponding interevent time distribution is  $\psi_j(\tau) = \eta_j e^{-\eta_j \tau}$ , so that  $\psi_j(\tau) d\tau$  measures the probability that node  $j$  will remain infected during a period of time  $\tau$ . In this work we limit our analysis to homogeneous nodes, so that all nodes have the same recovery rate  $\eta$ . Recall that the infection of a susceptible node is characterized by a constant transmission rate  $\beta$ .

---

<sup>1</sup>Except in some plant infections, for which the plants remain infectious until their death [98, 124].

<sup>2</sup>Some authors prefer the use of “removed” in order to explicitly indicate that these nodes no longer participate of the dynamics, including both recovered and deceased agents.

### 3.1.1 Transient and late-time behavior

Overall, the population converges to a stable attractor where all agents are healthy and the pathogen is eradicated from the system. This state is not unique, however, since the proportion of susceptible to recovered agents can vary greatly. Here we consider a patient zero scenario, where a single node becomes infected in an otherwise susceptible population. Strong pathogens are able to produce a sustained outbreak which affects a large number of individuals, while weak pathogens are unable to maintain the transmission chains and die out very quickly. The virulence of an outbreak is measured by  $r_\infty$ , the fraction of nodes that recover from the disease. Note that all the nodes that become infected during the outbreak eventually end up in the recovered state.

We define the effective spreading ratio as

$$\lambda = \frac{\langle \tau \rangle_{\text{rec}}}{\langle \tau \rangle_{\text{tra}}}, \quad (3.1)$$

the ratio between the average recovery time,

$$\langle \tau \rangle_{\text{rec}} = \int_0^\infty \tau \psi_{\text{rec}}(\tau) d\tau = \int_0^\infty \tau \eta e^{-\eta\tau} d\tau = \eta^{-1}, \quad (3.2)$$

and the average transmission time,

$$\langle \tau \rangle_{\text{tra}} = \int_0^\infty \tau \psi_{\text{tra}}(\tau) d\tau = \int_0^\infty \tau \beta e^{-\beta\tau} d\tau = \beta^{-1}. \quad (3.3)$$

Roughly speaking, a longer average recovery time or a shorter average transmission time enables infected nodes to transmit the pathogen to more contacts in the period during which they remain infectious. In terms of rates we have  $\lambda = \beta/\eta$ .

Respectively, the effective spreading ratio,  $\lambda$ , and the late-time fraction of recovered nodes,  $r_\infty$ , play the roles of control and order parameters. Globally, the system undergoes a phase transition at a critical value  $\lambda_c$ , which separates a healthy phase ( $\lambda < \lambda_c$ ) from an epidemic phase ( $\lambda > \lambda_c$ ). In the former, single-seed outbreaks die out very quickly and affect a small number of individuals ( $r_\infty \approx 0$ ). In the latter, on the other hand, outbreaks show a characteristic growth-decline pattern and, with a nonvanishing probability, infect a large fraction of nodes ( $r_\infty > 0$ ). In epidemiological jargon, the critical value  $\lambda_c$  is called epidemic threshold.

### 3.1.2 Simulation results

While finding a closed form for the temporal evolution of the SIR model is feasible for just a handful of contact topologies, many analytical approaches are available to study the late-time properties of the system. Nevertheless, here we resort to simulations. We start each run with a single randomly chosen infected node in a fully healthy system (all other nodes are susceptible). The realization is halted when the last remaining infected node recovers.<sup>3</sup> Once again, we use a random degree-regular network with  $k = 4$  and  $N = 10^4$  nodes. We compute the prevalence as  $\rho(t) = N_I(t)/N$  and the fraction of recovered nodes as  $r(t) = N_R(t)/N$ , with  $N_I(t)$  (respectively,  $N_R(t)$ ) the number of infected (recovered) nodes at time  $t$ . Without loss of generality, hereon forward we use units of time such that  $\eta = 1$ .<sup>4</sup>

Figure 3.1(a) shows the average trajectory of 100 independent simulations with  $\lambda = 1$ . The prevalence exhibits an initial growth followed by a gradual decay; as nodes recover, the number of susceptible targets diminishes, which inhibits the spread of the outbreak and causes its decline. Additionally, the fraction of recovered nodes increases monotonically until reaching the saturating value  $r_\infty = \lim_{t \rightarrow \infty} r(t)$ . Figure 3.1(b) shows the final fraction of recovered individuals for a range of the effective spreading ratio, sampled from 1000 independent runs. We clearly identify a continuous phase transition at  $\lambda_c \approx 0.5$ , which separates the healthy and epidemic phases. This value agrees nicely with the theoretical result for the epidemic threshold in random degree-regular networks,  $\lambda_c = k/(k^2 - 2k)$  [133].

## 3.2 Memory-induced complex contagion SIR model

Now we equip the SIR model with the memory-induced complex contagion infection mechanism introduced in Section 2.2. Recall that infected nodes have a constant infectivity rate,  $\nu$ , and continuously spread doses of contagion toward their entire neighborhood. They target all of their neighbors equally, transmitting pathogen along each edge at constant rate  $\nu$ . Susceptible nodes collect these toxins from all their neighbors, amassing a total viral load  $\kappa$ , and

<sup>3</sup>See Appendix C.2.1 for an outline of the core algorithm.

<sup>4</sup>See Appendix C.2.3 for simulation details.

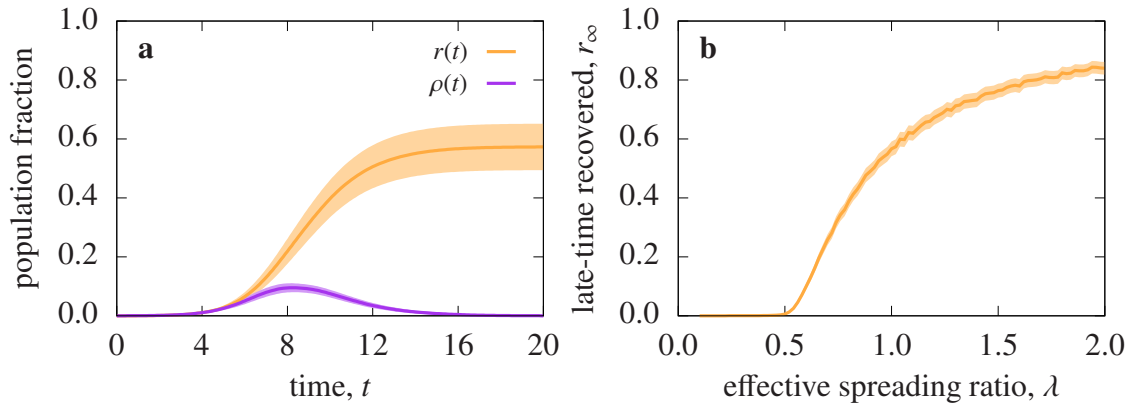


Figure 3.1: **Temporal evolution and late-time state of the standard SIR model.** Results for a random degree-regular network with  $k = 4$  and  $N = 10^4$ . Uncertainty intervals at 95% confidence level. **(a)** Average fraction of recovered (orange) and infected (purple) nodes of 100 independent simulations with  $\lambda = 1$ . **(b)** Late-time fraction of recovered nodes, averaged over 1000 independent runs.

transition to the infected state with probability  $\psi_{\text{inf}}^*(\kappa)d\kappa$ , where  $\psi_{\text{inf}}^*(\kappa)$  is the infection probability density. Additionally, infected nodes are unaffected by the toxins (their viral load does not increase) and recover spontaneously after a random time  $\tau$ , with interevent time distribution  $\psi_{\text{rec}}(\tau)$ . At recovery, their viral load is completely erased. Recovered nodes remain unaltered forever more.

### 3.2.1 Dormant nodes

As in the standard model, susceptible nodes whose nearest neighborhood is completely healthy cannot become infected. Since no active processes are associated to their state, they are irrelevant for the immediate evolution of the system. However, these inactive nodes play a crucial role in the long-term dynamics of the miccSIR model; we therefore assign them to an additional compartment, which we call dormant. A dormant node transitions to susceptible as soon as one of its neighbors becomes infected. Conversely, when the last infected neighbor of a susceptible node recovers, the latter transitions to the dormant state. At this point, the viral load it had previously amassed starts to deteriorate with relaxation time  $\zeta$ , modeling its long-term memory. This feature mimics the restoring of an individual's immune system or the gradual

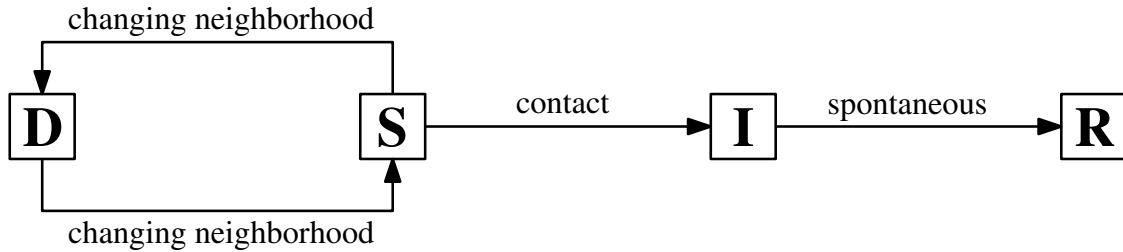


Figure 3.2: **Schematic overview of transitions in the miccSIR model.** Nodes transition between dormant and susceptible because of changes in their nearest neighborhood. The infection of a susceptible node requires contact from an infected neighbor. Infected nodes transition spontaneously to the (terminal) recovered state.

loss of interest of an opinion, idea, or trend.

In summary, infected (I) agents spread pathogen to all their neighbors and recover spontaneously. While susceptible (S) agents have at least one infected neighbor and continuously accumulate viral load, dormant (D) agents have a fully healthy neighborhood and cannot become infected. Recovered (R) agents do not participate actively in the dynamics. There are two types of active processes which entail one or possibly more transitions (see Fig. 3.2):

- Infection of susceptible agent  $j$ . Agent  $j$  transitions from susceptible to infected. Additionally, all of  $j$ 's neighbors that were dormant transition to susceptible (and resume their accumulation of viral load).
- Recovery of infected agent  $j$ . Agent  $j$  transitions from infected to recovered. Additionally, all of  $j$ 's neighbors that were susceptible and had only one infected neighbor (i.e., agent  $j$ ) transition to dormant (and their viral load starts to decay).

Finally, infected agents are unaffected by the viral load and ignore any new doses received from their infected neighbors. When an infected agent recovers it erases all its previously amassed viral load.

### 3.2.2 Parameter selection

In general, the relaxation time,  $\zeta_i$ , and the recovery interevent time distribution,  $\psi_i(\tau)$ , may vary from node to node. In order to eliminate the effects of node heterogeneities, in the present work we use the same  $\zeta$  and  $\psi_{\text{rec}}(\tau)$  for all nodes.

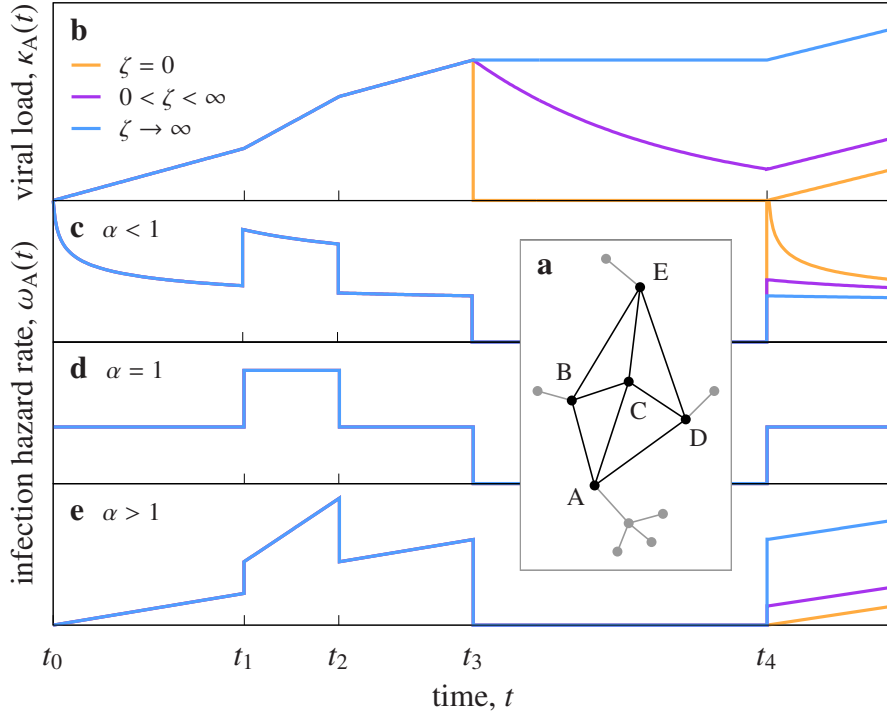


Figure 3.3: **Viral load accumulation in the miccSIR model.** (a) Small system considered in example. (b) Evolution of node A's viral load. In the interval  $t \in [t_3, t_4]$  node A is dormant and its viral load decays instantly (orange), at a finite nonvanishing rate (purple), or accumulates perpetually (blue). (c–e) Node A's instantaneous infection rate for (c)  $\alpha < 1$ , (d)  $\alpha = 1$ , and (e)  $\alpha > 1$ , evaluated using Eq. (3.4). In the interval  $t \in [t_3, t_4]$  node A's neighborhood is completely healthy and it cannot become infected ( $\omega_A = 0$ ).

To further isolate the effects of the modified infection mechanism, we treat recoveries as Poisson processes with constant hazard rate  $\omega_{\text{rec}} = \eta$ . Recall that infections are governed by a Weibull distribution with instantaneous hazard rate

$$\omega_{\text{inf}}(t) = v\alpha\mu^\alpha z(t) [\kappa(t)]^{\alpha-1}, \quad (3.4)$$

with  $z(t)$  the number of infected neighbors at time  $t$  (see Section 2.2.2).

Inspired by Eq. (3.1), we define the effective spreading ratio as

$$\lambda = v \frac{\langle \tau \rangle_{\text{rec}}}{\langle \kappa \rangle_{\text{inf}}}, \quad (3.5)$$

the average time required to recover,

$$\langle \tau \rangle_{\text{rec}} = \int_0^{\infty} \tau \psi_{\text{rec}}(\tau) d\tau = \int_0^{\infty} \tau \eta e^{-\eta\tau} d\tau = \eta^{-1}, \quad (3.6)$$

over the viral load needed to become infected,

$$\langle \kappa \rangle_{\text{inf}} = \int_0^{\infty} \kappa \psi_{\text{inf}}(\kappa) d\kappa = \int_0^{\infty} \alpha (\mu\kappa)^{\alpha} e^{-(\mu\kappa)^{\alpha}} d\kappa = (\mu\alpha)^{-1} \Gamma(\alpha^{-1}), \quad (3.7)$$

nondimensionalized by the infectivity rate,  $\nu$ . From here we find an expression for the scale parameter,

$$\mu = \eta \lambda (\nu\alpha)^{-1} \Gamma(\alpha^{-1}), \quad (3.8)$$

with  $\Gamma(x)$  the gamma function. Once again notice that  $\alpha = 1$  recovers the customary expression of the standard SIR model,  $\lambda = \nu\mu/\eta$  (with transmission rate  $\beta = \nu\mu$ ). Note also that this equivalence holds for all values of the relaxation time  $\zeta$ .

For illustrative purposes, consider the system depicted in Fig. 3.3(a), where all nodes are initially healthy except for E. Node B becomes infected at time  $t_0$  and subsequently infects C at  $t_1$ . During the interval  $t \in [t_0, t_1]$ , node A's viral load,  $\kappa_A$ , grows with rate  $\nu$ , but from  $t_1$  onwards it will increase with rate  $2\nu$ . At  $t_2$ , node C recovers and  $\kappa_A$  reduces its accumulation rate back to  $\nu$ , and when B recovers at  $t_3$ ,  $\kappa_A$  starts to decay with relaxation time  $\zeta$ . Finally, D becomes infected at  $t_4$  and  $\kappa_A$  resumes its growth at rate  $\nu$ . Figures 3.3(b)–(e) show the evolution of  $\kappa_A$  and  $\omega_A$  for various  $\zeta$  and  $\alpha$ .

### 3.2.3 Late-time and transient behavior

We start each run with a single randomly chosen infected node in a fully healthy system (all other nodes are susceptible); the realization is halted when the last remaining infected node recovers.<sup>5</sup> We use a random degree-regular network with  $k = 4$  and  $N = 10^4$  nodes and compute the prevalence as  $\rho(t) = N_I(t)/N$  and the fraction of recovered nodes as  $r(t) = N_R(t)/N$ , with  $N_I(t)$  (respectively,  $N_R(t)$ ) the number of infected (recovered) nodes at time  $t$ . Recall that we use units of time and viral load such that  $\eta = \nu = 1$ . As for the relaxation time of dormant nodes' viral load, we consider the limit cases of instantaneous decay,  $\zeta = 0$ , and perpetual accumulation,  $\zeta \rightarrow \infty$ .<sup>6</sup>

<sup>5</sup>See Appendix C.2.2 for an outline of the core algorithm.

<sup>6</sup>See Appendix C.2.3 for simulation details.

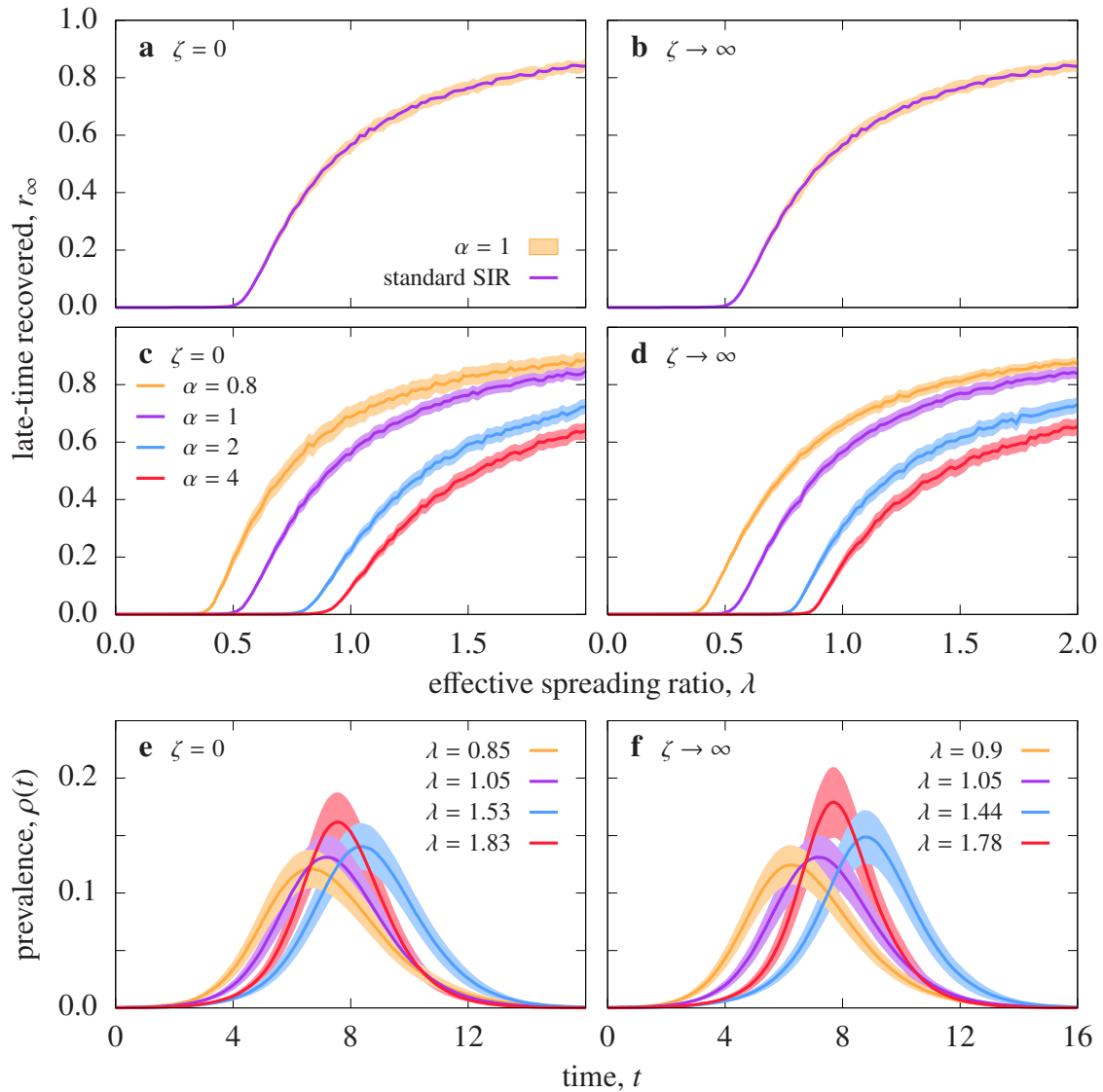


**Figure 3.4: Late-time state and temporal evolution of the miccSIR model.** Results for a random degree-regular network with  $k = 4$  and  $N = 10^4$ . Uncertainty intervals at 95% confidence level. **(a, b)** Late-time fraction of recovered nodes in the standard SIR model (purple curve) and miccSIR model (orange shaded area) with shape parameter  $\alpha = 1$ , for relaxation time **(a)**  $\zeta = 0$  and **(b)**  $\zeta \rightarrow \infty$ , averaged over 1000 independent runs. **(c, d)** Late-time fraction of recovered nodes in the miccSIR model for **(c)**  $\zeta = 0$  and **(d)**  $\zeta \rightarrow \infty$ , averaged over 1000 independent runs (shape parameter in legend). **(e, f)** Fraction of infected nodes for **(e)**  $\zeta = 0$  and **(f)**  $\zeta \rightarrow \infty$ , averaged over 100 independent simulations (spreading ratio in legend, shape parameters as in **c**).

With  $\zeta = 0$ , nodes instantly erase their viral load when they become dormant. If the outbreak reenters their neighborhood, they become susceptible starting afresh (with  $\kappa = 0$ ). Hence the only memory effect that is present is during the infection period (when the agent is actively exposed to doses of pathogen), which we interpret as a short-term memory mode. In Fig. 3.4(a) we verify that  $\alpha = 1$  recovers the standard SIR model. Figure 3.4(c) reveals that the epidemic threshold grows monotonically with  $\alpha$ , the shape parameter of the infection probability. Additionally, the growth of  $r_\infty$  is less abrupt for larger values of  $\alpha$ . In all cases, the transition from the healthy to the epidemic phase is continuous. Finally, Fig. 3.4(e) shows the temporal evolution of the prevalence for outbreaks that reach a final state of  $r_\infty \approx 0.6$ . Although these epidemic curves are not directly comparable, with  $\alpha < 1$  (respectively,  $\alpha > 1$ ) the outbreak is generally broader (narrower) and exhibits a smaller (larger) peak.

Next we consider the case  $\zeta \rightarrow \infty$ , where a dormant node's viral load remains frozen until the outbreak revisits its neighborhood. Besides the short-term memory that is present during the infection period, agents now possess an additional long-term memory mode that is capable of connecting very distant temporal points, causing the system to evolve in a highly nonlinear manner. Once again, in Fig. 3.4(b) we verify that  $\alpha = 1$  recovers the standard SIR model. Figure 3.4(d) shows that the transition is continuous and that the epidemic threshold grows with  $\alpha$ . In Fig. 3.4(f) we observe that, roughly speaking, the epidemic curves are broader (respectively, narrower) and shorter (taller) for  $\alpha < 1$  ( $\alpha > 1$ ).

Finally, Figs. 3.5(a)–(c) reveal that, if agents are equipped with a long-term memory mode, the late-time fraction of recovered nodes is slightly smaller (respectively, larger) for  $\alpha < 1$  ( $\alpha > 1$ ). However, the epidemic threshold does not change and the average outbreaks are very similar (see Figs. 3.5(d)–(f)).

### 3.2.4 Discussion

Concluding, the short-term mode ( $\zeta = 0$ ) of the memory-induced complex contagion infection mechanism causes a displacement of the epidemic threshold in the SIR model. In particular, smaller values of the infection probability's shape parameter  $\alpha$  enable weaker pathogens (i.e., lower values of the effective spreading ratio  $\lambda$ ) to cause sustained outbreaks. Notwithstanding, the transition between the healthy and epidemic phases remains continuous. More-

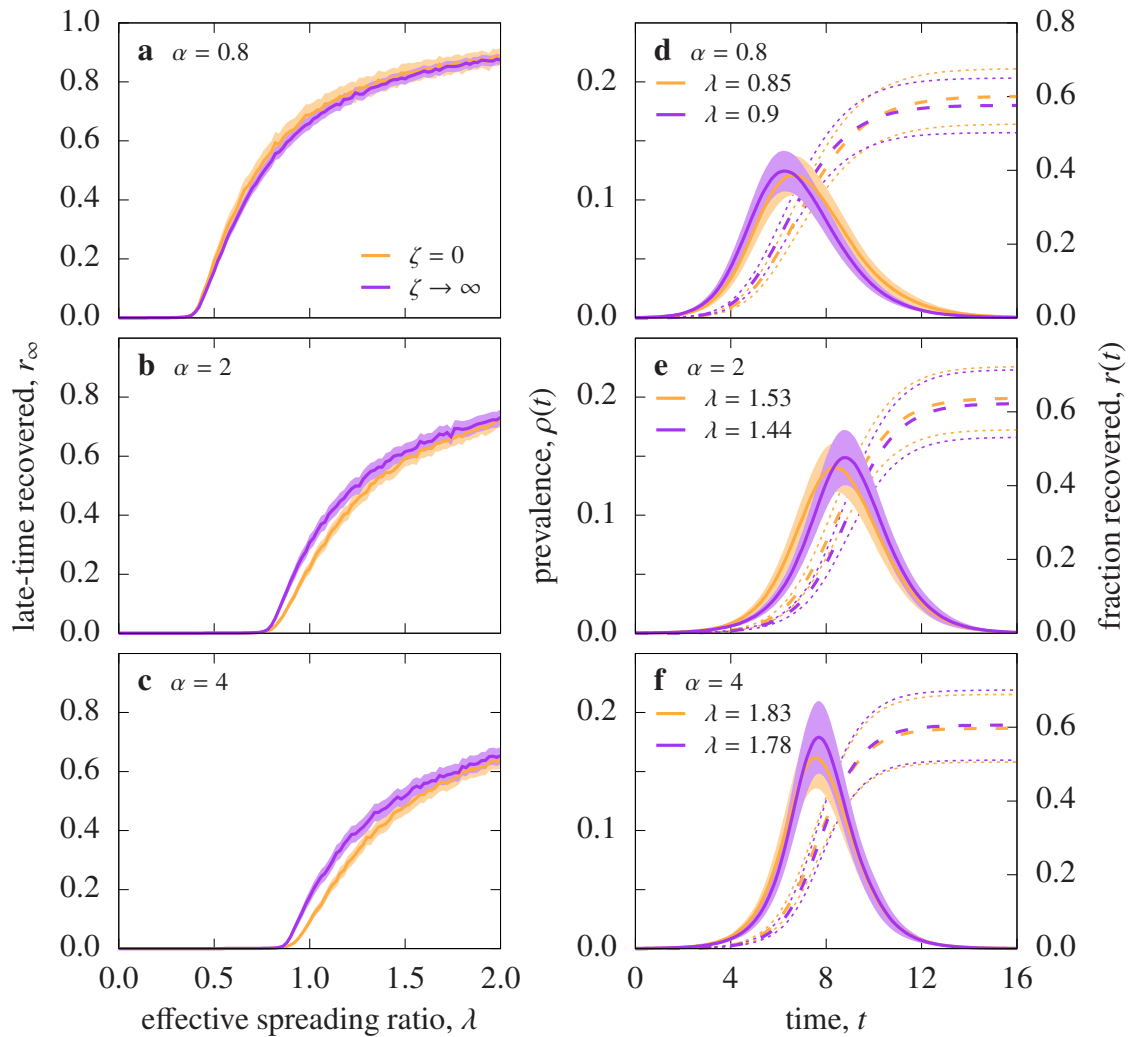


**Figure 3.5: Comparison between short- and long-term memory modes in the miccSIR model.** Results for a random degree-regular network with  $k = 4$  and  $N = 10^4$ . Uncertainty intervals at 95% confidence level. **(a–c)** Late-time fraction of recovered nodes in the miccSIR model for shape parameter **(a)**  $\alpha = 0.8$ , **(b)**  $\alpha = 2$ , and **(c)**  $\alpha = 4$ , averaged over 1000 independent runs (relaxation time in legend). **(d–f)** Temporal evolution of the prevalence (solid curve, shaded area) and fraction of recovered nodes (dashed curve, dotted area) for **(d)**  $\alpha = 0.8$ , **(e)**  $\alpha = 2$ , and **(f)**  $\alpha = 4$ , averaged over 100 independent runs (spreading ratio in legend, relaxation times as in **a**).

over, long-tailed infection probabilities ( $\alpha < 1$ ) yield outbreaks that initially evolve more rapidly but last longer than bell-shaped infection probabilities ( $\alpha > 1$ ). Notice that this observation is consistent with our findings for the miccSI model (see Section 2.2.6).

The overall picture is very similar if individuals possess an additional long-term memory ( $\zeta \rightarrow \infty$ ). Compared to the short-term memory mode, for  $\alpha > 1$  (respectively,  $\alpha < 1$ ) the outbreaks are slightly more (less) virulent, affecting a larger (smaller) fraction of the population. This observation is explained by the monotonically increasing (decreasing) infection rate. When the outbreak revisits a dormant node's neighborhood, its previously accumulated viral load facilitates (hinders) its infection, enabling (preventing) the expansion of the outbreak. Nevertheless, the effect of this phenomenon is undermined by the existence of recovered nodes, which act as (very efficient) blockers of the transmission chains and impede the outbreak to circulate freely around network.

Admittedly, the addition of recoveries to the memory-induced complex contagion infection mechanism has a mild effect in terms of macroscopic phenomenology. However, this novel infection mechanism shows its full potential in Chapter 4, where we include reinfections.



# The SIS model

---

## 4.1 Standard SIS model

The model discussed in the previous chapter ignores the possibility that recovered individuals can sometimes become reinfected. This is the case, for instance, with dengue fever, the common cold, and sexually transmitted diseases such as gonorrhea and chlamydia [98]. On the other hand, waning immunity (against measles or pertussis, for example) can also lead to reinfection [107]. Finally, a similar idea can be applied to the spread of rumors, which can spark renewed attention after a period of low interest [50, 94].

The susceptible-infected-susceptible (SIS) model incorporates the reinfection of recovered agents. Infected agents *i*) transmit the pathogen to their susceptible nearest-neighbors and ii) recover spontaneously, transitioning back to the susceptible state. As before, the population is embedded on an undirected, unweighted, static contact network. In the standard SIS model, the transmission of the pathogen from infected node *i* to susceptible node *j* is characterized by a constant transmission rate  $\beta_{i \rightarrow j}$ . Additionally, the recovery of infected node *j* is described by a constant recovery rate  $\eta_j$ . Once again, we limit our analysis to homogeneous nodes: the pathogen transmits along all the links at the same rate  $\beta$  and all nodes have the same recovery rate  $\eta$ . Finally, the definition of the effective spreading ratio remains unaltered,  $\lambda = \langle \tau \rangle_{\text{rec}} / \langle \tau \rangle_{\text{tra}} = \beta / \eta$ .

Overall, the macroscopic state of the system is measured by  $\rho_\infty$ , the late-time value of the prevalence. The bifurcation diagram typically shows a continuous, absorbing phase transition at the epidemic threshold  $\lambda_c$ . When  $\lambda < \lambda_c$ , the outbreak dies out exponentially fast and all agents are disease-free ( $\rho_\infty = 0$ ), representing an absorbing, healthy phase. For  $\lambda > \lambda_c$ , on the other hand, there is a nonvanishing fraction of infected agents ( $\rho_\infty > 0$ ), defining an active, endemic phase. Notice, however, that the latter constitutes a nonequilibrium steady state since individuals continuously recover and reinfect.

### 4.1.1 Analytic approximation

At time  $t$ , node  $i$  is described by its state  $n_i(t)$ , a discrete variable that takes two values:  $n_i = 0$  if it is susceptible or  $n_i = 1$  if it is infected. The state of node  $i$  changes with the transitions i) infected to healthy and ii) susceptible to infected. Recall the nonindependent variable  $z_i(t) = \sum_j a_{ij}n_j(t)$ , with  $a_{ij}$  the elements of the adjacency matrix, which encodes the number of  $i$ 's neighbors that are infected at time  $t$ . The evolution of these variables is governed by two microscopic, dichotomous, stochastic processes:

- i) Infected node  $i$  recovers ( $\xi_i = 1$ ) or remains infected ( $\xi_i = 0$ ), given by node  $i$ 's recovery rate  $\eta$ . The corresponding probabilities at  $\mathcal{O}(dt)$  are

$$\xi_i = \begin{cases} 1 & \eta dt \\ 0 & 1 - \eta dt \end{cases} . \quad (4.1)$$

- ii) Susceptible node  $i$  becomes infected ( $\pi_i = 1$ ) or remains susceptible ( $\pi_i = 0$ ), given by node  $i$ 's instantaneous infection rate  $\omega_i(t) = \beta z_i(t)$ . The corresponding probabilities at  $\mathcal{O}(dt)$  are

$$\pi_i = \begin{cases} 1 & \omega_i(t) dt \\ 0 & 1 - \omega_i(t) dt \end{cases} . \quad (4.2)$$

The state of node  $i$  at time  $t + dt$  is

$$n_i(t + dt) = n_i(t)(1 - \xi_i) + (1 - n_i(t))\pi_i , \quad (4.3)$$

where the first term corresponds to node  $i$  being infected ( $n_i(t)$ ) and not recovering ( $1 - \xi_i$ ), and the second term corresponds to node  $i$  being susceptible ( $1 - n_i(t)$ ) and becoming infected ( $\pi_i$ ). In order to obtain the dynamic equation, we first compute the expectation value conditioned on time  $t$ , which only affects the stochastic variables

$$\mathbb{E}[n_i(t + dt) | t] = n_i(t) \mathbb{E}[1 - \xi_i | t] + (1 - n_i(t)) \mathbb{E}[\pi_i | t] \quad (4.4)$$

$$= n_i(t)(1 - \eta dt) + (1 - n_i(t))\omega_i(t) dt \quad (4.5)$$

$$= n_i(t) - n_i(t)\eta dt + (1 - n_i(t))\beta z_i(t) dt . \quad (4.6)$$

Taking the ensemble average yields

$$\langle n_i(t + dt) \rangle = \langle \mathbb{E}[n_i(t + dt) | t] \rangle \quad (4.7)$$

$$= \langle n_i(t) \rangle - \eta \langle n_i(t) \rangle dt + \beta \langle (1 - n_i(t))z_i(t) \rangle dt , \quad (4.8)$$

from where we find

$$\frac{d\langle n_i(t) \rangle}{dt} = \frac{\langle n_i(t + dt) \rangle - \langle n_i(t) \rangle}{dt} = -\eta\langle n_i(t) \rangle + \beta\langle (1 - n_i(t))z_i(t) \rangle. \quad (4.9)$$

### 4.1.2 Late-time limit and mean-field approximation

Taking the late-time limit in Eq. (4.9) and dropping the explicit dependence with  $t$  we find

$$0 = -\eta\langle n_i \rangle + \beta\langle (1 - n_i)z_i \rangle. \quad (4.10)$$

And for uncorrelated networks we can apply a mean-field approximation

$$\langle (1 - n_i)z_i \rangle \approx \sum_j \frac{k_i k_j}{N\langle k \rangle} (\langle n_j \rangle - \langle n_i \rangle \langle n_j \rangle), \quad (4.11)$$

with  $k_i$  and  $k_j$  the degrees of nodes  $i$  and  $j$ , respectively, and  $\langle k \rangle$  the average degree (see Section 2.1.2). Particularly, in random degree-regular networks we have  $k_i = k_j = \langle k \rangle = k$ , and due to homogeneity,  $\langle n_i \rangle = \langle n_j \rangle = \rho$ . Then Eq. (4.10) becomes

$$0 = -\rho + \lambda k \rho (1 - \rho), \quad (4.12)$$

where  $\rho = \lim_{t \rightarrow \infty} \rho(t)$  is the late-time prevalence.<sup>1</sup>

Thus the dynamics of the standard SIS model is encapsulated by the function

$$f(\rho) = -\rho + \lambda k \rho (1 - \rho) \quad (4.13)$$

and its first and second derivatives

$$f'(\rho) = -1 + \lambda k (1 - 2\rho) \quad (4.14)$$

$$f''(\rho) = -2\lambda k. \quad (4.15)$$

The fixed points are given by  $f(\rho_*) = 0$ . Linear stability analysis reveals that these are stable when  $f'(\rho_*) < 0$  and unstable when  $f'(\rho_*) > 0$ . Moreover, the transition is continuous if  $f''(\rho_*) < 0$  and discontinuous if  $f''(\rho_*) > 0$ .

<sup>1</sup>For clarity, in this section we drop the subindex  $\infty$ .

From Eq. (4.12) we find that the healthy phase  $\rho_0 = 0$  is always a fixed point. It is stable for  $\lambda < 1/k$  and unstable for  $\lambda > 1/k$ , yielding the epidemic threshold  $\lambda_c = 1/k$ . Since  $f'' = -2\lambda k < 0, \forall \lambda$ , the transition is always continuous. The endemic phase is found by solving

$$0 = -1 + \lambda k(1 - \rho_+), \quad (4.16)$$

which gives

$$\rho_+ = 1 - \frac{1}{\lambda k} = \frac{\lambda - \lambda_c}{\lambda}. \quad (4.17)$$

Thus, near the critical point, the prevalence scales as  $\rho_+ \propto (\lambda - \lambda_c)^{\beta_c}$ , with  $\beta_c = 1$  the customary mean-field exponent [133].

### 4.1.3 Simulation results

In order to verify our analytic findings we perform extensive stochastic simulations.<sup>2</sup> We begin by using an adiabatic expansion–like approach to explore the position of the critical point,  $\lambda_c$ , which separates an absorbing (healthy) phase ( $\lambda < \lambda_c$ ) from an active (endemic) one ( $\lambda > \lambda_c$ ). Our simulations start well into the active phase ( $\lambda \gg \lambda_c$ ), with a fully infected population, and quasi-statically decrease the control parameter ( $\lambda$ ) until finite-size fluctuations trap the system in the absorbing state ( $\rho = 0$ ). Recall that we use random degree-regular networks with degree  $k = 4$  and units of time such that  $\eta = 1$ . Here we use networks with  $N = 10^3$  and  $N = 10^4$  nodes. We compute the prevalence as  $\rho(t) = N_I(t)/N$ , with  $N_I(t)$  the number of infected nodes at time  $t$ .<sup>3</sup> Figure 4.1(a) shows the late-time prevalence,  $\rho_\infty = \lim_{t \rightarrow \infty} \rho(t)$ , sampled from  $10^4$  states and time-averaged over various trajectories. We clearly identify a continuous phase transition at  $\lambda_c \approx 0.35$  (notice that the apparent discontinuity decreases with the system size). The value of the epidemic threshold deviates from our mean-field prediction ( $\lambda_c = 1/k = 0.25$ ), but agrees nicely with the result of a pairwise approach ( $\lambda_c = 1/(k - 1) = 0.\hat{3}$ ) [102, 106].

We complement these results with the analysis of the arrival of an infected agent in a previously unaffected population. This patient zero scenario models realistic situations such as the importation of an exotic disease, the introduction of an invasive species, or the emergence of a new idea, opinion, or trend.

<sup>2</sup>See Appendix C.3.1 for an outline of the core algorithm.

<sup>3</sup>See Appendix C.3.3 for simulation details.

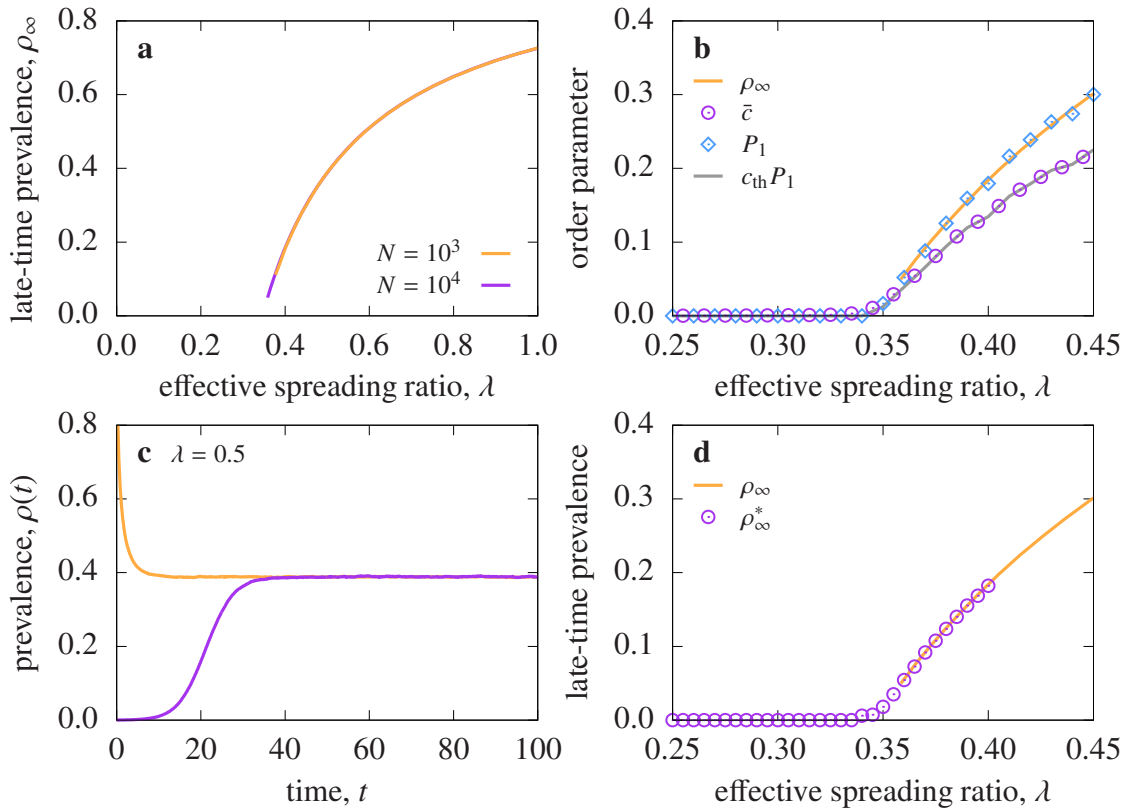


Figure 4.1: **Late-time prevalence and patient zero scenario in the standard SIS model.** Results for a random degree-regular network with  $k = 4$ . **(a)** Late-time prevalence of the active steady state for networks with  $N = 10^3$  and  $N = 10^4$  nodes, time-averaged over  $10^4$  samples. Uncertainty intervals not appreciable at this scale. **(b)** Late-time prevalence (orange curve), average coverage fraction (purple circles), and endemic probability (blue diamonds) for a network of size  $N = 10^4$ , averaged over  $10^4$  independent realizations. Uncertainty intervals comparable to symbol size. **(c)** Temporal evolution of endemic patient zero outbreaks (purple) and relaxation from a fully infected population (orange) in a network of  $N = 10^4$  nodes, averaged over 100 independent runs. Uncertainty intervals comparable to line width. **(d)** Late-time prevalence of adiabatic expansion (orange) and endemic single-seed outbreaks (purple) for a network of size  $N = 10^4$ , averaged over  $10^4$  independent realizations. Uncertainty intervals not appreciable at this scale.

We employ the lifespan method (introduced in [15] and developed in [115]), which simulates outbreaks that start from a single infected node. These outbreaks either return to the absorbing state (finite outbreaks) or evolve toward an active steady state (endemic outbreaks). Each single-seed realization is characterized by its lifetime and coverage,  $K$ , defined as the number of distinct nodes that have become infected at least once.

In the thermodynamic limit, endemic realizations have an infinite lifetime, a coverage equal to the system size, and are only possible in the active phase. On the other hand, finite realizations have a finite lifetime and coverage and can be found in both phases; nonetheless, their abundance decreases above the critical point. Thus the probability that an outbreak is endemic,  $P_\infty$ , vanishes in the absorbing phase and is nonzero in the active phase, playing the role of an order parameter. In finite systems, however, any realization is bound to reach the absorbing state, even though this might occur over astronomically long times. Therefore, the distinction between finite and endemic outbreaks is not clear. To overcome this hinderance we introduce a coverage threshold,  $K_{\text{th}} = c_{\text{th}}N$ , with  $0 < c_{\text{th}} < 1$ . A realization is declared endemic whenever its coverage reaches the threshold, and those that terminate without surpassing it are considered finite. Hereafter we use  $c_{\text{th}} = 0.75$ . As reported in [115], the value of  $c_{\text{th}}$  does not modify the qualitative results.

For a fixed value of the control parameter  $\lambda$  we run  $10^4$  independent realizations, each starting with a single randomly chosen infected node. We measure the average coverage fraction,  $\bar{c} = \langle K \rangle / N$ , and the probability that a realization surpasses the coverage threshold,  $P_1$ , which serves as a proxy for the true endemic probability,  $P_\infty$ .<sup>4</sup> As we can see in Fig. 4.1(b), the average coverage fraction and endemic probability show a continuous phase transition at roughly the same critical point as the late-time prevalence. Inasmuch as these three order parameters characterize the same two phases, their critical points are expected to coincide. However, the equivalence between  $P_1$  and  $\rho_\infty$  is both surprising and puzzling. The relation between  $\bar{c}$  and  $P_1$ , on the other hand, is explained by decomposing the former as  $\bar{c} = c_{\text{end}}P_1 + c_{\text{fin}}(1 - P_1)$ , where  $c_{\text{end}}$  (respectively,  $c_{\text{fin}}$ ) is the average coverage of endemic (finite) realizations. Since  $c_{\text{end}} = c_{\text{th}}$  and  $c_{\text{fin}} \approx 0$ , we find  $\bar{c} \approx c_{\text{th}}P_1$  (see grey curve in Fig. 4.1(b)). Finally, Fig 4.1(c) shows the temporal evolution of endemic outbreaks, which rapidly evolve toward their active steady state,  $\rho_\infty^*$ . Notice that, when we start our simulation with a fully infected population, the system relaxes to the same

<sup>4</sup>See Appendix C.3.4 for simulation details.

dynamic equilibrium. In Fig 4.1(d) we verify that the equivalence between  $\rho_\infty$  and  $\rho_\infty^*$  holds for all values of  $\lambda$ .

## 4.2 Memory-induced complex contagion SIS model

Here we equip the SIS model with the memory-induced complex contagion infection mechanism. Recall that infected nodes have a constant infectivity rate,  $\nu$ , and continuously spread doses of contagion toward their entire neighborhood. They target all of their neighbors equally, transmitting pathogen along each edge at constant rate  $\nu$ . Susceptible nodes collect these toxins from all their neighbors, amassing a total viral load  $\kappa$ , and transition to the infected state with probability  $\psi_{\text{inf}}^*(\kappa)d\kappa$ , where  $\psi_{\text{inf}}^*(\kappa)$  is the infection probability density. Additionally, infected nodes are unaffected by the toxins (their viral load does not increase) and recover spontaneously after a random time  $\tau$ , with interevent time distribution  $\psi_{\text{rec}}(\tau)$ . At recovery, their viral load is completely erased. Recoverd nodes may be reinfected.

We differentiate susceptible nodes, healthy nodes with one or more infected neighbors, from dormant nodes, healthy nodes whose nearest neighborhood is completely healthy; the latter cannot become infected and play a crucial role in the long-term dynamics of the miccSIS model. A dormant node transitions to susceptible as soon as one of its neighbors becomes infected. Conversely, when the last infected neighbor of a susceptible node recovers, the latter transitions to the dormant state. At this point, the viral load it had previously amassed starts to deteriorate with relaxation time  $\zeta$ , modeling its long-term memory. When an infected node recovers, it becomes either susceptible or dormant, depending on the configuration of its neighborhood.

In summary, infected (I) agents spread pathogen to all their neighbors and recover spontaneously. While susceptible (S) agents have at least one infected neighbor and continuously accumulate viral load, dormant (D) agents have a fully healthy neighborhood and cannot become infected. There are two types of active processes which entail one or possibly more transitions (see Fig. 4.2):

- Infection of susceptible agent  $j$ . Agent  $j$  transitions from susceptible to infected. Additionally, all of  $j$ 's neighbors that were dormant transition to susceptible (and resume their accumulation of viral load).

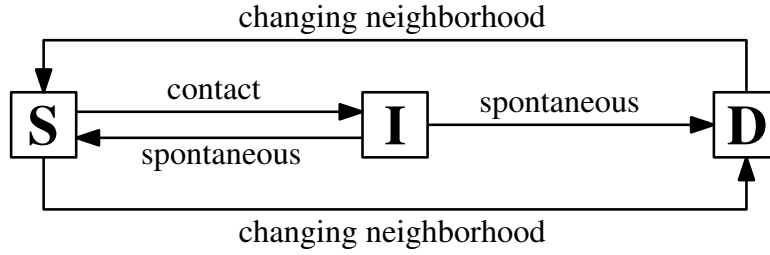


Figure 4.2: **Schematic overview of transitions in the miccSIS model.** Nodes transition between dormant and susceptible because of changes in their nearest neighborhood. The infection of a susceptible node requires contact from an infected neighbor. Depending on the configuration of their neighborhood, infected nodes transition spontaneously to susceptible or dormant.

- Recovery of infected agent  $j$ . If all of  $j$ 's neighbors are healthy,  $j$  transitions from infected to dormant; if at least one of  $j$ 's neighbors is infected,  $j$  transitions from infected to susceptible. Additionally, all of  $j$ 's neighbors that were susceptible and had only one infected neighbor (i.e., agent  $j$ ) transition to dormant (and their viral load starts to decay).

Finally, infected agents are unaffected by the viral load, and ignore any new doses received from their infected neighbors. When an infected agent recovers it erases all the previously amassed viral load.

In order to eliminate the effects of node heterogeneities, we use the same infectivity rate,  $\nu$ , relaxation time,  $\zeta$ , infection probability density,  $\psi_{\text{inf}}^*(\kappa)$ , and recovery interevent time distribution,  $\psi_{\text{rec}}(\tau)$ , for all nodes. Recall that infections are governed by the versatile Weibull distribution, with shape parameter  $\alpha$  and scale parameter  $\mu$ , and that recoveries are exponential. The corresponding instantaneous hazard rates are

$$\omega_{\text{inf}}(t) = \nu\alpha\mu^\alpha z(t) [\kappa(t)]^{\alpha-1} \quad (4.18)$$

$$\omega_{\text{rec}}(t) = \eta, \quad (4.19)$$

with  $z(t)$  the number of infected neighbors at time  $t$ . As before, the effective spreading ratio is defined as  $\lambda = \nu\langle\tau\rangle_{\text{rec}}/\langle\kappa\rangle_{\text{inf}}$ , from where we find an expression for the scale parameter  $\mu = \eta\lambda(\nu\alpha)^{-1}\Gamma(\alpha^{-1})$ , with  $\Gamma(x)$  the gamma function. Yet again, note that  $\alpha = 1$  recovers the standard SIS model for all values of the relaxation time  $\zeta$ .

For illustrative purposes, consider the system depicted in Fig. 4.3(a), where all nodes are initially healthy except for C. Node B becomes infected at time  $t_0$ ,

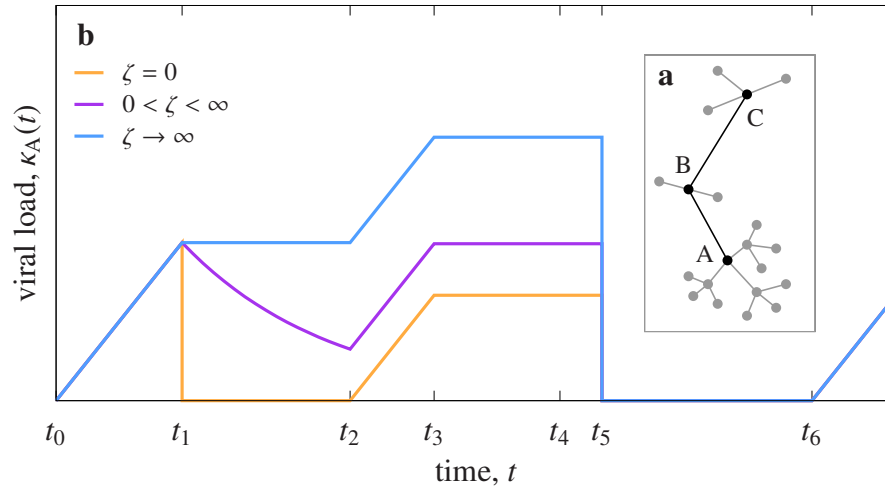


Figure 4.3: **Viral load accumulation in the miccSIS model.** (a) Small system considered in example. (b) Evolution of node A's viral load. Node A becomes dormant at  $t_1$  and its viral load decays instantly (orange), at a finite nonvanishing rate (purple), or accumulates perpetually (blue). When A recovers at  $t_5$ , its viral load is instantly erased.

recovers at  $t_1$ , and reinfects at time  $t_2$ . During the interval  $t \in [t_0, t_1]$ , node A's viral load,  $\kappa_A$ , grows with rate  $\nu$ . At  $t_1$  it starts to decay with relaxation time  $\zeta$  and resumes its growth at time  $t_2$ . Node A becomes infected at  $t_3$  and its viral load remains frozen; additionally, node B recovers at time  $t_4$ . When A recovers at  $t_5$ , its viral load is erased instantly. Finally, B becomes infected again at  $t_6$  and A starts amassing additional viral load. Figure 4.3(b) show the evolution of  $\kappa_A$  for various  $\zeta$ .

### 4.2.1 Short-term memory

We start our analysis considering the limit case  $\zeta = 0$ , for which nodes instantly erase their viral load when they become dormant. If the outbreak reenters their neighborhood, they become susceptible starting afresh (with  $\kappa = 0$ ). Hence the only memory effect that is present is during the infection period (when the agent is actively exposed to doses of pathogen), which we interpret as a short-term memory mode.

To describe node  $i$  at time  $t$  we need two variables: its state  $n_i(t)$  and its viral load  $\kappa_i(t)$ . The former is a discrete variable that can take two values,  $n_i(t) = 1$  if it is infected or  $n_i(t) = 0$  if it is healthy (susceptible or dormant).

The viral load, on the other hand, is a continuous variable with  $\kappa_i(t) \geq 0$ . The state of a node only changes with the transitions i) infected to healthy and ii) susceptible to infected; when a node transitions between susceptible and dormant, its state remains unaltered. On the other hand, the viral load i) remains unaltered while a node is infected, ii) is erased instantly when a node recovers, iii) increases proportionally to the number of infected neighbors while a node is susceptible, and iv) is erased instantly when a susceptible node becomes dormant.

Recall that the number of infected neighbors is  $z_i(t) = \sum_j a_{ij}n_j(t)$ , with  $a_{ij}$  the elements of the adjacency matrix. In particular, this variable aids in distinguishing healthy susceptible nodes,  $(1 - n_i(t))(1 - \delta_{z_i(t)}^0)$ , from healthy dormant nodes,  $(1 - n_i(t))\delta_{z_i(t)}^0$ , with  $\delta_m^\ell$  the Krönecker function

$$\delta_m^\ell = \begin{cases} 1 & m = \ell \\ 0 & m \neq \ell \end{cases} . \quad (4.20)$$

The evolution of these variables is governed by three microscopic, dichotomous, stochastic processes:

- i) Infected node  $i$  recovers ( $\xi_i = 1$ ) or remains infected ( $\xi_i = 0$ ), given by node  $i$ 's recovery rate  $\eta$ . The corresponding probabilities at  $\mathcal{O}(dt)$  are

$$\xi_i = \begin{cases} 1 & \eta dt \\ 0 & 1 - \eta dt \end{cases} . \quad (4.21)$$

- ii) Susceptible node  $i$  becomes infected ( $\pi_i = 1$ ) or remains susceptible ( $\pi_i = 0$ ), given by node  $i$ 's instantaneous infection rate  $\omega_i(t)$ . The corresponding probabilities at  $\mathcal{O}(dt)$  are

$$\pi_i = \begin{cases} 1 & \omega_i(t)dt \\ 0 & 1 - \omega_i(t)dt \end{cases} , \quad (4.22)$$

with  $\omega_i(t) = \nu\alpha\mu^\alpha z_i(t) [\kappa_i(t)]^{\alpha-1}$ .

- iii) Susceptible node  $i$  becomes dormant ( $\chi_i = 1$ ) or remains susceptible ( $\chi_i = 0$ ). This transition occurs if all of node  $i$ 's neighbors recover. At  $\mathcal{O}(dt)$  this reduces to node  $i$  having a single infected neighbor that recovers, thus

$$\chi_i = \begin{cases} 1 & \delta_{z_i(t)}^1 \eta dt \\ 0 & 1 - \delta_{z_i(t)}^1 \eta dt \end{cases} . \quad (4.23)$$

The state of node  $i$  at time  $t + dt$  is

$$n_i(t + dt) = n_i(t)(1 - \xi_i) + (1 - n_i(t))(1 - \delta_{z_i(t)}^0)\pi_i, \quad (4.24)$$

where the first term corresponds to node  $i$  being infected ( $n_i(t)$ ) and not recovering ( $1 - \xi_i$ ), and the second term corresponds to node  $i$  being susceptible ( $(1 - n_i(t))(1 - \delta_{z_i(t)}^0)$ ) and becoming infected ( $\pi_i$ ). Furthermore, the equation for the viral load of node  $i$  at time  $t + dt$  is

$$\begin{aligned} \kappa_i(t + dt) = & \kappa_i(t) - \kappa_i(t)n_i(t)\xi_i - \kappa_i(t)(1 - n_i(t))(1 - \delta_{z_i(t)}^0)(1 - \pi_i)\chi_i \\ & + (1 - n_i(t))(1 - \delta_{z_i(t)}^0)(1 - \pi_i)(1 - \chi_i)\nu z_i(t)dt. \end{aligned} \quad (4.25)$$

The first term corresponds to the previously amassed viral load ( $\kappa_i(t)$ ), and the second term describes the event where infected node  $i$  ( $n_i(t)$ ) recovers ( $\xi_i$ ) and erases its viral load ( $-\kappa_i(t)$ ). The third term corresponds to the event where susceptible node  $i$  ( $(1 - n_i(t))(1 - \delta_{z_i(t)}^0)$ ) becomes dormant ( $\chi_i$ ) and instantly erases its viral load ( $-\kappa_i(t)$ ). Finally, the fourth term corresponds to susceptible node  $i$  ( $(1 - n_i(t))(1 - \delta_{z_i(t)}^0)$ ) remaining susceptible (neither becoming infected ( $1 - \pi_i$ ) nor dormant ( $1 - \chi_i$ )) and accumulating additional viral load from its  $z_i(t)$  infected neighbors ( $\nu z_i(t)dt$ ).

Applying the same procedure as in Section 4.1.1 (expectation value conditioned on time  $t$  followed by ensemble average), we find the dynamic equations

$$\frac{d\langle n_i(t) \rangle}{dt} = -\eta\langle n_i(t) \rangle + \nu\alpha\mu^\alpha\langle (1 - n_i(t))z_i(t) [\kappa_i(t)]^{\alpha-1} \rangle \quad (4.26)$$

$$\frac{d\langle \kappa_i(t) \rangle}{dt} = -\eta\langle \kappa_i(t)n_i(t) \rangle - \eta\langle \kappa_i(t)(1 - n_i(t))\delta_{z_i(t)}^1 \rangle + \nu\langle (1 - n_i(t))z_i(t) \rangle. \quad (4.27)$$

In addition, we compute the dynamic equation of  $\kappa_i^\gamma(t)$ ,

$$\begin{aligned} \frac{d\langle \kappa_i^\gamma(t) \rangle}{dt} = & -\eta\langle \kappa_i^\gamma(t)n_i(t) \rangle - \eta\langle \kappa_i^\gamma(t)(1 - n_i(t))\delta_{z_i(t)}^1 \rangle \\ & + \gamma\nu\langle (1 - n_i(t))z_i(t) [\kappa_i(t)]^{\gamma-1} \rangle, \end{aligned} \quad (4.28)$$

for an arbitrary value  $\gamma > 0$ .<sup>5</sup>

<sup>5</sup>See Appendix A.3 for a detailed derivation of Eqs. (4.26), (4.27) and (4.28).

### 4.2.1.1 Late-time limit and mean-field approximation

Taking the late-time limit in Eqs. (4.26), (4.27), and (4.28) and dropping the explicit dependence with  $t$ , we find

$$0 = -\eta\langle n_i \rangle + \nu\alpha\mu^\alpha\langle(1 - n_i)z_i\kappa_i^{\alpha-1}\rangle \quad (4.29)$$

$$0 = -\eta\langle\kappa_i n_i\rangle - \eta\langle\kappa_i(1 - n_i)\delta_{z_i}^1\rangle + \nu\langle(1 - n_i)z_i\rangle \quad (4.30)$$

$$0 = -\eta\langle\kappa_i^\gamma n_i\rangle - \eta\langle\kappa_i^\gamma(1 - n_i)\delta_{z_i}^1\rangle + \gamma\nu\langle(1 - n_i)z_i\kappa_i^{\gamma-1}\rangle. \quad (4.31)$$

Setting  $\gamma = \alpha$  in Eq. (4.31) and combining with Eq. (4.29) yields a pair of equations

$$0 = -\langle\kappa_i^\alpha n_i\rangle - \langle\kappa_i^\alpha(1 - n_i)\delta_{z_i}^1\rangle + \mu^{-\alpha}\langle n_i \rangle \quad (4.32)$$

$$0 = -\langle\kappa_i n_i\rangle - \langle\kappa_i(1 - n_i)\delta_{z_i}^1\rangle + \nu\eta^{-1}\langle(1 - n_i)z_i\rangle. \quad (4.33)$$

The generic term  $\langle\kappa_i^\gamma n_i\rangle$  can be expanded as

$$\langle\kappa_i^\gamma n_i\rangle = \langle\kappa_i^\gamma n_i | n_i = 1\rangle \times \Pr(n_i = 1) + \langle\kappa_i^\gamma n_i | n_i = 0\rangle \times \Pr(n_i = 0) \quad (4.34)$$

$$= \langle\kappa_i^\gamma | n_i = 1\rangle\langle n_i \rangle + 0 \times (1 - \langle n_i \rangle). \quad (4.35)$$

Similarly, we find

$$\langle\kappa_i^\gamma(1 - n_i)\delta_{z_i}^1\rangle = \langle\kappa_i^\gamma | X_i = 1\rangle \times \Pr(X_i = 1), \quad (4.36)$$

with  $X_i = (n_i = 0 \cap \delta_{z_i}^1 = 1)$ , i.e., node  $i$  being susceptible and having a single infected neighbor. Substituting for  $\gamma = 1$  and  $\gamma = \alpha$  in Eqs. (4.32) and (4.33) and combining both equations yields

$$-\mu^{-\alpha}\langle n_i \rangle + A\nu\eta^{-1}\langle(1 - n_i)z_i\rangle - B\Pr(X_i = 1) = 0, \quad (4.37)$$

with

$$A = \frac{\langle\kappa_i^\alpha | n_i = 1\rangle}{\langle\kappa_i | n_i = 1\rangle} \quad (4.38)$$

and

$$B = A\langle\kappa_i | X_i = 1\rangle - \langle\kappa_i^\alpha | X_i = 1\rangle. \quad (4.39)$$

Notice that  $A > 0$ .

Assuming that the state of the nodes are uncorrelated we can write

$$\Pr(X_i = 1) = \Pr(n_i = 0 \cap \delta_{z_i}^1 = 1) \approx \Pr(n_i = 0) \times \Pr(\delta_{z_i}^1 = 1), \quad (4.40)$$

with  $\Pr(n_i = 0) = 1 - \langle n_i \rangle$  and

$$\Pr(\delta_{z_i}^1 = 1) \approx \binom{k_i}{1} \times \Pr(n_i = 1) \times [\Pr(n_i = 0)]^{k_i-1} \quad (4.41)$$

$$= k_i \langle n_i \rangle (1 - \langle n_i \rangle)^{k_i-1}. \quad (4.42)$$

Additionally, in Section 2.1.2 we applied a mean-field approximation for uncorrelated networks and derived

$$\langle (1 - n_i) z_i \rangle \approx \sum_j \frac{k_i k_j}{N \langle k \rangle} (\langle n_j \rangle - \langle n_i \rangle \langle n_j \rangle). \quad (4.43)$$

In random degree-regular networks we have  $k_i = k_j = \langle k \rangle = k$ , and due to homogeneity,  $\langle n_i \rangle = \langle n_j \rangle = \rho$ ; then Eq. (4.37) becomes

$$-\mu^{-\alpha} \rho + A \nu \eta^{-1} k \rho (1 - \rho) - B k \rho (1 - \rho)^k = 0, \quad (4.44)$$

with  $\rho = \lim_{t \rightarrow \infty} \rho(t)$  the late-time prevalence.

For  $\rho \approx 0$  it is reasonable to assume that the coefficients  $A$  and  $B$  are constant, hence we use the reduced coefficients  $a = \mu^{-\alpha} \nu \eta^{-1} A$  and  $b = \mu^{-\alpha} B$ . The dynamics of the system is then encapsulated by the function

$$f(\rho) = -\rho + a k \rho (1 - \rho) - b k \rho (1 - \rho)^k \quad (4.45)$$

and its first and second derivatives

$$f'(\rho) = -1 + a k (1 - 2\rho) - b k (1 - \rho)^k + b k^2 \rho (1 - \rho)^{k-1} \quad (4.46)$$

$$f''(\rho) = -2a k + 2b k^2 (1 - \rho)^{k-1} - b k^2 (k - 1) \rho (1 - \rho)^{k-2}. \quad (4.47)$$

The fixed points are given by  $f(\rho_*) = 0$ . Linear stability analysis reveals that these are stable when  $f'(\rho_*) < 0$  and unstable when  $f'(\rho_*) > 0$ . Moreover, the transition is continuous if  $f''(\rho_*) < 0$  and discontinuous if  $f''(\rho_*) > 0$ .

From Eq. (4.45) we find that the healthy phase  $\rho_0 = 0$  is always a fixed point. It is stable for  $b > a - 1/k$  and unstable for  $b < a - 1/k$ . The nature of the transition changes at  $b = a/k$ , and the intersection with  $b = a - 1/k$  yields a tricritical point located at  $a_{\text{tc}} = 1/(k - 1)$ ,  $b_{\text{tc}} = 1/k(k - 1)$ . Thus the phase

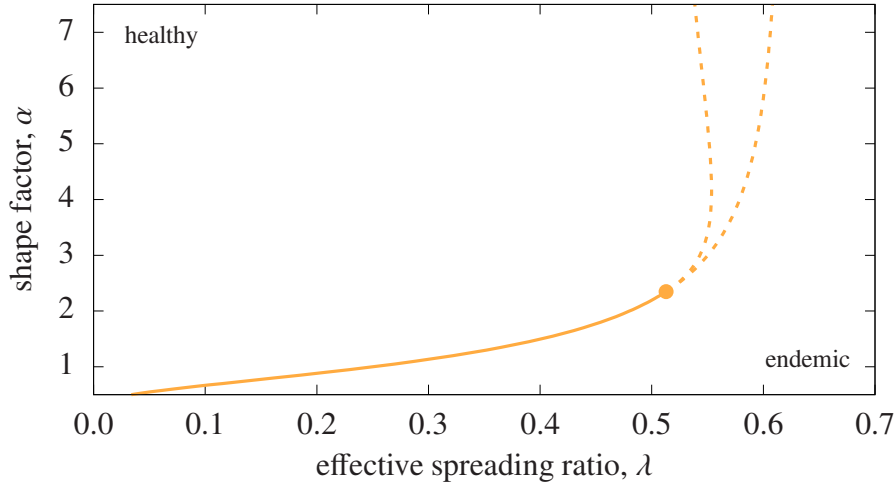


Figure 4.4: **Phase diagram of the miccSIS model with short-term memory.** The healthy phase becomes unstable when crossing from left to right. The solid curve indicates a continuous phase transition, the dashed lines delimit the region of coexistence (associated to a discontinuous phase transition), and the dot marks the tricritical point ( $\alpha_{tc} \approx 2.348$ ,  $\lambda_{tc} \approx 0.513$ ).

transition is continuous for  $b < b_{tc}$  and discontinuous for  $b > b_{tc}$ . The endemic phase is found by solving

$$-1 + ak(1 - \rho_+) - bk(1 - \rho_+)^k = 0. \quad (4.48)$$

Near the critical point  $b = a_c - 1/k$ ,  $\rho_+ \approx 0$  and we can expand

$$(1 - \rho_+)^k = 1 - k\rho_+ + k(k-1)\rho_+^2 + \mathcal{O}(\rho_+)^3. \quad (4.49)$$

For  $b < b_{tc}$ , Eq. (4.48) becomes

$$(a - a_c)k - ak\rho_+ + (a_c k - 1)\rho_+ + \mathcal{O}(\rho_+)^2 = 0 \quad (4.50)$$

and the prevalence scales as  $\rho_+ \propto (a - a_c)^{\beta_c}$ , with  $\beta_c = 1$  the customary mean-field exponent [133]. For  $b = b_{tc}$ , Eq. (4.48) is of the form

$$(a - a_c)k - ak(k-1)\rho_+^2 + \mathcal{O}(\rho_+)^3 = 0 \quad (4.51)$$

and the prevalence scales as  $\rho_+ \propto (a - a_c)^{\beta_{tc}}$ , with  $\beta_{tc} = 1/2$ .

Figure 4.4 shows the phase diagram in terms of the original parameters  $\alpha$  and  $\lambda$ .<sup>6</sup> We observe that the critical point initially increases monotonically

<sup>6</sup>See Appendix A.4 for details on recasting  $a$  and  $b$  in terms of the original parameters and Appendix C.4 for details on obtaining the numerical values of the phase diagram.

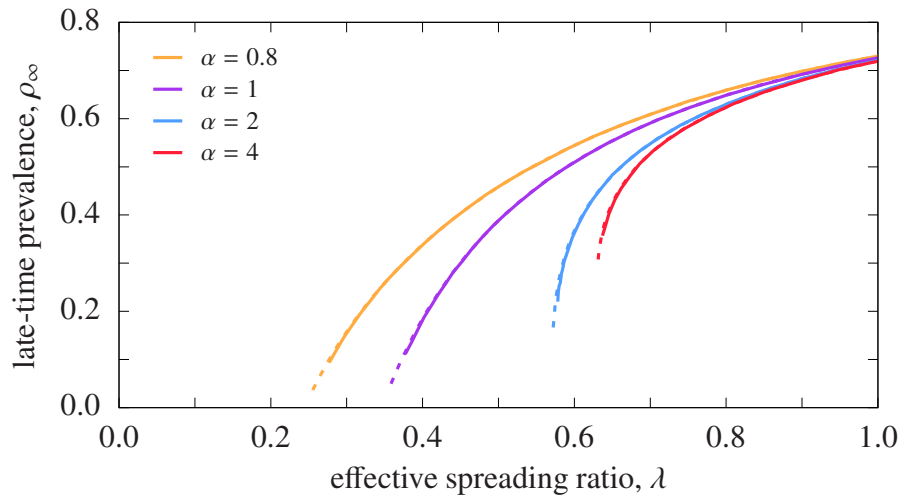


Figure 4.5: **Late-time prevalence in the miccSIS model with short-term memory.** Results for a random degree-regular network with  $k = 4$  and size  $N = 10^3$  (solid) and  $N = 10^4$  (dashed), time-averaged over  $10^4$  samples (shape parameter in legend). Uncertainty intervals not appreciable at this scale.

with  $\alpha$  but afterward saturates for  $\alpha \rightarrow \infty$ . This result is consistent with the possibly largest epidemic threshold reported in [110]. On the other hand, the transition to endemicity is discontinuous for  $\alpha > \alpha_{tc} \approx 2.348$ . Recall that the infection probability density presents a peak for  $\alpha > 1$  and, in fact, tends towards a delta function in the limit  $\alpha \rightarrow \infty$ . Thus a node requires a quasi-deterministic amount of viral load to become infected, mimicking a threshold model, which commonly exhibits a discontinuous phase transition [117].

#### 4.2.1.2 Simulation results

We perform extensive stochastic simulations to verify our analytic findings.<sup>7</sup> Given our previous experience with the standard SI and SIS models, the numerical results will most likely deviate from the mean-field approximation; nevertheless, we do expect a qualitative agreement. Once again, we begin with an adiabatic expansion-like approach to explore the position of the critical point. Our simulations start well into the active phase with a fully infected population and quasistatically decrease the control parameter,  $\lambda$ , until finite-size fluctuations trap the system in the absorbing state. We use random degree-regular networks with  $k = 4$  and sizes  $N = 10^3$  and  $N = 10^4$ , and

<sup>7</sup>See Appendix C.3.2 for an outline of the core algorithm.

units such that  $\eta = 1$  and  $\nu = 1$ . We compute the late-time prevalence as  $\rho_\infty = \lim_{t \rightarrow \infty} N_I(t)/N$ , with  $N_I(t)$  the number of infected nodes at time  $t$ , sampled from  $10^4$  states and time-averaged over various trajectories.<sup>8</sup>

As shown in Fig. 4.5, the epidemic threshold indeed increases with  $\alpha$ , and saturates for large values of  $\alpha$ . Moreover, for  $\alpha < 1$  the approach to the critical point is very similar to the standard SIS ( $\alpha = 1$ ),<sup>9</sup> consistent with a continuous phase transition with exponent  $\beta = 1$ . On the other hand, for  $\alpha = 4$  the curves terminate at a remarkably high prevalence, consistent with a discontinuous phase transition. Finally, the curves for  $\alpha = 2$  also terminate at a rather high prevalence, which deviates from the analytic prediction. Nonetheless, since the apparent discontinuity decreases with the system size, this observation is most likely related to finite-size effects.

We complement these results with the analysis of patient zero scenarios, the arrival of an infected agent in a previously unaffected population (see Section 4.1.3). For a fixed value of  $\lambda$  we run  $10^4$  realizations, each starting with a single randomly chosen infected node and a system cleared of all viral load. We compute the average coverage fraction,  $\bar{c}$ , and the endemic probability,  $P_1$ . If an outbreak becomes endemic, we extend the simulation until it reaches the steady state and then measure the late-time prevalence,  $\rho_\infty^*$ . Recall that we use a coverage threshold of  $c_{\text{th}} = 0.75$ .<sup>10</sup>

The results are shown in Figs. 4.6(a)–(d), which include the previously computed  $\rho_\infty$ . With  $\alpha < 1$  (Fig. 4.6(a)) we observe that the three order parameters ( $\rho_\infty$ ,  $\bar{c}$ , and  $P_1$ ) show a continuous phase transition at roughly the same critical point. Notice, however, that the endemic probability grows faster than in the standard SIS model ( $\alpha = 1$ , Fig. 4.6(b)). While  $\rho_\infty^*$  shows a discontinuous jump for  $\alpha = 4$  (Fig. 4.6(d)), with  $\alpha = 2$  (Fig. 4.6(c)) it grows continuously and coincides with  $\rho_\infty$ , supporting our analytic findings. Moreover, since  $\alpha = 2$  is close to tricritical point, a cross-over effect toward the exponent  $\beta_{\text{tc}}$  is expected, explaining the small gap and rather steep approach to the critical point. Note that the equivalence  $\bar{c} \approx c_{\text{th}}P_1$  holds for all values of  $\alpha$  (see grey curves in Figs. 4.6(a)–(d)).

Overall, our analytic and simulated results indicate that the system's macroscopic properties are drastically affected by the microscopic details of the in-

<sup>8</sup>See Appendix C.3.3 for simulation details.

<sup>9</sup>See Fig. D.1 in Appendix D for a verification of the equivalence between the standard SIS model and the miccSIS model with  $\alpha = 1$ .

<sup>10</sup>See Appendix C.3.4 for simulation details.

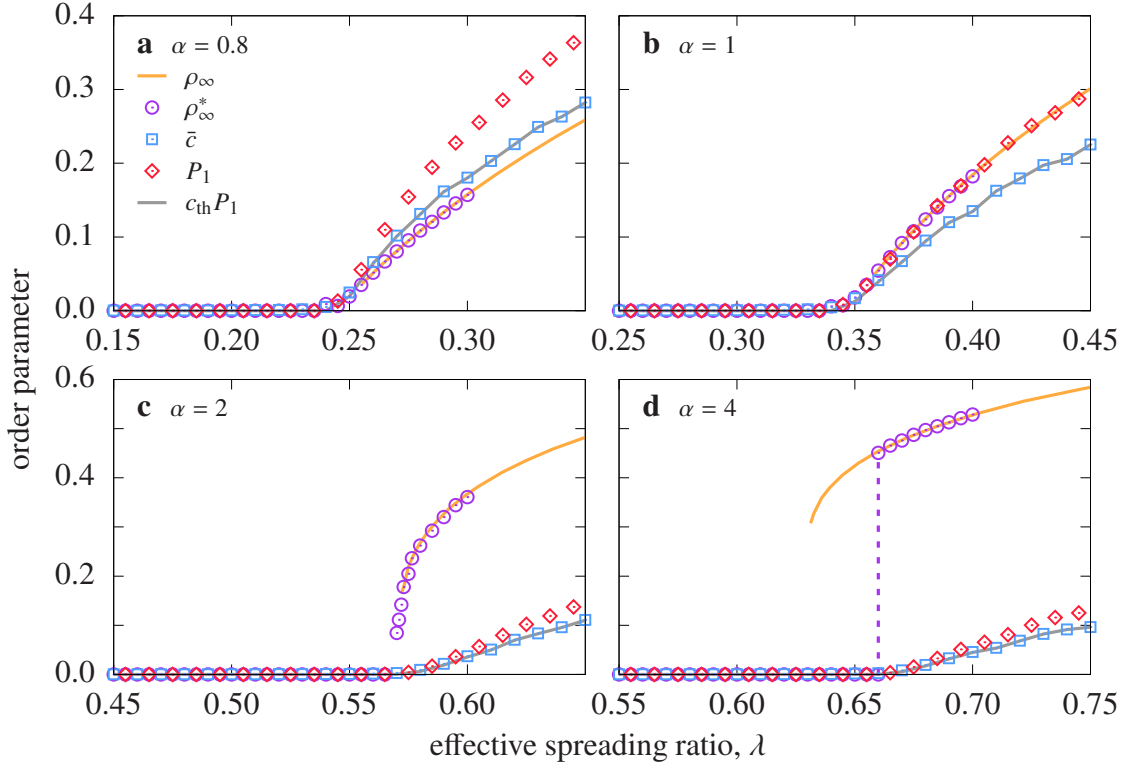


Figure 4.6: **Patient zero scenario in the miccSIS model with short-term memory.** Late-time prevalence of adiabatic expansion (orange curve) and endemic single-seed outbreaks (purple circles), average coverage fraction (blue squares), and endemic probability (red diamonds) for shape parameter (a)  $\alpha = 0.8$ , (b)  $\alpha = 1$ , (c)  $\alpha = 2$ , and (d)  $\alpha = 4$ , averaged over  $10^4$  independent realizations, in a random degree-regular network with  $k = 4$  and  $N = 10^4$ . Uncertainty intervals comparable to symbol size and line width.

fection mechanism. In particular, the critical point that separates the healthy from the endemic phase grows with  $\alpha$ , and the nature of the phase transition changes from continuous to discontinuous at the tricritical point  $\alpha_{tc}$ .

### 4.2.2 Long-term memory

Next we consider the case  $\zeta \rightarrow \infty$ , where a dormant node's viral load remains frozen until the outbreak revisits its neighborhood. Besides the short-term memory that is present during the infection period, agents now possess an additional long-term memory mode that is capable of connecting very distant temporal points, causing the system to evolve in a highly nonlinear manner.

At time  $t$ , node  $i$  is described by its state ( $n_i(t) = 0$  if it is healthy,  $n_i(t) = 1$  if it is infected) and viral load ( $\kappa_i(t) \geq 0$ ). The evolution of these variables is governed by three stochastic processes: i) the recovery of an infected node, ii) the infection of a susceptible node, and iii) the transition from susceptible to dormant. The corresponding probabilities at  $\mathcal{O}(dt)$  are given by Eqs. (4.21), (4.22), and (4.23), respectively. Recall that  $z_i(t)$  measures the number of infected neighbors at time  $t$ .

The viral load of a node i) is instantly erased when an infected node recovers, ii) increases proportionally to the number of infected neighbors while a node is susceptible, and iii) remains constant while the node is dormant. Then the equation for the viral load of node  $i$  at time  $t + dt$  reads

$$\begin{aligned} \kappa_i(t + dt) = & \kappa_i(t) - \kappa_i(t)n_i(t)\xi_i \\ & + (1 - n_i(t))(1 - \delta_{z_i(t)}^0)(1 - \pi_i)(1 - \chi_i)\nu z_i(t)dt, \end{aligned} \quad (4.52)$$

where the first term corresponds to the previously amassed viral load ( $\kappa_i(t)$ ), the second term describes the event where infected node  $i$  ( $n_i(t)$ ) recovers ( $\xi_i$ ) and erases its viral load ( $-\kappa_i(t)$ ), and the third term corresponds to susceptible node  $i$  ( $(1 - n_i(t))(1 - \delta_{z_i(t)}^0)$ ) remaining susceptible (neither becoming infected ( $1 - \pi_i$ ) nor dormant ( $1 - \chi_i$ )) and accumulating additional viral load from its  $z_i(t)$  infected neighbors ( $\nu z_i(t)dt$ ). Applying the same procedure as in Section 4.1.1 (expectation value conditioned on time  $t$  followed by ensemble average), we find the dynamic equation<sup>11</sup>

$$\frac{d\langle\kappa_i(t)\rangle}{dt} = -\eta\langle\kappa_i(t)n_i(t)\rangle + \nu\langle(1 - n_i(t))z_i(t)\rangle \quad (4.53)$$

and taking the late-time limit yields

$$0 = -\eta\langle\kappa_i n_i\rangle + \nu\langle(1 - n_i)z_i\rangle. \quad (4.54)$$

Applying the same reasoning as in Eq. (4.34), we can write

$$\langle\kappa_i n_i\rangle = \langle\kappa_i | n_i = 1\rangle\langle n_i\rangle. \quad (4.55)$$

The conditioned average  $\langle\kappa_i | n_i = 1\rangle$  measures the viral load of an infected node; since the viral load does not change while infected, this is equivalent

<sup>11</sup>In short, Eq. (4.53) is obtained by dropping the second term in the RHS of Eq. (4.27). See Appendix A.5 for a detailed derivation.

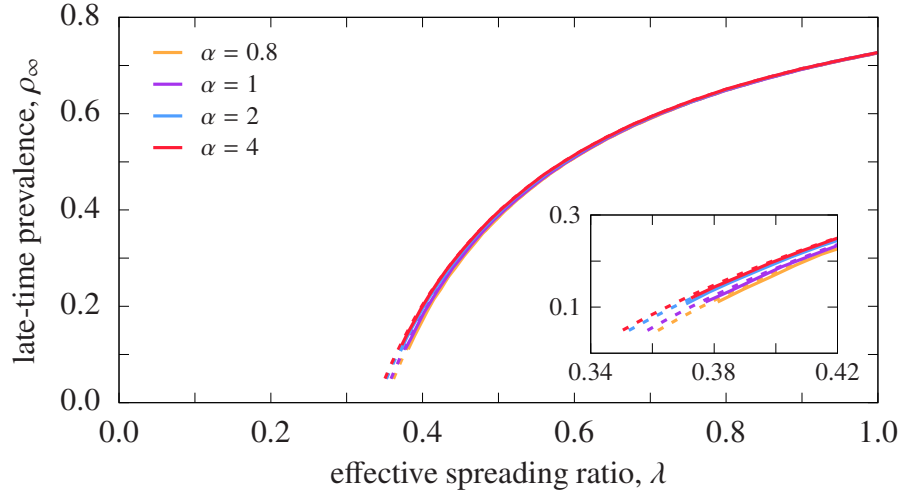


Figure 4.7: **Late-time prevalence in the miccSIS model with long-term memory.** Results for a random degree-regular network with  $k = 4$  and size  $N = 10^3$  (solid) and  $N = 10^4$  (dashed), time-averaged over  $10^4$  samples (shape parameter in legend). Uncertainty area not appreciable at this scale.

to measuring the viral load at infection. With  $\zeta \rightarrow \infty$ , nothing hinders the accumulation of viral load, i.e., nodes may freely amass any value of  $\kappa$ . Thus the probability of having  $\kappa$  at the moment of infection is simply the probability of becoming infected with  $\kappa$  (i.e.,  $\psi^*(\kappa)$ ). Using this probability density we find

$$\langle \kappa_i | n_i = 1 \rangle = \langle \kappa \rangle_{\text{inf}}, \quad (4.56)$$

which coincides with the value used in the definition of the effective spreading ratio,  $\lambda = \nu \langle \tau \rangle_{\text{rec}} / \langle \kappa \rangle_{\text{inf}}$ . Substituting in Eq. (4.54) gives

$$\langle n_i \rangle = \lambda \langle (1 - n_i) z_i \rangle. \quad (4.57)$$

Notice that this result is derived without implementing any mean-field approximation. Surprisingly, Eq. (4.57) is identical to Eq. (4.10), the first-order equation of the standard SIS model. This equivalence demonstrates that the miccSIS model with long-term memory and the standard SIS model have the same stationary properties. In particular, the late-time prevalence is independent of  $\alpha$  and identical to the Markovian model.<sup>12</sup>

<sup>12</sup>We provide a (lengthy) additional verification of this unexpected result in Appendix A.5.

In order to verify this remarkable analytic result, we perform extensive stochastic simulations.<sup>13</sup> Once again, we start our simulations well into the active phase with a fully infected population and quasistatically decrease the control parameter,  $\lambda$ , until finite-size fluctuations trap the system in the absorbing state. We use random degree-regular networks with  $k = 4$  and sizes  $N = 10^3$  and  $N = 10^4$ , and units such that  $\eta = 1$  and  $\nu = 1$ . We compute the late-time prevalence as  $\rho_\infty = \lim_{t \rightarrow \infty} N_I(t)/N$ , with  $N_I(t)$  the number of infected nodes at time  $t$ , sampled from  $10^4$  states and time-averaged over various trajectories.<sup>14</sup>

Figure 4.7 shows that the late-time prevalence curves indeed coincide for all values of  $\alpha$ . A small deviation occurs near the critical region (see inset of Fig. 4.7), which is caused by the residual clustering of the networks (due to their finite size). Compared to the short-term memory mode (recall Fig. 4.5), for  $\alpha > 1$  (respectively,  $\alpha < 1$ ) the endemic phase is enlarged (shrunk) by the long-term mode. This phenomenon is explained by the monotonically increasing (decreasing) infection rate: when the outbreak revisits a dormant node's neighborhood, its previously accumulated viral load facilitates (hinders) reinfection, enabling (preventing) the outbreak to remain active in a wider range of  $\lambda$ . These results reveal that the additional long-term memory completely suppresses the effects of the short-term mode. Specifically, it causes individuals with virtually infinite memory to behave, on the aggregate, as if they had no memory at all. This collective memory loss consequently renders the system's macroscopic state unable to distinguish between agents' microscopic properties.

In order to elucidate these findings, we proceed with the analysis of patient zero scenarios, where an infected agent arrives in a previously unaffected population. For a fixed value of  $\lambda$  we run  $10^4$  realizations, each starting with a single randomly chosen infected node and a system cleared of all viral load. We measure the average coverage fraction,  $\bar{c} = \langle K \rangle / N$ , and the probability that a realization surpasses the coverage threshold,  $P_1$ , which serves as a proxy for the true endemic probability,  $P_\infty$ , the probability that an outbreak becomes endemic in the thermodynamic limit.<sup>15</sup>

<sup>13</sup>See Appendix C.3.2 for an outline of the core algorithm.

<sup>14</sup>See Appendix C.3.3 for simulation details.

<sup>15</sup>See Appendix C.3.4 for simulation details.

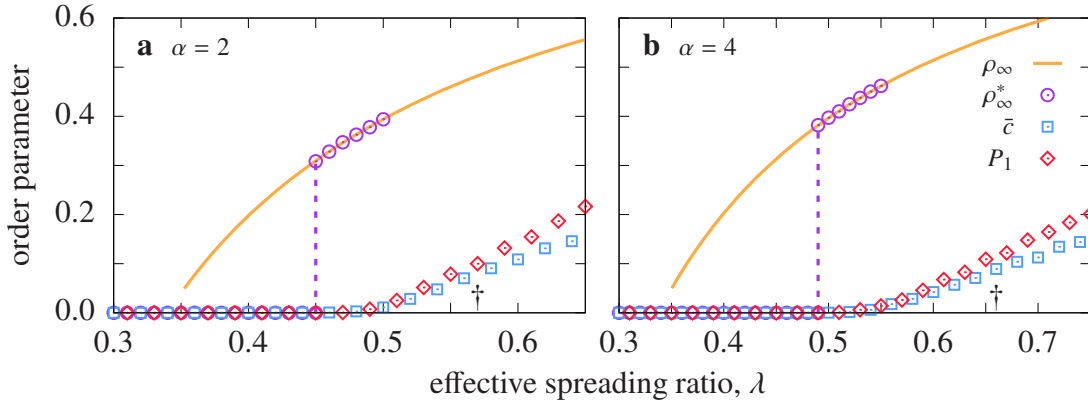


Figure 4.8: **Bistability in the miccSIS model with long-term memory.** Late-time prevalence of adiabatic expansion (orange curve) and endemic single-seed outbreaks (purple circles), average coverage fraction (blue squares), and endemic probability (red diamonds) for shape parameter (a)  $\alpha = 2$  and (b)  $\alpha = 4$ , averaged over  $10^4$  independent realizations, in a random degree-regular network with  $k = 4$  and  $N = 10^4$  nodes. Dagger indicates epidemic threshold for  $\zeta = 0$ . Uncertainty intervals comparable to symbol size and line width.

#### 4.2.2.1 Bistability

We first analyze  $\alpha > 1$ , for which the infection probability presents a peak and the instantaneous infection rate increases monotonically with the accumulated viral load. The patient zero results are shown in Figs. 4.8(a),(b), which include the previously computed  $\rho_\infty$  and the late-time prevalence of single-seed outbreaks that are able to become endemic,  $\rho_\infty^*$ . We find that the average coverage,  $\bar{c}$ , and the endemic probability,  $P_1$ , present a continuous phase transition at  $\lambda_c(\bar{c})$ <sup>16</sup> however, this point is notably larger than the critical point of the late-time prevalence,  $\lambda_c(\rho_\infty)$ . Whereas  $\rho_\infty$  presents a continuous phase transition,  $\rho_\infty^*$  exhibits a discontinuous phase transition at  $\lambda_c(\rho_\infty^*) = \lambda_c(\bar{c})$ . As expected, the two prevalence curves overlap after the abrupt jump.

This evidences the existence of an intermediate region  $\lambda \in [\lambda_c(\rho_\infty), \lambda_c(\bar{c})]$  where all single-seed outbreaks return to the absorbing state, but fully infected populations evolve toward an active steady state. The key ingredient to understand this phenomenon is the environment of frozen viral load. During the simulations that measure the late-time prevalence, the viral loads are well thermalized, enabling the outbreak to remain in an active state. Conversely, this

<sup>16</sup>For clarity, the equivalence  $\bar{c} \approx c_{\text{th}} P_1$  is not shown.

environment is deficient in single-seed outbreaks, as the system has not yet reached its steady state. Hence outbreaks are unable to produce sufficient new infections and rapidly become trapped in the absorbing state.

Furthermore, the environment of frozen viral load also explains the differences between single-seed outbreaks with  $\zeta = 0$  and  $\zeta \rightarrow \infty$ . In particular, the critical point  $\lambda_c(\bar{c})$  is lower in the latter case (see dagger in Figs. 4.8(a),(b)). When agents only possess a short-term memory mode, this environment is inexistent and outbreaks must produce sufficient direct infections in order to become endemic. Contrarily, if agents are equipped with an additional long-term memory mode, the environment of frozen viral load facilitates infection when the outbreak revisits a previously affected neighborhood. Thus less infective outbreaks are able to become endemic by repeatedly exploring the same areas of the network.

These results indicate that the system displays two attractors in this intermediate region. Then for  $\zeta \rightarrow \infty$  and  $\alpha > 1$  the system's phase diagram exhibits an additional bistable phase that separates the usual healthy and endemic phases. The associated hysteresis loop, however, has a rather exotic nature: although its lower branch presents the expected discontinuity, the upper branch connects the two attractors in a continuous manner. This contrasts with previous findings of bistability, where the hysteresis loop is bounded by two discontinuities [59, 80, 32]. Moreover, the transition to full endemicity is hybrid [24]: the endemic probability grows continuously at  $\lambda_c(\rho_\infty^*)$ , but the late-time prevalence jumps discontinuously.

#### 4.2.2.2 Excitability

Finally, we study  $\alpha < 1$ , for which the infection probability presents power law-like fat tails as the instantaneous infection rate decreases monotonically with the accumulated viral load. In Figs. 4.9(a),(b) we show the patient zero analysis for the standard SIS ( $\alpha = 1$ )<sup>17</sup> and broad-tailed infection distributions ( $\alpha < 1$ ). Here we additionally compute  $P_3$ , the probability that a single-seed outbreak reaches the coverage threshold three times.<sup>18</sup> With  $\alpha = 1$  (see Fig. 4.9(b)),  $P_1$  and  $P_3$  are identical (except for a very narrow region near the

<sup>17</sup>See Fig. D.1 in Appendix D for a verification of the equivalence between the standard SIS model and the miccSIS model with  $\alpha = 1$ .

<sup>18</sup>The coverage is reset to zero every time it hits the threshold. See Appendix C.3.4 for simulation details.

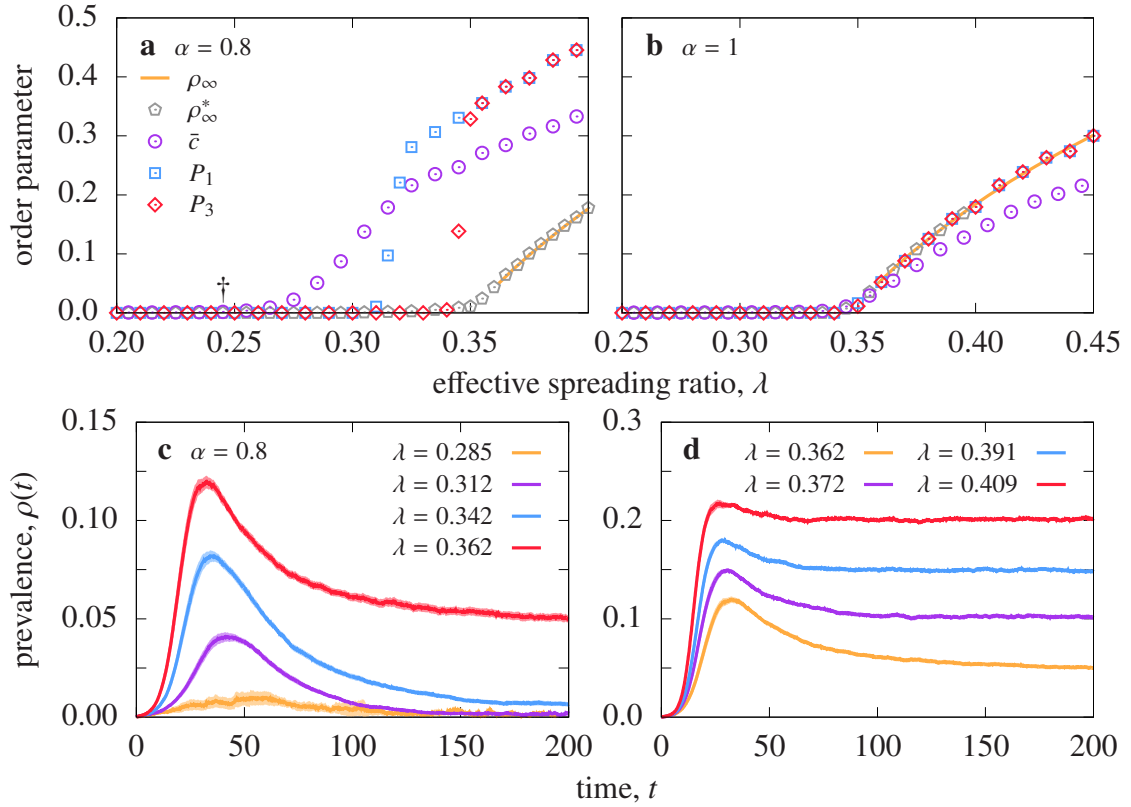


Figure 4.9: **Excitability in the miccSIS model with long-term memory.** Results for a random degree-regular network with  $k = 4$  and  $N = 10^4$  nodes. **(a, b)** Late-time prevalence of adiabatic expansion (orange curve) and endemic single-seed outbreaks (grey hexagons), average coverage fraction (purple circles), and endemic probabilities (blue squares and red diamonds) for shape parameter **(a)**  $\alpha = 0.8$  and **(b)**  $\alpha = 1$ , averaged over  $10^4$  independent realizations. Dagger indicates epidemic threshold for  $\zeta = 0$ . Uncertainty intervals comparable to symbol size and line width. **(c, d)** Temporal evolution of endemic outbreaks (single-seed realizations that surpass the coverage threshold at least once) for  $\alpha = 0.8$ , averaged over 100 independent runs (effective spreading ratio in legend). Uncertainty intervals at 95% confidence level.

critical point), indicating that an outbreak that surpasses the coverage threshold once remains active long enough to surpass the threshold two more times. Thus  $P_1$  is an adequate proxy for the true endemic probability,  $P_\infty$ , which additionally coincides with  $\rho_\infty$ .

For  $\alpha < 1$  (Fig. 4.9(a)) the situation is quite different. Firstly, the average coverage starts growing continuously at  $\lambda_c(\bar{c})$ , when all other order parameters are still identically zero. Note that  $\lambda_c(\bar{c})$  almost coincides with the epidemic threshold of the miccSIS model with  $\zeta = 0$  (see dagger in Fig. 4.9(a)). In addition, the late-time prevalence of adiabatic expansion ( $\rho_\infty$ ) coincides with the late-time prevalence of endemic outbreaks ( $\rho_\infty^*$ ), so that the transition to full endemicity is continuous. Finally, the transition point of  $P_1$  is significantly lower than that of  $P_3$ . Thus there is a wide interval where all outbreaks that surpass the threshold once eventually terminate in the absorbing state, evidencing the inadequateness of  $P_1$  as a measure of the true endemic probability. The inflection point of  $P_3$  is much closer to the transition point of  $\rho_\infty$ , which suggests that the critical point of the endemic probability ( $P_\infty$ , the probability to surpass the threshold an infinite amount of times) coincides with  $\lambda_c(\rho_\infty)$ . Beyond this point,  $\bar{c}$  is expected to coincide with  $c_{\text{th}}P_\infty$ , indicating that the endemic probability presents a discontinuous phase transition. Then the transition to full endemicity is again hybrid; nonetheless, here the late-time prevalence grows continuously, while the endemic probability jumps discontinuously.

In this case, we find an intermediate region  $\lambda \in [\lambda_c(\bar{c}), \lambda_c(\rho_\infty)]$  where outbreaks are unable to become endemic ( $P_\infty = 0$ ) but affect a macroscopic fraction of the population ( $\bar{c} > 0$ ). In Figs. 4.9(c),(d) we show the prevalence,  $\rho(t)$ , of realizations that surpass the coverage threshold once. For values of the spreading ratio that are located in the intermediate region (orange, purple, and blue curves in Fig. 4.9(c)), we observe that outbreaks grow up to a maximum, after which their prevalence gradually diminished until they reach the absorbing state. This behavior is reminiscent of excitable media and is typically observed in SIR-like dynamics (see Chapter 3). In the endemic phase (red curve in Fig. 4.9(c)), the outbreaks continue presenting a peak but afterward relax toward an active steady state; the initial peak disappears as  $\lambda$  increases (see Fig. 4.9(d)).

In conclusion, for  $\zeta \rightarrow \infty$  and  $\alpha < 1$  the usual healthy and endemic phases are separated by an additional excitable phase. This excitable behavior is again a consequence of the environment of frozen viral load. Independently of  $\zeta$ , an outbreak starts from a single infected node in a population cleared of viral

load. Then it initially evolves as if the agents only had the short-term memory mode, rapidly achieving a large coverage. When the outbreak revisits a previously affected area, the long-term memory mode is activated and the frozen viral load impedes new infections. Thus dormant nodes are effectively removed from the dynamic, impede the outbreak to grow, and eventually cause its extinction. To the extend of our knowledge, this excitable behavior has not been previously reported in comparable SIS-like models.

### 4.2.3 Medium-term memory

Finally, we consider a generic value of the relaxation time  $\zeta$ . In particular, we use an exponential function with time scale  $\zeta \geq 0$  to describe the decay of the viral load of dormant nodes. Imagine a dormant node that has amassed  $\kappa(t)$  units of viral load at time  $t$ . If the system remains unaltered in an interval  $dt$ , its viral load will decay by  $d\kappa = -\kappa(t)\zeta^{-1}dt$  units. The limit cases  $\zeta = 0$  and  $\zeta \rightarrow \infty$  correspond, respectively, to instantaneous decay and perpetual accumulation. Therefore we interpret a nonvanishing finite value of  $\zeta$  as a medium-term memory mode.

To describe node  $i$  at time  $t$  we need two variables: its state  $n_i(t)$  and its viral load  $\kappa_i(t)$ . The former is a discrete variable that can take two values,  $n_i(t) = 1$  if it is infected or  $n_i(t) = 0$  if it is healthy (susceptible or dormant). The viral load, on the other hand, is a continuous variable with  $\kappa_i(t) \geq 0$ . The state of a node only changes with the transitions i) infected to healthy and ii) susceptible to infected; when a node transitions between susceptible and dormant, its state remains unaltered. On the other hand, the viral load i) remains unaltered while a node is infected, ii) is erased instantly when a node recovers, iii) increases proportionally to the number of infected neighbors while a node is susceptible, and iv) decays exponentially while a node is dormant.

Recall that the number of infected neighbors is  $z_i(t) = \sum_j a_{ij}n_j(t)$ , with  $a_{ij}$  the elements of the adjacency matrix. In particular, this variable aids in distinguishing healthy susceptible nodes,  $(1 - n_i(t))(1 - \delta_{z_i(t)}^0)$ , from healthy dormant nodes,  $(1 - n_i(t))\delta_{z_i(t)}^0$ , with  $\delta_m^\ell$  the Krönecker function.<sup>19</sup> The evolution of these variables is governed by four microscopic, dichotomous, stochastic processes:

- i) Infected node  $i$  recovers ( $\xi_i = 1$ ) or remains infected ( $\xi_i = 0$ ), given by

---

<sup>19</sup> $\delta_m^\ell = 1$  if  $m = \ell$ , and  $\delta_m^\ell = 0$  if  $m \neq \ell$ .

node  $i$ 's recovery rate  $\eta$ . The corresponding probabilities at  $\mathcal{O}(dt)$  are

$$\xi_i = \begin{cases} 1 & \eta dt \\ 0 & 1 - \eta dt \end{cases} . \quad (4.58)$$

- ii) Susceptible node  $i$  becomes infected ( $\pi_i = 1$ ) or remains susceptible ( $\pi_i = 0$ ), given by node  $i$ 's instantaneous infection rate  $\omega_i(t)$ . The corresponding probabilities at  $\mathcal{O}(dt)$  are

$$\pi_i = \begin{cases} 1 & \omega_i(t)dt \\ 0 & 1 - \omega_i(t)dt \end{cases} , \quad (4.59)$$

with  $\omega_i(t) = \nu\alpha\mu^\alpha z_i(t) [k_i(t)]^{\alpha-1}$ .

- iii) Susceptible node  $i$  becomes dormant ( $\chi_i = 1$ ) or remains susceptible ( $\chi_i = 0$ ). This transition occurs if all of node  $i$ 's neighbors recover. At  $\mathcal{O}(dt)$  this reduces to node  $i$  having a single infected neighbor that recovers, thus

$$\chi_i = \begin{cases} 1 & \delta_{z_i(t)}^1 \eta dt \\ 0 & 1 - \delta_{z_i(t)}^1 \eta dt \end{cases} . \quad (4.60)$$

- iv) Dormant node  $i$  becomes susceptible ( $\varsigma_i = 1$ ) or remains dormant ( $\varsigma_i = 0$ ). This transition occurs whenever one of node  $i$ 's neighbors becomes infected. Writing an explicit form for the hazard rate of this event is rather involved, even at  $\mathcal{O}(dt)$ . Nevertheless, the exact expression is irrelevant for our derivations, so

$$\varsigma_i = \begin{cases} 1 & \varepsilon_i(t)dt \\ 0 & 1 - \varepsilon_i(t)dt \end{cases} , \quad (4.61)$$

with  $\varepsilon_i(t)$  a generic function of time.

The equation for the state of node  $i$  at time  $t + dt$  reads

$$n_i(t + dt) = n_i(t)(1 - \xi_i) + (1 - n_i(t))(1 - \delta_{z_i(t)}^0)\pi_i , \quad (4.62)$$

where the first term corresponds to node  $i$  being infected ( $n_i(t)$ ) and not recovering ( $1 - \xi_i$ ), and the second term corresponds to node  $i$  being susceptible

$((1 - n_i(t))(1 - \delta_{z_i(t)}^0))$  and becoming infected ( $\pi_i$ ). Furthermore, the equation for the viral load of node  $i$  at time  $t + dt$  is

$$\begin{aligned} \kappa_i(t + dt) = & \kappa_i(t) - \kappa_i(t)n_i(t)\xi_i - \kappa_i(t)(1 - n_i(t))\delta_{z_i(t)}^0(1 - \varsigma_i)\zeta^{-1}dt \\ & + (1 - n_i(t))(1 - \delta_{z_i(t)}^0)(1 - \pi_i)(1 - \chi_i)\nu z_i(t)dt. \end{aligned} \quad (4.63)$$

The first term corresponds to the previously amassed viral load ( $\kappa_i(t)$ ), and the second term describes the event where infected node  $i$  ( $n_i(t)$ ) recovers ( $\xi_i$ ) and erases its viral load ( $-\kappa_i(t)$ ). The third term corresponds to the event where dormant node  $i$  ( $(1 - n_i(t))\delta_{z_i(t)}^0$ ) does not become susceptible ( $1 - \varsigma_i$ ) and its viral load decays ( $-\kappa_i(t)\zeta^{-1}dt$ ). Finally, the fourth term corresponds to susceptible node  $i$  ( $(1 - n_i(t))(1 - \delta_{z_i(t)}^0)$ ) remaining susceptible (neither becoming infected ( $1 - \pi_i$ ) nor dormant ( $1 - \chi_i$ )) and accumulating additional viral load from its  $z_i(t)$  infected neighbors ( $\nu z_i(t)dt$ ).

Applying the familiar procedure of computing the expectation value conditioned on time  $t$  followed by the ensemble average (see Section 4.1.1), we find the dynamic equations

$$\frac{d\langle n_i(t) \rangle}{dt} = -\eta\langle n_i(t) \rangle + \nu\alpha\mu^\alpha\langle (1 - n_i(t))z_i(t) [\kappa_i(t)]^{\alpha-1} \rangle \quad (4.64)$$

$$\frac{d\langle \kappa_i(t) \rangle}{dt} = -\eta\langle \kappa_i(t)n_i(t) \rangle - \zeta^{-1}\langle \kappa_i(t)(1 - n_i(t))\delta_{z_i(t)}^0 \rangle + \nu\langle (1 - n_i(t))z_i(t) \rangle. \quad (4.65)$$

In addition, we compute the dynamic equation of  $\kappa_i^\gamma(t)$ ,

$$\begin{aligned} \frac{d\langle \kappa_i^\gamma(t) \rangle}{dt} = & -\eta\langle \kappa_i^\gamma(t)n_i(t) \rangle - \gamma\zeta^{-1}\langle \kappa_i^\gamma(t)(1 - n_i(t))\delta_{z_i(t)}^0 \rangle \\ & + \gamma\nu\langle (1 - n_i(t))z_i(t) [\kappa_i(t)]^{\gamma-1} \rangle, \end{aligned} \quad (4.66)$$

for an arbitrary value  $\gamma > 0$ .<sup>20</sup>

<sup>20</sup>See Appendix A.6 for a detailed derivation of Eqs. (4.64), (4.65), and (4.66).

### 4.2.3.1 Late-time limit and mean-field approximation

Taking the late-time limit in Eqs. (4.64), (4.65), and (4.66) and dropping the explicit dependence with  $t$ , we find

$$0 = -\eta\langle n_i \rangle + \nu\alpha\mu^\alpha\langle(1 - n_i)z_i\kappa_i^{\alpha-1}\rangle \quad (4.67)$$

$$0 = -\eta\langle\kappa_i n_i\rangle - \zeta^{-1}\langle\kappa_i(1 - n_i)\delta_{z_i}^0\rangle + \nu\langle(1 - n_i)z_i\rangle \quad (4.68)$$

$$0 = -\eta\langle\kappa_i^\gamma n_i\rangle - \gamma\zeta^{-1}\langle\kappa_i^\gamma(1 - n_i)\delta_{z_i}^0\rangle + \gamma\nu\langle(1 - n_i)z_i\kappa_i^{\gamma-1}\rangle. \quad (4.69)$$

Setting  $\gamma = \alpha$  in Eq. (4.69) and combining with Eq. (4.67) yields a pair of equations

$$0 = -\eta\langle\kappa_i^\alpha n_i\rangle - \alpha\zeta^{-1}\langle\kappa_i^\alpha(1 - n_i)\delta_{z_i}^0\rangle + \eta\mu^{-\alpha}\langle n_i \rangle \quad (4.70)$$

$$0 = -\eta\langle\kappa_i n_i\rangle - \zeta^{-1}\langle\kappa_i(1 - n_i)\delta_{z_i}^0\rangle + \nu\langle(1 - n_i)z_i\rangle. \quad (4.71)$$

The generic term  $\langle\kappa_i^\gamma n_i\rangle$  can be expanded as

$$\langle\kappa_i^\gamma n_i\rangle = \langle\kappa_i^\gamma n_i | n_i = 1\rangle \times \Pr(n_i = 1) + \langle\kappa_i^\gamma n_i | n_i = 0\rangle \times \Pr(n_i = 0) \quad (4.72)$$

$$= \langle\kappa_i^\gamma | n_i = 1\rangle\langle n_i \rangle + 0 \times (1 - \langle n_i \rangle). \quad (4.73)$$

Similarly, we find

$$\langle\kappa_i^\gamma(1 - n_i)\delta_{z_i}^0\rangle = \langle\kappa_i^\gamma | Y_i = 1\rangle \times \Pr(Y_i = 1), \quad (4.74)$$

with  $Y_i = (n_i = 0 \cap \delta_{z_i}^0 = 1)$ , i.e., node  $i$  being healthy and not having any infected neighbor (i.e., dormant). Substituting for  $\gamma = 1$  and  $\gamma = \alpha$  in Eqs. (4.32) and (4.33) and combining both equations yields

$$-\eta\mu^{-\alpha}\langle n_i \rangle + A\nu\langle(1 - n_i)z_i\rangle - B\zeta^{-1}\Pr(Y_i = 1) = 0, \quad (4.75)$$

with

$$A = \frac{\langle\kappa_i^\alpha | n_i = 1\rangle}{\langle\kappa_i | n_i = 1\rangle} \quad (4.76)$$

and

$$B = A\langle\kappa_i | Y_i = 1\rangle - \alpha\langle\kappa_i^\alpha | Y_i = 1\rangle. \quad (4.77)$$

Notice that  $A > 0$ .

Assuming that the state of the nodes are uncorrelated, we can write

$$\Pr(Y_i = 1) = \Pr(n_i = 0 \cap \delta_{z_i}^0 = 1) \approx \Pr(n_i = 0) \times \Pr(\delta_{z_i}^0 = 1), \quad (4.78)$$

with  $\Pr(n_i = 0) = 1 - \langle n_i \rangle$  and

$$\Pr(\delta_{z_i}^0 = 1) \approx \binom{k_i}{0} \times [\Pr(n_i = 0)]^{k_i} = (1 - \langle n_i \rangle)^{k_i}. \quad (4.79)$$

Additionally, in Section 2.1.2 we applied a mean-field approximation for uncorrelated networks and derived

$$\langle (1 - n_i)z_i \rangle \approx \sum_j \frac{k_i k_j}{N \langle k \rangle} (\langle n_j \rangle - \langle n_i \rangle \langle n_j \rangle). \quad (4.80)$$

In random degree-regular networks we have  $k_i = k_j = \langle k \rangle = k$ , and due to homogeneity,  $\langle n_i \rangle = \langle n_j \rangle = \rho$ ; then Eq. (4.75) becomes

$$-\eta \mu^{-\alpha} \rho + A v k \rho (1 - \rho) - B \zeta^{-1} (1 - \rho)^{k+1} = 0, \quad (4.81)$$

with  $\rho = \lim_{t \rightarrow \infty} \rho(t)$  the late-time prevalence.

Appendix A.7 provides the full (and rather lengthy) computation of the parameters  $A$  and  $B$ .<sup>21</sup> The dynamics of the system is encapsulated by the function

$$f(\rho) = -\rho + a k \rho (1 - \rho) - \left[ \frac{b_1 \hat{\zeta}^{-1}}{\rho + (k \hat{\zeta})^{-1}} - \frac{b_2 \alpha \hat{\zeta}^{-1}}{\rho + \alpha (k \hat{\zeta})^{-1}} \right] \rho (1 - \rho)^{k+1}, \quad (4.82)$$

with the nondimensional parameter  $\hat{\zeta} = \eta \zeta$ , and where the reduced parameters  $a$ ,  $b_1$ , and  $b_2$  are constant (a reasonable assumption for  $\rho \approx 0$ ). The fixed points ( $f(\rho_*) = 0$ ) are stable (respectively, unstable) when  $f'(\rho_*) < 0$  ( $f'(\rho_*) > 0$ ), and the transition is continuous (discontinuous) if  $f''(\rho_*) < 0$  ( $f''(\rho_*) > 0$ ). The healthy phase loses stability at

$$-1 + a k - k(b_1 - b_2) = 0, \quad (4.83)$$

the nature of the transition changes from continuous to discontinuous at

$$-2a k + 2k(k+1)(b_1 - b_2) + 2k^2 \hat{\zeta} \left[ b_1 - \frac{b_2}{\alpha} \right] = 0, \quad (4.84)$$

---

<sup>21</sup>In particular, we expect  $B \sim \rho$  because the healthy phase ( $\rho_0 = 0$ ) should always be a fixed point of Eq. (4.81).

and the endemic phase is found by solving

$$-1 + ak(1 - \rho_+) - \left[ \frac{b_1 \hat{\zeta}^{-1}}{\rho_+ + (k\hat{\zeta})^{-1}} - \frac{b_2 \alpha \hat{\zeta}^{-1}}{\rho_+ + \alpha(k\hat{\zeta})^{-1}} \right] (1 - \rho_+)^{k+1} = 0. \quad (4.85)$$

Note that in the limit  $\zeta \rightarrow 0$ , Eqs. (4.83) and (4.84) are functionally identical to the results obtained for the miccSIS model with short-term memory (see Section 4.2.1.1). Although the qualitative description of the phase diagram should coincide, we do not expect an exact numerical agreement.

Figure 4.10(c) shows the phase diagram in terms of the original parameters  $\alpha$  and  $\lambda$ .<sup>22</sup> First of all, notice that Eq. (4.83) does not depend on  $\zeta$ , implying that the epidemic threshold  $\lambda_c$  (i.e., the point at which the healthy phase becomes unstable) does not change with the relaxation time (grey curve). In particular, the right boundary of the discontinuous transitions is always located at the same value of  $\lambda$ . On the other hand, the left boundary and the tricritical point  $\alpha_{tc}$  consistently move toward lower values as  $\zeta$  increases. This means that, if the viral load decays more slowly, the coexistence region becomes wider and a first order phase transitions appears for smaller values of  $\alpha$  (note that  $\lim_{\zeta \rightarrow \infty} \alpha_{tc} = 1$ ). As expected, the curves for  $\zeta = 0$  (orange) are qualitatively identical to the results that we obtained for the miccSIS model with short-term memory (see Fig. 4.4). Nevertheless, the exact numeric values are different (e.g., the lower tricritical point).

Additionally, our analytic results are able to explain the exotic hysteresis loop that we uncovered in the miccSIS model with long-term memory (see Section 4.2.2.1). Figure 4.10(b) shows the typical bifurcation diagram of a discontinuous phase transition. The healthy phase ( $\rho = 0$ ) is stable in the region  $\lambda < \lambda_c$ , the endemic phase ( $\rho > 0$ ) is stable if  $\lambda > \lambda_-$ , and both solutions coexist for  $\lambda \in [\lambda_-, \lambda_c]$  (dashed curves in Fig. 4.10(c)). The prevalence jumps from 0 to  $\rho_-$  (respectively,  $\rho_c$ ) at the left (right) boundary of this bistable region. The orange curves in Fig. 4.10(a) show the values of  $\rho_c$  (solid) and  $\rho_-$  (dashed) when  $\zeta = 0$ , for all the values of the shape parameter  $\alpha$  that exhibit a first order transition. We see that both curves appear continuously at the tricritical point and grow rather quickly with increasing alpha. For larger values of the relaxation time we observe that the curves move toward the left ( $\alpha_{tr}$  decreases). Moreover, the prevalence gap at the left boundary of the coexistence region ( $\rho_-$ ) becomes smaller as  $\zeta$  increases. In the limit  $\zeta \rightarrow \infty$  it practically

<sup>22</sup>See Appendix C.4 for details on obtaining the numerical values of the phase diagram.

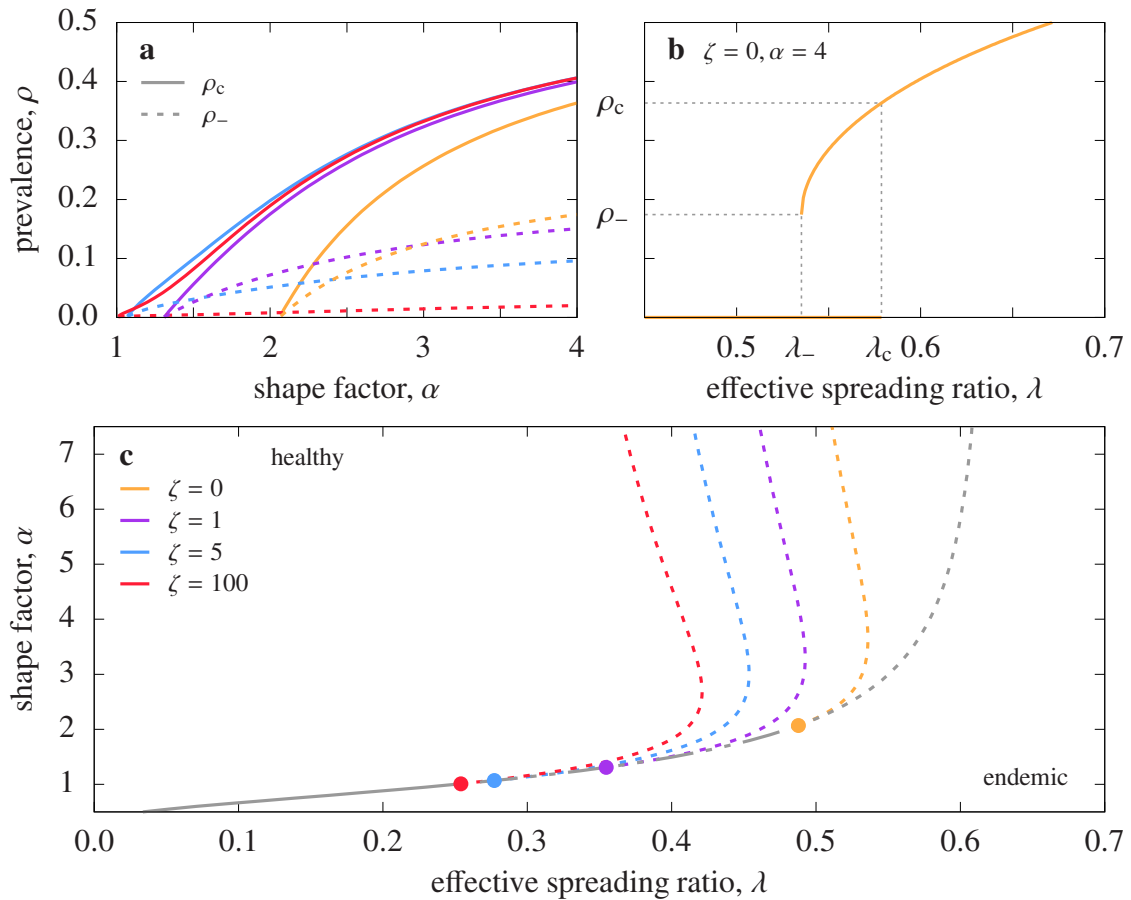


Figure 4.10: **Phase diagram of the miccSIS model with medium-term memory.** (a) Prevalence of a hysteresis loop's upper branch at the right (solid) and left (dashed) boundaries of the coexistence region (relaxation time as in c). (b) Bifurcation diagram of a first order phase transition. (c) Dashed lines delimit region of coexistence (relaxation time in legend), grey dashed curve indicates common right boundary, dot marks the tricritical point, solid grey curve indicates continuous phase transition, and dotted-dashed grey curve indicates continuous or discontinuous transition (depending on  $\zeta$ ).

vanishes and the upper branch of the hysteresis loop is indistinguishable from a continuous phase transition.<sup>23</sup>

Inasmuch as our analytical approach is based on the system's late-time properties, it is unable to explain the excitable behavior that we found for  $\zeta \rightarrow \infty$  and  $\alpha < 1$ . We do know that the lower limit of the excitable region (i.e., the point where the healthy phase becomes unstable) would be given by Eq. (4.83), which is independent of  $\zeta$ . In this case, the instability would lead to a transient, SIR-like epidemic curve.<sup>24</sup> Our results for the miccSIS model with long-term memory revealed that the late-time prevalence is independent of  $\alpha$  (see Section 4.2.2). Hence in the limit  $\zeta \rightarrow \infty$ , the right boundary of the excitable region would extend until  $\lambda_c$ , the epidemic threshold of the standard SIS model, for all values of  $\alpha$ . The question that remains unsolved is the location of the transition to full endemicity for finite nonvanishing relaxation times (i.e.,  $0 < \zeta < \infty$ ). Given the results for  $\alpha > 1$ , a plausible hypothesis is the existence of a secondary tricritical point (located somewhere at  $\alpha < 1$ ) that moves toward  $\alpha = 1$  as  $\zeta$  increases. Nonetheless, testing this hypothesis requires a whole different approach, capable of describing the system's transient state.

#### 4.2.3.2 Simulation results

We perform extensive simulations to verify our analytic findings and explore some of our hypothesis.<sup>25</sup> On the one hand we apply an adiabatic expansion-like approach to explore the position of the critical point. Our simulations start well into the active phase with a fully infected population and quasistatically decrease the control parameter,  $\lambda$ , until finite-size fluctuations trap the system in the absorbing state. We use random degree-regular networks with  $k = 4$  and sizes  $N = 10^3$  and  $N = 10^4$  nodes, and units such that  $\eta = 1$  and  $\nu = 1$ . We compute the late-time prevalence as  $\rho_\infty = \lim_{t \rightarrow \infty} N_I(t)/N$ , with  $N_I(t)$  the

<sup>23</sup>From a dynamical system's point of view, it would appear that the unstable solution that separates both attractors vanishes for  $\zeta \rightarrow \infty$ . To the extent of our knowledge, this would violate multiple mathematical principles. Bear in mind, however, that we have projected a two-dimensional system ( $n_i(t)$  and  $\kappa_i(t)$ ) into a single variable problem ( $\rho$ ). Working with the full system could complete the description, although the mathematical complexity would be extremely large.

<sup>24</sup>A thorough dynamical system-like description could reveal, perhaps, the appearance of a global bifurcation.

<sup>25</sup>See Appendix C.3.2 for an outline of the core algorithm.

number of infected nodes at time  $t$ , sampled from  $10^4$  states and time-averaged over various trajectories.<sup>26,27</sup>

Additionally, we complement these simulations with the analysis of patient zero scenarios, the arrival of an infected agent in a previously unaffected population. For a fixed value of  $\lambda$  we run  $10^4$  realizations, each starting with a single randomly chosen infected node and a system cleared of all viral load. We compute the average coverage fraction,  $\bar{c}$ , and the probability that an outbreak becomes endemic,  $P_1$ . If an outbreak becomes endemic, we extend the simulation until it reaches the steady state, and then measure the late-time prevalence,  $\rho_\infty^*$ . Finally, we also compute the probability that an outbreak reaches the coverage threshold three times,  $P_3$ . Remember that we use a coverage threshold of  $c_{\text{th}} = 0.75$ .<sup>28</sup>

Figure 4.12(a) shows the late-time prevalence with  $\alpha = 2$ , for various relaxation times. Recall that this value of the shape parameter shows a continuous phase transition in the miccSIS model with short-term memory (see Section 4.2.1). In that case, the curve terminates at a high prevalence due to finite-size effects (Fig. 4.12(b)). With increasing  $\zeta$ , however, this final gap first increases even more and afterward gradually decreases to almost zero (for  $\zeta \rightarrow \infty$ ); furthermore, the epidemic threshold moves consistently toward lower values as  $\zeta$  grows. In Figs. 4.12(c),(d) we show the late-time prevalence for  $\zeta = 0.1$  and  $\zeta = 0.5$ . In the former case we clearly see that the transition is continuous, while the latter exhibits a first-order phase transition.

These simulations (partially) corroborate our analytic results. In particular, the tricritical point moves toward lower values of  $\alpha$  as  $\zeta$  increases, so that the transition to endemicity becomes discontinuous. Notwithstanding, the numerical estimates are rather inadequate. For instance, our analytic approximation predicts that the right boundary of the coexistence region is not altered by  $\zeta$ . However, comparing the discontinuity in Figs. 4.12(d) and 4.12(e) we clearly observe a displacement toward lower values of  $\lambda$  as  $\zeta$  increases. Moreover, in the limit  $\zeta \rightarrow \infty$ , the upper branch of the hysteresis loop is independent of  $\alpha$  (Fig. 4.7). Therefore, the left boundary of the bistable region in Fig. 4.10(c) should tend to a vertical line that contains the limiting value  $\alpha_{\text{th}} = 1$ .

<sup>26</sup>See Appendix C.3.3 for simulation details.

<sup>27</sup>See Fig. D.2 in Appendix D for a verification of the equivalence between the limit cases of the miccSIS model with medium-term memory and the miccSIS model with short-term and long-term memory.

<sup>28</sup>See Appendix C.3.4 for simulation details.

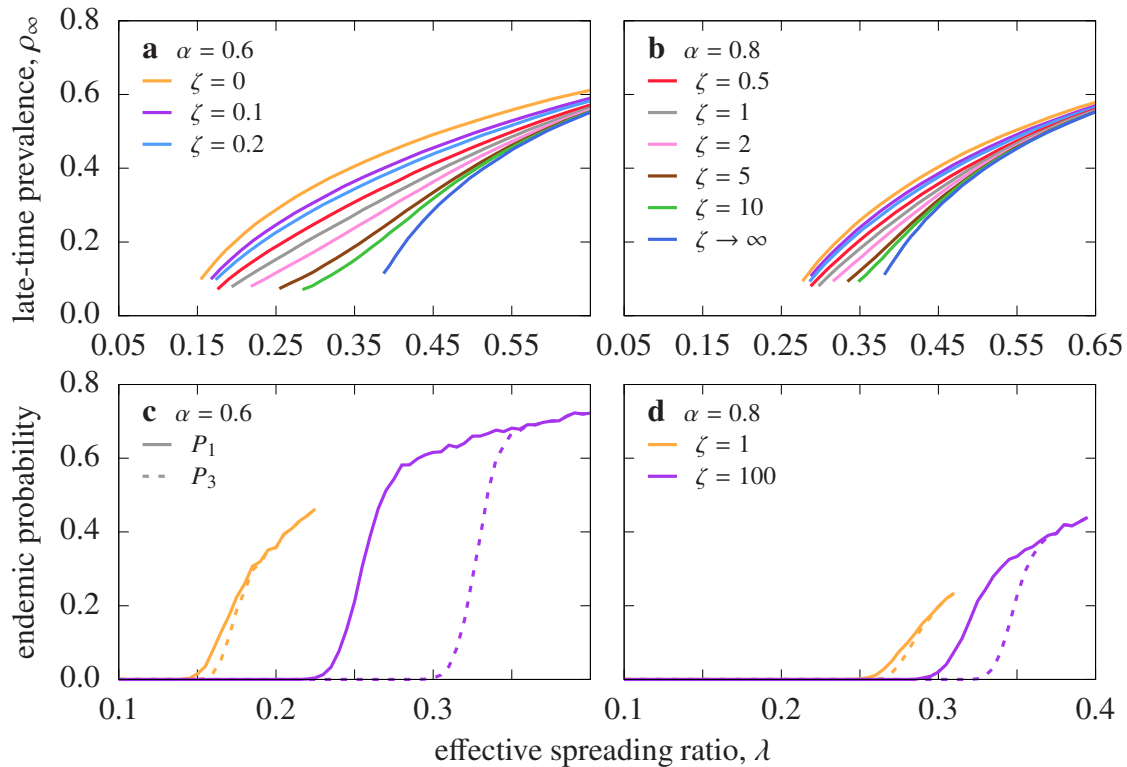


Figure 4.11: **Excitability in the miccSIS model with medium-term memory.** Results for a random degree-regular network with  $k = 4$  and  $N = 10^3$ . **(a, b)** Late-time prevalence for shape parameter **(a)**  $\alpha = 0.6$  and **(b)**  $\alpha = 0.8$ , time-averaged over  $10^4$  samples (relaxation time in legend). Uncertainty intervals not appreciable at this scale. **(c, d)** Probability that a single-seed outbreak reaches the coverage once (solid) and three times (dashed) for  $\zeta = 1$  (orange) and  $\zeta = 100$  (purple), with **(c)**  $\alpha = 0.6$  and **(d)**  $\alpha = 0.8$ , averaged over  $10^4$  independent realizations. Uncertainty intervals comparable to line width.

Finally, Figs. 4.11(a),(b) show the late-time prevalence curves for  $\alpha < 1$ . Unsurprisingly, the epidemic threshold shifts consistently toward higher values with increasing  $\zeta$ , more or less maintaining the same linear approach toward the critical point. Contrary to the analytic prediction, the left boundary of the excitable region (taken as the inflection point of  $P_1$ ) moves toward higher values of  $\lambda$  as  $\zeta$  increases; additionally, the right boundary (taken as the inflection point of  $P_3$ ) also moves to the right. With  $\zeta = 1$  the excitable region is practically nonexistent for both values of  $\alpha$ . On the other hand, with  $\zeta = 100$  both  $\alpha = 0.6$  and  $\alpha = 0.8$  exhibit an excitable region, although the latter is much narrower. As a final observation, notice that the endemic probabilities

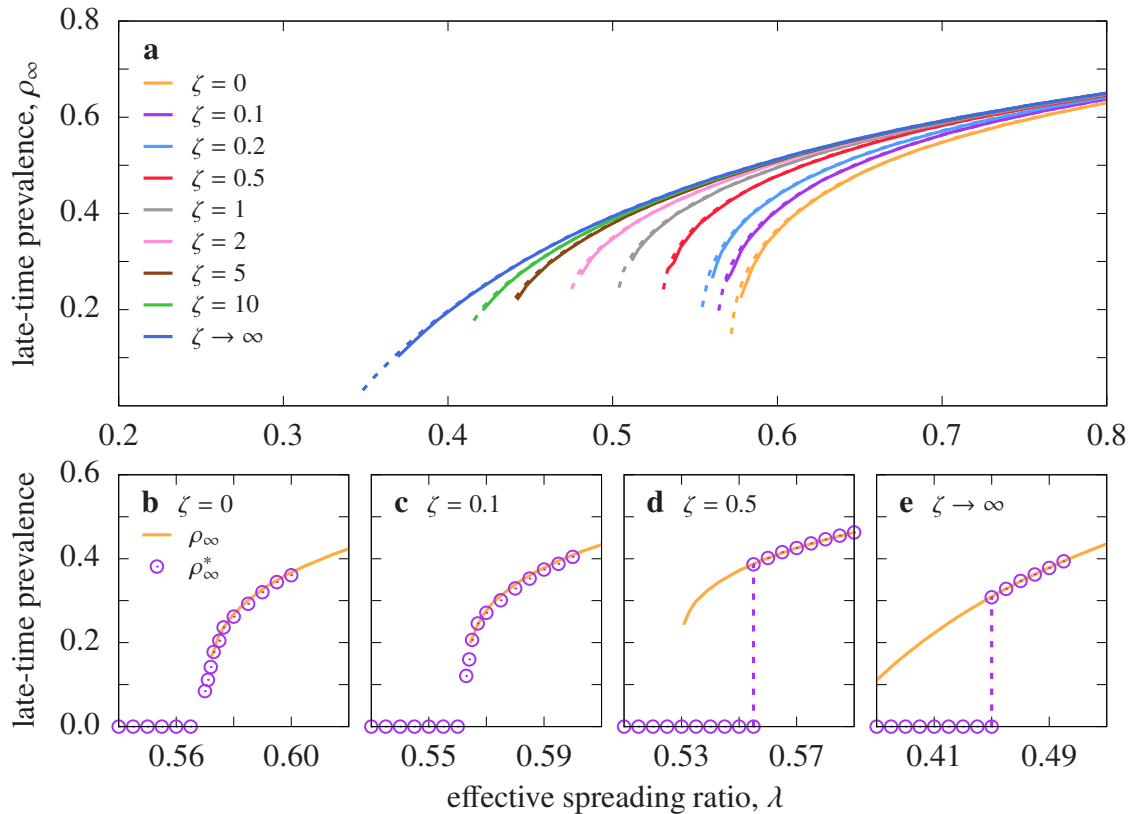


Figure 4.12: **Bistability in the miccSIS model with medium-term memory.** Results for random degree-regular networks with  $k = 4$  and shape parameter  $\alpha = 2$ . (a) Late-time prevalence for network size  $N = 10^3$  (solid) and  $N = 10^4$  (dashed), time-averaged over  $10^4$  samples (relaxation time in legend). Uncertainty intervals not appreciable at this scale. (b–e) Late-time prevalence of adiabatic expansion (orange curve) and endemic single-seed outbreaks (purple circles) for  $N = 10^4$  with relaxation time (b)  $\zeta = 0$ , (c)  $\zeta = 0.1$ , (d)  $\zeta = 0.5$ , and (e)  $\zeta \rightarrow \infty$ , averaged over  $10^4$  independent realizations. Uncertainty intervals comparable to symbol size and line width.

seem to evolve toward a common value.<sup>29</sup> Concluding, these preliminary results support our hypothesis regarding the existence of a secondary tricritical point that marks the onset of the excitable regions and moves toward  $\alpha = 1$  as the relaxation time increases. A complementary approach in terms of the system's transient properties would provide valuable knowledge into this peculiar behavior.

#### 4.2.4 Discussion

In summary, the possibility of node reinfection in the SIS model uncovers the full potential of the memory-induced complex contagion infection mechanism. The temporal profiles of the outbreaks (analyzed for the SI model) present a highly nonlinear interaction with the intricacies of node recovery and viral load accumulation (introduced in the SIR model). In particular, our analytic approximations and simulation results reveal a sophisticated interplay between a short-term and a long-term memory mode, displayed by a large variety of phenomena.

Compared to the standard SIS model, the macroscopic state of the system is greatly modified if agents possess a short-term memory mode ( $\zeta = 0$ ). For specific shapes of the infection probability ( $\alpha > \alpha_{tc}$ ), the customary second-order transition from the healthy to endemic phase may change its nature to discontinuous. Additionally, the system exhibits a cross-over region ( $\alpha \approx \alpha_{tc}$ ) where the continuous phase transition deviates from the expected mean-field predictions.

When agents possess an additional long-term memory mode ( $\zeta \rightarrow \infty$ ), the macroscopic properties of the system are indistinguishable from the standard, Markovian model. As a consequence, agents with a virtually infinite memory coalesce into an aggregate population that is effectively memoryless. To clarify, the particularities induced by the short-term memory mode are completely suppressed and cancelled out by the long-term memory mode. Note that this rather counter-intuitive memory loss resembles the situation where interacting pathogens are indistinguishable from complex contagion [90].

Nonetheless, widely distinct and clearly distinctive behaviors appear with the analysis of patient zero scenarios. A common effect of agents' memory is the breaking of the symmetry between the order parameters  $\bar{c}$ ,  $P$ , and  $\rho_\infty$ .

---

<sup>29</sup>See Fig. D.3 in Appendix D, which shows results for additional values of  $\zeta$ .

If agents are memoryless, all three order parameters are completely identical. This symmetry is broken by the long-term memory mode, and the critical points become dissociated. The system first transitions from the healthy phase to an either bistable or excitable intermediate regime, followed by a hybrid transition to the endemic phase. This differs from a double phase transition, where the same order parameter undergoes two consecutive phase transitions, a phenomenon usually associated to node and/or topological heterogeneities [59, 45, 3, 32].

Finally, our analytic results for finite nonvanishing relaxation times ( $0 < \zeta < \infty$ ) allow us to correctly interpolate between the limit cases of instantaneous decay ( $\zeta = 0$ ) and perpetual accumulation ( $\zeta \rightarrow \infty$ ). By developing a suitable mean-field approximation we are able to (qualitatively) predict the change of nature from a continuous to a discontinuous phase transition (as well as the corresponding tricritical point), and also to describe an exotic variant of the typical hysteresis loop (where the upper branch connects the two attractors in a continuous manner). However, this approach is unable to explain the transient instability associated to fat-tailed infection probabilities ( $\alpha < 1$ ).



# Nonhomogeneous networks

---

## 5.1 Network topology

Until now we have limited our analysis to random degree-regular networks, where all nodes are equivalent. Besides the fact that all agents have the same degree, the topology is locally tree-like. Nevertheless, it is widely known that node heterogeneity and nontrivial network structures can have a large effect on spreading properties. Examples include vanishing epidemic thresholds [134, 15], the appearance of localized states [119] and smeared phase transitions [85], and anomalous mesoscale diffusion [127, 174]. Here we explore the interplay between the memory-induced complex contagion infection mechanism and nonhomogeneous network topologies. In particular, we analyze two of the most relevant structural properties of real networks: clustering and node heterogeneity [123].

In terms of network topology, the most fundamental ingredient is the degree distribution. If a network has a total of  $N$  nodes, of which  $N_k$  have degree  $k$ , the degree distribution reads  $p(k) = N_k/N$ . For random degree-regular networks, where all the nodes have the same degree  $\bar{k}$ , we have  $p(k) = \delta_k^{\bar{k}}$ , with  $\delta_m^\ell$  the Kröneckel function.<sup>1</sup> In real-life networks, however, nodes are very heterogeneous: many nodes have a small number of neighbors, but some are extremely well-connected. This characteristic is reflected by the power law–like fat tails of the degree distribution,  $p(k) \sim k^{-\gamma}$ .

Clustering, on the other hand, measures the tendency of having common neighbors. Consider node  $i$  (which has degree  $k_i$ ) and its nearest neighbors. The clustering coefficient of node  $i$  is  $c_i = 2t_i/k_i(k_i - 1)$ , with  $t_i$  the number of edges between its nearest neighbors. The network’s overall clustering coefficient is obtained by averaging over all nodes,  $C = N^{-1} \sum_i c_i$ . Networks that are locally tree-like (i.a., random degree-regular networks) have a vanishing clus-

---

<sup>1</sup> $\delta_m^\ell = 1$  if  $m = \ell$ , and  $\delta_m^\ell = 0$  if  $m \neq \ell$ .

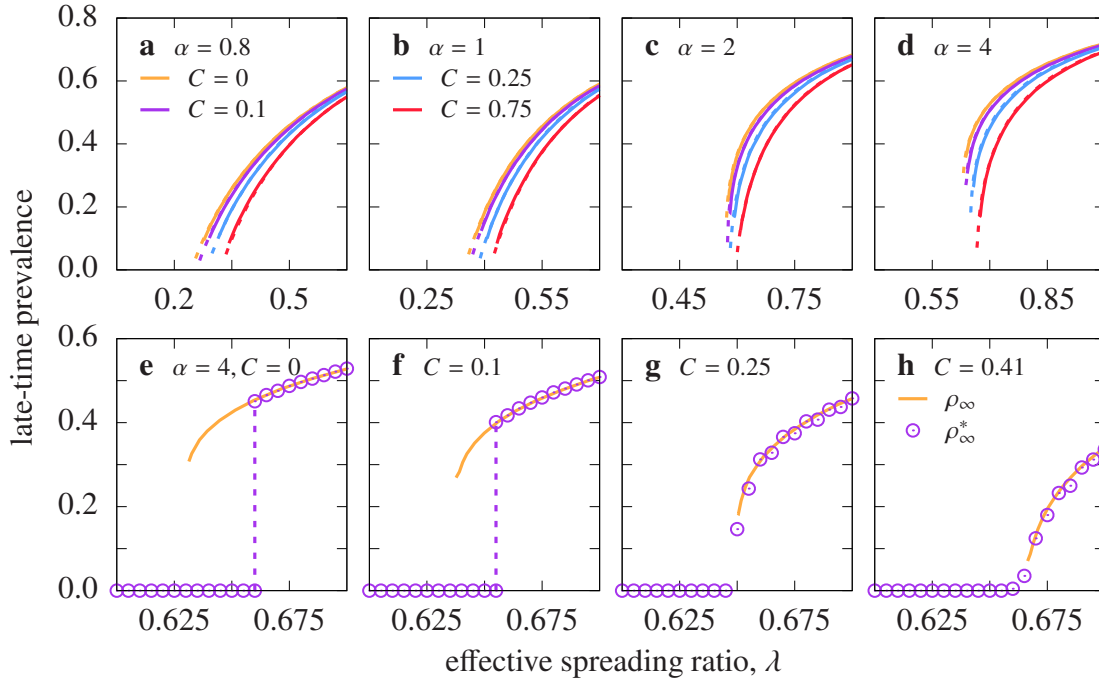


Figure 5.1: **Late-time prevalence in the miccSIS model with short-term memory on clustered networks.** Results for random degree-regular networks with  $k = 4$ . (a–d) Late-time prevalence for network size  $N = 10^3$  (solid) and  $N = 10^4$  (dashed) with shape parameter (a)  $\alpha = 0.8$ , (b)  $\alpha = 1$ , (c)  $\alpha = 2$ , and (d)  $\alpha = 4$ , time-averaged over  $10^4$  samples (clustering coefficient in legend). Uncertainty intervals not appreciable at this scale. (e–h) Late-time prevalence of adiabatic expansion (orange curve) and endemic single-seed outbreaks (purple circles) for  $\alpha = 4$  in a network with  $N = 10^4$  nodes and clustering coefficient (e)  $C = 0$ , (f)  $C = 0.1$ , (g)  $C = 0.25$ , and (h)  $C = 0.41$ , averaged over  $10^4$  independent realizations. Uncertainty intervals comparable to symbol size and line width.

tering coefficient,  $C \approx 0$ . Most real-life networks show high levels of clustering, although not as extreme as fully connected networks, which have  $C = 1$ .

Other network properties, such as degree-correlations or community structures, can have a strong impact on spreading dynamics; nonetheless, their analysis is beyond the scope of this work. Following the systematic approach of previous sections, we independently analyze the interaction of clustering and node heterogeneity with the memory-induced complex contagion infection mechanism. In addition, we only consider the miccSIS model since it exhibits a more diverse array of phenomenology and features. Although an-

alytic approximations are common for the study of spreading phenomena in networks, we expect highly involved mathematical derivations for the micc-SIS model. Given that this exceeds the scope of the present work, we resort directly to simulations.<sup>2</sup>

Once again, we start with an adiabatic expansion–like approach toward the critical point  $\lambda_c$ . Recall that we compute the late-time prevalence as  $\rho_\infty = \lim_{t \rightarrow \infty} N_I(t)/N$ , with  $N_I(t)$  the number of infected nodes at time  $t$ , sampled from  $10^4$  states and time-averaged over various trajectories.<sup>3</sup> Additionally, we simulate patient zero scenarios, where an infected agent arrives in a previously unaffected population. For a fixed value of  $\lambda$  we run  $10^4$  realizations, each starting with a single randomly chosen infected node and a system cleared of all viral load. We compute the average coverage fraction,  $\bar{c}$ , and the probability that an outbreak becomes endemic,  $P_1$ . If an outbreak becomes endemic, we extend the simulation until it reaches the steady state and then measure the late-time prevalence,  $\rho_\infty^*$ . Finally, we also compute the probability that an outbreak reaches the coverage threshold three times,  $P_3$ . Recall that we use a coverage threshold of  $c_{\text{th}} = 0.75$  and units such that  $\eta = 1$  and  $\nu = 1$ . We only consider the limit cases of instantaneous decay ( $\zeta = 0$ ) and perpetual accumulation ( $\zeta \rightarrow \infty$ ).<sup>4</sup>

## 5.2 Clustering

First we consider random degree-regular networks with  $k = 4$  and clustering coefficient  $C = \{0, 0.1, 0.25, 0.41\}$ , constructed by randomly rewiring the links until the clustering coefficient reaches its target.<sup>5</sup> The largest value,  $C = 0.41$ , corresponds to the maximum achieved for network size  $N = 10^4$ , selected from 10 independent generations. Note that we use a single network realization for each size and clustering coefficient; hence the results are not completely general. However, averaging over various networks can produce an artificial smoothing effect (especially for discontinuous phenomena), which could lead to false interpretations.

Figures 5.1(a)–(d) show the late-time prevalence with short-term mem-

<sup>2</sup>See Appendix C.3.2 for an outline of the core algorithm.

<sup>3</sup>See Appendix C.3.3 for simulation details.

<sup>4</sup>See Appendix C.3.4 for simulation details.

<sup>5</sup>See Appendix B.1 for details on generating these synthetic networks.

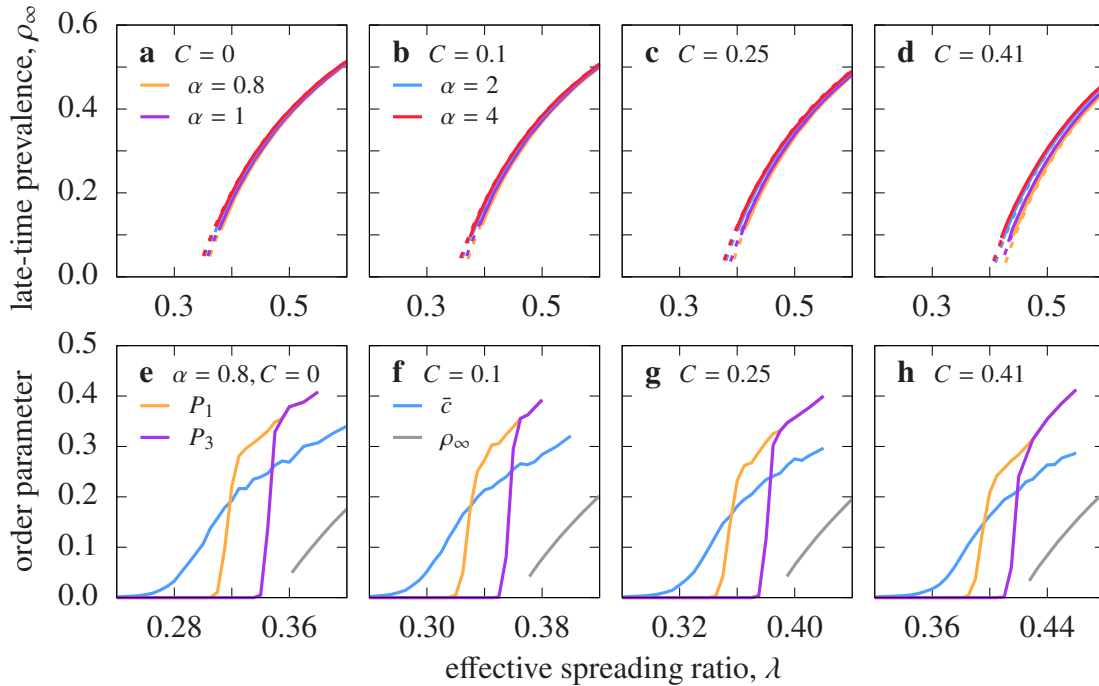


Figure 5.2: **Late-time prevalence and excitability in the miccSIS model with long-term memory on clustered networks.** Results for random degree-regular networks with  $k = 4$ . (a–d) Late-time prevalence for network size  $N = 10^3$  (solid) and  $N = 10^4$  (dashed) with clustering coefficient (a)  $C = 0$ , (b)  $C = 0.1$ , (c)  $C = 0.25$ , and (d)  $C = 0.41$ , time-averaged over  $10^4$  samples (shape parameter in legend). Uncertainty intervals not appreciable at this scale. (e–h) Endemic probabilities (orange and purple), average coverage fraction (blue), and late-time prevalence of adiabatic expansion (grey) for  $\alpha = 0.8$  in a network with  $N = 10^4$  nodes and clustering coefficient (e)  $C = 0$ , (f)  $C = 0.1$ , (g)  $C = 0.25$ , and (h)  $C = 0.41$ , averaged over  $10^4$  independent realizations. Uncertainty intervals comparable to line width.

ory. For all values of the shape parameter  $\alpha$ , we observe that the endemic phase shrinks consistently as  $C$  increases (the epidemic threshold moves to the right). Qualitatively,  $\alpha = 0.8$  and  $\alpha = 1$  remain unaltered, but for  $\alpha = 2$  the approach toward the critical point becomes less abrupt with a larger clustering coefficient. On the contrary, we see a very clear change with  $\alpha = 4$ . As clustering increases the curves appear to become continuous and the final gap decreases significantly with the system size, an indication of a second order phase transition. The corresponding results for patient zero scenarios are shown in Figs. 5.1(e)–(h), which clearly reveal that the discontinuous jump for

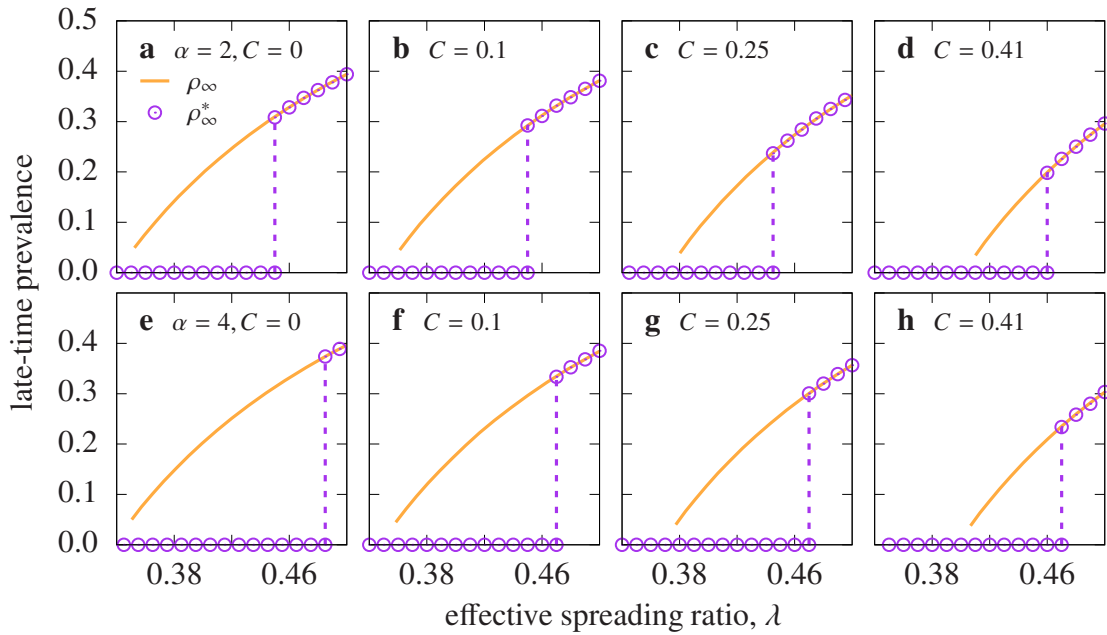


Figure 5.3: **Bistability in the miccSIS model with long-term memory on clustered networks.** Late-time prevalence of adiabatic expansion (orange curve) and endemic single-seed outbreaks (purple circles) for **(a–d)**  $\alpha = 2$  and **(e–h)**  $\alpha = 4$  in a random degree-regular network with  $k = 4$ ,  $N = 10^4$  and clustering coefficient **(a, e)**  $C = 0$ , **(b, f)**  $C = 0.1$ , **(c, g)**  $C = 0.25$ , and **(d, h)**  $C = 0.41$ , averaged over  $10^4$  independent realizations. Uncertainty intervals comparable to symbol size and line width.

low clustering ( $C = \{0, 0.1\}$ ) is substituted by a continuous transition when the clustering coefficient is high ( $C = \{0.25, 0.41\}$ ).

Figures 5.2(a)–(d) show the late-time prevalence with long-term memory. All values of  $C$  exhibit collective memory loss (the collapse of prevalence curves with different  $\alpha$ ), but the differences around the critical region become more noticeable as clustering increases. Figures 5.2(e)–(h) show the patient zero results for  $\alpha = 0.8$  and paint the same qualitative picture for clustered and unclustered networks. However, we do observe a slight narrowing of the excitable region with larger values of  $C$ . Finally, 5.3(a)–(d) show the patient zero results for  $\alpha = 2$ , and those for  $\alpha = 4$  are shown in Figs. 5.3(e)–(h). Once again, the qualitative description remains unchanged for clustered networks, which also display an (exotic) hysteresis loop; nevertheless, the bistable region shrinks as the clustering coefficient increases.

### 5.3 Node heterogeneity

Next we use the configuration model to generate unclustered networks with a heterogeneous degree distribution. Specifically, we construct scale-free networks with a power law distribution,  $p(k) \sim k^{-\gamma}$ , for exponents  $\gamma = 3.5$  and  $\gamma = 2.5$ .<sup>6</sup> The former yields a finite variance and we expect results that are similar to the mean-field approximation [133]. On the other hand, the unbounded variance for  $\gamma = 2.5$  is known to push the epidemic threshold toward very low values [15]. Once again, we use a single network realization for each size and exponent. Due to the node heterogeneity (specially with  $\gamma = 2.5$ ), averaging over different network realizations would surely lead to an artificial smoothing of the curves. Although results might not be completely general, we prefer to isolate these effects and avoid false interpretations.

With short-term memory,  $\gamma = 3.5$  yields clearly separated epidemic threshold for different values of  $\alpha$  (Fig. 5.4(a)). The location of  $\lambda_c$  is comparable to random degree-regular networks, but the approach toward the critical point is continuous and very smooth, including for  $\alpha > 1$ . Figs. 5.4(b) and 5.4(c) show the patient zero results for  $\alpha = 2$  and  $\alpha = 4$ , respectively. We observe that the transition is indeed continuous and also that the endemic probability is very low. On the other hand, in Fig. 5.4(d) we see that the curves for  $\gamma = 2.5$  gradually approach the limit  $\lambda_c \rightarrow 0$  as the system size increases, a known result for scale-free networks. Nonetheless,  $\alpha > 1$  shows a much smoother approach towards the critical point. This is evident from the patient zero results for  $\alpha = 2$  and  $\alpha = 4$  (Figs. 5.4(e) and 5.4(f), respectively), which show an extremely slow increase of the endemic probability (specially for  $\alpha = 4$ ) and could be indicative of an infinite order transition.

When agents are equipped with a long-term memory mode, both values of the power law exponent  $\gamma$  exhibit the phenomena of collective memory loss (Figs. 5.5(a),(e)) and excitability (Figs. 5.5(b),(f)). Notice, however, the very narrow excitable region with  $\gamma = 2.5$ . Figures 5.5(c),(d) reveal that the bistable region vanishes with  $\gamma = 3.5$  and that the growth of the endemic probability is extremely slow. With  $\gamma = 2.5$ , on the other hand,  $\alpha = 2$  shows a continuous transition (Fig. 5.5(g)), while  $\alpha = 4$  exhibits the familiar hysteresis loop (Fig. 5.5(h)). Notwithstanding, the endemic probability is again extremely small, indicating that the discontinuous jump could disappear if the number of realizations is increased.

---

<sup>6</sup>See Appendix B.2 for details on generating these synthetic networks.

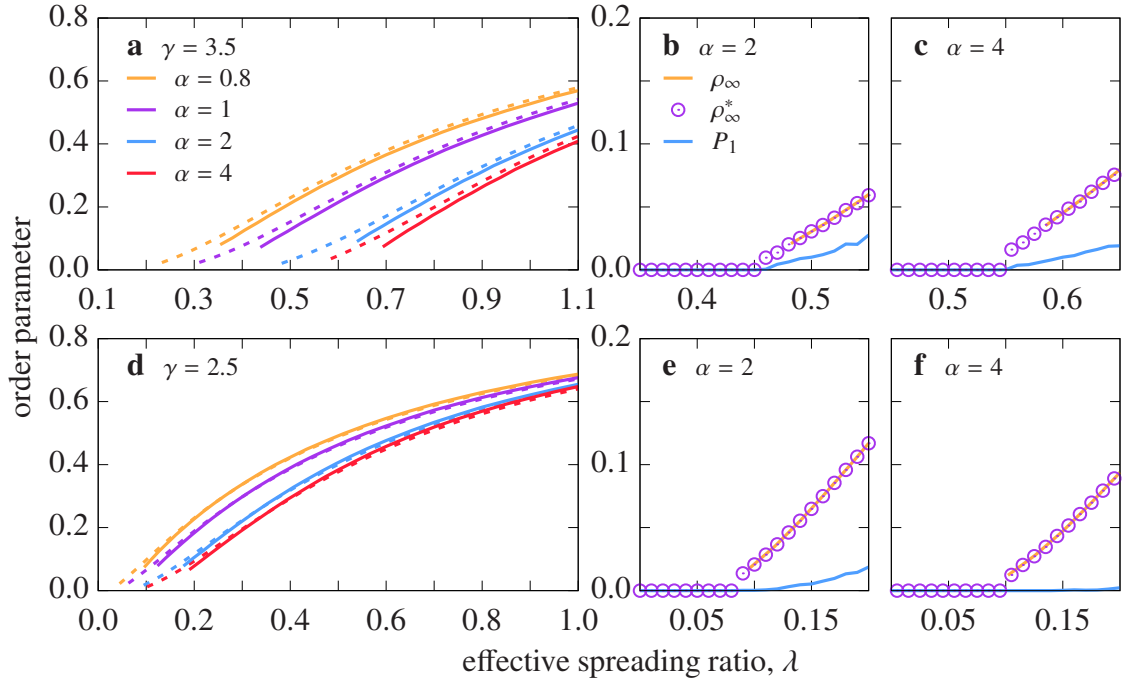


Figure 5.4: **Late-time prevalence in the miccSIS model with short-term memory on scale-free networks.** Results for scale-free networks with exponent (a–c)  $\gamma = 3.5$  and (d–f)  $\gamma = 2.5$ . (a, d) Late-time prevalence for network size  $N = 10^3$  (solid) and  $N = 10^4$  (dashed), time-averaged over  $10^4$  samples (shape parameter in legend). Uncertainty intervals not appreciable at this scale. (b, c, e, f) Late-time prevalence of adiabatic expansion (grey curve) and endemic single-seed outbreaks (purple circles), and endemic probability (blue curve) for (b, e)  $\alpha = 2$  and (c, f)  $\alpha = 4$  in a network with  $N = 10^4$ , averaged over  $10^4$  independent realizations. Uncertainty intervals comparable to symbol size and line width.

## 5.4 Discussion

In conclusion, large values of the clustering coefficient causes the transition with  $\alpha = 4$  and  $\zeta = 0$  to become continuous, but the system continues displaying the excitable and bistable regions when  $\zeta \rightarrow \infty$ . With medium-term memory we expect the same behavior as for unclustered random degree-regular networks, where the intermediate phases gradually appear as the agent’s memory increases (see Section 4.2.3). Hence we hypothesize that the tricritical point grows with the clustering coefficient, but maintains the limit value  $\lim_{\zeta \rightarrow \infty} \alpha_{\text{tr}} = 1$ . Figure 5.6 shows a schematic representation of the hypotheti-

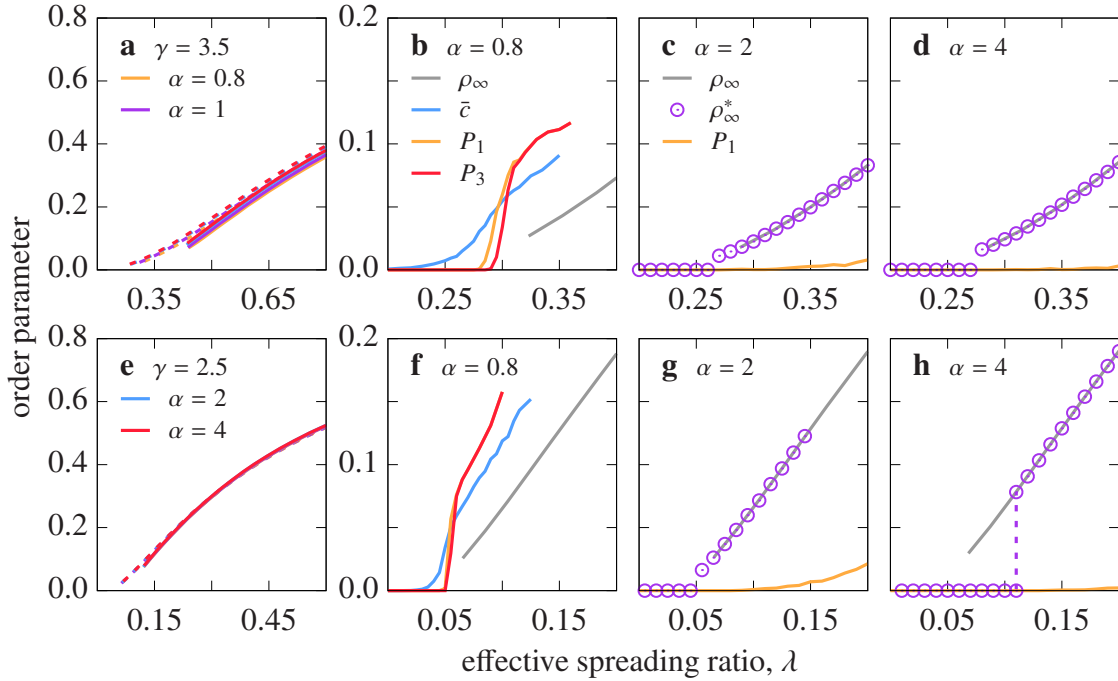


Figure 5.5: **Collective memory loss, excitability and bistability in the micc-SIS model with long-term memory on scale-free networks.** Results for scale-free networks with exponent (a–d)  $\gamma = 2.5$  and (e–h)  $\gamma = 3.5$ . (a, e) Late-time prevalence for network size  $N = 10^3$  (solid) and  $N = 10^4$  (dashed), time-averaged over  $10^4$  samples (shape parameter in legend). Uncertainty intervals not appreciable at this scale. (b, f) Endemic probabilities (orange and red), average coverage fraction (blue) and late-time prevalence of adiabatic expansion (grey) for  $\alpha = 0.8$  in a network with  $N = 10^4$ , averaged over  $10^4$  independent realizations. Uncertainty intervals comparable to line width. (c, d, g, h) Late-time prevalence of adiabatic expansion (grey curve) and endemic single-seed outbreaks (purple circles), and endemic probability (orange curve) for (c, g)  $\alpha = 2$  and (d, h)  $\alpha = 4$  in a network with  $N = 10^4$ , averaged over  $10^4$  independent realizations. Uncertainty intervals comparable to symbol size and line width.

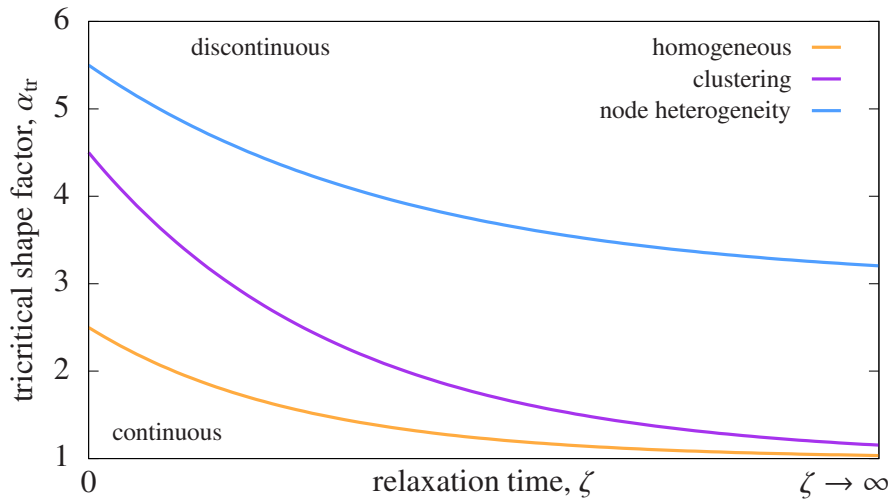


Figure 5.6: **Phase diagram of the miccSIS model on clustered and scale-free networks.** Schematic representation of the hypothetical phase diagram in terms of the tricritical shape factor of the infection probability density,  $\alpha_{\text{tr}}$ , and the relaxation time of viral loads,  $\zeta$ . The numerical values on the vertical axis are orientative.

cal phase diagram in terms of the shape parameter  $\alpha$  and relaxation time  $\zeta$ .

Node heterogeneity, on the other hand, also causes the transition with  $\alpha = 4$  and  $\zeta = 0$  to become continuous, considerably shrinks the excitable phase, and destroys the bistable region when  $\alpha = 2$  and  $\zeta \rightarrow \infty$ . Except for the displacement of the epidemic threshold and the discontinuous jump with  $\alpha = 4$  and  $\zeta \rightarrow \infty$ , the two values of the power law exponent  $\gamma$  yield qualitatively similar results. Thus the tricritical point seemingly grows with node heterogeneity and tends toward a limit value  $\lim_{\zeta \rightarrow \infty} \alpha_{\text{tr}} > 1$  (see Fig. 5.6).

Recall that we have used a single network realization for each system size and clustering coefficient or power law exponent. Although the quantitative details would vary (specially for large clustering coefficients and small power-law exponents), we expect the same qualitative picture for different network realizations.<sup>7</sup>

<sup>7</sup>See Figs. D.4, D.5, and D.6 in Appendix D for additional plots that partially verify this hypothesis.



# The voter model

---

## 6.1 Standard voter model

The voter model describes a population where each individual holds one of two opinions (for instance, buy or sell in a financial market or Democratic vs. Republican in American politics). The system's evolution lies at the interface between agents with opposing states, and is based on the fundamental assumption of imitation (individuals adopt the opinion of their peers). First introduced in 1973 to study competing species [40, 88], it was quickly reinterpreted as a model for opinions. Due to its simplicity and versatility, the voter model has become one of the most paradigmatic models of opinion dynamics. Applications and extensions range from herding behavior [118, 147] and electoral patterns [70], to the analysis of catalytic reactions [65, 66] and the evolution of bilingualism [27].

The classical formulation of the voter model is in discrete time: at each time step we randomly choose one of the agents, and the selected individual (node  $i$ ) randomly picks one of its neighbors (node  $j$ ) and adopts their opinion. Notice that the state of node  $i$  does not change if nodes  $i$  and  $j$  already shared the same opinion. Hence the system remains unaltered when it reaches consensus (all nodes have the same opinion). Nevertheless, this constitutes an active absorbing phase since agents keep imitating their peers. Note that a usual variant consists in describing the activation process of node  $i$  as a continuous-time stochastic process but maintaining the imitation step as a separate element.

Here we recast the voter model as a transmission phenomenon. The event where node  $i$  imitates node  $j$  can be interpreted as node  $j$  transmitting their opinion to node  $i$ . Then for any pair of neighbors  $i$  and  $j$  we consider two transmission channels,  $i \rightarrow j$  and  $j \rightarrow i$ . Albeit the similarities with the epidemic models of previous sections, the most fundamental difference lies in the transitions between states. On one hand, the SIS model is described by two distinct processes: infection requires contact but recovery is spontaneous. Conversely, the voter model possesses a unique symmetry: the mechanism to

change from opinion A to opinion B is identical to the mechanism that allows to change from B to A.

### 6.1.1 Continuous-time opinion transmissions

This “gauge invariance” of the voter model may be broken by a suitable modification. For example, one could consider that agents with opinion A are more successful in convincing their peers. However, we prefer to maintain the symmetry between opinions and, instead, distinguish two transmission processes: persuasion and reaffirmation. The former describes the transmission of an opinion to a node that holds the opposing view; on the contrary, the latter corresponds to the interaction between nodes that already have the same opinion.

Our formulation of the voter model as a spreading phenomenon describes a population of individuals that hold either opinion A or B and is embedded on an undirected and unweighted contact network. In its Markovian incarnation, nodes are persuaded by their peers at a constant rate  $\beta_p$  (corresponding to the links  $A \rightarrow B$  and  $B \rightarrow A$ ). Moreover, nodes reaffirm their opinion at a constant rate  $\beta_r$  (corresponding to the links  $A \rightarrow A$  and  $B \rightarrow B$ ). Then at any time the system counts  $2E = \sum_i k_i$  active transmission processes, where  $E$  is the total number of (undirected) links and  $k_i$  the degree of node  $i$ .

Borrowing the notation used for magnetic systems, we map the opinions A and B to the states  $\theta = -1$  and  $\theta = +1$ , respectively. Then we can write the magnetization at time  $t$  as  $m(t) = \sum_i \theta_i(t)$ , with  $\theta_i(t)$  the opinion state of node  $i$  at time  $t$ . As it turns out, the (weighted) ensemble average of the magnetization is conserved by the dynamics [118] and is therefore only a function of the initial conditions. Although this property is useful to evaluate certain late-time characteristic, it also reveals that the magnetization is useless as order parameter. A suitable alternative is to use the interface density,  $\rho$ , which measures the fraction of links that connect nodes with opposing opinions.

In uncorrelated networks, finite systems evolve exponentially toward one of the consensus states [166]. However, if the average degree is  $\langle k \rangle > 2$ , the system falls in a quasi-stationary state in which the interface density is constant. The life-time of this quasi-stationary state grows with the system size; consequently, infinite systems remain forever trapped in this active state. Finally, the average interface density decays exponentially,  $\log \rho(t) \propto t/\tau$ , and the characteristic time  $\tau$  increases with the system size.

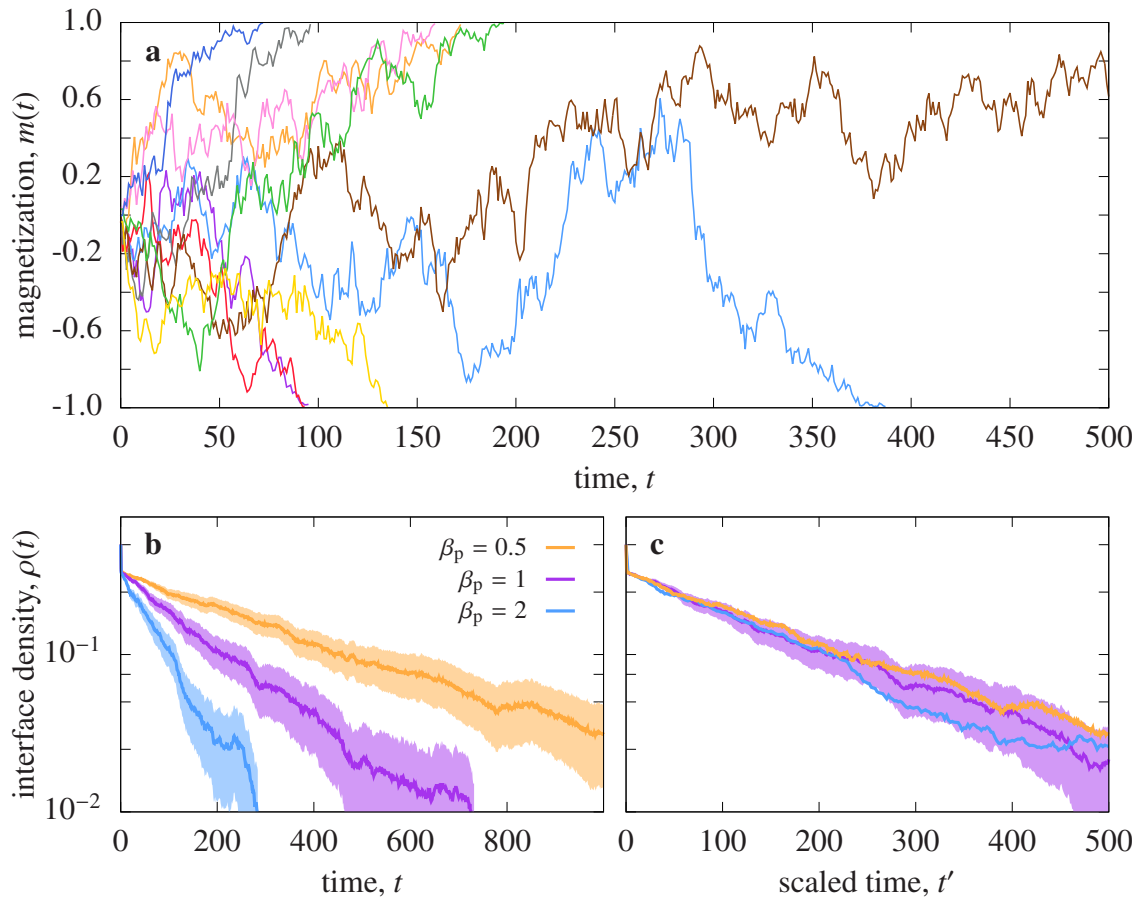


Figure 6.1: **Temporal evolution of the standard voter model.** Results for a random degree-regular network with  $k = 4$  and  $N = 10^3$  and initial condition  $m_0 = 0$ . Uncertainty intervals at 95% confidence level. **(a)** Magnetization for 10 independent simulations with persuasion rate  $\beta_p = 1$ . **(b)** Average interface density of 100 independent simulations (persuasion rate in legend). Note the log-scale in the vertical axis. **(c)** Averaged curves with scaled time  $t' = \beta_p t$  (colors as in **b**).

### 6.1.2 Simulation results

We perform extensive stochastic simulations to verify these analytic predictions.<sup>1</sup> We start each run with an initial magnetization of  $m_0 = 0$  and terminate the simulation when the system reaches consensus.<sup>2</sup> We use a random degree-regular network with  $k = 4$  and  $N = 10^3$  nodes, and compute the magnetization as  $m(t) = (N_+(t) - N_-(t))/N$ , with  $N_+(t)$  (respectively,  $N_-(t)$ ) the number of nodes with opinion  $\theta = +1$  ( $\theta = -1$ ) at time  $t$ , and the interface density as  $\rho(t) = E_p(t)/E$ , with  $E_p(t)$  the number of persuasion links, i.e., (undirected) links that connect nodes with opposing opinions at time  $t$ . Without loss of generality we use units of time such that  $\beta_r = 1$ .

Figure 6.1(a) shows the magnetization for 10 independent runs, of which approximately half reach the final consensus  $m = +1$ . Notice the large variation in terms of consensus times. In Fig. 6.1(b) we verify that the interface density decays exponentially. Additionally, we observe that the time scale is smaller as the persuasion rate grows. However, these differences are eliminated by scaling time as  $t' = \beta_p t$ , as we can see in Fig. 6.1(c).

## 6.2 Memory-induced complex contagion voter model

Next we equip the voter model with the memory-induced complex contagion infection mechanism. Nodes have a constant infectivity rate,  $\nu$ , and continuously spread bits of opinion toward their entire neighborhood. They target all of their neighbors equally, transmitting “pathogen” along each edge at constant rate  $\nu$ . At the same time, nodes collect these “toxins” from all their neighbors, and accumulate two opinion loads:  $\kappa_r$  from neighbors with whom they share the same opinion, and  $\kappa_p$  from neighbors that hold the opposing view. Nodes reaffirm their opinion with probability  $\psi_r^*(\kappa_r)d\kappa_r$  and are persuaded to switch state with probability  $\psi_p^*(\kappa_p)d\kappa_p$ , with  $\psi_r^*(\kappa_r)$  and  $\psi_p^*(\kappa_p)$  the corresponding infection probability densities.

Regarding the decay of the opinion loads we consider a very simple program. Besides controlling the reaffirmation (respectively, persuasion) process,  $\kappa_r$  ( $\kappa_p$ ) stores the cumulative evidence in favor of maintaining (switching) its

<sup>1</sup>See Appendix C.5.1 for an outline of the core algorithm.

<sup>2</sup>See Appendix C.5.3 for simulation details.

opinion state. Thus, when a reaffirmation process is triggered, the node erases its persuasion load  $\kappa_p$  but the reaffirmation load  $\kappa_r$  remains unaltered. On the other hand, if a node is persuaded to switch opinions, it transfers  $\kappa_p$  to  $\kappa_r$  (after changing state, the evidence in favor of the opposing opinion becomes evidence in favor of its current opinion) and erases  $\kappa_p$ .

In summary, agents spread pathogen to all their neighbors and continuously accumulate reaffirmation (same opinion) and persuasion (opposing opinion) load from all their neighbors. For each node there are two active processes, which entail a single or no transition:

- Reaffirmation of agent  $j$ . Agent  $j$  resets its persuasion load,  $\kappa_{p,j} \leftarrow 0$ .
- Persuasion of agent  $j$ . Agent  $j$  converts its persuasion load into reaffirmation load,  $\kappa_{r,j} \leftarrow \kappa_{p,j}$ , resets its persuasion load,  $\kappa_{p,j} \leftarrow 0$ , and changes its opinion state,  $\theta_j \leftarrow -\theta_j$ .

In general, the infectivity rate,  $\nu$ , may vary from node to node and can be different between persuasion and reaffirmation processes. For example, one could model individuals that are very persuasive to new followers (large  $\nu_p$ ) but less successful in strengthening the bond with loyal adherents (small  $\nu_r$ ). Similarly, the infection probability densities  $\psi_p^*$  and  $\psi_r^*$  could vary between nodes. Notwithstanding, in order to eliminate the effects of node heterogeneity, in the present work we use the same  $\nu$ ,  $\psi_p^*$ , and  $\psi_r^*$  for all nodes, and the same  $\nu$  for both persuasion and reaffirmation processes.

The two infection processes are governed by the versatile Weibull distribution, with shape parameter  $\alpha$  and scale parameter  $\mu$ . The corresponding instantaneous hazard rates are

$$\omega_r(t) = \nu \alpha_r [\mu_r]^{\alpha_r} z_r(t) [\kappa_r(t)]^{\alpha_r - 1} \quad (6.1)$$

$$\omega_p(t) = \nu \alpha_p [\mu_p]^{\alpha_p} z_p(t) [\kappa_p(t)]^{\alpha_p - 1} , \quad (6.2)$$

with  $z_r(t)$  (respectively,  $z_p(t)$ ) the number of neighbors that hold the same (opposing) opinion at time  $t$ . Notice that  $\alpha_r = \alpha_p = 1$  recovers the Markovian voter model presented in Section 6.1 (with  $\nu\mu_r$  and  $\nu\mu_p$  as reaffirmation and persuasion rates). Given that time can be scaled adequately by both rates (recall Fig. 6.1(c)), hereon forward we use  $\mu_r = \mu_p = 1$ . Hence we only consider two parameters,  $\alpha_r$  and  $\alpha_p$ , the shape factors for the reaffirmation and persuasion infection probability densities. Recall that  $\alpha < 1$  (respectively,  $\alpha > 1$ ) corresponds to a monotonically decreasing (increasing) hazard rate (see Fig. 2.2).

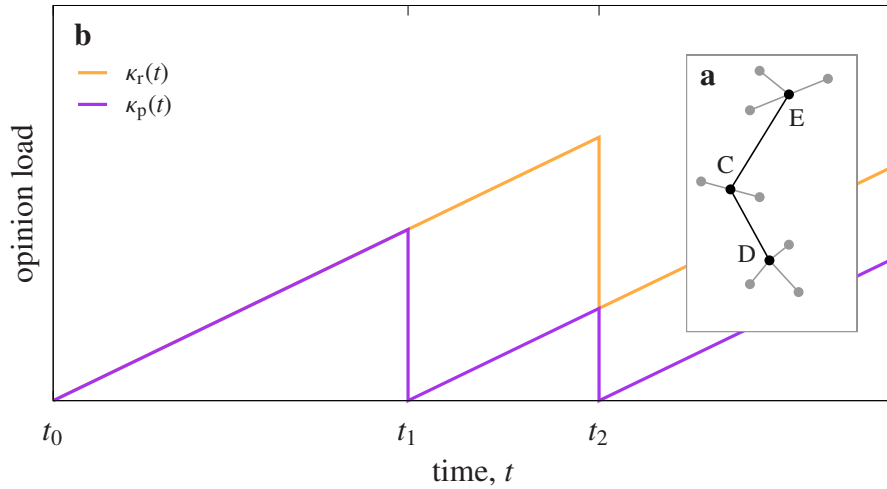


Figure 6.2: **Opinion load accumulation in the micc voter model.** (a) Small system considered in example. (b) Evolution of node C's opinion loads. Node C reaffirms its opinion at  $t_1$  and its persuasion load decays instantly (purple). When C is persuaded at  $t_2$ , it exchanges opinion loads and erases its persuasion load. Node C holds opinion A in the interval  $t \in [t_1, t_2]$  and opinion B for  $t > t_2$ .

Then we can interpret the former as an impulsive reaction (the occurrence probability is higher with little evidence) while the latter represents a meditative process (the event is more likely as more evidence becomes available). Finally,  $\alpha = 1$  corresponds to a purely random event.

For illustrative purposes, consider the system depicted in Fig. 6.2(a). At time  $t_0$ , nodes C and D hold opinion A, and node E has opinion B. During the interval  $t \in [t_0, t_1]$ , node C's reaffirmation load,  $\kappa_r$ , and persuasion load,  $\kappa_p$ , both grow at rate  $\nu$ . Node C reaffirms its opinion at time  $t_1$  and instantly erases its persuasion load. Afterward, both opinion loads grow at the same rate  $\nu$ . When C is persuaded at time  $t_2$ , it swaps opinion loads, resets its persuasion load, and switches to opinion B. Afterward both opinion loads grow again at rate  $\nu$ . Figure 6.2(b) shows the evolution of node C's opinion loads.

### 6.2.1 Simulation results

In order to explore the effects of the memory-induced complex contagion infection mechanism in the voter model we perform extensive stochastic simulations.<sup>3</sup> We start each run with an initial magnetization of  $m_0 = 0$  and ter-

<sup>3</sup>See Appendix C.5.2 for an outline of the core algorithm.

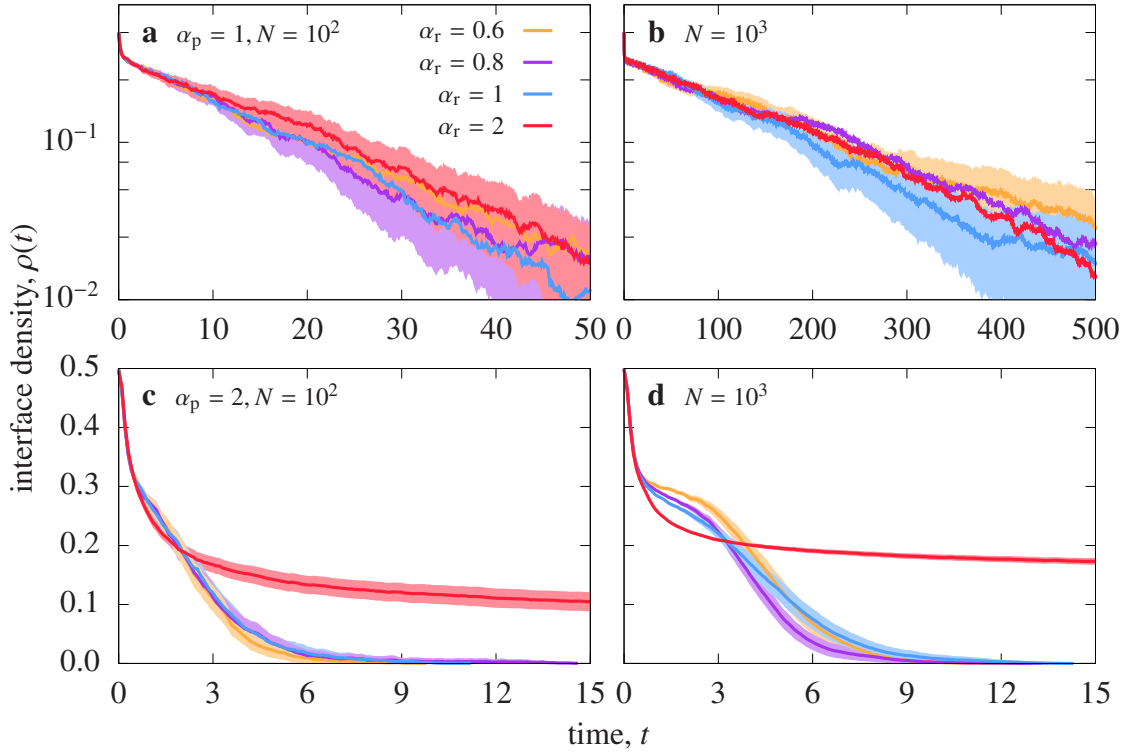


Figure 6.3: **Consensus in the micc voter model.** Average interface density of 100 independent simulations with initial condition  $m_0 = 0$  and persuasion parameter (**a, b**)  $\alpha_p = 1$  and (**c, d**)  $\alpha_p = 2$ , in a random degree-regular network with  $k = 4$  and (**a, c**)  $N = 10^2$  and (**b, d**)  $N = 10^3$  nodes (reaffirmation parameter in legend). Uncertainty intervals at 95% confidence level. Note the log-scale in the vertical axis in (**a, b**).

minate the simulation when the system reaches consensus.<sup>4</sup> We use random degree-regular networks with  $k = 4$  and  $N = 10^2$  and  $N = 10^3$  nodes, and compute the magnetization as  $m(t) = (N_+(t) - N_-(t))/N$ , with  $N_+(t)$  (respectively,  $N_-(t)$ ) the number of nodes with opinion  $\theta = +1$  ( $\theta = -1$ ) at time  $t$ , and the interface density as  $\rho(t) = E_p(t)/E$ , with  $E_p(t)$  the number of persuasion links, i.e., (undirected) links that connect nodes with opposing opinions at time  $t$ . We use units of the opinion load such that  $\nu = 1$  and, without loss of generality, set  $\mu_r = \mu_p = 1$ .

Figures 6.3(a),(b) show the results for persuasion parameter  $\alpha_p = 1$ . Independently of the reaffirmation parameter,  $\alpha_r$ , we recover the results for the

<sup>4</sup>See Appendix C.5.3 for simulation details.

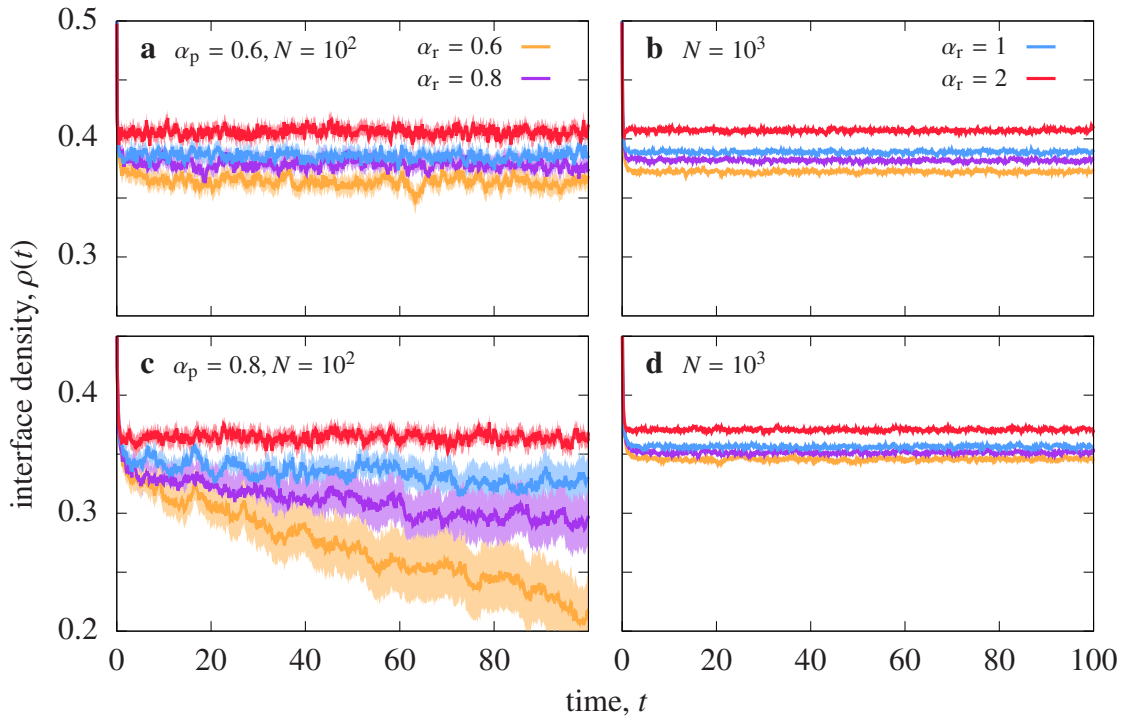


Figure 6.4: **Dynamic equilibrium in the micc voter model.** Average interface density of 100 independent simulations with initial condition  $m_0 = 0$  and persuasion parameter (a, b)  $\alpha_p = 0.6$  and (c, d)  $\alpha_p = 0.8$ , in a random degree-regular network with  $k = 4$  and (a, c)  $N = 10^2$  and (b, d)  $N = 10^3$  nodes (reaffirmation parameter in legend). Uncertainty intervals at 95% confidence level.

Markovian model (recall Fig. 6.1(c)). We also verify that the characteristic decay time scales linearly with  $N$ .

The results for persuasion parameter  $\alpha_p = 2$  are shown in Figs. 6.3(c),(d). With reaffirmation parameter  $\alpha_r < 1$  the population reaches consensus in a very short time. After a small plateau, the interface density decays almost linearly with  $t$ , although it exhibits a slower final relaxation. Note that the duration of the initial plateau increases with system size. On the other hand, with reaffirmation parameter  $\alpha_r = 2$  the decay toward consensus is extremely slow, and reduces even more for larger  $N$ . Additionally, notice the very narrow uncertainty intervals in both panels.

Finally, Figs. 6.4(a)–(d) show the results for persuasion parameter  $\alpha_p < 1$ . Independently of the reaffirmation parameter, with  $\alpha_p = 0.6$  the system stabilizes in an active state where  $\lim_{t \rightarrow \infty} \rho(t) > 0$  (Figs. 6.4(a),(b)). Conversely,

$\alpha_p = 0.8$  yields a more diverse phenomenology. The small population (see Fig. 6.4(c)) evolves linearly toward consensus with  $\alpha_r < 1$ , although the trend is more gradual as the reaffirmation parameter grows. With  $\alpha_r \geq 1$ , on the other hand, the system presents an active steady state with  $\rho > 0$ . Nevertheless, this variety of phenomena disappears in the larger population (Fig. 6.4(d)), which exhibits a dynamic equilibrium for all values of the reaffirmation parameter.

### 6.2.2 Discussion

With  $\alpha_p < 1$  we observe that the dynamic equilibrium already appears for finite systems, hinting toward the possibility that it is a true attractor (instead of a quasi-stationary state due to infinite size, as is the case for the Markovian voter model). Nonetheless, for  $\alpha_p = 0.8$  we do see the system evolving in the direction of consensus (for some values of  $\alpha_r$ ), which could be indicative of a cross-over effect toward the quasi-stationary state. On the other hand, the results with  $\alpha_p > 1$  show a richer phenomenology. For  $\alpha_r \leq 1$  the system orders in a very short time. However, the initial plateau grows with the population size, which could become a metastable state for infinite systems. Furthermore, the very narrow uncertainty intervals indicate that different runs follow the same regular pattern. Finally, for  $\alpha_r > 1$  (and large networks) the system becomes trapped in a frozen quasi-stationary state, where none of the nodes update their opinion.

In broad terms, we can classify the micro- and macroscopic behavior in three groups (see Fig. 6.5). With a small persuasion parameter,  $\alpha_p < 1$ , the reaffirmation parameter is irrelevant and the population continuously fluctuates (dynamic equilibrium). These individuals are prone to rapidly change their opinion, which can be interpreted as a progressive mindset. If the persuasion parameter is large,  $\alpha_p > 1$ , individuals are meditative in terms of changing their opinion. If this is combined with a large reaffirmation parameter ( $\alpha_r > 1$ ), this yields a group of people that are insecure (they don't take any decision) and the system freezes. Conversely, when  $\alpha_r < 1$  individuals are prone to rapidly reaffirm their views, somewhat bigoted. In combination with a resistance to change ( $\alpha_p > 1$ ), this can be interpreted as a conservative mindset. Surprisingly, these populations achieve consensus in a very short period of time.

Evidently, a more thorough analysis is needed to verify the generality of this heuristic description. In particular, these preliminary results clearly reveal

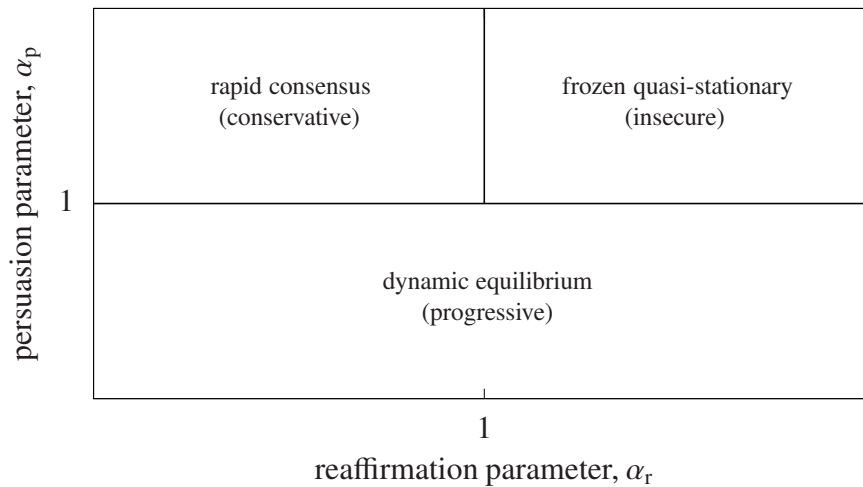


Figure 6.5: **Phase diagram of the micc voter model.** Schematic representation of the hypothetical phase diagram in terms of the reaffirmation parameter,  $\alpha_r$ , and the persuasion parameter,  $\alpha_p$ .

that small-size effects play an important role. This could have important implications for the study of mixed populations, where individuals are described by different parameters, and hints toward a nontrivial interplay with structured contact substrates.

# Airport delays

---

## 7.1 Dataset description and exploratory analysis

In this chapter we abandon the comfortable “bubble of theory” and confront the messiness of real life. Our goal is to study the joint effects of memory and multiple infectors in an empiric spreading phenomenon. In particular, we analyze the interplay between airport congestion and the propagation of delays in the air transportation network. Roughly speaking, the cumulative effect of delayed arrivals (“incoming pathogen”) causes the airport to become congested (“infected”) and leads to delayed departures (“outgoing pathogen”). Obviously, this schematic interpretation does not capture the detailed intricacies of air traffic management. Bear in mind that our intent is far from providing a complete and actionable description of airport delays, nor do we expect to apply the micc model to reproduce the data. We simply wish to explore the particularities and imperfections of a real-life scenario and gauge the merits and limitations of epidemic modeling.

We use the airline on-time performance data provided by the Bureau of Transportation Statistics of the United States Department of Transportation [23]. National carriers are required to report on-time data for domestic flights, including schedules and actual departure and arrival times, and canceled and diverted flights. Since international carriers are not included, we limit our analysis to New York City’s LaGuardia airport (IATA code LGA) and Ronald Reagan National airport (DCA, serving Washington D.C.), two of the busiest domestic airports in the US (respectively, 30 and 24 million passengers in 2018 [132, 120]). Both airports count 3 routes operated by Canadian Airlines, which is not required to report data on its on-time performance. However, given this low number we are confident that the impact on our analysis will be minor to nonexistent.

Figures 7.1(a),(b) show the number of scheduled arrivals and departures during the years 2018 and 2019. We observe that the number of daily arrivals

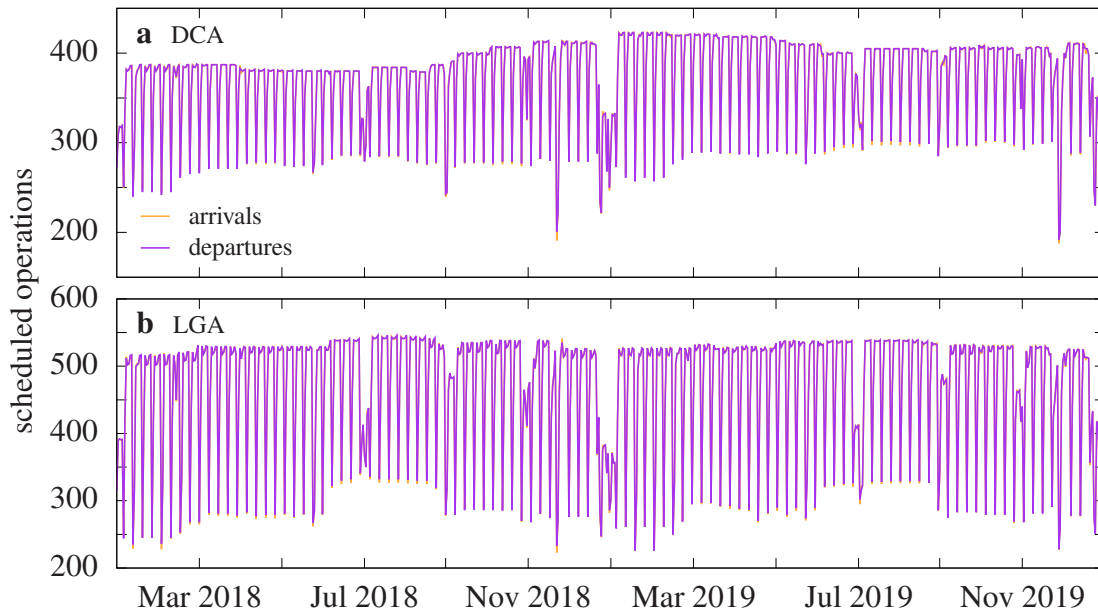


Figure 7.1: **Schedules operations.** Daily number of scheduled arrivals (orange) and departures (purple) for (a) Ronald Reagan National and (b) LaGuardia airports in 2018 and 2019.

and departures is almost identical, and that both airports present a clear reduction of operations during the weekend. This last observation is consistent with the fact that the majority of domestic travels are business-related [156]. Notice also the drop in activity during the 4th of July, 9/11 (more marked in New York), Halloween (end of October), Thanksgiving (end of November), and Christmas (end of December).

The fraction of canceled flights is shown in Figs. 7.2(a),(b). We see that the patterns are similar for arrivals and delays, and present some difference between the two airports; although relatively close in terms of geography, they are sufficiently distant so that the weather has a varying impact. On the other hand, the fraction of diverted operations is clearly larger for arrivals than for departures (Figs. 7.2(c),(d)). Nevertheless, the baseline fraction of diverted operations is very low (less than 1%), except for some specific days. In order to remove possible confounding factors, we exclude days with an irregular amount of scheduled, canceled, and diverted operations.<sup>1</sup>

Finally, Figs. 7.3(a)–(d) show the daily distributions of scheduled oper-

<sup>1</sup>See Appendix C.6 for a detailed description on the detection of outliers.

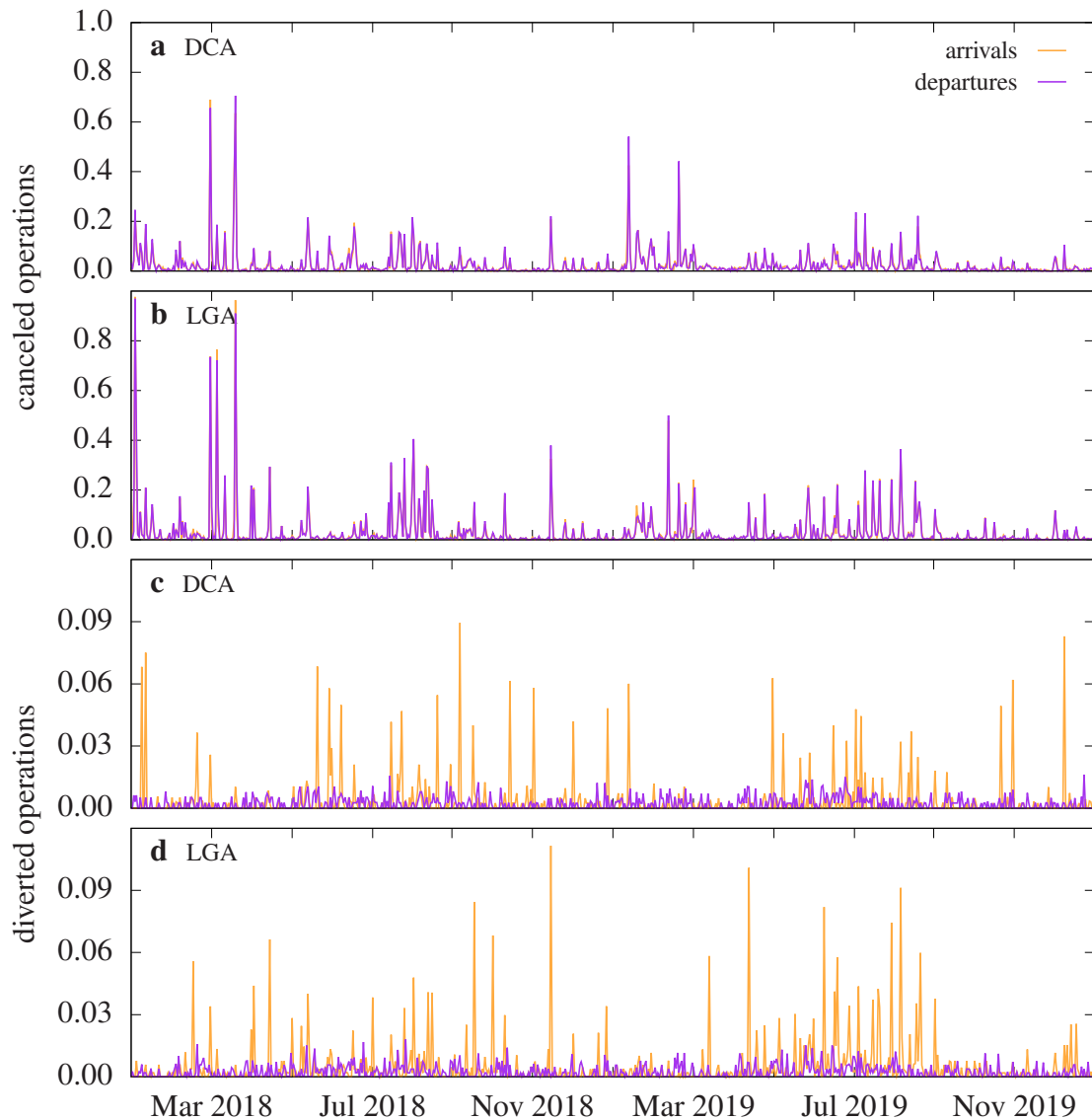


Figure 7.2: **Canceled and diverted operations.** Daily fraction of (a, b) canceled and (c, d) diverted arrivals (orange) and departures (purple) for (a, c) Ronald Reagan National and (b, d) LaGuardia airports in 2018 and 2019.

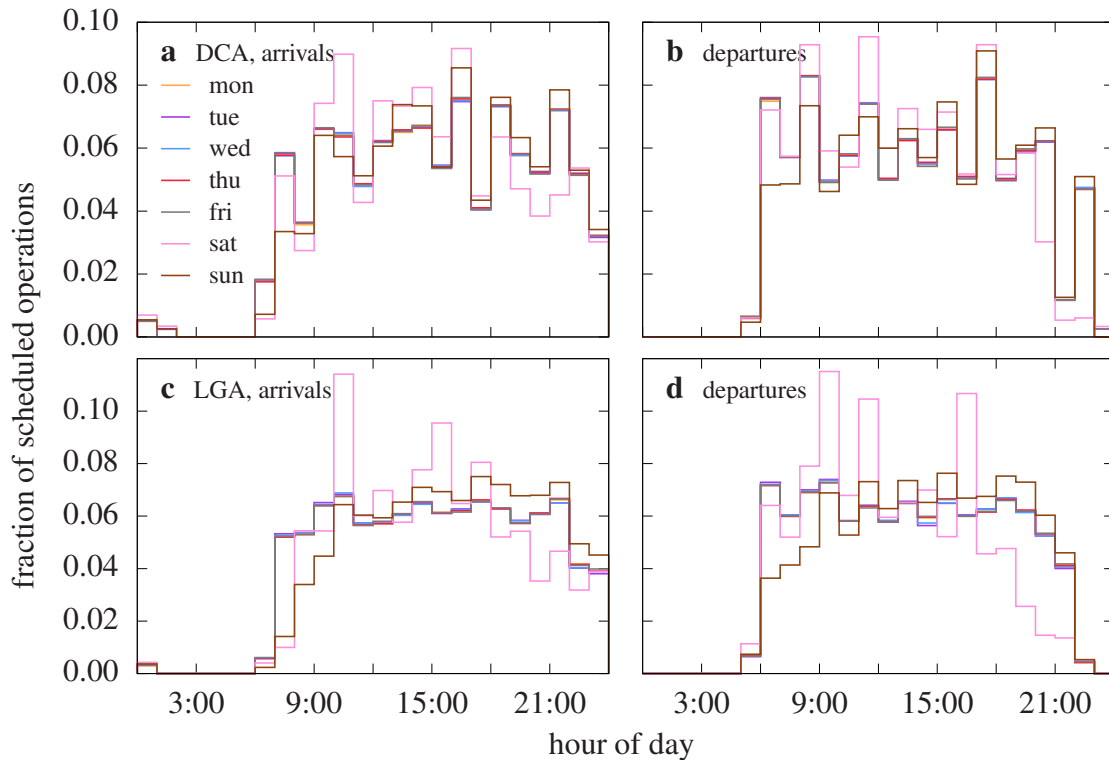


Figure 7.3: **Daily distribution of scheduled operations.** Within-day fraction of scheduled (a, c) arrivals and (b, d) departures for (a, b) Ronald Reagan National and (c, d) LaGuardia airports in 2018 and 2019 (day of week in legend).

ations (considering only valid days). During weekdays, LaGuardia has an almost constant number of operations per hour; in contrast, Reagan National exhibits more variability during the day (although the profiles are practically identical for all weekdays). Saturdays and Sundays, on the other hand, present their own particular pattern (for both airports). Notwithstanding, the differences with weekdays are not extreme, hence we decide to treat all days equally.

## 7.2 Delays, infective periods, and infectors

Next we move to the analysis and propagation of delays, defined simply as the difference between the actual and scheduled arrival or departure time.<sup>2</sup>

<sup>2</sup>Previously we compute the corrected timestamp, since the data set reports the date and time separately. See Appendix C.7 for details on this procedure.

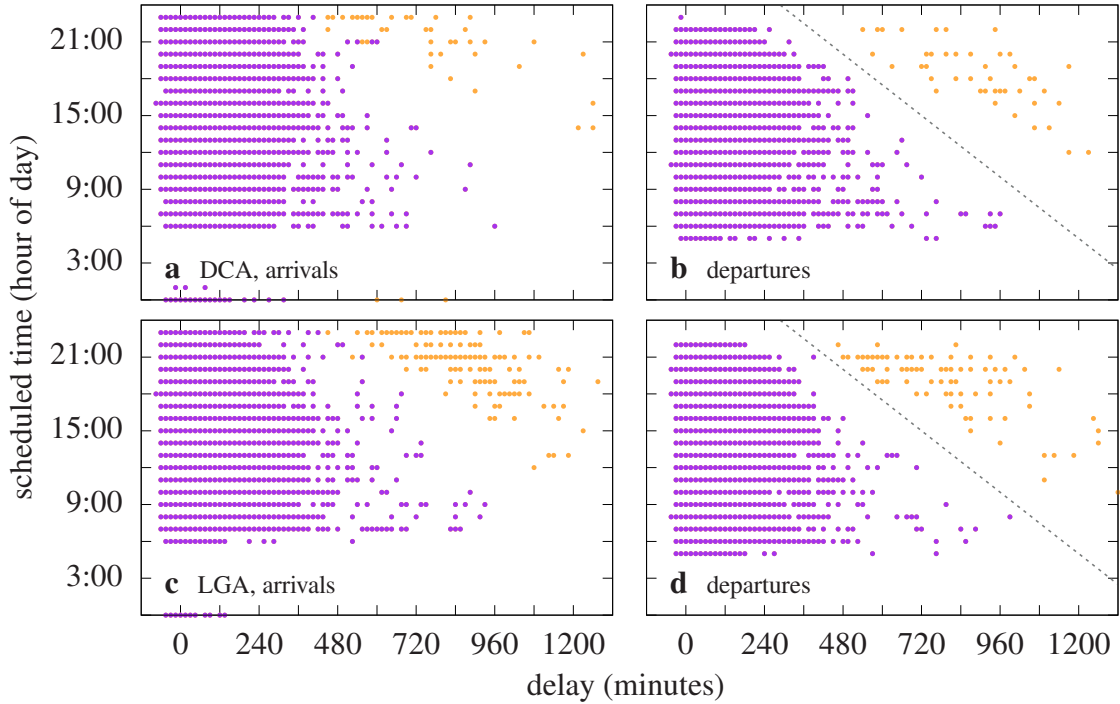


Figure 7.4: **Distribution of delays by scheduled time.** Delays (horizontal axis) are discretized by 15 minutes and scheduled times (vertical axis) by the hour. Each dot represents one or more flights in the corresponding bin (outliers in orange). (a, c) Arrivals and (b, d) departures for (a, b) Ronald Reagan National and (c, d) LaGuardia airports in 2018 and 2019.

Figures 7.4(a)–(d) show the relation between the duration of the delay and the scheduled time of the corresponding operation. In general, the longest delays occur earlier in the day (as reported in [184]). For afternoon departures we observe a peculiar pattern, where a group of flights appears completely separated from the rest. This phenomenon occurs for both LaGuardia and Reagan National airports, and is related to the fact that airports reduce or cease operations during the night. Notice that the two clusters are separated by a stripe that corresponds roughly to 4 hours, the typical duration of overnight closures.<sup>3</sup> We manually remove the flights that satisfy

$$\text{scheduled departure time} > 30 - \frac{\text{departure delay}}{48}, \quad (7.1)$$

<sup>3</sup>Most airports do not operate between 1:00 and 5:00, approximately.

with the delay measured in minutes (dashed curves in Figs. 7.4(b),(d)). As a consequence, the arrivals that displayed an anomalous pattern are also removed (orange dots in Figs. 7.4(a),(c)).

Both the US Federal Aviation Administration and the European Organisation for the Safety of Air Navigation (EUROCONTROL) allow a grace period of 15 minutes for delayed operations [64]. Hereon forward we use the same definition and use the corresponding “excess delay”

$$\text{excess delay} = \text{delay} - 15, \quad (7.2)$$

measured in minutes. Note also that the temporal resolution is 1 minute.

Next we analyze the number of simultaneously delayed departures, which gives an idea of the congestion of an airport. Figure 7.5(a) shows the case of LaGuardia airport on January 10th, 2018. We see that there was at least 1 delayed departure during practically the whole day, and up to a maximum of 7 simultaneously delayed departures. In order to compare different days we compute the average daily stress, which is simply the area under the curve divided by the period of scheduled activity. This is also the average number of simultaneously delayed departures. As we can see from the distributions in Figs. 7.5(b),(d), this value varies greatly between different days. The averages of these distributions, 2.94 for DCA and 3.96 for LGA, give a reference value that allows us to determine when an airport is “infected”. For example, we consider that LaGuardia airport is infected when it counts 4 or more simultaneously delayed departures. Thus the dashed curve in Fig. 7.5(a) defines 14 infective periods, ranging from very short (around 22:00) to 2-hour long periods (approximately from 16:00 to 18:00). For Reagan National airport we lower the threshold to 3.

Finally, with these definitions we measure the distribution of infective periods. In our mapping of the problem as an epidemic model, these would correspond to the inter-event time distribution of recoveries. Figures 7.5(c),(e) show that they are approximately exponential, with a very fast initial decay and a final cut-off. Note that this is compatible with a Markovian assumption, which is usual in technical systems.

At last, we correlate the “infection” of an airport with delayed arrivals. First we compute the number of simultaneously delayed arrivals, which maps to the number of infectors in an epidemic model. If the contagion were simple, the probability to become infected would grow linearly with the number of simultaneously delayed arrivals. Since we work with discrete timesteps, we

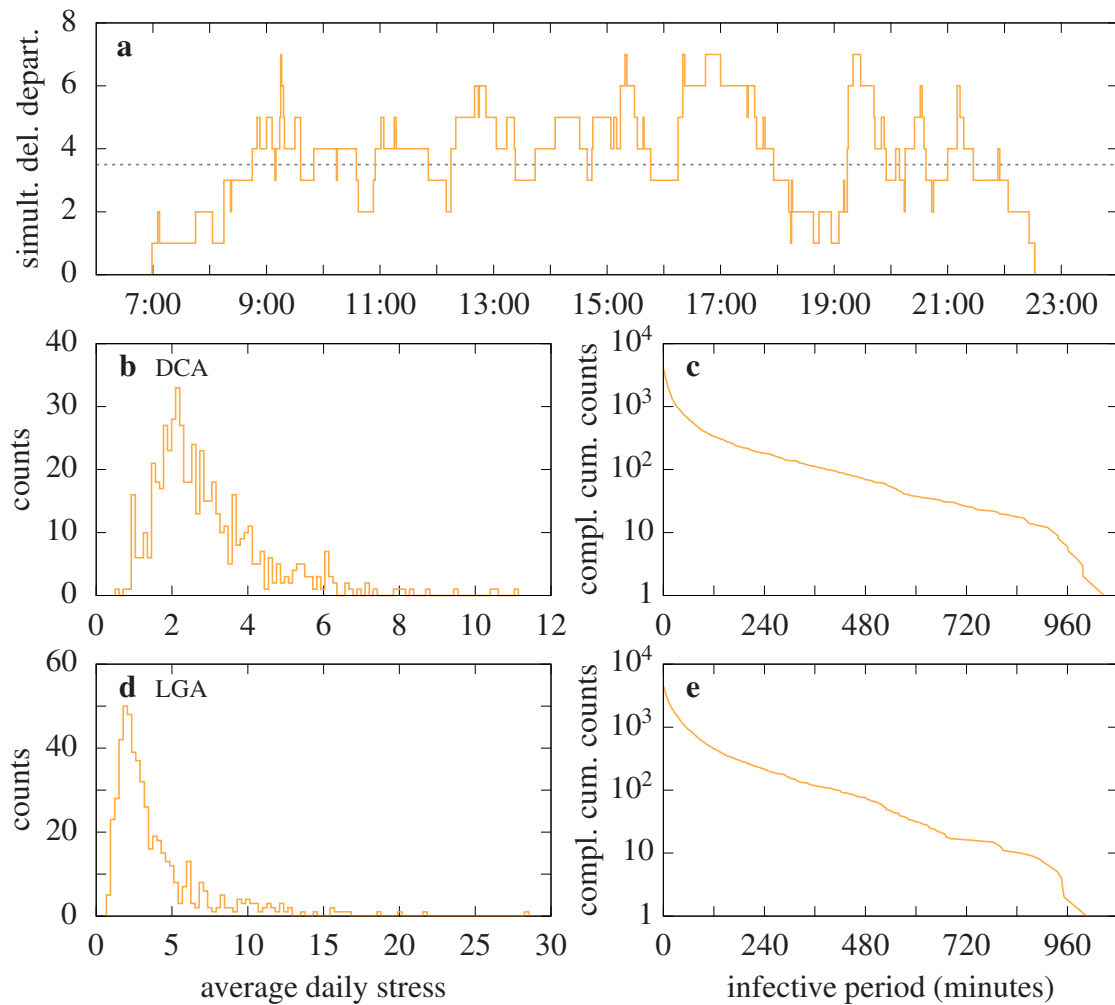


Figure 7.5: **Daily stress and infective periods.** (a) Number of simultaneously delayed departures on January 10th, 2018, at LaGuardia airport. Dashed line indicates infectivity threshold. (b, d) Distribution of average daily stress and (c, e) complementary cumulative counts of infective periods for (b, c) Ronald Reagan National and (d, e) LaGuardia airports in 2018 and 2019. Note the log-scale in the vertical axis in (c, e)

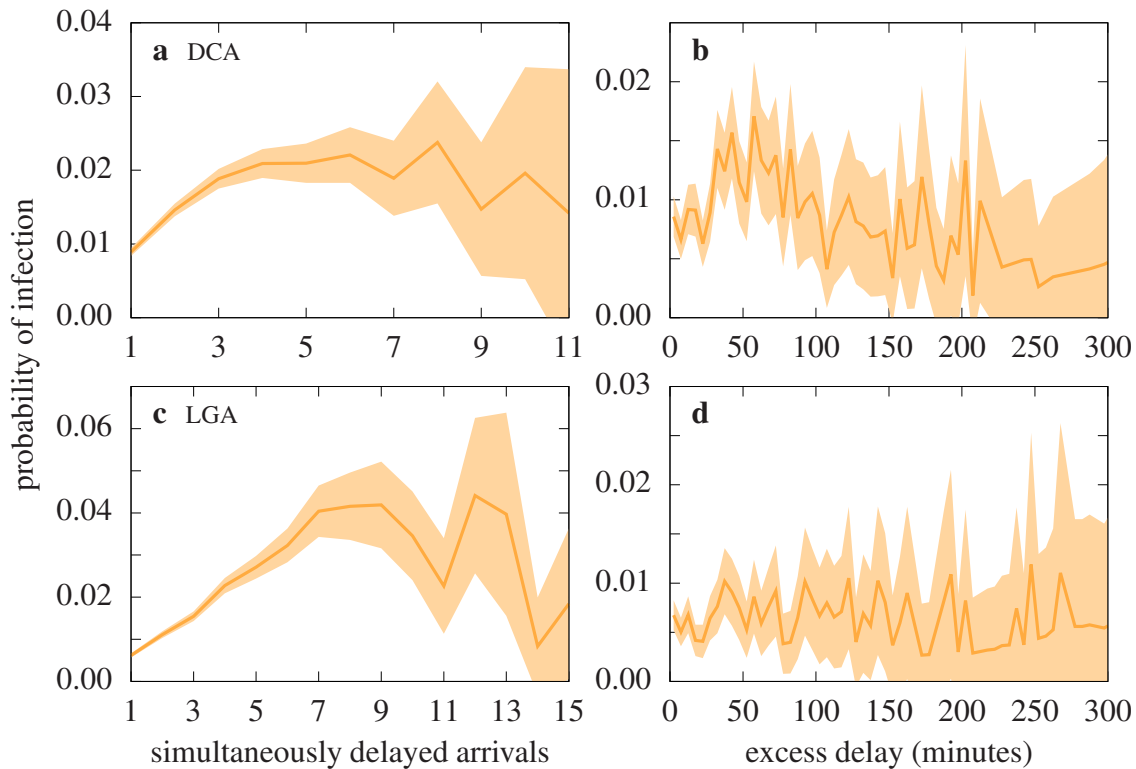


Figure 7.6: **Infection probabilities.** Probability to become infected conditioned on (a, c) the number of simultaneously delayed arrivals and (b, d) the excess delay of a single delayed arrival, for (a, b) Ronald Reagan National and (c, d) LaGuardia airports in 2018 and 2019.

compute the probability to become infected at time  $t + 1$  conditioned on having  $k$  infectors at time  $t$ . As we see in Figs. 7.6(a),(c), the probability initially increases with the number of infectors but afterward fluctuates around a constant value.

In order to study the effects of memory, we only consider timesteps with a single delayed arrival. Here we map the excess delay to the accumulated exposition time of our epidemic model; if the dynamics were Markovian, the probability would be constant. We compute the probability to become infected at time  $t + 1$  conditioned on having accumulated  $x$  “units of pathogen” (excess delay) from a single infector at time  $t$ . Reagan National airport (Fig. 7.6(b)) exhibits an initial increase followed by a relaxation toward a constant value. On the other hand, LaGuardia airport (Fig. 7.6(d)) shows a pattern that is compatible with a constant value.

Our exploratory analysis reveals that airport congestion can play an im-

portant role in the propagation of air-transportation delays. In particular, the aggregate effect of multiple delayed arrivals can cause a disruption of ground operations, which ripples through the airport's schedule and leads to delayed departures. These preliminary results confirm that the contagion mechanism is not purely simple. Nonetheless, more evidence is required in order to rule out the Markovian aspect.



# Conclusions

---

## 8.1 Background

Epidemic modeling has proven to be a powerful tool for the study of contagion processes in biological, social, and technological systems. Variations of the benchmark susceptible-infected-recovered (SIR) and susceptible-infected-susceptible (SIS) models have been applied to study the spread of diseases, opinions, information, rumors, and innovation. Various adaptations and extensions—some very simple and clean but others rather elaborate and complicated—have provided valuable insights into the nature of spreading mechanisms, the dynamics of outbreaks, and the viability of containment protocols. More recently, the inclusion of real-life contact networks and mobility patterns has led to astonishingly accurate results, prompting the use of epidemic models as real-time predictive tools.

For years, the go-to modeling scheme for contact-based contagion assumed Markov processes and isolated transmissions. The Markov property translates into exponentially distributed interevent times and renders the system memoryless—its evolution is independent of its history. Although this approximation is most often justified because of the reduced mathematical (and computational) tractability of nonexponential distribution, its inappropriateness is widely supported by empirical evidence. Prototypical examples include the peaked distributions of infection periods of numerous diseases and the bursty human activity patterns in social networks, well described by heavy-tailed distributions.

On the other hand, assuming isolated transmissions leads to infection channels that are not influenced by their local environment; consequently, the infection likelihood can be written as the sum of statistically independent exposures. Nevertheless, experimental observations support the existence of more complex, nondyadic mechanisms in a variety of scenarios. The most cited example is social contagion, but evidence has also been found in fungal and bacterial pathogen colonization and—paradoxically—the proliferation of

noncommunicable diseases. Clearly, the time has come to overcome these outdated modeling limitations.

In recent years, an important amount of research has ventured into the scarcely explored area of memoryful and complex epidemics. Regarding memory, a wide array of modifications has been analyzed, such as two-step infection models, nonexponential distributions, and time-varying transmission probabilities. Similarly, a plethora of complex contagion schemes has been proposed to mediate the assumption of independent transmissions; examples include correlated, nonlinear transmission channels, extended neighborhood effects, and deterministic threshold models. So far, not many endeavors have focused on tackling both modeling assumptions simultaneously, and little is known about how these two features interact. Such a combined approach is of particular interest for contagion phenomena that include a social component, such as awareness and vaccination campaigns or the spread of noncommunicable diseases (e.g., obesity, anxiety, and substance abuse).

My thesis contributes to the analysis of the synergies between memory and nondyadic interactions in spreading processes. I develop a model that bypasses the usual framework of edge-based transmissions and recasts the infection process as a node-centric mechanism. Specifically, the memory-induced complex contagion (micc) model describes diseased nodes as infectious sources that spread doses of pathogen to their entire neighborhood. Healthy nodes, on the other hand, gather the toxins from all their neighbors—present and past—and become infected given the total viral load they have amassed. As a consequence of this infection mechanism, a notion of social reinforcement/inhibition arises organically, and the concepts of non-Markovian dynamics and complex contagion become intrinsically coupled.

The micc model provides a generic description of memoryful and complex spreading phenomena. However, in order to actually investigate its properties, one must particularize two ingredients: the infection probability density and the accumulation and decay of the viral load. I have chosen to describe the former by the versatile Weibull function, characterized by its shape parameter  $\alpha$ . For starters,  $\alpha = 1$  recovers the exponential distribution of the standard Markovian formulation, which enables the comparison to a well-known benchmark. Other values of the shape parameter interpolate between power law–like fat-tailed distributions ( $\alpha < 1$ ) and bell curve–like peaked distributions ( $\alpha > 1$ ). Regarding the viral load, I have chosen a simple linear accumulation and an exponential decay, with characteristic time  $\zeta$ . This choice allows me to inter-

polate between a short-term memory mode ( $\zeta = 0$ ) and a long-term memory mode ( $\zeta \rightarrow \infty$ ). Furthermore, I have limited the analysis to the basic epidemic models (SI, SIR, and SIS) and a short exploration of the voter model. Finally, when the prescription of recoveries is required (SIR and SIS models), I maintain the exponential distribution of the standard Markovian formulation; this choice allows me to focus unequivocally on the effects of the memory-induced complex contagion infection mechanism.

## 8.2 Results

The SI model only allows the transition between the susceptible and infected states, thus any healthy population will eventually become completely diseased. The temporal dynamics of this evolution varies greatly in the miccSI model, where agents are equipped with the memory-induced complex contagion infection mechanism. Fat-tailed distributions describe nodes that are “impulsive”—reactionary, even—and require very little viral load to become infected. The outbreaks initially grow very rapidly but then decelerate and converge slowly toward the fully infected state. With peaked infection distributions, on the other hand, nodes are more “meditative” and become infected with a higher value of the viral load. In this case, outbreaks present a gradual initial growth and afterward saturate very quickly; additionally, they are more uniform and show a notably regular pattern. Although somewhat expected, these results lay the foundations for upcoming—more spectacular—features.

In the SIR model, infected nodes may overcome their ailment, transitioning to a final recovered compartment. On a whole, the system evolves towards a terminal state that is characterized by the absence of infected agents. Depending on the parameters of the pathogen, encapsulated via the effective spreading ratio, the outbreaks can be either very short-lived or develop into havoc-wreaking disruptions. These two phases are separated by a continuous phase transition at the epidemic threshold.

The short-term memory mode of the miccSIR model causes a displacement of the epidemic threshold toward higher values as the shape parameter of the infection probability grows. Thus more reactive agents (smaller values of the shape parameter) enable the existence of sustained outbreaks that are caused by weaker pathogens (lower values of the spreading ratio). In accordance with our findings for the miccSI model, meditative individuals re-

quire a longer build-up but cause a more concentrated explosive effect. On the contrary, the outbreaks for fat-tailed infection distributions are slightly less virulent and affect a smaller fraction of the population if agents possess an additional long-term memory. This phenomenon reveals the crucial role played by dormant nodes, which hinder the infection chains when the outbreak revisits previously afflicted areas of the network. In contrast, with peaked infection distributions their previously accumulated viral load facilitates the expansion of the outbreak, which becomes more violent.

Things get more interesting with the introduction of reinfections. In the SIS model, infected nodes that recover become once again susceptible and may reinfect at a later stage. This feature results in a nontrivial active steady state, where nodes repeatedly infect and recover, but overall the fraction of infected nodes remains more or less constant; nonetheless, less virulent outbreaks are still eradicated very quickly. With the conventional assumptions of Markovianity and simple contagion, the phase transition between the healthy and endemic phases is typically continuous.

The miccSIS model with peaked infection distributions can be studied with the use of an adequate analytical framework—and by applying (many) suitable approximations. When agents are endowed solely with a short-term memory, the system displays a tricritical point where the customary second-order phase transition gives way to a discontinuous transition. Then the customary healthy and endemic phases are separated by a bistable region where two stable attractors coexist. Additionally, as agents increase their memory span, this intermediate region already emerges for lower values of the shape parameter  $\alpha$ . Notice that bistability in SIS-like models is usually obtained by explicitly prescribing some sort of coordination—either cooperative or competitive—between neighboring nodes. However, here it arises organically from the memory-induced complex contagion infection mechanism.

Even though this analytical framework paints an exquisite qualitative picture, stochastic simulations are required to fill in the details. In particular, they reveal that the width of the previously discussed bistable region shrinks as the memory span of individuals increases. They are also necessary to analyze the miccSIS model with fat-tailed infection distributions. In this case, if agents only have short-term memory, the system behaves very similar to the standard Markovian model; conversely, the healthy and endemic phases are separated by an excitable region when agents possess a long-term memory mode. In this intermediate phase, outbreaks initially expand rapidly through the system but

afterward slow down and are eventually eradicated, surprisingly resembling a SIR-like curve.

Concluding, if nodes are equipped with a long-term memory mode, the system experiences a global memory loss. Specifically, agents that have an infinite memory span behave on aggregate as if they had no memory at all. Nevertheless, important differences with respect to the Markovian model are revealed when looking at the dynamical properties of the outbreaks. The three order parameters—average coverage, endemic probability, and late-time prevalence—are identical if agents are memoryless; when the long-term memory mode is activated, this delicate balance is broken and a second critical point emerges. In particular, the system first transitions from the healthy phase to an either bistable or excitable intermediate region, followed by a hybrid transition to the endemic phase.

In terms of phenomenology, the standard SIS model in unstructured networks yields rather unexciting results, but more interesting properties arise when a nontrivial contact structure is added. The miccSIS model, on the other hand, shows a plethora of features in degree-regular networks, revealing that network structure is not an essential ingredient in order to obtain a richer phenomenology. Unexpectedly, this variety is reduced with the introduction of nonhomogeneous networks. Particularly, clustering mitigates the impact of the short-term memory mode while node heterogeneity partially suppresses the effects of the long-term memory mode—the excitable region for fat-tailed infection distributions survives, but with peaked distributions the intermediate bistable phase vanishes.

Finally, the voter model—a paradigmatic description of opinion dynamics—can be recast as a spreading phenomenon with symmetric transitions between the two opinion states. In its Markovian formulation, the population becomes trapped in a transient quasi-stationary state but eventually evolves toward one of the two consensus states. When introducing the memory-induced complex contagion “infection” mechanism, it is important to distinguish between the processes of persuasion and reaffirmation. In the former, a node is “convinced” to change its opinion, while the latter corresponds to a node increasing their confidence in their belief. It turns out that the specific numerical values of the reaffirmation process are irrelevant—the dynamics is aptly described in terms of the persuasion process. Depending on the response of an individual to new stimuli (either meditative or impulsive), the system reaches consensus in a very short time or becomes trapped in a dynamic equilibrium.

### 8.3 Outlook

All in all, my analysis of the stylized yet feature-rich micc mechanism evidences a crucial role of non-Markovianity in the spread of epidemic outbreaks. In particular, agents' memory span dramatically alters the effect and impact of newly introduced pathogens. Currently, this topic is a very active field of epidemic modeling, with applications that range from the appearance of exotic diseases to the dissemination of fake news on social media.

However, I believe it is important to stress that the inclusion of memory is in no way imperative. Most of the interesting phenomenology has already been found in Markovian models, albeit via elaborate schemes or intricate network topologies. This conformity evidences the robustness of previous results and supports the appropriateness of their employment in many scenarios. Notwithstanding, memoryful epidemics add a nuanced layer of complexity that can lead to novel behaviors. Even so, to the extent of my knowledge, the only feature that has not been widely reported in previous studies is the appearance of excitable outbreaks in SIS-like models.

Inasmuch as time and space are limited, I had to exclude some topics from this work. Personally, I am intrigued by the perfect overlap of the endemic probability and the late-time prevalence in the Markovian SIS model, and I think that elucidating this apparent coincidence is definitely worth the while. Moreover, the development of an adequate analytical framework to study the temporal properties of outbreaks in the miccSIS model could shed (a lot of) light on the peculiar excitable intermediate region that appears with fat-tailed infection distributions. In addition, the fact that the results for the voter model are (practically) independent of the reaffirmation parameters enables the possibility of studying the problem with an analytical approach. Finally, an exhaustive exploration is required to find suitable data sets and provide supplementary empirical analyses, without excluding the possibility of designing and executing a controlled experiment.

I finish with the usual list of potential extensions and ways forward. The analysis of additional network characteristics—such as degree correlations or meso-scale structures—would supply renewed insights on the relevance of microscopic mechanisms and topological aspects in contagion processes. Another interesting variation consists in using mixed population groups, which would allow us to gauge the effect of demographic features on the dynamical and late-time properties of the system. Last but not least, we could explore

other infection probability distributions or include realistic nonexponential recoveries. All in the hope of increasing our understanding of epidemic spreading and improving our ability to shield the world from catastrophe.



# Mathematical derivations

---

## A.1 Closed-form solution for the standard SI model

Here we show the step-by-step solution for the prevalence in the standard SI model, presented in Section 2.1.2. We start from the separable differential equation

$$\frac{d\rho(t)}{dt} = \beta k \rho(t)(1 - \rho(t)) \quad (\text{A.1})$$

and integrate both sides

$$\int \frac{d\rho(t)}{\rho(t)(1 - \rho(t))} = \int \beta k dt \quad (\text{A.2})$$

$$\int \frac{d\rho(t)}{\rho(t)} + \int \frac{d\rho(t)}{1 - \rho(t)} = \int \beta k dt \quad (\text{A.3})$$

$$\log \rho(t) - \log(1 - \rho(t)) = \beta k t + \log C, \quad (\text{A.4})$$

where  $C$  is an arbitrary constant. Solving for the prevalence gives

$$\frac{\rho(t)}{1 - \rho(t)} = C e^{\beta k t} \quad (\text{A.5})$$

$$\rho(t) = \frac{C e^{\beta k t}}{1 + C e^{\beta k t}}. \quad (\text{A.6})$$

Substituting the initial condition,  $\rho(0) = \rho_0$ , in Eq. (A.5) we find a value for the integration constant  $C = \rho_0/(1 - \rho_0)$ , and substitution in Eq. (A.6) yields the final result

$$\rho(t) = \frac{\rho_0 e^{\beta k t}}{1 - \rho_0 + \rho_0 e^{\beta k t}}. \quad (\text{A.7})$$

## A.2 Dynamic equations of the miccSI model

To obtain Eqs. (2.34) and (2.35) we start from

$$n_i(t + dt) = n_i(t) + (1 - n_i(t))\pi_i \quad (\text{A.8})$$

$$\kappa_i(t + dt) = \kappa_i(t) + (1 - n_i(t))(1 - \pi_i)\nu z_i(t)dt, \quad (\text{A.9})$$

with

$$\pi_i = \begin{cases} 1 & \omega_i(t)dt \\ 0 & 1 - \omega_i(t)dt \end{cases}, \quad (\text{A.10})$$

and  $\omega_i(t) = \nu\alpha\mu^\alpha z_i(t) [\kappa_i(t)]^{\alpha-1}$ . First we compute the expectation value conditioned on time  $t$ , which only affects the stochastic variable  $\pi_i$

$$\mathbb{E}[n_i(t + dt) | t] = n_i(t) + (1 - n_i(t)) \mathbb{E}[\pi_i | t] \quad (\text{A.11})$$

$$= n_i(t) + (1 - n_i(t))\omega_i(t)dt \quad (\text{A.12})$$

$$= n_i(t) + (1 - n_i(t))\nu\alpha\mu^\alpha z_i(t) [\kappa_i(t)]^{\alpha-1} dt \quad (\text{A.13})$$

$$\mathbb{E}[\kappa_i(t + dt) | t] = \kappa_i(t) + (1 - n_i(t)) \mathbb{E}[1 - \pi_i | t]\nu z_i(t)dt \quad (\text{A.14})$$

$$= \kappa_i(t) + (1 - n_i(t))(1 - \omega_i(t)dt)\nu z_i(t)dt \quad (\text{A.15})$$

$$= \kappa_i(t) + (1 - n_i(t))\nu z_i(t)dt + \mathcal{O}(dt)^2. \quad (\text{A.16})$$

Next we take the ensemble average up to  $\mathcal{O}(dt)$

$$\langle n_i(t + dt) \rangle = \langle \mathbb{E}[n_i(t + dt) | t] \rangle \quad (\text{A.17})$$

$$= \langle n_i(t) \rangle + \nu\alpha\mu^\alpha \langle (1 - n_i(t))z_i(t) [\kappa_i(t)]^{\alpha-1} \rangle dt \quad (\text{A.18})$$

$$\langle \kappa_i(t + dt) \rangle = \langle \mathbb{E}[\kappa_i(t + dt) | t] \rangle \quad (\text{A.19})$$

$$= \langle \kappa_i(t) \rangle + \nu \langle (1 - n_i(t))z_i(t) \rangle dt, \quad (\text{A.20})$$

from where we find

$$\frac{d\langle n_i(t) \rangle}{dt} = \frac{\langle n_i(t + dt) \rangle - \langle n_i(t) \rangle}{dt} = \nu\alpha\mu^\alpha \langle (1 - n_i(t))z_i(t) [\kappa_i(t)]^{\alpha-1} \rangle \quad (\text{A.21})$$

$$\frac{d\langle \kappa_i(t) \rangle}{dt} = \frac{\langle \kappa_i(t + dt) \rangle - \langle \kappa_i(t) \rangle}{dt} = \nu \langle (1 - n_i(t))z_i(t) \rangle. \quad (\text{A.22})$$

### A.3 Dynamic equations of the miccSIS model with short-term memory

To obtain Eq. (4.26), the dynamic equation for the state of node  $i$ , we start from

$$n_i(t + dt) = n_i(t)(1 - \xi_i) + (1 - n_i(t))(1 - \delta_{z_i(t)}^0)\pi_i, \quad (\text{A.23})$$

with

$$\xi_i = \begin{cases} 1 & \eta dt \\ 0 & 1 - \eta dt \end{cases} \quad (\text{A.24})$$

$$\pi_i = \begin{cases} 1 & \omega_i(t) dt \\ 0 & 1 - \omega_i(t) dt \end{cases} \quad (\text{A.25})$$

and  $\omega_i(t) = \nu\alpha\mu^\alpha z_i(t) [\kappa_i(t)]^{\alpha-1}$ . First we compute the expectation value conditioned on time  $t$ , which only affects the stochastic variables  $\xi_i$  and  $\pi_i$

$$x_1 = \mathbb{E}[n_i(t + dt) | t] \quad (\text{A.26})$$

$$= n_i(t) \mathbb{E}[1 - \xi_i | t] + (1 - n_i(t))(1 - \delta_{z_i(t)}^0) \mathbb{E}[\pi_i | t] \quad (\text{A.27})$$

$$= n_i(t)(1 - \eta dt) + (1 - n_i(t))(1 - \delta_{z_i(t)}^0)\omega_i(t) dt \quad (\text{A.28})$$

$$= n_i(t) - n_i(t)\eta dt + \nu\alpha\mu^\alpha(1 - n_i(t))z_i(t) [\kappa_i(t)]^{\alpha-1} dt. \quad (\text{A.29})$$

Note that the delta term cancels since  $\delta_{z_i(t)}^0 z_i(t) = 0$ . Taking the ensemble average yields

$$\langle n_i(t + dt) \rangle = \langle \mathbb{E}[n_i(t + dt) | t] \rangle \quad (\text{A.30})$$

$$= \langle x_1 \rangle \quad (\text{A.31})$$

$$= \langle n_i(t) \rangle - \eta \langle n_i(t) \rangle dt + \nu\alpha\mu^\alpha \langle (1 - n_i(t))z_i(t) [\kappa_i(t)]^{\alpha-1} \rangle dt, \quad (\text{A.32})$$

from where we find

$$\frac{d\langle n_i(t) \rangle}{dt} = \frac{\langle n_i(t + dt) \rangle - \langle n_i(t) \rangle}{dt} \quad (\text{A.33})$$

$$= -\eta \langle n_i(t) \rangle + \nu\alpha\mu^\alpha \langle (1 - n_i(t))z_i(t) [\kappa_i(t)]^{\alpha-1} \rangle. \quad (\text{A.34})$$

To obtain Eq. (4.27), the dynamic equation for the viral load of node  $i$ , we start from

$$\begin{aligned} \kappa_i(t + dt) = & \kappa_i(t) - \kappa_i(t)n_i(t)\xi_i - \kappa_i(t)(1 - n_i(t))(1 - \delta_{z_i(t)}^0)(1 - \pi_i)\chi_i \\ & + (1 - n_i(t))(1 - \delta_{z_i(t)}^0)(1 - \pi_i)(1 - \chi_i)\nu z_i(t)dt . \end{aligned} \quad (\text{A.35})$$

with  $\xi_i$  and  $\pi_i$  given, respectively, by Eqs. (A.24) and (A.25), and

$$\chi_i = \begin{cases} 1 & \delta_{z_i(t)}^1 \eta dt \\ 0 & 1 - \delta_{z_i(t)}^1 \eta dt \end{cases} . \quad (\text{A.36})$$

First we compute the expectation value conditioned on time  $t$ , which only affects the stochastic variables

$$x_2 = \mathbb{E}[\kappa_i(t + dt) | t] \quad (\text{A.37})$$

$$\begin{aligned} &= \kappa_i(t) - \kappa_i(t)n_i(t) \mathbb{E}[\xi_i | t] \\ &\quad - \kappa_i(t)(1 - n_i(t))(1 - \delta_{z_i(t)}^0) \mathbb{E}[1 - \pi_i | t] \mathbb{E}[\chi_i | t] \\ &\quad + (1 - n_i(t))(1 - \delta_{z_i(t)}^0) \mathbb{E}[1 - \pi_i | t] \mathbb{E}[1 - \chi_i | t] \nu z_i(t)dt \end{aligned} \quad (\text{A.38})$$

$$\begin{aligned} &= \kappa_i(t) - \kappa_i(t)n_i(t)\eta dt \\ &\quad - \kappa_i(t)(1 - n_i(t))(1 - \delta_{z_i(t)}^0)(1 - \omega_i(t)dt)\delta_{z_i(t)}^1 \eta dt \\ &\quad + (1 - n_i(t))(1 - \delta_{z_i(t)}^0)(1 - \omega_i(t)dt)(1 - \delta_{z_i(t)}^1 \eta dt)\nu z_i(t)dt \end{aligned} \quad (\text{A.39})$$

$$\begin{aligned} &= \kappa_i(t) - \kappa_i(t)n_i(t)\eta dt + (1 - n_i(t))(1 - \delta_{z_i(t)}^0)\nu z_i(t)dt \\ &\quad - \kappa_i(t)(1 - n_i(t))(1 - \delta_{z_i(t)}^0)\delta_{z_i(t)}^1 \eta dt + \mathcal{O}(dt)^2 \end{aligned} \quad (\text{A.40})$$

$$\begin{aligned} &= \kappa_i(t) - \kappa_i(t)n_i(t)\eta dt + (1 - n_i(t))\nu z_i(t)dt \\ &\quad - \kappa_i(t)(1 - n_i(t))\delta_{z_i(t)}^1 \eta dt + \mathcal{O}(dt)^2 . \end{aligned} \quad (\text{A.41})$$

Next we take the ensemble average up to  $\mathcal{O}(dt)$

$$\langle \kappa_i(t + dt) \rangle = \langle \mathbb{E}[\kappa_i(t + dt) | t] \rangle \quad (\text{A.42})$$

$$= \langle x_2 \rangle \quad (\text{A.43})$$

$$\begin{aligned} &= \langle \kappa_i(t) \rangle - \eta \langle \kappa_i(t)n_i(t) \rangle dt + \nu \langle (1 - n_i(t))z_i(t) \rangle dt \\ &\quad - \eta \langle \kappa_i(t)(1 - n_i(t))\delta_{z_i(t)}^1 \rangle dt , \end{aligned} \quad (\text{A.44})$$

from where we find

$$\frac{d\langle \kappa_i(t) \rangle}{dt} = \frac{\langle \kappa_i(t + dt) \rangle - \langle \kappa_i(t) \rangle}{dt} \quad (\text{A.45})$$

$$= -\eta \langle \kappa_i(t)n_i(t) \rangle - \eta \langle \kappa_i(t)(1 - n_i(t))\delta_{z_i(t)}^1 \rangle + \nu \langle (1 - n_i(t))z_i(t) \rangle . \quad (\text{A.46})$$

Finally, in order to obtain Eq. (4.28), the dynamic equation for  $\kappa_i^\gamma(t)$ , we start from

$$\begin{aligned} \kappa_i^\gamma(t + dt) = & \left[ \kappa_i(t) - \kappa_i(t)n_i(t)\xi_i - \kappa_i(t)(1 - n_i(t))(1 - \delta_{z_i(t)}^0)(1 - \pi_i)\chi_i \right. \\ & \left. + (1 - n_i(t))(1 - \delta_{z_i(t)}^0)(1 - \pi_i)(1 - \chi_i)v_{z_i}(t)dt \right]^\gamma. \end{aligned} \quad (\text{A.47})$$

In this case, the computation of the expectation value conditioned on time  $t$  is a little more involved and is given by the generic expression

$$\begin{aligned} x_3 = & \mathbb{E}[\kappa_i^\gamma(t + dt) | t] \quad (\text{A.48}) \\ = & \Pr(\xi_i = 0, \pi_i = 0, \chi_i = 0) \times \kappa_i^\gamma(t + dt; \xi_i = 0, \pi_i = 0, \chi_i = 0) \\ & + \Pr(\xi_i = 0, \pi_i = 0, \chi_i = 1) \times \kappa_i^\gamma(t + dt; \xi_i = 0, \pi_i = 0, \chi_i = 1) \\ & + \Pr(\xi_i = 0, \pi_i = 1, \chi_i = 0) \times \kappa_i^\gamma(t + dt; \xi_i = 0, \pi_i = 1, \chi_i = 0) \\ & + \Pr(\xi_i = 1, \pi_i = 0, \chi_i = 0) \times \kappa_i^\gamma(t + dt; \xi_i = 1, \pi_i = 0, \chi_i = 0) \\ & + \mathcal{O}(dt)^2. \end{aligned} \quad (\text{A.49})$$

Computing the necessary terms

$$\Pr(\xi_i = 0, \pi_i = 0, \chi_i = 0) = 1 - (\eta + \omega_i(t) + \delta_{z_i(t)}^1 \eta)dt + \mathcal{O}(dt)^2 \quad (\text{A.50})$$

$$\Pr(\xi_i = 0, \pi_i = 0, \chi_i = 1) = \delta_{z_i(t)}^1 \eta dt + \mathcal{O}(dt)^2 \quad (\text{A.51})$$

$$\Pr(\xi_i = 0, \pi_i = 1, \chi_i = 0) = \omega_i(t)dt + \mathcal{O}(dt)^2 \quad (\text{A.52})$$

$$\Pr(\xi_i = 1, \pi_i = 0, \chi_i = 0) = \eta dt + \mathcal{O}(dt)^2 \quad (\text{A.53})$$

$$x_4 = \kappa_i^\gamma(t + dt; \xi_i = 0, \pi_i = 0, \chi_i = 0) \quad (\text{A.54})$$

$$= \left[ \kappa_i(t) + (1 - n_i(t))(1 - \delta_{z_i(t)}^0)v_{z_i}(t)dt \right]^\gamma \quad (\text{A.55})$$

$$= [\kappa_i(t) + (1 - n_i(t))v_{z_i}(t)dt]^\gamma \quad (\text{A.56})$$

$$= \kappa_i^\gamma(t) \left[ 1 + \frac{(1 - n_i(t))v_{z_i}(t)dt}{\kappa_i(t)} \right]^\gamma \quad (\text{A.57})$$

$$= \kappa_i^\gamma(t) \left[ 1 + \frac{\gamma(1 - n_i(t))v_{z_i}(t)dt}{\kappa_i(t)} \right] + \mathcal{O}(dt)^2 \quad (\text{A.58})$$

$$x_5 = \kappa_i^\gamma(t + dt; \xi_i = 0, \pi_i = 0, \chi_i = 1) \quad (\text{A.59})$$

$$= \left[ \kappa_i(t) - \kappa_i(t)(1 - n_i(t))(1 - \delta_{z_i(t)}^0) \right]^\gamma \quad (\text{A.60})$$

$$= \kappa_i^\gamma(t) \left[ 1 - (1 - n_i(t))(1 - \delta_{z_i(t)}^0) \right]^\gamma \quad (\text{A.61})$$

$$= \kappa_i^\gamma(t) \left[ 1 - (1 - n_i(t))(1 - \delta_{z_i(t)}^0) \right] \quad (\text{A.62})$$

$$x_6 = \kappa_i^\gamma(t + dt; \xi_i = 0, \pi_i = 1, \chi_i = 0) \quad (\text{A.63})$$

$$= \kappa_i^\gamma(t) \quad (\text{A.64})$$

$$x_7 = \kappa_i^\gamma(t + dt; \xi_i = 1, \pi_i = 0, \chi_i = 0) \quad (\text{A.65})$$

$$= \left[ \kappa_i(t) - \kappa_i(t)n_i(t) + (1 - n_i(t))(1 - \delta_{z_i(t)}^0)\nu_{z_i}(t)dt \right]^\gamma \quad (\text{A.66})$$

$$= [\kappa_i(t)(1 - n_i(t)) + (1 - n_i(t))\nu_{z_i}(t)dt]^\gamma \quad (\text{A.67})$$

$$= (1 - n_i(t))^\gamma [\kappa_i(t) + \nu_{z_i}(t)dt]^\gamma \quad (\text{A.68})$$

$$= (1 - n_i(t))\kappa_i^\gamma(t) \left[ 1 + \frac{\nu_{z_i}(t)dt}{\kappa_i(t)} \right]^\gamma \quad (\text{A.69})$$

$$= (1 - n_i(t))\kappa_i^\gamma(t) \left[ 1 + \frac{\gamma\nu_{z_i}(t)dt}{\kappa_i(t)} \right] + \mathcal{O}(dt)^2 \quad (\text{A.70})$$

and substituting in Eq. (A.49) yields

$$\begin{aligned} x_3 &= x_4 \times \Pr(\xi_i = 0, \pi_i = 0, \chi_i = 0) + x_5 \times \Pr(\xi_i = 0, \pi_i = 0, \chi_i = 1) \\ &\quad + x_6 \times \Pr(\xi_i = 0, \pi_i = 1, \chi_i = 0) + x_7 \times \Pr(\xi_i = 1, \pi_i = 0, \chi_i = 0) \\ &\quad + \mathcal{O}(dt)^2 \end{aligned} \quad (\text{A.71})$$

$$\begin{aligned} &= \left[ 1 - (\eta + \omega_i(t) + \delta_{z_i(t)}^1\eta)dt \right] \kappa_i^\gamma(t) \left[ 1 + \frac{\gamma(1 - n_i(t))\nu_{z_i}(t)dt}{\kappa_i(t)} \right] \\ &\quad + (\delta_{z_i(t)}^1\eta dt)\kappa_i^\gamma(t) \left[ 1 - (1 - n_i(t))(1 - \delta_{z_i(t)}^0) \right] + (\omega_i(t)dt)\kappa_i^\gamma(t) \\ &\quad + (\eta dt)(1 - n_i(t))\kappa_i^\gamma(t) \left[ 1 + \frac{\gamma\nu_{z_i}(t)dt}{\kappa_i(t)} \right] + \mathcal{O}(dt)^2 \end{aligned} \quad (\text{A.72})$$

$$\begin{aligned} &= \kappa_i^\gamma(t) \left[ 1 - (\eta + \omega_i(t) + \delta_{z_i(t)}^1\eta)dt + \frac{\gamma(1 - n_i(t))\nu_{z_i}(t)dt}{\kappa_i(t)} \right] \\ &\quad + \left[ \delta_{z_i(t)}^1\eta(1 - (1 - n_i(t))) + \omega_i(t) + \eta(1 - n_i(t)) \right] \kappa_i^\gamma(t)dt \\ &\quad + \mathcal{O}(dt)^2 \end{aligned} \quad (\text{A.73})$$

$$\begin{aligned} &= \kappa_i^\gamma(t) - \eta\kappa_i^\gamma(t)n_i(t)dt - \eta\kappa_i^\gamma(t)(1 - n_i(t))\delta_{z_i(t)}^1dt \\ &\quad + \gamma\nu(1 - n_i(t))z_i(t)[\kappa_i(t)]^{\gamma-1}dt + \mathcal{O}(dt)^2 . \end{aligned} \quad (\text{A.74})$$

Then we take the ensemble average up to  $O(dt)$

$$\langle \kappa_i^\gamma(t+dt) \rangle = \langle \mathbb{E}[\kappa_i^\gamma(t+dt) | t] \rangle \quad (\text{A.75})$$

$$= \langle x_3 \rangle \quad (\text{A.76})$$

$$= \langle \kappa_i^\gamma(t) \rangle - \eta \langle \kappa_i^\gamma(t) n_i(t) \rangle dt - \eta \langle \kappa_i^\gamma(t) (1 - n_i(t)) \delta_{z_i(t)}^1 \rangle dt + \gamma \nu \langle (1 - n_i(t)) z_i(t) [\kappa_i(t)]^{\gamma-1} \rangle dt \quad (\text{A.77})$$

and finally find

$$\frac{d\langle \kappa_i^\gamma(t) \rangle}{dt} = \frac{\langle \kappa_i^\gamma(t+dt) \rangle - \langle \kappa_i^\gamma(t) \rangle}{dt} \quad (\text{A.78})$$

$$= -\eta \langle \kappa_i^\gamma(t) n_i(t) \rangle - \eta \langle \kappa_i^\gamma(t) (1 - n_i(t)) \delta_{z_i(t)}^1 \rangle + \gamma \nu \langle (1 - n_i(t)) z_i(t) [\kappa_i(t)]^{\gamma-1} \rangle. \quad (\text{A.79})$$

## A.4 Mean-field parameters of the miccSIS model with short-term memory

In order to obtain the coefficient  $A$  in Eq. (4.38) we need to compute the moments  $\langle \kappa_i^\gamma | n_i = 1 \rangle$  for  $\gamma = 1$  and  $\gamma = \alpha$ . These moments are conditioned on  $n_i = 1$ , i.e., node  $i$  being infected. Since the viral load does not change while infected, measuring  $\kappa_i$  of infected node  $i$  yields the same results as measuring  $\kappa_i$  at the moment  $i$  became infected. Within the mean-field approximation, these quantities are the same for all nodes, hence we drop the  $i$  index. We denote the required density by  $\phi(\kappa)$ , i.e., the probability that a node had amassed  $\kappa$  viral load at the moment it became infected.

The difference between  $\phi(\kappa)$  and the infection probability,  $\psi^*(\kappa)$ , is subtle but crucial in the case of short-term memory. Recall that with  $\zeta = 0$  a susceptible node instantly erases its viral load when it becomes dormant. Thus reaching a viral load of  $\kappa$  is conditioned on being continuously exposed to the pathogen. Simply put,  $\psi^*(\kappa)$  measures the probability of becoming infected when the accumulated viral load is  $\kappa$ , while  $\phi(\kappa)$  measures the probability that the viral load is  $\kappa$  at infection. The latter is equivalent to the probability of reaching an accumulated viral load of  $\kappa$  and then becoming infected.

When  $\rho \approx 0$  we can assume that susceptible node  $i$  has only one infected neighbor  $j$ ; moreover,  $i$  transitioned from dormant to susceptible at the same time that  $j$  became infected. Thus node  $i$  is exposed to a single source of

pathogen, and the time since  $j$  became infected ( $t$ ) and the viral load accumulated by  $i$  ( $\kappa$ ) are proportional ( $\kappa = \nu t$ ). Then  $\phi(\kappa)$  is the probability of  $i$  becoming infected when its viral load is  $\kappa$  ( $\psi_{\text{inf}}^*(\kappa)$ ) times the probability that  $j$  does not recover before  $t$  ( $\Psi_{\text{rec}}(t)$ ). Expressed in terms of  $\kappa$  this is

$$\phi(\kappa) = N^{-1} \psi_{\text{inf}}^*(\kappa) \Psi_{\text{rec}}(\nu^{-1} \kappa) = N^{-1} \alpha \mu^\alpha \kappa^{\alpha-1} e^{-(\mu\kappa)^\alpha} e^{-\eta\nu^{-1}\kappa}, \quad (\text{A.80})$$

with

$$N = \int_0^\infty \psi_{\text{inf}}^*(\kappa) \Psi_{\text{rec}}(\nu^{-1} \kappa) d\kappa. \quad (\text{A.81})$$

Defining the integral

$$I(x) = \int_0^\infty \kappa^x e^{-(\mu\kappa)^\alpha} e^{-\eta\nu^{-1}\kappa} d\kappa, \quad (\text{A.82})$$

the corresponding moments are

$$\langle \kappa^\gamma \mid n = 1 \rangle = \int_0^\infty \kappa^\gamma \phi(\kappa) d\kappa \quad (\text{A.83})$$

$$= \frac{I(\gamma + \alpha - 1)}{I(\alpha - 1)}. \quad (\text{A.84})$$

We proceed in a similar way for the moments  $\langle \kappa_i^\gamma \mid X_i = 1 \rangle$ , required to obtain coefficient  $B$  in Eq. (4.39). Now we are sampling the state of a node that is susceptible and has only one infected neighbor. For  $\rho \approx 0$  we assume the same scenario as before: since becoming susceptible, node  $i$  has been exposed continuously to a single infected neighbor  $j$ . Node  $i$  transitions to state  $X_i = 0$  either when  $j$  recovers or when  $i$  becomes infected itself. This event occurs when  $i$  has accumulated  $\kappa$  units of viral load with probability density

$$\varphi(\kappa) = N^{-1} \left[ \nu^{-1} \psi_{\text{rec}}(\nu^{-1} \kappa) \Psi_{\text{inf}}^*(\kappa) + \psi_{\text{inf}}^*(\kappa) \Psi_{\text{rec}}(\kappa) \right] \quad (\text{A.85})$$

$$= N^{-1} \left[ \eta\nu^{-1} + \alpha\mu^\alpha \kappa^{\alpha-1} \right] e^{-(\mu\kappa)^\alpha} e^{-\eta\nu^{-1}\kappa}, \quad (\text{A.86})$$

with

$$N = \int_0^\infty \left[ \nu^{-1} \psi_{\text{rec}}(\nu^{-1} \kappa) \Psi_{\text{inf}}^*(\kappa) + \psi_{\text{inf}}^*(\kappa) \Psi_{\text{rec}}(\kappa) \right] d\kappa. \quad (\text{A.87})$$

Note that the first term corresponds to node  $j$  recovering ( $\nu^{-1}\psi_{\text{rec}}(\nu^{-1}\kappa)$ ) and node  $i$  not becoming infected ( $\Psi_{\text{inf}}^*(\kappa)$ ), while the second term describes  $i$  becoming infected ( $\psi_{\text{inf}}^*(\kappa)$ ) and  $j$  not recovering ( $\Psi_{\text{rec}}(\nu^{-1}\kappa)$ ). Recall also that the viral load accumulated by node  $i$  is proportional to the time since node  $j$  became infected ( $\kappa = \nu t$ ).

Then the probability density to sample node  $i$  in state  $X_i = 1$  with a viral load of  $\kappa$  is [48]

$$\phi(\kappa) = \frac{\Phi(\kappa)}{\langle \kappa \rangle_\varphi}, \quad (\text{A.88})$$

with

$$\Phi(\kappa) = \int_\kappa^\infty \varphi(\kappa) d\kappa = N^{-1} \int_\kappa^\infty [\eta\nu^{-1} + \alpha\mu^\alpha s^{\alpha-1}] e^{-(\mu s)^\alpha} e^{-\eta\nu^{-1}s} ds \quad (\text{A.89})$$

$$\langle \kappa \rangle_\varphi = \int_0^\infty \kappa \varphi(\kappa) d\kappa = N^{-1} \int_0^\infty [\eta\nu^{-1}\kappa + \alpha\mu^\alpha \kappa^\alpha] e^{-(\mu\kappa)^\alpha} e^{-\eta\nu^{-1}\kappa} d\kappa. \quad (\text{A.90})$$

Defining the integrals

$$J_1(\kappa) = \int_\kappa^\infty [\alpha\mu^\alpha s^{\alpha-1} + \eta\nu^{-1}] e^{-(\mu s)^\alpha} e^{-\eta\nu^{-1}s} ds \quad (\text{A.91})$$

$$J_2 = \int_0^\infty [\alpha\mu^\alpha \kappa^\alpha + \eta\nu^{-1}\kappa] e^{-(\mu\kappa)^\alpha} e^{-\eta\nu^{-1}\kappa} d\kappa, \quad (\text{A.92})$$

the corresponding moments are

$$\langle \kappa^\gamma | X = 1 \rangle = \int_0^\infty \kappa^\gamma \phi(\kappa) d\kappa \quad (\text{A.93})$$

$$= \frac{1}{J_2} \int_0^\infty \kappa^\gamma J_1(\kappa) d\kappa. \quad (\text{A.94})$$

The numerical evaluation of the parameters is detailed in Appendix C.4.

## A.5 Dynamic equations of the miccSIS model with long-term memory

To obtain Eq. (4.53), the dynamic equation for the viral load of node  $i$ , we start from

$$\begin{aligned} \kappa_i(t + dt) = & \kappa_i(t) - \kappa_i(t)n_i(t)\xi_i \\ & + (1 - n_i(t))(1 - \delta_{z_i(t)}^0)(1 - \pi_i)(1 - \chi_i)vz_i(t)dt . \end{aligned} \quad (\text{A.95})$$

with  $\xi_i$ ,  $\pi_i$ , and  $\chi_i$  given, respectively, by Eqs. (A.24), (A.25), and (A.36). This equation is very similar to the corresponding equation for the miccSIS model with short-term memory, Eq. (A.35). The only difference is that here we have dropped the term corresponding to a susceptible node becoming dormant and instantly erasing its viral load. Following the derivation of the previous section we find the expectation value conditioned on time  $t$

$$\mathbb{E}[\kappa_i(t + dt) | t] = \kappa_i(t) - \kappa_i(t)n_i(t)\eta dt + (1 - n_i(t))vz_i(t)dt + \mathcal{O}(dt)^2 , \quad (\text{A.96})$$

the ensemble average up to  $\mathcal{O}(dt)$

$$\langle \kappa_i(t + dt) \rangle = \langle \mathbb{E}[\kappa_i(t + dt) | t] \rangle \quad (\text{A.97})$$

$$= \langle \kappa_i(t) \rangle - \eta \langle \kappa_i(t)n_i(t) \rangle dt + v \langle (1 - n_i(t))z_i(t) \rangle dt , \quad (\text{A.98})$$

and, finally, the dynamic equation

$$\frac{d\langle \kappa_i(t) \rangle}{dt} = \frac{\langle \kappa_i(t + dt) \rangle - \langle \kappa_i(t) \rangle}{dt} \quad (\text{A.99})$$

$$= -\eta \langle \kappa_i(t)n_i(t) \rangle + v \langle (1 - n_i(t))z_i(t) \rangle . \quad (\text{A.100})$$

The derivation of the dynamic equation for the state of node  $i$  is identical to the procedure in Appendix A.3, which yields

$$\frac{d\langle n_i(t) \rangle}{dt} = -\eta \langle n_i(t) \rangle + v\alpha\mu^\alpha \langle (1 - n_i(t))z_i(t) [\kappa_i(t)]^{\alpha-1} \rangle . \quad (\text{A.101})$$

On the other hand, to obtain the dynamic equation for  $\langle \kappa_i^\gamma(t) \rangle$  we start from

$$\begin{aligned} \kappa_i^\gamma(t + dt) = & \left[ \kappa_i(t) - \kappa_i(t)n_i(t)\xi_i \right. \\ & \left. + (1 - n_i(t))(1 - \delta_{z_i(t)}^0)(1 - \pi_i)(1 - \chi_i)vz_i(t)dt \right]^\gamma . \end{aligned} \quad (\text{A.102})$$

We use Eq. (A.49) to compute the expectation value conditioned on time  $t$ . All the terms are identical as in Appendix A.3 except for

$$x_5 = \kappa_i^\gamma(t + dt; \xi_i = 0, \pi_i = 0, \chi_i = 1) \quad (\text{A.103})$$

$$= \kappa_i^\gamma(t), \quad (\text{A.104})$$

thus

$$\begin{aligned} \mathbb{E}[\kappa_i^\gamma(t + dt) | t] &= \kappa_i^\gamma(t) - \eta \kappa_i^\gamma(t) n_i(t) dt \\ &\quad + \gamma \nu (1 - n_i(t)) z_i(t) [\kappa_i(t)]^{\gamma-1} dt + \mathcal{O}(dt)^2. \end{aligned} \quad (\text{A.105})$$

Finally, we take the ensemble average up to  $\mathcal{O}(dt)$

$$\langle \kappa_i^\gamma(t + dt) \rangle = \langle \mathbb{E}[\kappa_i^\gamma(t + dt) | t] \rangle \quad (\text{A.106})$$

$$\begin{aligned} &= \langle \kappa_i^\gamma(t) \rangle - \eta \langle \kappa_i^\gamma(t) n_i(t) \rangle dt \\ &\quad + \gamma \nu \langle (1 - n_i(t)) z_i(t) [\kappa_i(t)]^{\gamma-1} \rangle dt, \end{aligned} \quad (\text{A.107})$$

and find the dynamic equation

$$\frac{d\langle \kappa_i^\gamma(t) \rangle}{dt} = \frac{\langle \kappa_i^\gamma(t + dt) \rangle - \langle \kappa_i^\gamma(t) \rangle}{dt} \quad (\text{A.108})$$

$$= -\eta \langle \kappa_i^\gamma(t) n_i(t) \rangle + \gamma \nu \langle (1 - n_i(t)) z_i(t) [\kappa_i(t)]^{\gamma-1} \rangle. \quad (\text{A.109})$$

Taking the late-time limit in Eqs. (A.101) and (A.109), dropping the dependence with  $t$ , and setting  $\gamma = \alpha$  gives

$$0 = -\eta \langle n_i \rangle + \nu \alpha \mu^\alpha \langle (1 - n_i) z_i \kappa_i^{\alpha-1} \rangle \quad (\text{A.110})$$

$$0 = -\eta \langle \kappa_i^\alpha n_i \rangle + \alpha \nu \langle (1 - n_i) z_i \kappa_i^{\alpha-1} \rangle. \quad (\text{A.111})$$

Combining both equations and using the expansion

$$\langle \kappa_i^\alpha n_i \rangle = \langle \kappa_i^\alpha n_i | n_i = 1 \rangle \times \Pr(n_i = 1) + \langle \kappa_i^\alpha n_i | n_i = 0 \rangle \times \Pr(n_i = 0) \quad (\text{A.112})$$

$$= \langle \kappa_i^\alpha | n_i = 1 \rangle \langle n_i \rangle + 0 \times (1 - \langle n_i \rangle), \quad (\text{A.113})$$

yields

$$\langle \kappa_i^\alpha | n_i = 1 \rangle = \mu^{-\alpha}. \quad (\text{A.114})$$

This recovers the result of

$$\langle \kappa^\alpha \rangle_{\text{inf}} = \int_0^\infty \kappa^\alpha \psi^*(\kappa) d\kappa = \int_0^\infty \alpha \mu^\alpha \kappa^{2\alpha-1} e^{-(\mu\kappa)^\alpha} d\kappa = \mu^{-\alpha}, \quad (\text{A.115})$$

and validates the computation of  $\langle \kappa_i | n_i = 1 \rangle$  using  $\psi^*(\kappa)$  in Section 4.2.2. Notice that this is an exact result, obtained without implementing any approximation.

## A.6 Dynamic equations of the miccSIS model with medium-term memory

The stochastic processes that govern the dynamics are given by

$$\xi_i = \begin{cases} 1 & \eta dt \\ 0 & 1 - \eta dt \end{cases} \quad (\text{A.116})$$

$$\pi_i = \begin{cases} 1 & \omega_i(t) dt \\ 0 & 1 - \omega_i(t) dt \end{cases} \quad (\text{A.117})$$

$$\chi_i = \begin{cases} 1 & \delta_{z_i(t)}^1 \eta dt \\ 0 & 1 - \delta_{z_i(t)}^1 \eta dt \end{cases} \quad (\text{A.118})$$

$$s_i = \begin{cases} 1 & \varepsilon_i(t) dt \\ 0 & 1 - \varepsilon_i(t) dt \end{cases}, \quad (\text{A.119})$$

with  $\omega_i(t) = \nu \alpha \mu^\alpha z_i(t) [\kappa_i(t)]^{\alpha-1}$  and  $\varepsilon_i(t)$  a generic function of time. The derivation of Eq. (4.64), the dynamic equation for the state of node  $i$ , is identical to the procedure in Appendix A.3. To obtain Eq. (4.65), the dynamic equation for the viral load of node  $i$ , we start from

$$\begin{aligned} \kappa_i(t + dt) = & \kappa_i(t) - \kappa_i(t) n_i(t) \xi_i - \kappa_i(t) (1 - n_i(t)) \delta_{z_i(t)}^0 (1 - s_i) \zeta^{-1} dt \\ & + (1 - n_i(t)) (1 - \delta_{z_i(t)}^0) (1 - \pi_i) (1 - \chi_i) \nu z_i(t) dt. \end{aligned} \quad (\text{A.120})$$

First we compute the expectation value conditioned on time  $t$ , which only affects the stochastic variables

$$x_1 = \mathbb{E}[\kappa_i(t + dt) | t] \quad (\text{A.121})$$

$$\begin{aligned} &= \kappa_i(t) - \kappa_i(t)n_i(t) \mathbb{E}[\xi_i | t] \\ &\quad - \kappa_i(t)(1 - n_i(t))\delta_{z_i(t)}^0 \mathbb{E}[1 - \varsigma_i | t]\zeta^{-1} dt \\ &\quad + (1 - n_i(t))(1 - \delta_{z_i(t)}^0) \mathbb{E}[1 - \pi_i | t] \mathbb{E}[1 - \chi_i | t] \nu z_i(t) dt \end{aligned} \quad (\text{A.122})$$

$$\begin{aligned} &= \kappa_i(t) - \kappa_i(t)n_i(t)\eta dt \\ &\quad - \kappa_i(t)(1 - n_i(t))\delta_{z_i(t)}^0 (1 - \varepsilon_i(t)dt)\zeta^{-1} dt \\ &\quad + (1 - n_i(t))(1 - \delta_{z_i(t)}^0)(1 - \omega_i(t)dt)(1 - \delta_{z_i(t)}^1 \eta dt) \nu z_i(t) dt \end{aligned} \quad (\text{A.123})$$

$$\begin{aligned} &= \kappa_i(t) - \kappa_i(t)n_i(t)\eta dt + (1 - n_i(t))(1 - \delta_{z_i(t)}^0) \nu z_i(t) dt \\ &\quad - \kappa_i(t)(1 - n_i(t))\delta_{z_i(t)}^0 \zeta^{-1} dt + \mathcal{O}(dt)^2 \end{aligned} \quad (\text{A.124})$$

$$\begin{aligned} &= \kappa_i(t) - \kappa_i(t)n_i(t)\eta dt + (1 - n_i(t)) \nu z_i(t) dt \\ &\quad - \kappa_i(t)(1 - n_i(t))\delta_{z_i(t)}^0 \zeta^{-1} dt + \mathcal{O}(dt)^2 . \end{aligned} \quad (\text{A.125})$$

Next we take the ensemble average up to  $\mathcal{O}(dt)$

$$\langle \kappa_i(t + dt) \rangle = \langle \mathbb{E}[\kappa_i(t + dt) | t] \rangle \quad (\text{A.126})$$

$$= \langle x_1 \rangle \quad (\text{A.127})$$

$$\begin{aligned} &= \langle \kappa_i(t) \rangle - \eta \langle \kappa_i(t)n_i(t) \rangle dt + \nu \langle (1 - n_i(t))z_i(t) \rangle dt \\ &\quad - \zeta^{-1} \langle \kappa_i(t)(1 - n_i(t))\delta_{z_i(t)}^0 \rangle dt , \end{aligned} \quad (\text{A.128})$$

from where we find

$$\frac{d\langle \kappa_i(t) \rangle}{dt} = \frac{\langle \kappa_i(t + dt) \rangle - \langle \kappa_i(t) \rangle}{dt} \quad (\text{A.129})$$

$$= -\eta \langle \kappa_i(t)n_i(t) \rangle - \zeta^{-1} \langle \kappa_i(t)(1 - n_i(t))\delta_{z_i(t)}^0 \rangle + \nu \langle (1 - n_i(t))z_i(t) \rangle . \quad (\text{A.130})$$

Finally, in order to obtain Eq. (4.66), the dynamic equation for  $\kappa_i^\gamma(t)$ , we start from

$$\begin{aligned} \kappa_i^\gamma(t + dt) &= \left[ \kappa_i(t) - \kappa_i(t)n_i(t)\xi_i - \kappa_i(t)(1 - n_i(t))\delta_{z_i(t)}^0 (1 - \varsigma_i)\zeta^{-1} dt \right. \\ &\quad \left. + (1 - n_i(t))(1 - \delta_{z_i(t)}^0)(1 - \pi_i)(1 - \chi_i)\nu z_i(t) dt \right]^\gamma . \end{aligned} \quad (\text{A.131})$$

In this case, the computation of the expectation value conditioned on time  $t$  is a little more involved and is given by the generic expression

$$x_2 = \mathbb{E}[\kappa_i^\gamma(t + dt) | t] \quad (\text{A.132})$$

$$\begin{aligned} &= \Pr(\vec{u}_i = (0, 0, 0, 0)) \times \kappa_i^\gamma(t + dt; \vec{u}_i = (0, 0, 0, 0)) \\ &\quad + \Pr(\vec{u}_i = (0, 0, 0, 1)) \times \kappa_i^\gamma(t + dt; \vec{u}_i = (0, 0, 0, 1)) \\ &\quad + \Pr(\vec{u}_i = (0, 0, 1, 0)) \times \kappa_i^\gamma(t + dt; \vec{u}_i = (0, 0, 1, 0)) \\ &\quad + \Pr(\vec{u}_i = (0, 1, 0, 0)) \times \kappa_i^\gamma(t + dt; \vec{u}_i = (0, 1, 0, 0)) \\ &\quad + \Pr(\vec{u}_i = (1, 0, 0, 0)) \times \kappa_i^\gamma(t + dt; \vec{u}_i = (1, 0, 0, 0)) \\ &\quad + \mathcal{O}(dt)^2, \end{aligned} \quad (\text{A.133})$$

with  $\vec{u}_i = (\xi_i, \pi_i, \chi_i, \varsigma_i)$ . Computing the necessary terms

$$x_3 = \Pr(\xi_i = 0, \pi_i = 0, \chi_i = 0, \varsigma_i = 0) \quad (\text{A.134})$$

$$= 1 - (\eta + \omega_i(t) + \delta_{z_i(t)}^1 \eta + \varepsilon_i(t))dt + \mathcal{O}(dt)^2 \quad (\text{A.135})$$

$$x_4 = \Pr(\xi_i = 0, \pi_i = 0, \chi_i = 0, \varsigma_i = 1) \quad (\text{A.136})$$

$$= \varepsilon_i(t)dt + \mathcal{O}(dt)^2 \quad (\text{A.137})$$

$$x_5 = \Pr(\xi_i = 0, \pi_i = 0, \chi_i = 1, \varsigma_i = 0) \quad (\text{A.138})$$

$$= \delta_{z_i(t)}^1 \eta dt + \mathcal{O}(dt)^2 \quad (\text{A.139})$$

$$x_6 = \Pr(\xi_i = 0, \pi_i = 1, \chi_i = 0, \varsigma_i = 0) \quad (\text{A.140})$$

$$= \omega_i(t)dt + \mathcal{O}(dt)^2 \quad (\text{A.141})$$

$$x_7 = \Pr(\xi_i = 1, \pi_i = 0, \chi_i = 0, \varsigma_i = 0) \quad (\text{A.142})$$

$$= \eta dt + \mathcal{O}(dt)^2 \quad (\text{A.143})$$

$$x_8 = \kappa_i^\gamma(t + dt; \xi_i = 0, \pi_i = 0, \chi_i = 0, \varsigma_i = 0) \quad (\text{A.144})$$

$$= \left[ \kappa_i(t) + (1 - n_i(t))(1 - \delta_{z_i(t)}^0) \nu z_i(t) dt - \kappa_i(t)(1 - n_i(t)) \delta_{z_i(t)}^0 \zeta^{-1} dt \right]^\gamma \quad (\text{A.145})$$

$$= \left[ \kappa_i(t) + (1 - n_i(t)) \nu z_i(t) dt - \kappa_i(t)(1 - n_i(t)) \delta_{z_i(t)}^0 \zeta^{-1} dt \right]^\gamma \quad (\text{A.146})$$

$$= \kappa_i^\gamma(t) \left[ 1 + (1 - n_i(t)) \left( \frac{\nu z_i(t)}{\kappa_i(t)} - \delta_{z_i(t)}^0 \zeta^{-1} \right) dt \right]^\gamma \quad (\text{A.147})$$

$$= \kappa_i^\gamma(t) \left[ 1 + \gamma(1 - n_i(t)) \left( \frac{\nu z_i(t)}{\kappa_i(t)} - \delta_{z_i(t)}^0 \zeta^{-1} \right) dt \right] + \mathcal{O}(dt)^2 \quad (\text{A.148})$$

$$x_9 = \kappa_i^\gamma(t + dt; \xi_i = 0, \pi_i = 0, \chi_i = 0, \varsigma_i = 1) \quad (\text{A.149})$$

$$= \left[ \kappa_i(t) + (1 - n_i(t))(1 - \delta_{z_i(t)}^0) \nu z_i(t) dt \right]^\gamma \quad (\text{A.150})$$

$$= [\kappa_i(t) + (1 - n_i(t)) \nu z_i(t) dt]^\gamma \quad (\text{A.151})$$

$$= \kappa_i^\gamma(t) \left[ 1 + \frac{(1 - n_i(t)) \nu z_i(t) dt}{\kappa_i(t)} \right]^\gamma \quad (\text{A.152})$$

$$= \kappa_i^\gamma(t) \left[ 1 + \frac{\gamma(1 - n_i(t)) \nu z_i(t) dt}{\kappa_i(t)} \right] + \mathcal{O}(dt)^2 \quad (\text{A.153})$$

$$x_{10} = \kappa_i^\gamma(t + dt; \xi_i = 0, \pi_i = 0, \chi_i = 1, \varsigma_i = 0) \quad (\text{A.154})$$

$$= \left[ \kappa_i(t) - \kappa_i(t)(1 - n_i(t)) \delta_{z_i(t)}^0 \zeta^{-1} dt \right]^\gamma \quad (\text{A.155})$$

$$= \kappa_i^\gamma(t) \left[ 1 - (1 - n_i(t)) \delta_{z_i(t)}^0 \zeta^{-1} dt \right]^\gamma \quad (\text{A.156})$$

$$= \kappa_i^\gamma(t) \left[ 1 - \gamma(1 - n_i(t)) \delta_{z_i(t)}^0 \zeta^{-1} dt \right] + \mathcal{O}(dt)^2 \quad (\text{A.157})$$

$$x_{11} = \kappa_i^\gamma(t + dt; \xi_i = 0, \pi_i = 1, \chi_i = 0, \varsigma_i = 0) \quad (\text{A.158})$$

$$= \left[ \kappa_i(t) - \kappa_i(t)(1 - n_i(t)) \delta_{z_i(t)}^0 \zeta^{-1} dt \right]^\gamma \quad (\text{A.159})$$

$$= x_{10} \quad (\text{A.160})$$

$$x_{12} = \kappa_i^\gamma(t + dt; \xi_i = 1, \pi_i = 0, \chi_i = 0, \varsigma_i = 0) \quad (\text{A.161})$$

$$= \left[ \kappa_i(t) - \kappa_i(t)n_i(t) + (1 - n_i(t))(1 - \delta_{z_i(t)}^0) \nu z_i(t) dt - \kappa_i(t)(1 - n_i(t)) \delta_{z_i(t)}^0 \zeta^{-1} dt \right]^\gamma \quad (\text{A.162})$$

$$= \left[ \kappa_i(t)(1 - n_i(t)) + (1 - n_i(t))(\nu z_i(t) - \kappa_i(t) \delta_{z_i(t)}^0 \zeta^{-1}) dt \right]^\gamma \quad (\text{A.163})$$

$$= (1 - n_i(t))^\gamma \left[ \kappa_i(t) + (\nu z_i(t) - \kappa_i(t) \delta_{z_i(t)}^0 \zeta^{-1}) dt \right]^\gamma \quad (\text{A.164})$$

$$= (1 - n_i(t)) \kappa_i^\gamma(t) \left[ 1 + \left( \frac{\nu z_i(t)}{\kappa_i(t)} - \delta_{z_i(t)}^0 \zeta^{-1} \right) dt \right]^\gamma \quad (\text{A.165})$$

$$= (1 - n_i(t)) \kappa_i^\gamma(t) \left[ 1 + \gamma \left( \frac{\nu z_i(t)}{\kappa_i(t)} - \delta_{z_i(t)}^0 \zeta^{-1} \right) dt \right] + \mathcal{O}(dt)^2 \quad (\text{A.166})$$

and substituting in Eq. (A.133) yields

$$x_2 = x_3 x_8 + x_4 x_9 + x_5 x_{10} + x_6 x_{11} + x_7 x_{12} + \mathcal{O}(dt)^2 \quad (\text{A.167})$$

$$\begin{aligned} &= \left[ 1 - (\eta + \omega_i(t) + \delta_{z_i(t)}^1 \eta + \varepsilon_i(t)) dt \right] \\ &\quad \times \kappa_i^\gamma(t) \left[ 1 + \gamma(1 - n_i(t)) \left( \frac{\nu z_i(t)}{\kappa_i(t)} - \delta_{z_i(t)}^0 \zeta^{-1} \right) dt \right] \\ &\quad + (\varepsilon_i(t) dt) \kappa_i^\gamma(t) \left[ 1 + \frac{\gamma(1 - n_i(t)) \nu z_i(t) dt}{\kappa_i(t)} \right] \\ &\quad + \left[ (\delta_{z_i(t)}^1 \eta + \omega_i(t)) dt \right] \kappa_i^\gamma(t) \left[ 1 - \gamma(1 - n_i(t)) \delta_{z_i(t)}^0 \zeta^{-1} dt \right] \\ &\quad + (\eta dt)(1 - n_i(t)) \kappa_i^\gamma(t) \left[ 1 + \gamma \left( \frac{\nu z_i(t)}{\kappa_i(t)} - \delta_{z_i(t)}^0 \zeta^{-1} \right) dt \right] + \mathcal{O}(dt)^2 \end{aligned} \quad (\text{A.168})$$

$$\begin{aligned} &= \left[ 1 - (\eta + \omega_i(t) + \delta_{z_i(t)}^1 \eta + \varepsilon_i(t)) dt \right] \kappa_i^\gamma(t) \\ &\quad + \gamma(1 - n_i(t)) \left( \frac{\nu z_i(t)}{\kappa_i(t)} - \delta_{z_i(t)}^0 \zeta^{-1} \right) \kappa_i^\gamma(t) dt \\ &\quad + \left[ \delta_{z_i(t)}^1 \eta + \omega_i(t) + \varepsilon_i(t) + \eta(1 - n_i(t)) \right] \kappa_i^\gamma(t) dt + \mathcal{O}(dt)^2 \end{aligned} \quad (\text{A.169})$$

$$\begin{aligned} &= \kappa_i^\gamma(t) - \eta \kappa_i^\gamma(t) n_i(t) dt - \gamma \kappa_i^\gamma(t) (1 - n_i(t)) \delta_{z_i(t)}^0 \zeta^{-1} dt \\ &\quad + \gamma \nu (1 - n_i(t)) z_i(t) [\kappa_i(t)]^{\gamma-1} dt + \mathcal{O}(dt)^2 . \end{aligned} \quad (\text{A.170})$$

Then we take the ensemble average up to  $O(dt)$

$$\langle \kappa_i^\gamma(t+dt) \rangle = \langle \mathbb{E}[\kappa_i^\gamma(t+dt) | t] \rangle \quad (\text{A.171})$$

$$= \langle x_2 \rangle \quad (\text{A.172})$$

$$= \langle \kappa_i^\gamma(t) \rangle - \eta \langle \kappa_i^\gamma(t) n_i(t) \rangle dt - \gamma \zeta^{-1} \langle \kappa_i^\gamma(t) (1 - n_i(t)) \delta_{z_i(t)}^0 \rangle dt + \gamma \nu \langle (1 - n_i(t)) z_i(t) [\kappa_i(t)]^{\gamma-1} \rangle dt \quad (\text{A.173})$$

and finally find

$$\frac{d\langle \kappa_i^\gamma(t) \rangle}{dt} = \frac{\langle \kappa_i^\gamma(t+dt) \rangle - \langle \kappa_i^\gamma(t) \rangle}{dt} \quad (\text{A.174})$$

$$= -\eta \langle \kappa_i^\gamma(t) n_i(t) \rangle - \gamma \zeta^{-1} \langle \kappa_i^\gamma(t) (1 - n_i(t)) \delta_{z_i(t)}^0 \rangle + \gamma \nu \langle (1 - n_i(t)) z_i(t) [\kappa_i(t)]^{\gamma-1} \rangle. \quad (\text{A.175})$$

Notice that, in the limit  $\zeta \rightarrow \infty$ , the dynamic equations for  $\kappa_i(t)$  and  $\kappa_i^\gamma(t)$  (respectively, Eqs. (A.130) and (A.175)) are identical to the equations obtained in Appendix A.5 for the miccSIS model with long-term memory (Eqs. (A.100) and (A.109), respectively).

## A.7 Mean-field parameters of the miccSIS model with medium-term memory

The computation of the moments  $\langle \kappa_i^\gamma | n_i = 1 \rangle$ , which are required to obtain the coefficient  $A$  in Eq. (4.76), is identical to the procedure in Appendix A.4, and yields

$$\langle \kappa^\gamma | n = 1 \rangle = \frac{I(\gamma + \alpha - 1)}{I(\alpha - 1)}. \quad (\text{A.176})$$

with

$$I(x) = \int_0^\infty \kappa^x e^{-(\mu\kappa)^\alpha} e^{-\eta\nu^{-1}\kappa} d\kappa. \quad (\text{A.177})$$

In order to obtain the coefficient  $B$  in Eq. (4.77) we need to compute the moments  $\langle \kappa_i^\gamma | Y_i = 1 \rangle$  for  $\gamma = 1$  and  $\gamma = \alpha$ . These moments are conditioned on  $Y_i = 1$ , i.e., node  $i$  being dormant. Within the mean-field approximation, all

nodes are considered identical, hence we drop the  $i$  index. When  $\rho \approx 0$  we can assume that susceptible node  $i$  has only one infected neighbor  $j$ . Moreover,  $i$  transitioned from dormant to susceptible at the same time that  $j$  became infected. Thus node  $i$  is exposed to a single source of pathogen, and the time since  $j$  became infected ( $t$ ) and the viral load accumulated by  $i$  ( $\kappa$ ) are proportional ( $\kappa = \nu t$ ).

Let  $\phi^*(\kappa)$  measure the probability density that node  $i$  has accumulated  $\kappa$  units of viral load when it becomes dormant. This event is conditioned on  $j$  recovering at time  $t$  ( $\psi_{\text{rec}}(t)$ ) and  $i$  not becoming infected ( $\Psi_{\text{inf}}^*(\kappa)$ ). Expressed in terms of  $\kappa$  this reads

$$\phi^*(\kappa) = N^{-1} \nu^{-1} \psi_{\text{rec}}(\nu^{-1} \kappa) \Psi_{\text{inf}}^*(\kappa) = N^{-1} \eta \nu^{-1} e^{-(\mu\kappa)^\alpha} e^{-\eta \nu^{-1} \kappa}, \quad (\text{A.178})$$

with

$$N = \int_0^\infty \nu^{-1} \psi_{\text{rec}}(\nu^{-1} \kappa) \Psi_{\text{inf}}^*(\kappa) d\kappa. \quad (\text{A.179})$$

After some time  $t$  since node  $i$  became dormant, its viral load has decayed such that

$$\kappa(t) = \kappa e^{-t/\zeta}. \quad (\text{A.180})$$

With  $\phi(t)$  the probability to sample node  $i$  in state  $Y_i = 1$  (i.e., dormant) at time  $t$  (measured since  $i$  became dormant), the necessary moments are

$$\langle \kappa^\gamma | Y = 1 \rangle = \int \kappa^\gamma(t) \phi^*(\kappa) \phi(t) d\kappa dt \quad (\text{A.181})$$

$$= \int [\kappa e^{-t/\zeta}]^\gamma \phi^*(\kappa) \phi(t) d\kappa dt. \quad (\text{A.182})$$

For simplicity, we assume that node  $i$  ceases to be dormant (i.e., becomes susceptible) when node  $j$  is reinfected. Let  $\varphi(t)$  denote the probability that node  $j$  reinfected at time  $t$  (measured since node  $i$  became dormant). Then the probability to sample node  $i$  in state  $Y_i = 1$  at time  $t$  is [48]

$$\phi(t) = \frac{\Phi(t)}{\langle t \rangle_\varphi}, \quad (\text{A.183})$$

with

$$\Phi(t) = \int_t^\infty \varphi(t') dt' \quad (\text{A.184})$$

and

$$\langle t \rangle = \int_0^{\infty} t\varphi(t)dt . \quad (\text{A.185})$$

Finding an expression for  $\varphi(t)$ , however, is highly nontrivial. Here we apply a reasonable mean-field approximation. Imagine a single link between a healthy and an infected node. Near equilibrium, the probability of transmission and recovery are balanced, thus the transmission rate can be approximated by the recovery rate  $\eta$ . Within a mean-field approximation we can assume that the transmissions are independent and, moreover, the probability of any node being infected is  $\rho$ . Then we can consider an effective infection rate

$$\bar{\omega} = k\rho\eta , \quad (\text{A.186})$$

with  $k$  the average degree, which yields

$$\varphi(t) = \phi(t) = \bar{\omega}e^{-\bar{\omega}t} . \quad (\text{A.187})$$

Finally we find the moments

$$\langle \kappa^\gamma | Y = 1 \rangle = \int_0^{\infty} \bar{\omega}e^{-(\bar{\omega}+\gamma/\zeta)t} dt \int_0^{\infty} \kappa^\gamma \bar{\phi}(\kappa) d\kappa \quad (\text{A.188})$$

$$= \frac{\bar{\omega}\zeta}{\bar{\omega}\zeta + \gamma} \frac{I(\gamma)}{I(0)} , \quad (\text{A.189})$$

with the integral  $I(x)$  given by Eq. (A.177).

Substituting in the expression for the coefficient  $B$  gives

$$B = A\langle \kappa_i | Y_i = 1 \rangle - \alpha\langle \kappa_i^\alpha | Y_i = 1 \rangle \quad (\text{A.190})$$

$$= A \frac{k\rho\eta\zeta}{k\rho\eta\zeta + 1} \frac{I(1)}{I(0)} - \alpha \frac{k\rho\eta\zeta}{k\rho\eta\zeta + \alpha} \frac{I(\alpha)}{I(0)} \quad (\text{A.191})$$

$$= \rho \left[ A \frac{I(1)}{I(0)} \frac{1}{\rho + (k\hat{\zeta})^{-1}} - \alpha \frac{I(\alpha)}{I(0)} \frac{1}{\rho + \alpha(k\hat{\zeta})^{-1}} \right] , \quad (\text{A.192})$$

with  $\hat{\zeta} = \eta\zeta$ . The equation of state, Eq. (4.81), then becomes

$$- \eta\mu^{-\alpha}\rho + Avk\rho(1 - \rho) - \left[ A \frac{I(1)}{I(0)} \frac{\zeta^{-1}}{\rho + (k\hat{\zeta})^{-1}} - \alpha \frac{I(\alpha)}{I(0)} \frac{\zeta^{-1}}{\rho + \alpha(k\hat{\zeta})^{-1}} \right] \rho(1 - \rho)^{k+1} = 0 , \quad (\text{A.193})$$

and defining the reduced coefficients  $a = A\eta^{-1}\nu\mu^\alpha$ ,  $b_1 = A\mu^\alpha \frac{I(1)}{I(0)}$ , and  $b_2 = \mu^\alpha \frac{I(\alpha)}{I(0)}$  we find Eq. (4.82)

$$f(\rho) = -\rho + ak\rho(1-\rho) - \left[ \frac{b_1\hat{\zeta}^{-1}}{\rho + (k\hat{\zeta})^{-1}} - \frac{b_2\alpha\hat{\zeta}^{-1}}{\rho + \alpha(k\hat{\zeta})^{-1}} \right] \rho(1-\rho)^{k+1}. \quad (\text{A.194})$$

Its first and second derivatives are given by

$$\begin{aligned} f'(\rho) = & -1 + ak(1-2\rho) + \left[ \frac{b_1\hat{\zeta}^{-1}}{(\rho + (k\hat{\zeta})^{-1})^2} - \frac{b_2\alpha\hat{\zeta}^{-1}}{(\rho + \alpha(k\hat{\zeta})^{-1})^2} \right] \rho(1-\rho)^{k+1} \\ & - \left[ \frac{b_1\hat{\zeta}^{-1}}{\rho + (k\hat{\zeta})^{-1}} - \frac{b_2\alpha\hat{\zeta}^{-1}}{\rho + \alpha(k\hat{\zeta})^{-1}} \right] [(1-\rho)^{k+1} - \rho(k+1)(1-\rho)^k] \end{aligned} \quad (\text{A.195})$$

and

$$\begin{aligned} f''(\rho) = & -2ak - 2 \left[ \frac{b_1\hat{\zeta}^{-1}}{(\rho + (k\hat{\zeta})^{-1})^3} - \frac{b_2\alpha\hat{\zeta}^{-1}}{(\rho + \alpha(k\hat{\zeta})^{-1})^3} \right] \rho(1-\rho)^{k+1} \\ & + 2 \left[ \frac{b_1\hat{\zeta}^{-1}}{(\rho + (k\hat{\zeta})^{-1})^2} - \frac{b_2\alpha\hat{\zeta}^{-1}}{(\rho + \alpha(k\hat{\zeta})^{-1})^2} \right] (1-\rho)^k [1 - \rho(k+2)] \\ & - \left[ \frac{b_1\hat{\zeta}^{-1}}{\rho + (k\hat{\zeta})^{-1}} - \frac{b_2\alpha\hat{\zeta}^{-1}}{\rho + \alpha(k\hat{\zeta})^{-1}} \right] (k+1)(1-\rho)^{k-1} [\rho(k+1) - 2]. \end{aligned} \quad (\text{A.196})$$

The numerical evaluation of the parameters is detailed in Appendix C.4.

# Synthetic networks

---

## B.1 Random degree-regular networks

We use the configuration model to generate undirected random degree-regular network with degree  $k$ . The steps are the following:

1. Generate a list of stubs where each of the  $N$  nodes appears  $k$  times. Note that the product  $N \times k$  must be an even number.
2. Randomly select two stubs,  $s_1$  and  $s_2$ , from the remaining stub list.
  - (a) If  $s_1 = s_2$  or if the links  $(s_1, s_2)$  or  $(s_2, s_1)$  are already present in the network, place both stubs back in the list and go back to step 2;
  - (b) else, add the link  $(s_1, s_2)$  to the network and remove both stubs from the list.
3. Repeat step 2 until the stub list is empty.

This algorithm may not converge, particularly when the degree sequence is heterogeneous. The solution is to keep track of the acceptance rate (the fraction of times that two randomly selected stubs were successfully added to the network). When it drops below a given threshold, the iteration is halted and we start again from step 1. An implementation is available in [87].

Using the configuration model yields a network with residual clustering  $C \approx 0$ , which is adequate for our analysis in homogeneous networks. However, when we study the interplay between the miccSIS model and network properties we need random degree-regular networks with higher clustering coefficients (see Section 5.2). Therefore we use a simulated annealing–like algorithm developed in [46, 45, 128]. In short, it randomly selects two edges and switches the endpoints. For example, if we select the edges  $(A, B)$  and  $(C, D)$ , after the rewiring we have  $(A, D)$  and  $(C, B)$ . This procedure yields maximally random networks while preserving the degree distribution. The

“temperature” is gradually lowered until the network reaches the target average clustering coefficient  $C$ . We use the code available in [47].

Although random degree-regular networks are almost surely connected if  $k \geq 3$  [19], we run a breadth-first search [123] in order to verify that all nodes belong to the same component. An implementation is available in [87].

## B.2 Unclustered scale-free networks

The degree distribution of scale-free networks is given by a power law with exponent  $\gamma > 2$ ,

$$p(x) = (\gamma - 1)x_{\min}^{\gamma-1}x^{-\gamma}, \quad (\text{B.1})$$

for  $x \geq x_{\min}$ . In finite systems, the maximum degree is limited by the fact that a node cannot have more neighbors than available nodes. This natural cut-off is given by

$$\int_{x_{\max}}^{\infty} p(x)dx < \frac{1}{N}, \quad (\text{B.2})$$

with  $N$  the system size [18]. In short, Eq. (B.2) states that the number of nodes with degree  $x_{\max}$  or higher must be smaller than  $N$ . Solving Eq. (B.2) yields

$$x_{\max} > x_{\min}N^{\frac{1}{\gamma-1}}. \quad (\text{B.3})$$

In practice, we sample the degree sequence from a discrete probability function

$$p(k) = Ak^{-\gamma}, \quad (\text{B.4})$$

for  $k_{\min} \leq k \leq k_{\max}$ . In order to guarantee a connected network we choose  $k_{\min} = 2$ , and from Eq. (B.3) we find

$$k_{\max} = \left\lceil k_{\min}N^{\frac{1}{\gamma-1}} \right\rceil. \quad (\text{B.5})$$

Finally, the normalization constant yields  $A = \zeta(\gamma, k_{\min}) - \zeta(\gamma, k_{\max} + 1)$ , with  $\zeta(x, \ell)$  the Hurwitz zeta function

$$\zeta(x, \ell) = \sum_{k=0}^{\infty} (k + \ell)^{-x} = \sum_{k=\ell}^{\infty} k^{-x}. \quad (\text{B.6})$$

We apply the configuration model outlined in Section B.1. The stub list is generated from the degree sequence, sampling Eq. B.4 with a rejection method. An implementation is available in [87].

# Computational implementations

---

## C.1 Simulations of the SI model

### C.1.1 Core algorithm standard SI

For a fixed value of  $\beta$ , at a given time  $t$  the nodes are separated in two lists: infected (I) and susceptible (S). We also keep a list of the  $N_A$  active transmission, i.e., the (directed) links that connect an infected node with a susceptible one. The contact network is encoded in an adjacency matrix or list.

1. Compute the total hazard rate  $\Omega = \beta N_A$ .
2. Sample the interval  $\tau = -\log(u_1)/\Omega$ , with  $u_1 \in U(0, 1)$ , and update the time,  $t \leftarrow t + \tau$ .
3. Draw  $u_2 \in U(0, 1)$  to sample link  $i \rightarrow j$  from the list of active links.
  - (a) Move node  $j$  from the susceptible to the infected list.
  - (b) For all of  $j$ 's neighbors:
    - If node  $\ell$  is infected, deactivate link  $\ell \rightarrow j$ .
    - If node  $\ell$  is susceptible, activate link  $j \rightarrow \ell$ .

### C.1.2 Core algorithm miccSI

For fixed values of  $\alpha$ ,  $\mu$ , and  $\nu$ , at a given time  $t$  the nodes are separated in two lists: infected (I) and susceptible (S). For susceptibles we store their accumulated viral load  $\kappa$  and also the number of infected neighbors  $z$ . The contact network is encoded in an adjacency matrix or list.

1. Sample the interval  $\tau$ , solving  $\Phi(\tau) = u$ , with  $u \in U(0, 1)$  and

$$\Phi(\tau) = \prod_{j \in S} \frac{e^{-[\mu(\kappa_j + z_j \tau)]^\alpha}}{e^{-(\mu \kappa_j)^\alpha}}. \quad (\text{C.1})$$

2. Update the time,  $t \leftarrow t + \tau$ , and the viral load of susceptible nodes,  $\kappa_j \leftarrow \kappa_j + z_j \tau$ .
3. Compute the hazard rate for susceptible nodes,  $\omega_j = \nu \alpha \mu^\alpha z_j \kappa_j^{\alpha-1}$ , and the total hazard rate,  $\Omega = \sum_{j \in S} \omega_j$ .
4. Compute the discrete distribution  $\Pi_k = \omega_k / \Omega$  and sample node  $k$  from the list of susceptible nodes.
  - (a) Move node  $k$  from the susceptible list to the infected list.
  - (b) For all of  $k$ 's neighbors, increase the number of infected neighbors by one,  $z_\ell \leftarrow z_\ell + 1$ .

### C.1.3 Single-seed outbreaks

Each outbreak starts with a single randomly chosen infected node. All other nodes are healthy, with zero viral load. An outbreak is terminated when it reaches the absorbing state (i.e., all nodes are infected). We store the prevalence  $\rho_i(t)$  of each run  $i$  at given times, with time interval  $\Delta t$ . For a given network of size  $N$  and a fixed value of  $\lambda$  we average  $Z$  trajectories, at fixed values of  $t$ :  $\langle \rho(t) \rangle = Z^{-1} \sum_{j=1}^Z \rho_j(t)$  and  $\langle \rho^2(t) \rangle = Z^{-1} \sum_{j=1}^Z \rho_j^2(t)$ . We estimate the prevalence as  $\rho(t) = \langle \rho(t) \rangle$  and compute its standard deviation as  $\sigma(\rho(t)) = \sqrt{\langle \rho^2(t) \rangle - \langle \rho(t) \rangle^2}$ . We use  $\Delta t = 0.1$  and  $Z = 100$ .

## C.2 Simulations of the SIR model

### C.2.1 Core algorithm standard SIR

For fixed values of  $\beta$  and  $\eta$ , at a given time  $t$  the nodes are separated in three lists: infected (I), susceptible (S), and recovered (R). We also keep a list of the  $N_A$  active transmission, i.e., the (directed) links that connect an infected node with a susceptible one. The contact network is encoded in an adjacency matrix or list.

1. Compute the total hazard rate  $\Omega = \eta N_I + \beta N_A$ .
2. Sample the interval  $\tau = -\log(u_1) / \Omega$ , with  $u_1 \in U(0, 1)$ , and update the time,  $t \leftarrow t + \tau$ .

3. Compute the probability of a recovery,  $\Pi_{\text{rec}} = \eta N_I / \Omega$ , and sample  $u_2 \in U(0, 1)$ .
  - If  $u_2 \leq \Pi_{\text{rec}}$ , draw  $u_3 \in U(0, 1)$  to sample node  $k$  from the list of infected nodes.
    - (a) Move node  $k$  from the infected list to the recovered list.
    - (b) For all of  $k$ 's neighbors:
      - If node  $\ell$  is susceptible, deactivate the link  $k \rightarrow \ell$ .
  - If  $u_2 > \Pi_{\text{rec}}$ , draw  $u_3 \in U(0, 1)$  to sample link  $i \rightarrow j$  from the list of active links.
    - (a) Move node  $j$  from the susceptible to the infected list.
    - (b) For all of  $j$ 's neighbors:
      - If node  $\ell$  is infected, deactivate link  $\ell \rightarrow j$ .
      - If node  $\ell$  is susceptible, activate link  $j \rightarrow \ell$ .

### C.2.2 Core algorithm miccSIR

For fixed values of  $\alpha$ ,  $\mu$ ,  $\nu$ ,  $\eta$ , and  $\zeta$ , at a given time  $t$  the nodes are separated in four lists: infected (I), dormant (D), susceptible (S), and recovered (R). For dormants we store their accumulated viral load  $\kappa$ . For susceptibles we store  $\kappa$  and also the number of infected neighbors  $z$ . The contact network is encoded in an adjacency matrix or list.

1. Sample the interval  $\tau$ , solving  $\Phi(\tau) = u$ , with  $u \in U(0, 1)$  and

$$\Phi(\tau) = \prod_{i \in I} e^{-\eta\tau} \prod_{j \in S} \frac{e^{-[\mu(\kappa_j + z_j\tau)]^\alpha}}{e^{-(\mu\kappa_j)^\alpha}}. \quad (\text{C.2})$$

2. Update the time,  $t \leftarrow t + \tau$ , and the viral load of susceptible nodes,  $\kappa_j \leftarrow \kappa_j + z_j\tau$ .
3. Compute the hazard rate for infected nodes,  $\omega_i = \eta$ , the hazard rate for susceptible nodes,  $\omega_j = \nu\alpha\mu^\alpha z_j \kappa_j^{\alpha-1}$ , and the total hazard rate,  $\Omega = \sum_{i \in I} \omega_i + \sum_{j \in S} \omega_j$ .
4. Compute the discrete distribution  $\Pi_k = \omega_k / \Omega$  and sample the next-occurring event.

- If infected node  $k$  recovers:
  - (a) Move node  $k$  from the infected list to the recovered list.
  - (b) For all of  $k$ 's neighbors, decrease the number of infected neighbors by one,  $z_\ell \leftarrow z_\ell - 1$ .
    - If  $z_\ell = 0$ , move node  $\ell$  from the susceptible list to the dormant list.
    - \* If  $\zeta = 0$  (short-term memory), set  $\kappa_\ell = 0$ .
- If susceptible node  $k$  becomes infected:
  - (a) Move node  $k$  from the susceptible list to the infected list.
  - (b) For all of  $k$ 's neighbors, increase the number of infected neighbors by one,  $z_\ell \leftarrow z_\ell + 1$ .
    - If  $z_\ell = 1$ , move node  $\ell$  from the dormant list to the susceptible list and store  $z_\ell$ .

### C.2.3 Single-seed outbreaks

Each outbreak starts with a single randomly chosen infected node. All other nodes are healthy, with zero viral load. An outbreak is terminated when it reaches the absorbing state (i.e., all nodes are infected). To obtain the temporal profile, we store the prevalence  $\rho_i(t)$  of each run  $i$  at given times, with time interval  $\Delta t$ . For a given network of size  $N$  and a fixed value of  $\lambda$  we average  $Z$  trajectories, at fixed values of  $t$ :  $\langle \rho(t) \rangle = Z^{-1} \sum_{j=1}^Z \rho_j(t)$  and  $\langle \rho^2(t) \rangle = Z^{-1} \sum_{j=1}^Z \rho_j^2(t)$ . We estimate the prevalence as  $\rho(t) = \langle \rho(t) \rangle$ , compute its standard deviation as  $\sigma(\rho(t)) = \sqrt{\langle \rho^2(t) \rangle - \langle \rho(t) \rangle^2}$ , and estimate the standard error as  $s(\rho(t)) = \sigma(\rho(t))/Z$ . We construct the 95% uncertainty intervals as  $\rho(t) \pm 1.96 \times s(\rho(t))$ , and use  $\Delta t = 0.1$  and  $Z = 100$ .

To obtain the late-time fraction of recovered nodes we simulate  $Z$  independent runs and record the final values  $R$  and  $R^2$  of each outbreak. Afterwards we compute the averages  $\langle R \rangle = Z^{-1} \sum_{j=1}^Z R_j$  and  $\langle R^2 \rangle = Z^{-1} \sum_{j=1}^Z R_j^2$ . We estimate the late-time fraction of recovered nodes as  $r_\infty = \langle R \rangle / N$ , compute the standard deviation as  $\sigma(r_\infty) = N^{-1} \sqrt{\langle R^2 \rangle - \langle R \rangle^2}$ , and estimate the standard error as  $s(r_\infty) = \sigma(r_\infty) / Z$ . We construct the 95% uncertainty intervals as  $r_\infty \pm 1.96 \times s(r_\infty)$  and use  $Z = 10^4$ .

## C.3 Simulations of the SIS model

### C.3.1 Core algorithm standard SIS

For fixed values of  $\beta$  and  $\eta$ , at a given time  $t$  the nodes are separated in two lists: infected (I) and susceptible (S). We also keep a list of the  $N_A$  active transmission, i.e., the (directed) links that connect an infected node with a susceptible one. The contact network is encoded in an adjacency matrix or list.

1. Compute the total hazard rate  $\Omega = \eta N_I + \beta N_A$ .
2. Sample the interval  $\tau = -\log(u_1)/\Omega$ , with  $u_1 \in U(0, 1)$ , and update the time,  $t \leftarrow t + \tau$ .
3. Compute the probability of a recovery,  $\Pi_{\text{rec}} = \eta N_I/\Omega$ , and sample  $u_2 \in U(0, 1)$ .
  - If  $u_2 \leq \Pi_{\text{rec}}$ , draw  $u_3 \in U(0, 1)$  to sample node  $k$  from the list of infected nodes.
    - (a) Move node  $k$  from the infected list to the susceptible list.
    - (b) For all of  $k$ 's neighbors:
      - If node  $\ell$  is infected, activate the link  $\ell \rightarrow k$ .
      - If node  $\ell$  is susceptible, deactivate the link  $k \rightarrow \ell$ .
  - If  $u_2 > \Pi_{\text{rec}}$ , draw  $u_3 \in U(0, 1)$  to sample link  $i \rightarrow j$  from the list of active links.
    - (a) Move node  $j$  from the susceptible list to the infected list.
    - (b) For all of  $j$ 's neighbors:
      - If node  $\ell$  is infected, deactivate link  $\ell \rightarrow j$ .
      - If node  $\ell$  is susceptible, activate link  $j \rightarrow \ell$ .

### C.3.2 Core algorithm miccSIS

For fixed values of  $\alpha$ ,  $\mu$ ,  $\nu$ ,  $\eta$ , and  $\zeta$ , at a given time  $t$  the nodes are separated in three lists: infected (I), dormant (D), and susceptible (S). For dormants we store their accumulated viral load  $\kappa$ . For susceptibles we store  $\kappa$  and also the number of infected neighbors  $z$ . The contact network is encoded in an adjacency matrix or list.

1. Sample the interval  $\tau$ , solving  $\Phi(\tau) = u$ , with  $u \in U(0, 1)$  and

$$\Phi(\tau) = \prod_{i \in I} e^{-\eta\tau} \prod_{j \in S} \frac{e^{-[\mu(\kappa_j + z_j\tau)]^\alpha}}{e^{-(\mu\kappa_j)^\alpha}}. \quad (\text{C.3})$$

2. Update the time,  $t \leftarrow t + \tau$ , and the viral load of susceptible nodes,  $\kappa_j \leftarrow \kappa_j + z_j\tau$ .

- If  $0 < \zeta < \infty$  (medium-term memory), decrease the viral load of dormant nodes,  $\kappa_j \leftarrow \kappa_j e^{-\tau/\zeta}$ .

3. Compute the hazard rate for infected nodes,  $\omega_i = \eta$ , the hazard rate for susceptible nodes,  $\omega_j = \nu\alpha\mu^\alpha z_j \kappa_j^{\alpha-1}$ , and the total hazard rate,  $\Omega = \sum_{i \in I} \omega_i + \sum_{j \in S} \omega_j$ .

4. Compute the discrete distribution  $\Pi_k = \omega_k/\Omega$  and sample the next-occurring event.

- If infected node  $k$  recovers:

- (a) Compute its number of infected neighbors,  $z_k$ .

- If  $z_k = 0$ , move node  $k$  from the infected list to the dormant list with  $\kappa_k = 0$ .
- If  $z_k > 0$ , move node  $k$  from the infected list to the susceptible list with  $\kappa_k = 0$  and store  $z_k$ .

- (b) For all of  $k$ 's neighbors, decrease the number of infected neighbors by one,  $z_\ell \leftarrow z_\ell - 1$ .

- If  $z_\ell = 0$ , move node  $\ell$  from the susceptible list to the dormant list.
- \* If  $\zeta = 0$  (short-term memory), set  $\kappa_\ell = 0$ .

- If susceptible node  $k$  becomes infected:

- (a) Move node  $k$  from the susceptible list to the infected list.

- (b) For all of  $k$ 's neighbors, increase the number of infected neighbors by one,  $z_\ell \leftarrow z_\ell + 1$ .

- If  $z_\ell = 1$ , move node  $\ell$  from the dormant list to the susceptible list and store  $z_\ell$ .

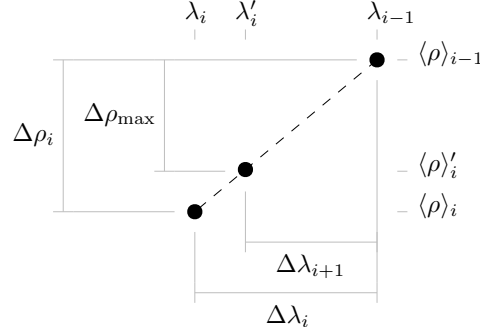


Figure C.1: **Adjusting the descend of the adiabatic expansion.** Interpolation construction if  $\Delta \rho_i > \Delta \rho_{\max}$ , yielding  $\lambda'_i$ ,  $\langle \rho \rangle'_i$ , and  $\Delta \lambda_{i+1}$ .

### C.3.3 Adiabatic expansion

Given the stochastic nature of the dynamics we must average over independent realizations in order to obtain a representative  $\rho_\infty(\lambda)$  curve. Additionally, we want to control the spacing in the  $\rho_\infty$  axis and handle the increasing correlation time as we approach the critical point. We employ a two-step simulation scheme: in the first step we elaborate a preparatory list of  $\lambda$  values that will be used in the second step to extensively sample  $\rho_\infty$ .

For a given network of size  $N$ , we start at  $\lambda = \lambda_0$  and infect all nodes. We evolve the system during  $25 \times M_0$  events (with  $M_0 = N$ ), record the final value of  $\rho = N_I/N$  and store the system's final state. We repeat this for  $R$  independent runs, starting each time at  $\lambda_0$  with all nodes infected, and storing each final state separately. We compute the average  $\langle \rho \rangle_0$  (of the  $R$  measures) and write  $\lambda_0$  and  $M_0$  to the output file. Next we decrease the control parameter,  $\lambda_i = \lambda_{i-1} - \Delta \lambda_i$ . For each run we load the corresponding initial state from storage and iterate  $25 \times M_i$  events. Then we record the final value of  $\rho$  and store the system's final state. After repeating this for the  $R$  runs, we compute  $\langle \rho \rangle_i$  and  $\Delta \rho_i = \langle \rho \rangle_{i-1} - \langle \rho \rangle_i$ . If  $\Delta \rho_i > \Delta \rho_{\max}$ , we interpolate the results (see Fig. C.1 for a schematic illustration), setting  $\Delta \lambda_{i+1} = \Delta \lambda_i \Delta \rho_{\max} / \Delta \rho_i$ , and reassigning  $\lambda_i \leftarrow \lambda_i + \Delta \lambda_i - \Delta \lambda_{i+1}$  and  $\langle \rho \rangle_i \leftarrow \langle \rho \rangle_{i-1} - \Delta \rho_{\max}$ . In addition, we increase the event interval,  $M_{i+1} = M_i^\epsilon$ , with  $\epsilon > 1$ . Finally we write  $\lambda_i$  and  $M_i$  to the output file (note that  $\lambda_1 = \lambda_0$  and  $M_1 = M_0$ ). A run is deactivated when it reaches the absorbing state ( $N_I = 0$ ): we stop simulating its dynamics and it is no longer included in the computation of  $\langle \rho \rangle$ . We keep decreasing the control parameter  $\lambda$  until all runs are deactivated, the point at which the simulation is halted.

Following this preparatory step we proceed with an extensive sampling of

the order parameter. We infect all nodes and load  $\lambda$  and  $M$  from the input file. We thermalize the system during  $20 \times M$  events and afterward measure  $\rho$  and  $\rho^2$  of  $X$  states, each separated by a window of  $M$  events. We repeat this thermalization-sampling procedure for the next entry on the input list, using the last visited state as initial condition. The simulation is halted when the list is fully iterated or whenever the system reaches the absorbing state. We repeat the whole procedure for  $Y$  independent runs, using the same input file. The results are temporally averaged, i.e., each measure  $j$  is weighted by its residency time  $\tau_j$ :  $\langle \rho \rangle = w^{-1} \sum_{j=1}^Z \tau_j \rho_j$  and  $\langle \rho^2 \rangle = w^{-1} \sum_{j=1}^Z \tau_j \rho_j^2$ , with  $w = \sum_{j=1}^Z \tau_j$  and  $Z$  the total number of samples (note that, since the input file may not be fully iterated,  $Z \leq X \times Y$ ). We estimate the order parameter as  $\rho_\infty = \langle \rho \rangle$ , compute its standard deviation as  $\sigma(\rho_\infty) = \sqrt{\langle \rho^2 \rangle - \langle \rho \rangle^2}$ , and estimate the standard error as  $s(\rho_\infty) = \sigma(\rho_\infty)/Z$ . We construct the 95% uncertainty interval as  $\rho_\infty \pm 1.96 \times s(\rho_\infty)$  and use  $\lambda_0 = 1.2$ ,  $R = 20$ ,  $\Delta\lambda_0 = 0.05$ ,  $\Delta\rho_{\max} = 0.025$ ,  $\epsilon = 1.01$ ,  $X = 500$ , and  $Y = 20$ .

### C.3.4 Single-seed outbreaks

For a given network of size  $N$  and a fixed value of  $\lambda$  we simulate  $Z$  independent runs. Each outbreak starts with a single randomly chosen infected node. All other nodes are healthy, with zero viral load, and the coverage  $K$  is set to zero. During the evolution of the outbreak we keep track of all the nodes' first infection label. Whenever a node is infected for the first time, we change its label and increase the coverage by one unit,  $K \leftarrow K + 1$ . An outbreak is terminated when it reaches the absorbing state (finite realization) or when the coverage reaches the threshold,  $K_{\text{th}} = c_{\text{th}}N$  (endemic realization). We record the final values  $K$  and  $K^2$  of all outbreaks, and count the number of endemic realizations,  $z_{\text{end}}^{(1)}$ . Afterward we compute the averages  $\langle K \rangle = Z^{-1} \sum_{j=1}^Z K_j$  and  $\langle K^2 \rangle = Z^{-1} \sum_{j=1}^Z K_j^2$ . We estimate the average coverage fraction as  $\bar{c} = \langle K \rangle/N$  and the endemic probability as  $P_1 = z_{\text{end}}^{(1)}/Z$ , with standard deviation  $\sigma(\bar{c}) = N^{-1} \sqrt{\langle K^2 \rangle - \langle K \rangle^2}$  and  $\sigma(P_1) = \sqrt{P_1(1 - P_1)}$ , and standard error  $s(\bar{c}) = \sigma(\bar{c})/Z$  and  $s(P_1) = \sigma(P_1)/Z$ . We construct the 95% uncertainty intervals as  $\bar{c} \pm 1.96 \times s(\bar{c})$  and  $P_1 \pm 1.96 \times s(P_1)$ .

To compute  $P_3$  we proceed from the same initial setting. Now, however, when an outbreak reaches the coverage threshold we reset the coverage to zero and erase all first infection labels (regardless of whether the node is healthy or infected at that moment). Then we continue evolving the same outbreak, keep-

ing track again of each of the nodes' "first infection", changing the labels and increasing the coverage accordingly. When the coverage threshold is reached for a second time, this reset is performed once again. We count the number of realizations that are able to reach the coverage a third time,  $z_{\text{end}}^{(3)}$ , and compute  $P_3 = z_{\text{end}}^{(3)}/Z$ ,  $\sigma(P_3) = \sqrt{P_3(1 - P_3)}$ , and  $s(P_3) = \sigma(P_3)/Z$ . We construct the 95% uncertainty intervals as  $P_3 \pm 1.96 \times s(P_3)$  and use  $c_{\text{th}} = 0.75$  and  $Z = 10^4$ .

### C.3.4.1 Late-time prevalence

To measure the late-time prevalence of endemic outbreaks,  $\rho_{\infty}^*$ , we only consider realizations that become endemic. If the outbreak reaches the coverage threshold at time  $t = T$ , we let the system evolve until  $t = m \times T$ . At this point the outbreak has had sufficient time to reach its active steady state. Afterward we measure  $\rho$  and  $\rho^2$  of  $X$  states, each separated by a window of  $N$  events. For a given  $\lambda$  we record a maximum of  $W$  states, running a maximum of  $Y$  outbreaks. The results are temporally averaged, i.e., each measure  $j$  is weighted by its residency time  $\tau_j$ :  $\langle \rho \rangle = w^{-1} \sum_{j=1}^Z \tau_j \rho_j$  and  $\langle \rho^2 \rangle = w^{-1} \sum_{j=1}^Z \tau_j \rho_j^2$ , with  $w = \sum_{j=1}^Z \tau_j$  and  $Z$  the total number of samples (note that  $Z \leq W$ ). We estimate the late-time prevalence as  $\rho_{\infty}^* = \langle \rho \rangle$ , compute its standard deviation as  $\sigma(\rho_{\infty}^*) = \sqrt{\langle \rho^2 \rangle - \langle \rho \rangle^2}$ , and estimate the standard error as  $s(\rho_{\infty}^*) = \sigma(\rho_{\infty}^*)/Z$ . We construct the 95% uncertainty intervals as  $\rho_{\infty}^* \pm 1.96 \times s(\rho_{\infty}^*)$  and use  $m = 10$ ,  $X = 10^2$ ,  $W = 10^4$ , and  $Y = 10^4$ .

### C.3.4.2 Temporal profile

To represent the evolution of single-seed outbreaks that reach the coverage threshold,  $\rho(t)$ , we start run  $i$  from the usual initial setting and store the prevalence  $\rho_i(t)$  at given times, with time interval  $\Delta t$ . If the system becomes trapped in the absorbing state before reaching the threshold, we discard the trajectory and start again. If the system is able to surpass the coverage threshold, we continue tracking its evolution while the outbreaks remains active, up to  $t_{\text{max}}$ . For a given network of size  $N$  and a fixed value of  $\lambda$  we average  $Z$  trajectories, at fixed values of  $t$ :  $\langle \rho(t) \rangle = Z^{-1} \sum_{j=1}^Z \rho_j(t)$  and  $\langle \rho^2(t) \rangle = Z^{-1} \sum_{j=1}^Z \rho_j^2(t)$ . We estimate the prevalence as  $\rho(t) = \langle \rho(t) \rangle$ , compute its standard deviation as  $\sigma(\rho(t)) = \sqrt{\langle \rho^2(t) \rangle - \langle \rho(t) \rangle^2}$ , and estimate the corresponding standard error as  $s(\rho(t)) = \sigma(\rho(t))/Z$ . We construct the 95% uncertainty intervals as

$\rho(t) \pm 1.96 \times s(\rho(t))$ , and use  $\Delta t = 0.1$ ,  $t_{\max} = 200$ , and  $Z = 100$ .

## C.4 Phase diagram of the miccSIS model

Here we explain how we obtain the phase diagrams for the miccSIS model with short-term (see Section 4.2.1.1 and Fig. 4.4) and medium-term memory (see Section 4.2.3.1 and Fig. 4.10). Note that the equations of state for short-term and medium-term memory (Eqs. (4.45) and (4.82), respectively) have the form

$$f(\rho) = \rho g(\rho). \quad (\text{C.4})$$

As a general note, for a given  $\lambda$  and  $\alpha$  we compute  $\langle \kappa^\gamma \mid n = 1 \rangle$ ,  $\langle \kappa^\gamma \mid X = 1 \rangle$ , and  $\langle \kappa^\gamma \mid Y = 1 \rangle$  with  $\eta = \nu = 1$ . The integrals  $I$ ,  $J_1$ , and  $J_2$  (Eqs. (A.82), (A.91), and (A.92), respectively) are evaluated numerically (using the Python package SciPy). With these results we compute the coefficients  $A$  and  $B$ , and from there the reduced coefficients  $a$ ,  $b$ ,  $b_1$ , and  $b_2$ . Recall that  $\mu$  is computed from Eq. (3.8).

The first step is to find the epidemic threshold  $\lambda_c$ , the point where the healthy phase  $\rho_0 = 0$  loses stability. For a fixed value of  $\alpha$  we numerically solve the equation  $f'(0) = 0$  for  $\lambda$ . The sign of  $f''(0)$  marks the nature of the transition. We sweep over a range of  $\alpha$  with a given precision (we choose  $\Delta\alpha = 0.05$ ) and evaluate the tricritical point  $\alpha_{\text{tr}}$  as the lowest value that yields a discontinuous transition.

For  $\alpha > \alpha_{\text{tr}}$ , the epidemic threshold  $\lambda_c$  correspond to the right boundary of the region of coexistence (see Fig. C.2(a)). We find the left boundary,  $\lambda_-$ , by studying the endemic phase  $\rho_+ > 0$ , which is found by solving  $g(\rho) = 0$ . As shown in Fig. C.2(b), a solution for  $\rho_+$  exists in the range  $\lambda > \lambda_-$ . For a fixed value of  $\alpha$ :

1. We start at the critical point  $\lambda_c$ .
2. We decrease the order parameter with a given precision (we choose  $\Delta\lambda = 0.01$ ) and find the solution of  $g'(\rho) = 0$  (which lies in the interval  $[0, 1]$ ). This yields the values  $\rho_{\max}$  and  $g_{\max} = g(\rho_{\max})$ .
  - (a) If  $g_{\max} > 0$ , we repeat step 2,
  - (b) else, we have found  $\lambda_-$  and also  $\rho_- = \rho_{\max}$ .

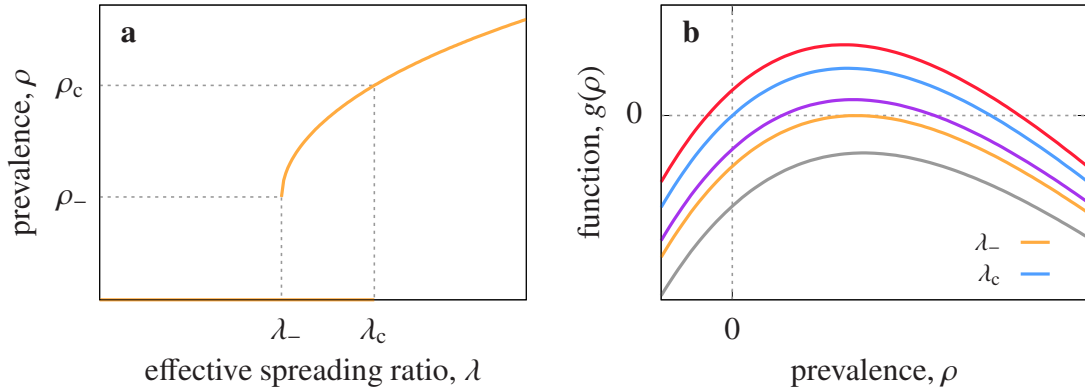


Figure C.2: **Bifurcation diagram for a generic discontinuous phase transition.** (a) Left ( $\lambda_-$ ) and right ( $\lambda_c$ ) boundaries of bistable region, and corresponding prevalence values ( $\rho_-$  and  $\rho_c$ , respectively). (b) The endemic phase ( $\rho_+ > 0$ ) is unstable for  $\lambda < \lambda_-$  (grey) and becomes stable at  $\lambda_-$  (orange). For  $\lambda_- < \lambda < \lambda_c$  (purple),  $g(\rho)$  has two roots in the interval  $\rho \in [0, 1]$  (the largest value is stable, the smallest value is unstable). At  $\lambda_c$  (blue) the healthy phase  $\rho_0 = 0$  becomes unstable. For  $\lambda > \lambda_c$  (red) both solutions of  $g(\rho) = 0$  are stable, but only the largest lies in the interval  $\rho \in [0, 1]$ .

3. With  $\lambda_c$  we compute the maximum of  $g(\rho)$ , located at  $\rho_{\max} \in [0, 1]$ . Finally, we find  $\rho_c$  by solving  $g(\rho) = 0$  in the interval  $[\rho_{\max}, 1]$ .

We use a hybrid bisection-secant method for the various root-finding problems.

## C.5 Simulations of the voter model

### C.5.1 Core algorithm standard voter

For fixed values of  $\beta_p$  and  $\beta_r$ , at a given time  $t$  the nodes are separated in two lists depending on their opinion. We also keep a list of the  $N_p$  persuasion links (between nodes with different opinion) and the  $N_r$  reaffirmation links (between nodes with the same opinion). We maintain the directionality of the links, so that the total number is  $N_p + N_r = 2E$ , with  $E$  the number of undirected links. The contact network is encoded in an adjacency matrix or list.

1. Compute the total hazard rate  $\Omega = \beta_p N_p + \beta_r N_r$ .

2. Sample the interval  $\tau = -\log(u_1)/\Omega$ , with  $u_1 \in U(0, 1)$ , and update the time,  $t \leftarrow t + \tau$ .
3. Compute the probability of a persuasion,  $\Pi_p = \beta_p N_p / \Omega$ , and sample  $u_2 \in U(0, 1)$ .
  - If  $u_2 \leq \Pi_p$ , draw  $u_3 \in U(0, 1)$  to sample node link  $i \rightarrow j$  from the list of persuasion links.
    - (a) For all of node  $j$ 's neighbors:
      - If  $\theta_\ell = \theta_j$ , move the links  $j \rightarrow \ell$  and  $\ell \rightarrow j$  from the list of reaffirmation links to the list of persuasion links.
      - If  $\theta_\ell \neq \theta_j$ , move the links  $j \rightarrow \ell$  and  $\ell \rightarrow j$  from the list of persuasion links to the list of reaffirmation links.
    - (b) Move node  $j$  from one opinion list to the other.
  - If  $u_2 > \Pi_p$ , do nothing.

### C.5.2 Core algorithm micc voter

For fixed values of  $\alpha_r$ ,  $\alpha_p$ ,  $\mu_r$ ,  $\mu_p$ , and  $\nu$ , at a given time  $t$  the nodes are separated in two lists depending on their opinion. We also store their accumulated reaffirmation load  $\kappa_r$  and persuasion load  $\kappa_p$ , the number of neighbors with the same opinion  $z_r$ , and the number of neighbors with the opposing opinion  $z_p$ . The contact network is encoded in an adjacency matrix or list.

1. Sample the interval  $\tau$ , solving  $\Phi(\tau) = u$ , with  $u \in U(0, 1)$  and

$$\Phi(\tau) = \prod_j \frac{e^{-[\mu_r(\kappa_{r,j} + z_{r,j}\tau)]^{\alpha_r}} e^{-[\mu_p(\kappa_{p,j} + z_{p,j}\tau)]^{\alpha_p}}}{e^{-(\mu_r \kappa_{r,j})^{\alpha_r}} e^{-(\mu_p \kappa_{p,j})^{\alpha_p}}}. \quad (\text{C.5})$$

2. Update the time,  $t \leftarrow t + \tau$ , and the opinion loads of all nodes,  $\kappa_{r,j} \leftarrow \kappa_{r,j} + z_{r,j}\tau$  and  $\kappa_{p,j} \leftarrow \kappa_{p,j} + z_{p,j}\tau$ .
3. Compute the reaffirmation hazard rate for each node,  $\omega_{r,j} = \nu \alpha_r \mu_r^{\alpha_r} z_{r,j} \kappa_{r,j}^{\alpha_r - 1}$ , the persuasion hazard rate for each node,  $\omega_{p,j} = \nu \alpha_p \mu_p^{\alpha_p} z_{p,j} \kappa_{p,j}^{\alpha_p - 1}$ , and the total hazard rate,  $\Omega = \sum_j (\omega_{r,j} + \omega_{p,j})$ .
4. Compute the discrete distribution  $\Pi_k = \omega_k / \Omega$  and sample the next-occurring event.

- If node  $j$  reaffirms its opinion:
  - (a) Reset node  $j$ 's persuasion load,  $\kappa_{p,j} \leftarrow 0$ .
- If node  $j$  is persuaded:
  - (a) For all of node  $j$ 's neighbors:
    - If  $\theta_\ell = \theta_j$ :
      - i. Move the links  $j \rightarrow \ell$  and  $\ell \rightarrow j$  from the list of reaffirmation links to the list of persuasion links.
      - ii. Increase their number of “persuasion neighbors” by one unit,  $z_{p,j} \leftarrow z_{p,j} + 1$  and  $z_{p,\ell} \leftarrow z_{p,\ell} + 1$ .
      - iii. Decrease their number of “reaffirmation neighbors” by one unit,  $z_{r,j} \leftarrow z_{r,j} - 1$  and  $z_{r,\ell} \leftarrow z_{r,\ell} - 1$ .
    - If  $\theta_\ell \neq \theta_j$ :
      - i. Move the links  $j \rightarrow \ell$  and  $\ell \rightarrow j$  from the list of persuasion links to the list of reaffirmation links.
      - ii. Increase their number of “reaffirmation” neighbors by one unit,  $z_{r,j} \leftarrow z_{r,j} - 1$  and  $z_{r,\ell} \leftarrow z_{r,\ell} - 1$ .
      - iii. Decrease their number of “persuasion” neighbors by one unit,  $z_{p,j} \leftarrow z_{p,j} + 1$  and  $z_{p,\ell} \leftarrow z_{p,\ell} + 1$ .
  - (b) Move node  $j$  from one opinion list to the other.
  - (c) Exchange node  $j$ 's opinion loads,  $\kappa_{r,j} \leftarrow \kappa_{p,j}$ .
  - (d) Reset node  $j$ 's persuasion load,  $\kappa_{p,j} \leftarrow 0$ .

### C.5.3 Temporal profiles

At the beginning of each realization we assign the nodes to state  $\theta = +1$  with probability  $(1 + m_0)/2$ . All nodes start with zero persuasion and reaffirmation loads. We store the interface density  $\rho_i(t)$  of each run  $i$  at given times, with time interval  $\Delta t$ . The realization is halted when it reaches  $t_{\max}$ . For a given network of size  $N$  and fixed values of  $\alpha_r$  and  $\alpha_p$  we average  $Z$  trajectories, at fixed values of  $t$ :  $\langle \rho(t) \rangle = Z^{-1} \sum_{j=1}^Z \rho_j(t)$  and  $\langle \rho^2(t) \rangle = Z^{-1} \sum_{j=1}^Z \rho_j^2(t)$ . We estimate the interface density as  $\rho(t) = \langle \rho(t) \rangle$ , compute its standard deviation as  $\sigma(\rho(t)) = \sqrt{\langle \rho^2(t) \rangle - \langle \rho(t) \rangle^2}$ , and estimate the corresponding standard error as  $s(\rho(t)) = \sigma(\rho(t))/Z$ . We construct the 95% uncertainty intervals as  $\rho(t) \pm 1.96 \times s(\rho(t))$  and use  $m_0 = 0$ ,  $\Delta t = 0.1$ , and  $Z = 100$ . The value of  $t_{\max}$  varies for each combination of  $\alpha_p$  and  $N$ .

## C.6 Detecting and excluding outliers

Here we briefly outline how to detect outliers in the airport delays data set. For the number of scheduled operations we compute the lower and upper bound as

$$x_- = q_{25} - 1.5 \times \text{IQR} \quad (\text{C.6})$$

$$x_+ = q_{75} + 1.5 \times \text{IQR} , \quad (\text{C.7})$$

with  $q_{25}$  and  $q_{75}$ , respectively, the first and third quartiles, and  $\text{IQR} = q_{75} - q_{25}$  the inter-quartile range. For the fraction of canceled and diverted operations we compute the maximum acceptable value as

$$x_{\max} = q_{75} + 1.5 \times \text{IQR} . \quad (\text{C.8})$$

We consider as valid days those that have

- a fraction of canceled arrivals, canceled departures, diverted arrivals, and diverted departures below the corresponding  $x_{\max}$ ,
- and a number of scheduled arrivals and departures between the corresponding  $x_-$  and  $x_+$ .

## C.7 Correcting timestamps

Each record in the airline on-time performance data set correspond to a single flight. The date is given in format YYYY-MM-DD and corresponds to the date of departure. All of the hours (departures and arrivals, scheduled and actual) are given in the format HHMM. We compute the delays as

$$\text{delay} = \text{actual time} - \text{scheduled time} , \quad (\text{C.9})$$

which may be negative if the flight departed or arrived before the scheduled time. However, since the date and time are given separately, this gives place to some inconsistencies:

- i) Flights that are scheduled to depart slightly after 0:00 present a huge delay if they advance their departure to 23:59 or before. We correct the actual departure timestamp by subtracting 1 calendar day.

- 
- ii) Flights that depart on the day after they were supposed to present a negative departure delay. However, negative delays also occur if a flight departs before its scheduled time. Thus we introduce a manual threshold. If a flight presents a departure delay that is smaller than -60 minutes we correct the actual departure and arrival timestamps by adding 1 calendar day.
  - iii) Flights that are scheduled to arrive on the day after present a negative scheduled flight time (i.e., scheduled arrival time – scheduled departure time). We correct the scheduled arrival timestamp by adding 1 calendar day.
  - iv) Flights that arrive on the day after present a negative flight time (i.e., actual arrival time – actual departure time). We correct the actual arrival timestamp by adding 1 calendar day.



# Supplementary figures

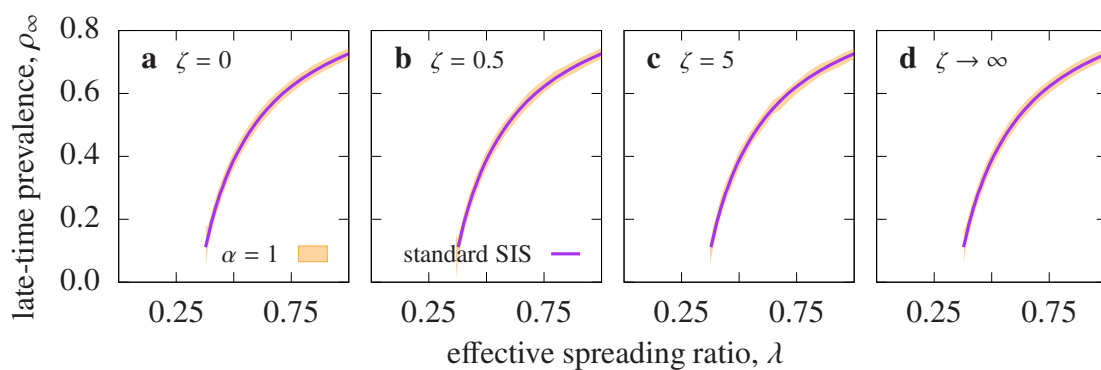


Figure D.1: **Equivalence between the standard SIS model and the miccSIS model with  $\alpha = 1$ .** Average late-time prevalence for the standard SIS model (purple curve) and standard deviation for the miccSIS model (orange shaded area) with shape parameter  $\alpha = 1$  and relaxation time (a)  $\zeta = 0$ , (b)  $\zeta = 0.5$ , (c)  $\zeta = 5$ , and (d)  $\zeta \rightarrow \infty$ , time-averaged over  $10^4$  samples, in a random degree-regular network with  $k = 4$  and  $N = 10^3$ .

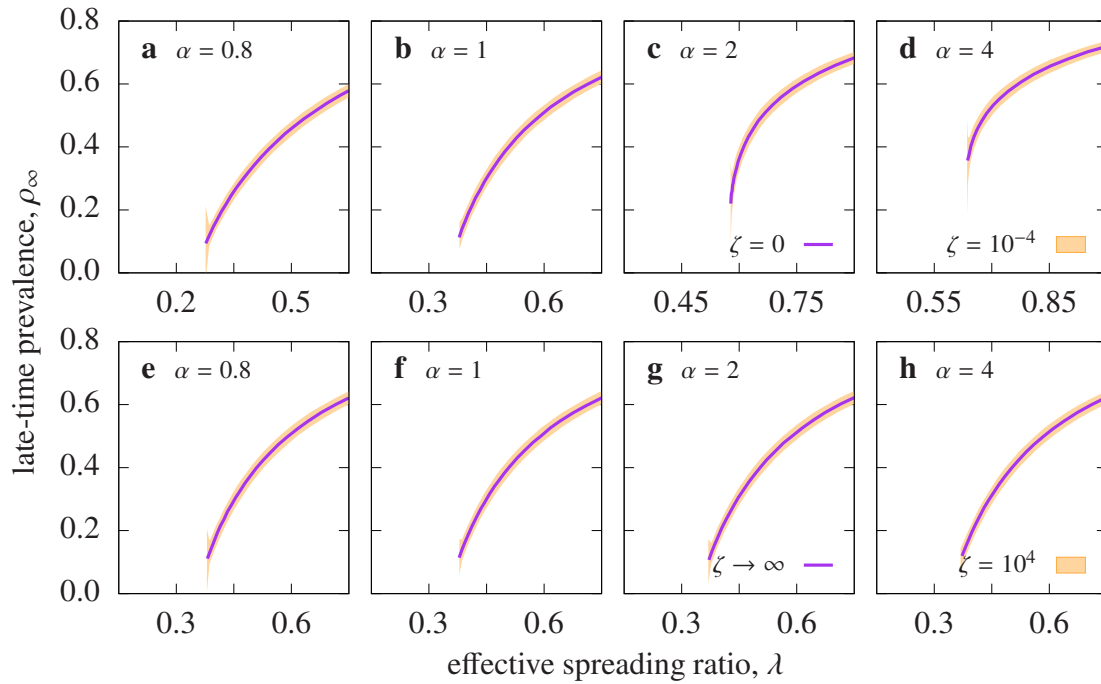


Figure D.2: **Equivalence between the miccSIS model with short-term, long-term, and limit cases of medium-term memory.** (a–d) Average late-time prevalence for short-term memory (purple curve) and standard deviation for medium-term memory with  $\zeta = 10^{-4}$  (orange shaded area), and (e–f) average late-time prevalence for long-term memory (purple curve) and standard deviation for medium-term memory with  $\zeta = 10^4$  (orange shaded area), with shape parameter (a, e)  $\alpha = 0.8$ , (b, f)  $\alpha = 1$ , (c, g)  $\alpha = 2$ , and (d, h)  $\alpha = 4$ , time-averaged over  $10^4$  samples, in a random degree-regular network with  $k = 4$  and  $N = 10^3$ .

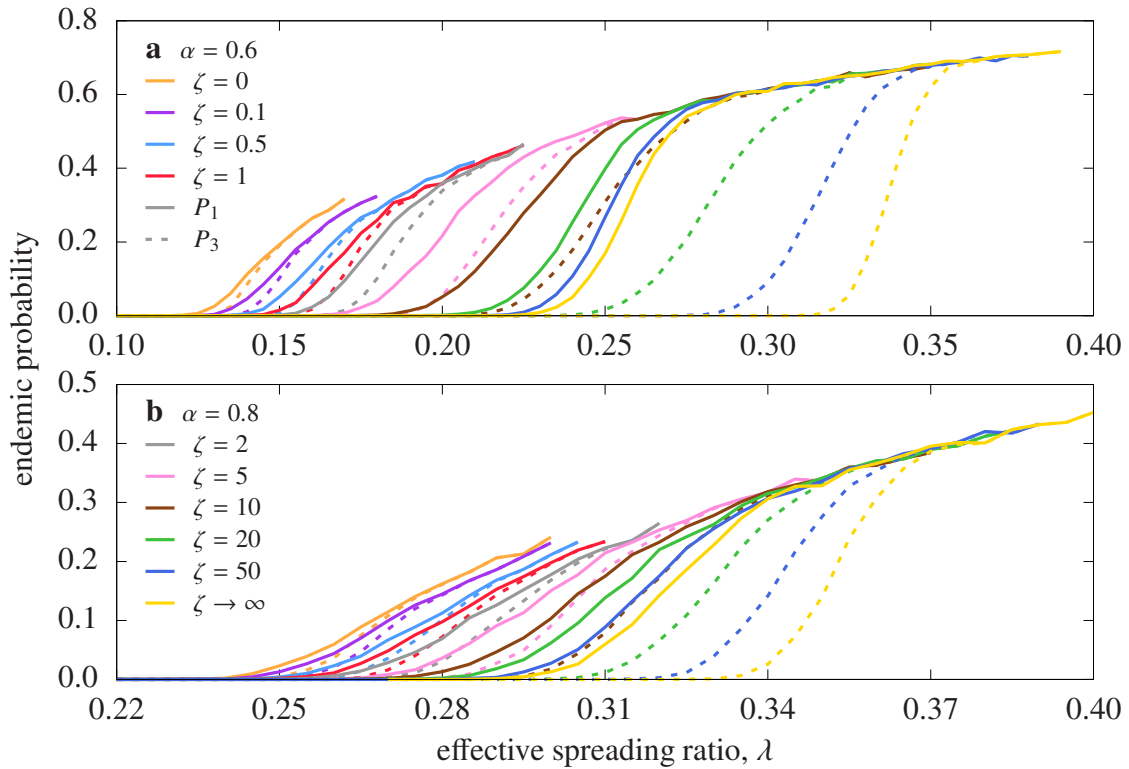


Figure D.3: **Endemic probability in the miccSIS model with medium-term memory and fat-tailed infection probabilities.** Probability that a single-seed outbreak reaches the coverage once (solid) and three times (dashed) with (a)  $\alpha = 0.6$  and (b)  $\alpha = 0.8$ , averaged over  $10^4$  independent realizations, in a random degree-regular network with  $k = 4$  and  $N = 10^3$  (relaxation time in legend). Uncertainty intervals comparable to line width.

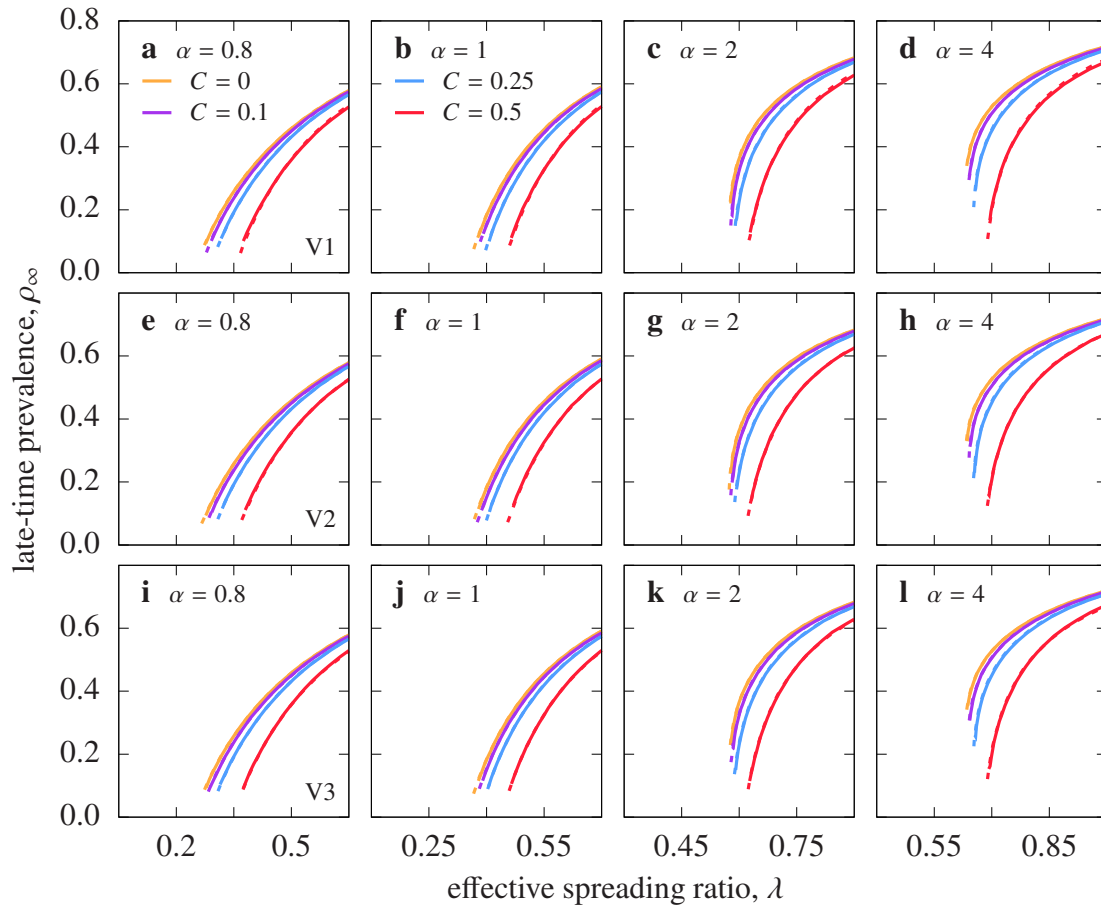


Figure D.4: **Late-time prevalence in the miccSIS model with short-term memory on clustered networks.** Results for three realizations of random degree-regular networks with  $k = 4$ ,  $N = 1000$  (solid) and  $N = 2000$  (dashed), and shape parameter (a, e, i)  $\alpha = 0.8$ , (b, f, j)  $\alpha = 1$ , (c, g, k)  $\alpha = 2$ , and (d, h, l)  $\alpha = 4$ , time-averaged over  $10^4$  samples (clustering coefficient in legend). Uncertainty intervals not appreciable at this scale.

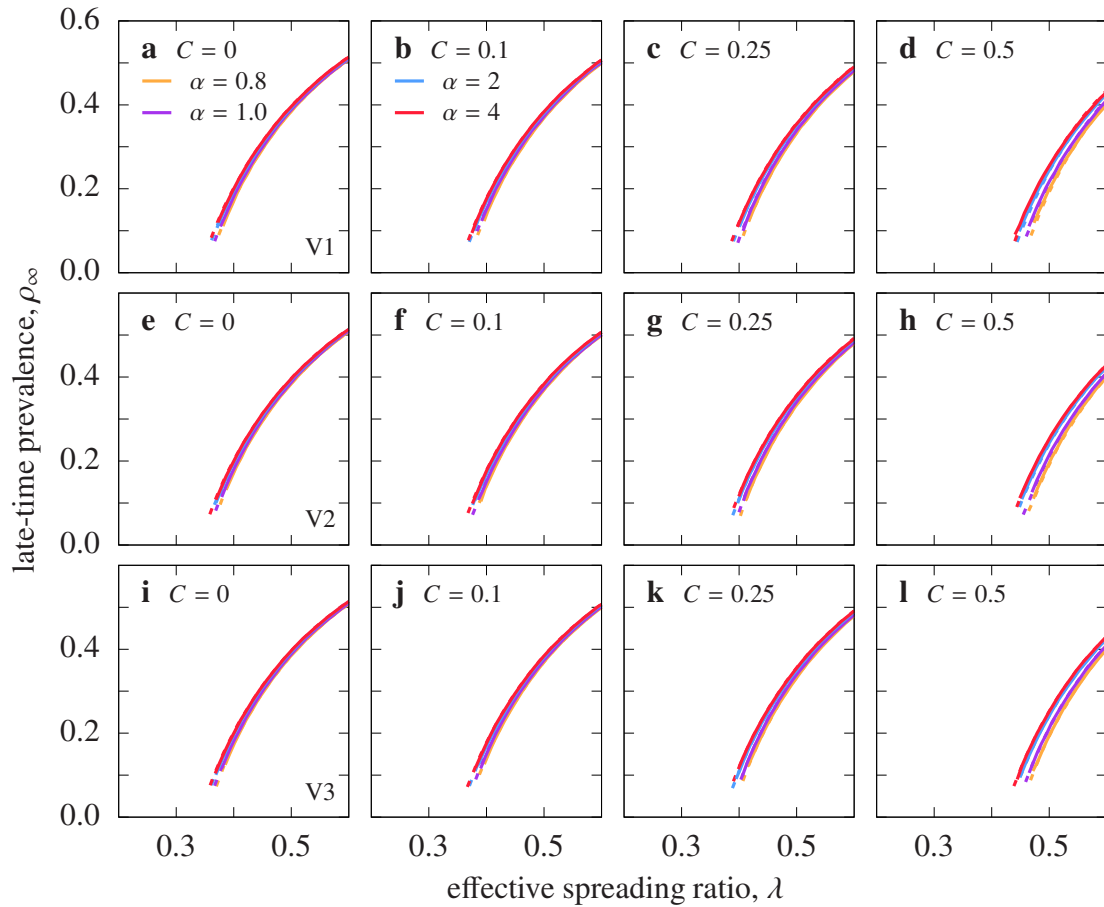


Figure D.5: **Late-time prevalence in the miccSIS model with long-term memory on clustered networks.** Results for three realizations of random degree-regular networks with  $k = 4$ ,  $N = 1000$  (solid) and  $N = 2000$  (dashed), and clustering coefficient (a, e, i)  $C = 0$ , (b, f, j)  $C = 0.1$ , (c, g, k)  $C = 0.25$ , and (d, h, l)  $C = 0.5$ , time-averaged over  $10^4$  samples (shape parameter in legend). Uncertainty intervals not appreciable at this scale.

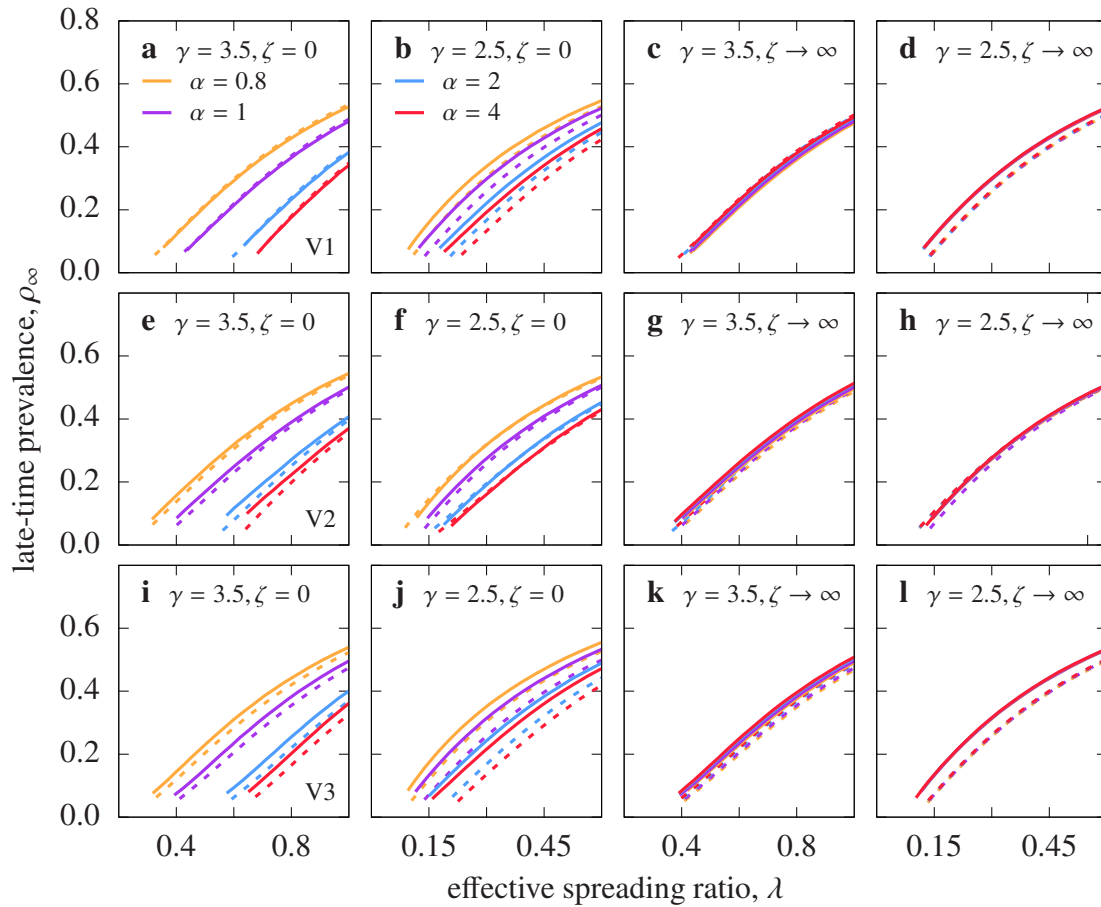


Figure D.6: **Late-time prevalence in the miccSIS model on scale-free networks.** Results for three realizations of random degree-regular networks with  $k = 4$ ,  $N = 1000$  (solid) and  $N = 2000$  (dashed), and exponent (a, c, e, g, i, k)  $\gamma = 3.5$  and (b, d, f, h, j, l)  $\gamma = 2.5$ , for (a, b, e, f, i, j) short-term and (c, d, g, h, k, l) long-term memory, time-averaged over  $10^4$  samples (shape parameter in legend). Uncertainty intervals not appreciable at this scale.

# References

- [1] R. Albert, & A.-L. Barabási (2002). Statistical mechanics of complex networks. *Reviews of Modern Physics*, 74(1), 47–97. <https://doi.org/10.1103/RevModPhys.74.47>. 5
- [2] R. Albert, H. Jeong, & A.-L. Barabási (1999). Diameter of the worldwide web. *Nature*, 401(6749), 130–131. <https://doi.org/10.1038/43601>. 5
- [3] A. Allard, B. M. Althouse, S. V. Scarpino, & L. Hébert-Dufresne (2017). Asymmetric percolation drives a double transition in sexual contact networks. *Proceedings of the National Academy of Sciences*, 114(34), 8969–8973. <https://doi.org/10.1073/pnas.1703073114>. 79
- [4] R. M. Anderson, & R. M. May (1991). *Infectious diseases of humans: Dynamics and control*. Oxford University Press. 4, 6
- [5] S. Aral, & D. Walker (2011). Creating social contagion through viral product design: A randomized trial of peer influence in networks. *Management Science*, 57(9), 1623–1639. <https://doi.org/10.1287/mnsc.1110.1421>. 8
- [6] N. T. Bailey (1975). *The mathematical theory of infectious diseases and its applications*, 2nd edition. Griffin. 4
- [7] P. Bajardi, C. Poletto, J. J. Ramasco, M. Tizzoni, V. Colizza, & A. Vespignani (2011). Human mobility networks, travel restrictions, and the global spread of 2009 H1N1 pandemic. *PLOS ONE*, 6(1), Article 16591. <https://doi.org/10.1371/journal.pone.0016591>. 7
- [8] D. Balcan, V. Colizza, B. Gonçalves, H. Hu, J. J. Ramasco, & A. Vespignani (2009). Multiscale mobility networks and the spatial spreading of infectious diseases. *Proceedings of the National Academy of Sciences*, 106(51), 21484–21489. <https://doi.org/10.1073/pnas.0906910106>. 7

- [9] D. Balcan, B. Gonçalves, H. Hu, J. J. Ramasco, V. Colizza, & A. Vespignani (2010). Modeling the spatial spread of infectious diseases: The global epidemic and mobility computational model. *Journal of Computational Science*, 1(3), 132–145. <https://doi.org/10.1016/j.jocs.2010.07.002>. 7
- [10] D. Balcan, H. Hu, B. Goncalves, P. Bajardi, C. Poletto, J. J. Ramasco, D. Paolotti, N. Perra, M. Tizzoni, W. Van den Broeck, V. Colizza, & A. Vespignani (2009). Seasonal transmission potential and activity peaks of the new influenza A(H1N1): a Monte Carlo likelihood analysis based on human mobility. *BMC Medicine*, 7(1), Article 45. <https://doi.org/10.1186/1741-7015-7-45>. 7
- [11] F. Battiston, G. Cencetti, I. Iacopini, V. Latora, M. Lucas, A. Patania, J.-G. Young, & G. Petri (2020). Networks beyond pairwise interactions: Structure and dynamics. *Physics Reports*, 874, 1–92. <https://doi.org/https://doi.org/10.1016/j.physrep.2020.05.004>. Networks beyond pairwise interactions: Structure and dynamics. 11
- [12] F. Battiston, F. Musciotto, D. Wang, A.-L. Barabási, M. Szell, & R. Sinatra (2019). Taking census of physics. *Nature Reviews Physics*, 1(1), 89–97. <https://doi.org/10.1038/s42254-018-0005-3>. 8
- [13] D. Bernoulli, & S. Blower (2004). An attempt at a new analysis of the mortality caused by smallpox and of the advantages of inoculation to prevent it. *Reviews in Medical Virology*, 14(5), 275–288. <https://doi.org/10.1002/rmv.443>. 1
- [14] S. P. Blythe, & R. M. Anderson (1988). Variable infectiousness in HIV transmission models. *Mathematical Medicine and Biology*, 5(3), 181–200. <https://doi.org/10.1093/imamb/5.3.181>. 10
- [15] M. Boguñá, C. Castellano, & R. Pastor-Satorras (2013). Nature of the epidemic threshold for the susceptible-infected-susceptible dynamics in networks. *Physical Review Letters*, 111(6), Article 068701. <https://doi.org/10.1103/PhysRevLett.111.068701>. 48, 81, 86
- [16] M. Boguñá, R. Pastor-Satorras, & A. Vespignani (2003). Absence of epidemic threshold in scale-free networks with degree correlations.

- Physical Review Letters*, 90(2), Article 028701. <https://doi.org/10.1103/PhysRevLett.90.028701>. 5
- [17] M. Boguñá, L. F. Lafuerza, R. Toral, & M. Á. Serrano (2014). Simulating non-Markovian stochastic processes. *Physical Review E*, 90(4), Article 042108. <https://doi.org/10.1103/PhysRevE.90.042108>. 27
- [18] M. Boguñá, R. Pastor-Satorras, & A. Vespignani (2004). Cut-offs and finite size effects in scale-free networks. *The European Physical Journal B*, 38(2), 205–209. <https://doi.org/10.1140/epjb/e2004-00038-8>. 140
- [19] B. Bollobás (2001). *Random graphs*, 2nd edition. Cambridge University Press. <https://doi.org/10.1017/CBO9780511814068>. 140
- [20] R. M. Bond, C. J. Fariss, J. J. Jones, A. D. I. Kramer, C. Marlow, J. E. Settle, & J. H. Fowler (2012). A 61-million-person experiment in social influence and political mobilization. *Nature*, 489(7415), 295–298. <https://doi.org/10.1038/nature11421>. 9
- [21] F. Brauer, & C. Castillo-Chavez (2012). *Mathematical models in population biology and epidemiology*, 2nd edition. Springer. <https://doi.org/10.1007/978-1-4614-1686-9>. 2, 3
- [22] D. Brockmann, & D. Helbing (2013). The hidden geometry of complex, network-driven contagion phenomena. *Science*, 342(6164), 1337–1342. <https://doi.org/10.1126/science.1245200>. 11
- [23] Bureau of Transportation Statistics (2020). *Airline on-time performance data* [Data set]. United States Department of Transportation. [https://www.transtats.bts.gov/tables.asp?Table\\_ID=236&SYS\\_Table\\_Name=T\\_ONTIME\\_REPORTING](https://www.transtats.bts.gov/tables.asp?Table_ID=236&SYS_Table_Name=T_ONTIME_REPORTING). 101
- [24] W. Cai, L. Chen, F. Ghanbarnejad, & P. Grassberger (2015). Avalanche outbreaks emerging in cooperative contagions. *Nature Physics*, 11(11), 936–940. <https://doi.org/10.1038/nphys3457>. 64
- [25] E. Campbell, & M. Salathé (2013). Complex social contagion makes networks more vulnerable to disease outbreaks. *Scientific Reports*, 3(1), Article 1905. <https://doi.org/10.1038/srep01905>. 10

- [26] C. Castellano, S. Fortunato, & V. Loreto (2009). Statistical physics of social dynamics. *Reviews of Modern Physics*, 81(2), 591–646. <https://doi.org/10.1103/RevModPhys.81.591>. 9
- [27] X. Castelló, V. M. Eguíluz, & M. San Miguel (2006). Ordering dynamics with two non-excluding options: bilingualism in language competition. *New Journal of Physics*, 8(12), 308–308. <https://doi.org/10.1088/1367-2630/8/12/308>. 91
- [28] Center for Disease Control and Prevention (2016). *History of smallpox*. <https://www.cdc.gov/smallpox/history/history.html>. 1, 5
- [29] D. Centola (2010). The spread of behavior in an online social network experiment. *Science*, 329(5996), 1194–1197. <https://doi.org/10.1126/science.1185231>. 8
- [30] D. Centola, & M. Macy (2007). Complex contagions and the weakness of long ties. *American Journal of Sociology*, 113(3), 702–734. <https://doi.org/10.1086/521848>. 8, 9
- [31] L. Chen, F. Ghanbarnejad, & D. Brockmann (2017). Fundamental properties of cooperative contagion processes. *New Journal of Physics*, 19(10), Article 103041. <https://doi.org/10.1088/1367-2630/aa8bd2>. 11
- [32] X. Chen, R. Wang, M. Tang, S. Cai, H. E. Stanley, & L. A. Braunstein (2018). Suppressing epidemic spreading in multiplex networks with social-support. *New Journal of Physics*, 20(1), Article 013007. <https://doi.org/10.1088/1367-2630/aa9cda>. 64, 79
- [33] M. Chinazzi, J. T. Davis, M. Ajelli, C. Gioannini, M. Litvinova, S. Merler, A. Pastore y Piontti, K. Mu, L. Rossi, K. Sun, C. Viboud, X. Xiong, H. Yu, M. E. Halloran, I. M. Longini, & A. Vespignani (2020). The effect of travel restrictions on the spread of the 2019 novel coronavirus (COVID-19) outbreak. *Science*, 368(6489), 395–400. <https://doi.org/10.1126/science.aba9757>. 7
- [34] W. Choi, D. Lee, & B. Kahng (2017). Critical behavior of a two-step contagion model with multiple seeds. *Physical Review E*, 95(6), Article 062115. <https://doi.org/10.1103/PhysRevE.95.062115>. 11

- [35] W. Choi, D. Lee, & B. Kahng (2017). Mixed-order phase transition in a two-step contagion model with a single infectious seed. *Physical Review E*, 95(2), Article 022304. <https://doi.org/10.1103/PhysRevE.95.022304>. 11
- [36] G. Chowell, & H. Nishiura (2014). Transmission dynamics and control of Ebola virus disease (EVD): a review. *BMC Medicine*, 12(1), Article 196. <https://doi.org/10.1186/s12916-014-0196-0>. 10
- [37] N. A. Christakis, & J. H. Fowler (2007). The spread of obesity in a large social network over 32 years. *New England Journal of Medicine*, 357(4), 370–379. <https://doi.org/10.1056/NEJMs066082>. 10
- [38] N. A. Christakis, & J. H. Fowler (2008). The collective dynamics of smoking in a large social network. *New England Journal of Medicine*, 358(21), 2249–2258. <https://doi.org/10.1056/NEJMs0706154>. 10
- [39] N. A. Christakis, & J. H. Fowler (2013). Social contagion theory: examining dynamic social networks and human behavior. *Statistics in Medicine*, 32(4), 556–577. <https://doi.org/10.1002/sim.5408>. 10
- [40] P. Clifford, & A. Sudbury (1973). A model for spatial conflict. *Biometrika*, 60(3), 581–588. <https://doi.org/10.1093/biomet/60.3.581>. 9, 91
- [41] T. J. Coates, L. Richter, & C. Caceres (2008). Behavioural strategies to reduce HIV transmission: how to make them work better. *The Lancet*, 372(9639), 669–684. [https://doi.org/10.1016/S0140-6736\(08\)60886-7](https://doi.org/10.1016/S0140-6736(08)60886-7). 10
- [42] R. Cohen, S. Havlin, & D. ben-Avraham (2003). Efficient immunization strategies for computer networks and populations. *Physical Review Letters*, 91(24), Article 247901. <https://doi.org/10.1103/PhysRevLett.91.247901>. 6
- [43] V. Colizza, A. Barrat, M. Barthélemy, A.-J. Valleron, & A. Vespignani (2007). Modeling the worldwide spread of pandemic influenza: Baseline case and containment interventions. *PLOS Medicine*, 4(1), Article 13. <https://doi.org/10.1371/journal.pmed.0040013>. 7

- [44] V. Colizza, A. Barrat, M. Barthélemy, & A. Vespignani (2006). The role of the airline transportation network in the prediction and predictability of global epidemics. *Proceedings of the National Academy of Sciences*, 103(7), 2015–2020. <https://doi.org/10.1073/pnas.0510525103>. 7
- [45] P. Colomer-de-Simón, & M. Boguñá (2014). Double percolation phase transition in clustered complex networks. *Physical Review X*, 4(4), Article 041020. <https://doi.org/10.1103/PhysRevX.4.041020>. 79, 139
- [46] P. Colomer-de Simón, M. Á. Serrano, M. G. Beiró, J. I. Alvarez-Hamelin, & M. Boguñá (2013). Deciphering the global organization of clustering in real complex networks. *Scientific Reports*, 3(1), Article 2517. <https://doi.org/10.1038/srep02517>. 139
- [47] P. Colomer-de-Simón (2017). *RandNetGen* [Code repository]. Github. <https://github.com/polcolomer/RandNetGen>. 140
- [48] D. Cox (1970). *Renewal theory*. Methuen & Co. 10, 14, 27, 127, 136
- [49] D. Cucinotta, & M. Vanelli (2020). WHO declares COVID-19 a pandemic. *Acta Biomedica*, 91(1), 157–160. <https://doi.org/10.23750/abm.v91i1.9397>. 1
- [50] D. J. Daley, & J. Gani (1999). *Epidemic modelling: An introduction*. Cambridge University Press. <https://doi.org/10.1017/CB09780511608834>. 1, 3, 8, 43
- [51] G. F. de Arruda, E. Cozzo, T. P. Peixoto, F. A. Rodrigues, & Y. Moreno (2017). Disease localization in multilayer networks. *Phys. Rev. X*, 7(1), Article 011014. <https://doi.org/10.1103/PhysRevX.7.011014>. 11
- [52] G. F. de Arruda, G. Petri, F. A. Rodrigues, & Y. Moreno (2020). Impact of the distribution of recovery rates on disease spreading in complex networks. *Physical Review Research*, 2(1), Article 013046. <https://doi.org/10.1103/PhysRevResearch.2.013046>. 11

- [53] M. De Domenico, C. Granell, M. A. Porter, & A. Arenas (2016). The physics of spreading processes in multilayer networks. *Nature Physics*, 12(10), 901–906. <https://doi.org/10.1038/nphys3865>. 11
- [54] F. R. DeLeo, & B. J. Hinnebusch (2005). A plague upon the phagocytes. *Nature Medicine*, 11(9), 927–928. <https://doi.org/10.1038/nm0905-927>. 7
- [55] P. della Briotta Parolo, R. Kujala, K. Kaski, & M. Kivelä (2020). Tracking the cumulative knowledge spreading in a comprehensive citation network. *Physical Review Research*, 2(1), Article 013181. <https://doi.org/10.1103/PhysRevResearch.2.013181>. 8
- [56] K. P. Devakumar (2020). *SARS 2003 outbreak dataset* (version 5) [Data set]. Kaggle. <https://www.kaggle.com/imdevskp/sars-outbreak-2003-complete-dataset>. 8
- [57] Z. Dezső, & A.-L. Barabási (2002). Halting viruses in scale-free networks. *Physical Review E*, 65(5), Article 055103(R). <https://doi.org/10.1103/PhysRevE.65.055103>. 6
- [58] K. Dietz, & J. A. P. Heesterbeek (2002). Daniel Bernoulli’s epidemiological model revisited. *Mathematical Biosciences*, 180(1), 1–21. [https://doi.org/10.1016/S0025-5564\(02\)00122-0](https://doi.org/10.1016/S0025-5564(02)00122-0). 1
- [59] P. S. Dodds, & D. J. Watts (2004). Universal behavior in a generalized model of contagion. *Physical Review Letters*, 92(21), Article 218701. <https://doi.org/10.1103/PhysRevLett.92.218701>. 11, 19, 64, 79
- [60] P. S. Dodds, & D. J. Watts (2005). A generalized model of social and biological contagion. *Journal of Theoretical Biology*, 232(4), 587–604. <https://doi.org/10.1016/j.jtbi.2004.09.006>. 19
- [61] V. M. Eguíluz, & K. Klemm (2002). Epidemic threshold in structured scale-free networks. *Physical Review Letters*, 89(10), Article 108701. <https://doi.org/10.1103/PhysRevLett.89.108701>. 5
- [62] R. W. Eisinger, & A. S. Fauci (2018). Ending the HIV/AIDS pandemic. *Emerging Infectious Diseases*, 24(3), 413–416. <https://doi.org/10.3201/eid2403.171797>. 1

- [63] P. D. En'ko (1989). On the course of epidemics of some infectious diseases. *International Journal of Epidemiology*, 18(4), 749–755. <https://doi.org/10.1093/ije/18.4.749>. 3
- [64] EUROCONTROL & FAA (2019). *2018 comparison of air traffic management related operational performance: US/Europe*. <https://ec.europa.eu/transport/sites/transport/files/us-europe-comparison-of-atm-related-operational-performance-2018.pdf>. 106
- [65] J. W. Evans (1991). Kinetic phase transitions in catalytic reaction models. *Langmuir*, 7(11), 2514–2519. <https://doi.org/10.1021/la00059a020>. 91
- [66] J. W. Evans, & T. R. Ray. Kinetics of the monomer-monomer surface reaction model. *Physical Review E*, 47(2), 1018–1025. <https://doi.org/10.1103/PhysRevE.47.1018>. 91
- [67] M. Faloutsos, P. Faloutsos, & C. Faloutsos (1999). On power-law relationships of the internet topology. *ACM SIGCOMM Computer Communication Review*, 29(4), 251–262. <https://doi.org/10.1145/316194.316229>. 5
- [68] M. Feng, S.-M. Cai, M. Tang, & Y.-C. Lai (2019). Equivalence and its invalidation between non-Markovian and Markovian spreading dynamics on complex networks. *Nature Communications*, 10(1), Article 3748. <https://doi.org/10.1038/s41467-019-11763-z>. 11
- [69] P. G. Fennell, S. Melnik, & J. P. Gleeson (2016). Limitations of discrete-time approaches to continuous-time contagion dynamics. *Physical Review E*, 94(5), Article 052125. <https://doi.org/10.1103/PhysRevE.94.052125>. 19
- [70] J. Fernández-Gracia, K. Suchecki, J. J. Ramasco, M. San Miguel, & V. M. Eguíluz (2014). Is the voter model a model for voters? *Physical Review Letters*, 112(15), Article 158701. <https://doi.org/10.1103/PhysRevLett.112.158701>. 9, 91
- [71] P. Fine, C. G. Victora, K. J. Rothman, P. S. Moore, Y. Chang, V. Curtis, D. L. Heymann, G. Slutkin, R. M. May, V. Patel, I. Roberts, R. Wortley,

- C. Torgerson, & A. Deaton (2013). John Snow's legacy: epidemiology without borders. *The Lancet*, 381(9874), 1302–1311. [https://doi.org/10.1016/S0140-6736\(13\)60771-0](https://doi.org/10.1016/S0140-6736(13)60771-0). 2
- [72] P. E. M. Fine (1977). A commentary on the mechanical analogue to the Reed-Frost epidemic model. *American Journal of Epidemiology*, 106(2), 87–100. <https://doi.org/10.1093/oxfordjournals.aje.a112449>. 4
- [73] S. Fortunato, & D. Hric (2016). Community detection in networks: A user guide. *Physics Reports*, 659, 1–44. <https://doi.org/https://doi.org/10.1016/j.physrep.2016.09.002>. 9
- [74] W. H. Frost (1976). Some conceptions of epidemics in general. *American Journal of Epidemiology*, 103(2), 141–151. <https://doi.org/10.1093/oxfordjournals.aje.a112212>. 4
- [75] F. Fu, N. A. Christakis, & J. H. Fowler (2017). Dueling biological and social contagions. *Scientific Reports*, 7(1), Article 43634. <https://doi.org/10.1038/srep43634>. 11
- [76] G. García-Pérez, A. Allard, M. Á. Serrano, & M. Boguñá (2019). Mercator: uncovering faithful hyperbolic embeddings of complex networks. *New Journal of Physics*, 21(12), Article 123033. <https://doi.org/10.1088/1367-2630/ab57d2>. 11
- [77] D. T. Gillespie (1976). A general method for numerically simulating the stochastic time evolution of coupled chemical reactions. *Journal of Computational Physics*, 22(4), 403–434. [https://doi.org/10.1016/0021-9991\(76\)90041-3](https://doi.org/10.1016/0021-9991(76)90041-3). 16
- [78] D. T. Gillespie (1977). Exact stochastic simulation of coupled chemical reactions. *The Journal of Physical Chemistry*, 81(25), 2340–2361. <https://doi.org/10.1021/j100540a008>. 16
- [79] W. Goffman, & V. A. Newill (1964). Generalization of epidemic theory: An application to the transmission of ideas. *Nature*, 204(4955), 225–228. <https://doi.org/10.1038/204225a0>. 8

- [80] J. Gómez-Gardeñes, L. Lotero, S. N. Taraskin, & F. J. Pérez-Reche (2016). Explosive contagion in networks. *Scientific Reports*, 6(1), Article 19767. <https://doi.org/10.1038/srep19767>. 23, 64
- [81] C. Granell, S. Gómez, & A. Arenas (2013). Dynamical interplay between awareness and epidemic spreading in multiplex networks. *Physical Review Letters*, 111(12), Article 128701. <https://doi.org/10.1103/PhysRevLett.111.128701>. 10
- [82] M. S. Granovetter (1973). The strength of weak ties. *American Journal of Sociology*, 78(6), 1360–1380. <http://www.jstor.org/stable/2776392>. 9
- [83] G. R. Grimmett, & D. R. Stirzaker (2020). *Probability and random processes*, 4th edition. Oxford University Press. 10, 20
- [84] D. Guilbeault, J. Becker, & D. Centola (2018). Complex contagions: A decade in review. In S. Lehmann, & Y.-Y. Ahn (Eds.) *Complex spreading phenomena in social systems: Influence and contagion in real-world social networks* (pp. 3–25). Springer International Publishing. [https://doi.org/10.1007/978-3-319-77332-2\\_1](https://doi.org/10.1007/978-3-319-77332-2_1). 9
- [85] L. Hébert-Dufresne, & A. Allard (2019). Smear phase transitions in percolation on real complex networks. *Physical Review Research*, 1(1), Article 013009. <https://doi.org/10.1103/PhysRevResearch.1.013009>. 81
- [86] H. W. Hethcote (2000). The mathematics of infectious diseases. *SIAM Review*, 42(4), 599–653. <https://doi.org/10.1137/S0036144500371907>. 1, 3
- [87] X. R. Hoffmann (2021). *networks* [Code repository]. Github. <https://github.com/xhoffmann/networks>. 139, 140
- [88] R. A. Holley, & T. M. Liggett (1975). Ergodic theorems for weakly interacting infinite systems and the voter model. *Annals of Probability*, 3(4), 643–663. <https://doi.org/10.1214/aop/1176996306>. 9, 91

- [89] B. A. Huberman, & L. A. Adamic (1999). Growth dynamics of the world-wide web. *Nature*, 401(6749), 131. <https://doi.org/10.1038/43604.5>
- [90] L. Hébert-Dufresne, S. V. Scarpino, & J.-G. Young (2020). Macroscopic patterns of interacting contagions are indistinguishable from social reinforcement. *Nature Physics*, 16(4), 426–431. <https://doi.org/10.1038/s41567-020-0791-2>. 11, 78
- [91] I. Iacopini, G. Petri, A. Barrat, & V. Latora (2019). Simplicial models of social contagion. *Nature Communications*, 10(1), Article 2485. <https://doi.org/10.1038/s41467-019-10431-6>. 11
- [92] H. Jeong, B. Tombor, R. Albert, Z. N. Oltvai, & A.-L. Barabási (2000). The large-scale organization of metabolic networks. *Nature*, 407(6804), 651–654. <https://doi.org/10.1038/35036627.5>
- [93] R. Jie, J. Qiao, G. Xu, & Y. Meng (2016). A study on the interaction between two rumors in homogeneous complex networks under symmetric conditions. *Physica A*, 454, 129–142. <https://doi.org/https://doi.org/10.1016/j.physa.2016.02.048>. 11
- [94] F. Jin, E. Dougherty, P. Saraf, Y. Cao, & N. Ramakrishnan (2013). Epidemiological modeling of news and rumors on Twitter. *Proceedings of the 7th Workshop on Social Network Mining and Analysis*, (p. Article 8). <https://doi.org/10.1145/2501025.2501027>. 8, 43
- [95] J. H. Jones, & M. S. Handcock (2003). Sexual contacts and epidemic thresholds. *Nature*, 423(6940), 605–606. <https://doi.org/10.1038/423605a.5>
- [96] M. Karsai, G. Iñiguez, K. Kaski, & J. Kertész (2014). Complex contagion process in spreading of online innovation. *Journal of The Royal Society Interface*, 11(101), Article 20140694. <https://doi.org/10.1098/rsif.2014.0694>. 8
- [97] M. Karsai, H.-H. Jo, & K. Kaski (2018). *Bursty human dynamics*. Springer. <https://doi.org/10.1007/978-3-319-68540-3>. 11
- [98] M. J. Keeling, & P. Rohani (2008). *Modeling infectious diseases in humans and animals*. Princeton University Press. 2, 4, 31, 43

- [99] W. O. Kermack, & A. G. McKendrick (1927). A contribution to the mathematical theory of epidemics. *Proceedings of the Royal Society A*, 115(772), 700–721. <https://doi.org/10.1098/rspa.1927.0118>. 3
- [100] W. O. Kermack, & A. G. McKendrick (1932). Contributions to the mathematical theory of epidemics. II: The problem of endemicity. *Proceedings of the Royal Society A*, 138(834), 55–83. <https://doi.org/10.1098/rspa.1932.0171>. 3
- [101] W. O. Kermack, & A. G. McKendrick (1933). Contributions to the mathematical theory of epidemics. III: Further studies of the problem of endemicity. *Proceedings of the Royal Society A*, 141(843), 94–122. <https://doi.org/10.1098/rspa.1933.0106>. 3
- [102] I. Z. Kiss, J. C. Miller, & P. L. Simon (2017). *Mathematics of epidemics on networks*. Springer. <https://doi.org/10.1007/978-3-319-50806-1>. 11, 18, 46
- [103] I. Z. Kiss, G. Röst, & Z. Vizi (2015). Generalization of pairwise models to non-Markovian epidemics on networks. *Physical Review Letters*, 115(7), Article 078701. <https://doi.org/10.1103/PhysRevLett.115.078701>. 11
- [104] C. J. Kuhlman, V. S. A. Kumar, M. V. Marathe, S. S. Ravi, & D. J. Rosenkrantz (2011). Effects of opposition on the diffusion of complex contagions in social networks: An empirical study. *4th International Conference on Social Computing, Behavioral-Cultural Modeling and Prediction*, (pp. 188–196). [https://doi.org/10.1007/978-3-642-19656-0\\_28](https://doi.org/10.1007/978-3-642-19656-0_28). 10
- [105] J. M. Last (2007). *A dictionary of public health*, 2nd edition. Oxford University Press. <https://doi.org/10.1093/acref/9780195160901.001.0001>. 2
- [106] T. Leng, & M. J. Keeling (2020). Improving pairwise approximations for network models with susceptible-infected-susceptible dynamics. *Journal of Theoretical Biology*, 500, Article 110328. <https://doi.org/10.1016/j.jtbi.2020.110328>. 18, 46

- [107] T. Leung, P. T. Campbell, B. D. Hughes, F. Frascoli, & J. M. McCaw (2018). Infection-acquired versus vaccine-acquired immunity in an SIRWS model. *Infectious Disease Modelling*, 3, 118–135. <https://doi.org/10.1016/j.idm.2018.06.002>. 43
- [108] F. Liljeros, C. R. Edling, L. A. N. Amaral, H. E. Stanley, & Y. Åberg (2001). The web of human sexual contacts. *Nature*, 411(6840), 907–908. <https://doi.org/10.1038/35082140>. 5
- [109] Z.-H. Lin, M. Feng, M. Tang, Z. Liu, C. Xu, P. M. Hui, & Y.-C. Lai (2020). Non-Markovian recovery makes complex networks more resilient against large-scale failures. *Nature Communications*, 11(1), Article 2490. <https://doi.org/10.1038/s41467-020-15860-2>. 11
- [110] Q. Liu, & P. Van Mieghem (2018). Burst of virus infection and a possibly largest epidemic threshold of non-Markovian susceptible-infected-susceptible processes on networks. *Physical Review E*, 97(2), Article 022309. <https://doi.org/10.1103/PhysRevE.97.022309>. 11, 57
- [111] Q.-H. Liu, W. Wang, M. Tang, T. Zhou, & Y.-C. Lai (2017). Explosive spreading on complex networks: The role of synergy. *Physical Review E*, 95(4), Article 042320. <https://doi.org/10.1103/PhysRevE.95.042320>. 23
- [112] J. O. Lloyd-Smith, S. J. Schreiber, P. E. Kopp, & W. M. Getz (2005). Superspreading and the effect of individual variation on disease emergence. *Nature*, 438(7066), 355–359. <https://doi.org/10.1038/nature04153>. 7
- [113] L. Lü, D.-B. Chen, & T. Zhou (2011). The small world yields the most effective information spreading. *New Journal of Physics*, 13(12), Article 123005. <https://doi.org/10.1088/1367-2630/13/12/123005>. 11
- [114] A. Maritan, F. Colaiori, A. Flammini, M. Cieplak, & J. R. Banavar (1996). Universality classes of optimal channel networks. *Science*, 272(5264), 984–986. <https://doi.org/10.1126/science.272.5264.984>. 5

- [115] A. S. Mata, M. Boguñá, C. Castellano, & R. Pastor-Satorras (2015). Lifespan method as a tool to study criticality in absorbing-state phase transitions. *Physical Review E*, 91(5), Article 052117. <https://doi.org/10.1103/PhysRevE.91.052117>. 48
- [116] S. Milgram (1967). The small-world problem. *Psychology Today*, 1(1), 61–67. 5
- [117] B. Min, & M. San Miguel (2018). Competing contagion processes: Complex contagion triggered by simple contagion. *Scientific Reports*, 8(1), Article 10422. <https://doi.org/10.1038/s41598-018-28615-3>. 57
- [118] G. Mosquera-Doñate, & M. Boguñá (2015). Follow the leader: Herding behavior in heterogeneous populations. *Physical Review E*, 91(5), Article 052804. <https://doi.org/10.1103/PhysRevE.91.052804>. 91, 92
- [119] M. A. Muñoz, R. Juhász, C. Castellano, & G. Ódor (2010). Griffiths phases on complex networks. *Physical Review Letters*, 105(12), Article 128701. <https://doi.org/10.1103/PhysRevLett.105.128701>. 81
- [120] Metropolitan Washington Airports Authority (2019). *Dulles International and Reagan National airports passenger traffic tops 47.5 million in 2018*. <https://www.mwaa.com/about/dulles-international-and-reagan-national-airports-passenger-traffic-tops-475-million-2018>. 101
- [121] S. A. Myers, & J. Leskovec (2012). Clash of the contagions: Cooperation and competition in information diffusion. *2012 IEEE 12th International Conference on Data Mining*, (pp. 539–548). <https://doi.org/10.1109/ICDM.2012.159>. 11
- [122] S. Myneni, K. Fujimoto, N. Cobb, & T. Cohen (2015). Content-driven analysis of an online community for smoking cessation: Integration of qualitative techniques, automated text analysis, and affiliation networks. *American Journal of Public Health*, 105(6), 1206–1212. <https://doi.org/10.2105/AJPH.2014.302464>. 10

- [123] M. E. J. Newman (2010). *Networks: An introduction*. Oxford University Press. <https://doi.org/10.1093/acprof:oso/9780199206650.001.0001>. 5, 10, 81, 140
- [124] X. Nie, & T. Molen (2015). Host recovery and reduced virus level in the upper peaves after *Potato virus Y* infection occur in tobacco and tomato but not in potato plants. *Viruses*, 7(2), 680–698. 31
- [125] D. Normile (2013). The metropole, superspreaders, and other mysteries. *Science*, 339(6125), 1272–1273. <https://doi.org/10.1126/science.339.6125.1272>. 7
- [126] T. Ohira, & R. Sawatari (1998). Phase transition in a computer network traffic model. *Physical Review E*, 58(1), 193–195. <https://doi.org/10.1103/PhysRevE.58.193>. 8
- [127] J.-P. Onnela, J. Saramäki, J. Hyvönen, G. Szabó, D. Lazer, K. Kaski, J. Kertész, & A.-L. Barabási (2007). Structure and tie strengths in mobile communication networks. *Proceedings of the National Academy of Sciences*, 104(18), 7332–7336. <https://doi.org/10.1073/pnas.0610245104>. 9, 81
- [128] C. Orsini, M. M. Dankulov, P. Colomer-de Simón, A. Jamakovic, P. Mahadevan, A. Vahdat, K. E. Bassler, Z. Toroczkai, M. Boguñá, G. Caldarelli, S. Fortunato, & D. Krioukov (2015). Quantifying randomness in real networks. *Nature Communications*, 6(1), Article 8627. <https://doi.org/10.1038/ncomms9627>. 139
- [129] E. Ortiz, M. Starnini, & M. Á. Serrano (2017). Navigability of temporal networks in hyperbolic space. *Scientific Reports*, 7(1), Article 15054. <https://doi.org/10.1038/s41598-017-15041-0>. 11
- [130] E. Oster, & R. Thornton (2012). Determinants of technology adoption: Peer effects in menstrual cup take-up. *Journal of the European Economic Association*, 10(6), 1263–1293. <https://doi.org/10.1111/j.1542-4774.2012.01090.x>. 8
- [131] D. J. P. O’Sullivan, G. J. O’Keeffe, P. G. Fennell, & J. P. Gleeson (2015). Mathematical modeling of complex contagion on clustered

- networks. *Front. Phys.*, 3, Article 71. <https://doi.org/10.3389/fphy.2015.00071>. 23
- [132] Port Authority of New York and New Jersey (2019). *2018 anual airport traffic report*. <https://www.panynj.gov/content/dam/airports/statistics/statistics-general-info/annual-atr/ATR2018.pdf>. 101
- [133] R. Pastor-Satorras, C. Castellano, P. Van Mieghem, & A. Vespignani (2015). Epidemic processes in complex networks. *Reviews of Modern Physics*, 87(3), 925–979. <https://doi.org/10.1103/RevModPhys.87.925>. 15, 19, 33, 46, 56, 86
- [134] R. Pastor-Satorras, & A. Vespignani (2001). Epidemic spreading in scale-free networks. *Physical Review Letters*, 86(14), 3200–3203. 5, 81
- [135] R. Pastor-Satorras, & A. Vespignani (2002). Immunization of complex networks. *Physical Review E*, 65(3), Article 036104. <https://doi.org/10.1103/PhysRevE.65.036104>. 6
- [136] R. Pastor-Satorras, & A. Vespignani (2004). *Evolution and structure of the internet: A statistical physics approach*. Cambridge University Press. <https://doi.org/10.1017/CB09780511610905>. 6
- [137] J. A. Patz, A. K. Githeko, J. P. McCarty, S. Hussein, U. Con-falonieri, & N. de Wet (2003). Climate change and infectious diseases. In A. McMichael, D. Campbell-Lendrum, C. Corvalán, K. Ebi, A. Githeko, J. Scheraga, & A. Woodward (Eds.) *Climate change and human health: Risks and responses* (pp. 103–132). World Health Organization. <https://www.who.int/globalchange/publications/cchhbook/en/>. 1
- [138] M. Perc (2019). Diffusion dynamics and information spreading in multilayer networks: An overview. *The European Physical Journal Special Topics*, 228(11), 2351–2355. <https://doi.org/10.1140/epjst/e2019-900201-4>. 11

- [139] F. J. Pérez-Reche, J. J. Ludlam, S. N. Taraskin, & C. A. Gilligan (2011). Synergy in spreading processes: From exploitative to explorative foraging strategies. *Physical Review Letters*, 106(21), Article 218701. <https://doi.org/10.1103/PhysRevLett.106.218701>. 23
- [140] F. Pinotti, E. Fleury, D. Guillemot, P.-Y. Böelle, & C. Poletto (2019). Host contact dynamics shapes richness and dominance of pathogen strains. *PLOS Computational Biology*, 15(5), Article 1006530. <https://doi.org/10.1371/journal.pcbi.1006530>. 11
- [141] C. Poletto, V. Colizza, & P.-Y. Boëlle (2016). Quantifying spatiotemporal heterogeneity of MERS-CoV transmission in the Middle East region: A combined modelling approach. *Epidemics*, 15, 1–9. <https://doi.org/https://doi.org/10.1016/j.epidem.2015.12.001>. 7
- [142] S. Redner (1998). How popular is your paper? An empirical study of the citation distribution. *The European Physical Journal B*, 4(2), 131–134. <https://doi.org/10.1007/s100510050359>. 5
- [143] H. Rinne (2008). *The weibull distribution*. Chapman and Hall/CRC. <https://doi.org/10.1201/9781420087444>. 21
- [144] E. M. Rogers (2003). *Diffusion of innovations*, 5th edition. Simon & Schuster. 30
- [145] V. Rosato, L. Issacharoff, F. Tiriticco, S. Meloni, S. De Porcellinis, & R. Setola (2008). Modelling interdependent infrastructures using interacting dynamical models. *International Journal of Critical Infrastructures*, 4(1), 63–79. <https://doi.org/10.1504/IJCIS.2008.016092>. 8
- [146] K. J. Rothman (1996). Lessons from John Graunt. *The Lancet*, 347(8993), 37–39. [https://doi.org/10.1016/S0140-6736\(96\)91562-7](https://doi.org/10.1016/S0140-6736(96)91562-7). 1
- [147] L. Rozanova, & M. Boguñá (2017). Dynamical properties of the herding voter model with and without noise. *Physical Review E*, 96(1), Article 012310. <https://doi.org/10.1103/PhysRevE.96.012310>. 91

- [148] M. Salathé, & S. Bonhoeffer (2008). The effect of opinion clustering on disease outbreaks. *Journal of The Royal Society Interface*, 5(29), 1505–1508. <https://doi.org/10.1098/rsif.2008.0271>. 10
- [149] A. Schneeberger, C. H. Mercer, S. A. J. Gregson, N. M. Ferguson, C. A. Nyamukapa, R. M. Anderson, A. M. Johnson, & G. P. Garnett (2004). Scale-free networks and sexually transmitted diseases: A description of observed patterns of sexual contacts in Britain and Zimbabwe. *Sexually Transmitted Diseases*, 31(6), 380–387. [https://journals.lww.com/stdjournal/Fulltext/2004/06000/Scale\\_Free\\_Networks\\_and\\_Sexually\\_Transmitted.12.aspx](https://journals.lww.com/stdjournal/Fulltext/2004/06000/Scale_Free_Networks_and_Sexually_Transmitted.12.aspx). 5
- [150] T. Sellke (1983). On the asymptotic distribution of the size of a stochastic epidemic. *Journal of Applied Probability*, 20(2), 390–394. <https://doi.org/10.2307/3213811>. 19
- [151] N. Sherborne, J. C. Miller, K. B. Blyuss, & I. Z. Kiss (2018). Mean-field models for non-Markovian epidemics on networks. *Journal of Mathematical Biology*, 76(3), 755–778. <https://doi.org/10.1007/s00285-017-1155-0>. 11
- [152] C. I. Siettos, & L. Russo (2013). Mathematical modeling of infectious disease dynamics. *Virulence*, 4(4), 295–306. <https://doi.org/10.4161/viru.24041>. 3
- [153] J. Snow (1854). *Snow-cholera-map-1* [Image]. Wikimedia. <https://commons.wikimedia.org/wiki/File:Snow-cholera-map-1.jpg>. 3
- [154] J. Snow (1855). *On the mode of communication of cholera*, 2nd edition. John Churchill. 2, 3
- [155] M. Starnini, J. P. Gleeson, & M. Boguñá (2017). Equivalence between Non-Markovian and Markovian dynamics in epidemic spreading processes. *Physical Review Letters*, 118(12), Article 128301. <https://doi.org/10.1103/PhysRevLett.118.128301>. 11, 23
- [156] Statista (2020). *Number of domestic business and leisure trips in the United States from 2008 to 2023*. <https://www.statista.com/statistics/1091144/number-of-domestic-business-and-leisure-trips-in-the-us/>

- [//www.statista.com/statistics/207103/forecasted-number-of-domestic-trips-in-the-us/](http://www.statista.com/statistics/207103/forecasted-number-of-domestic-trips-in-the-us/). 102
- [157] G. Streftaris, & G. J. Gibson (2012). Non-exponential tolerance to infection in epidemic systems—modeling, inference, and assessment. *Biostatistics*, 13(4), 580–593. <https://doi.org/10.1093/biostatistics/kxs011>. 10
- [158] K. Sun, A. Baronchelli, & N. Perra (2015). Contrasting effects of strong ties on SIR and SIS processes in temporal networks. *The European Physical Journal B*, 88(12), Article 326. <https://doi.org/10.1140/epjb/e2015-60568-4>. 11
- [159] M. Tizzoni, P. Bajardi, C. Poletto, J. J. Ramasco, D. Balcan, B. Gonçalves, N. Perra, V. Colizza, & A. Vespignani (2012). Real-time numerical forecast of global epidemic spreading: case study of 2009 A/H1N1pdm. *BMC Medicine*, 10(1), Article 165. <https://doi.org/10.1186/1741-7015-10-165>. 7
- [160] J. Travers, & S. Milgram (1969). An experimental study of the small world problem. *Sociometry*, 32(4), 425–443. 5
- [161] R. C. Tyson, S. D. Hamilton, A. S. Lo, B. O. Baumgaertner, & S. M. Krone (2020). The timing and nature of behavioural responses affect the course of an epidemic. *Bulletin of Mathematical Biology*, 82(1), Article 14. <https://doi.org/10.1007/s11538-019-00684-z>. 11
- [162] E. Valdano, L. Ferreri, C. Poletto, & V. Colizza (2015). Analytical computation of the epidemic threshold on temporal networks. *Physical Review X*, 5(2), Article 021005. <https://doi.org/10.1103/PhysRevX.5.021005>. 11
- [163] E. Valdano, M. R. Fiorentin, C. Poletto, & V. Colizza (2018). Epidemic threshold in continuous-time evolving networks. *Physical Review Letters*, 120(6), Article 068302. <https://doi.org/10.1103/PhysRevLett.120.068302>. 11
- [164] P. Van Mieghem, & Q. Liu (2019). Explicit non-Markovian susceptible-infected-susceptible mean-field epidemic threshold for Weibull and

- Gamma infections but Poisson curings. *Physical Review E*, 100(2), Article 022317. <https://doi.org/10.1103/PhysRevE.100.022317>. 11
- [165] P. Van Mieghem, & R. van de Bovenkamp (2013). Non-Markovian infection spread dramatically alters the susceptible-infected-susceptible epidemic threshold in networks. *Physical Review Letters*, 110(10), Article 108701. <https://doi.org/10.1103/PhysRevLett.110.108701>. 11, 23
- [166] F. Vazquez, & V. M. Eguíluz (2008). Analytical solution of the voter model on uncorrelated networks. *New Journal of Physics*, 10(6), Article 063011. <https://doi.org/10.1088/1367-2630/10/6/063011>. 92
- [167] S. Vosoughi, D. Roy, & S. Aral (2018). The spread of true and false news online. *Science*, 359(6380), 1146–1151. <https://doi.org/10.1126/science.aap9559>. 8
- [168] A. Vázquez, J. G. Oliveira, Z. Dezsó, K.-I. Goh, I. Kondor, & A.-L. Barabási (2006). Modeling bursts and heavy tails in human dynamics. *Physical Review E*, 73(3), Article 036127. <https://doi.org/10.1103/PhysRevE.73.036127>. 11
- [169] A. Vázquez, B. Rácz, A. Lukács, & A.-L. Barabási (2007). Impact of non-poissonian activity patterns on spreading processes. *Physical Review Letters*, 98(15), Article 158702. <https://doi.org/10.1103/PhysRevLett.98.158702>. 11
- [170] P. Wang, M. C. González, C. A. Hidalgo, & A.-L. Barabási (2009). Understanding the spreading patterns of mobile phone viruses. *Science*, 324(5930), 1071–1076. <https://doi.org/10.1126/science.1167053>. 7
- [171] W. Wang, M. Tang, H.-F. Zhang, & Y.-C. Lai (2015). Dynamics of social contagions with memory of nonredundant information. *Physical Review E*, 92(1), Article 012820. <https://doi.org/10.1103/PhysRevE.92.012820>. 11, 19

- [172] D. J. Watts (2002). A simple model of global cascades on random networks. *Proceedings of the National Academy of Sciences*, 99(9), 5766–5771. <https://doi.org/10.1073/pnas.082090499>. 23
- [173] D. J. Watts, & S. H. Strogatz (1998). Collective dynamics of “small-world” networks. *Nature*, 393(6684), 440–442. <https://doi.org/10.1038/30918>. 5
- [174] L. Weng, F. Menczer, & Y.-Y. Ahn (2013). Virality prediction and community structure in social networks. *Scientific Reports*, 3(1), Article 2522. <https://doi.org/10.1038/srep02522>. 8, 9, 81
- [175] World Health Organization (2003). *Climate change and human health: Risks and responses. Summary*. <https://www.who.int/globalchange/summary/en/>. 1
- [176] World Health Organization (2009). *Dengue guidelines for diagnosis, treatment, prevention and control: new edition*. World Health Organization. <https://apps.who.int/iris/handle/10665/44188>. 10
- [177] World Health Organization (2018). *The top 10 causes of death*. <https://www.who.int/news-room/fact-sheets/detail/the-top-10-causes-of-death>. 9
- [178] World Health Organization (2020). *Antibiotic resistance*. <https://www.who.int/news-room/fact-sheets/detail/antibiotic-resistance>. 1
- [179] O. E. Williams, F. Lillo, & V. Latora (2019). Effects of memory on spreading processes in non-Markovian temporal networks. *New Journal of Physics*, 21(4), Article 043028. <https://doi.org/10.1088/1367-2630/ab13fb>. 11
- [180] L.-X. Yang, & X. Yang (2014). A new epidemic model of computer viruses. *Communications in Nonlinear Science and Numerical Simulation*, 19(6), 1935–1944. <https://doi.org/https://doi.org/10.1016/j.cnsns.2013.09.038>. 7
- [181] R. Zenner (2014). *Pestilence spreading 1347-1351 europe* [Image]. Wikimedia. [https://commons.wikimedia.org/wiki/File:Pestilence\\_spreading\\_1347-1351\\_europe.png](https://commons.wikimedia.org/wiki/File:Pestilence_spreading_1347-1351_europe.png). 6

- 
- [182] Q. Zhang, K. Sun, M. Chinazzi, A. Pastore y Piontti, N. E. Dean, D. P. Rojas, S. Merler, D. Mistry, P. Poletti, L. Rossi, M. Bray, M. E. Halloran, I. M. Longini, & A. Vespignani (2017). Spread of Zika virus in the Americas. *Proceedings of the National Academy of Sciences*. <https://doi.org/10.1073/pnas.1620161114>. 7
- [183] Y. Zhou, Z. Yue, Q.-H. Liu, & W. Wang (2019). Social reinforcement inducing discontinuous spreading in complex networks. *Europhysics Letters*, 128(6), Article 68002. <https://doi.org/10.1209/0295-5075/128/68002>. 11, 19
- [184] M. Zámková, M. Prokop, & R. Stolín (2017). Factors influencing flight delays of a European airline. *Acta Universitatis Agriculturae et Silviculturae Mendelianae Brunensis*, 65(5), 1799–1807. <https://doi.org/10.11118/actaun201765051799>. 105